Carbon Nanotube quantum dots: Transport, mechanical charge detection, and fabrication development

DISSERTATION
zur Erlangung des Doktorgrades der Naturwissenschaften
(Dr. rer. nat.)
der Fakultät für Physik
der Universität Regensburg
vorgelegt von

Karl Johann Georg Götz

aus Willenhofen

im Jahr 2017

Die Arbeit wurde von PD Dr. Andreas Hüttel angeleitet.
Das Promotionsgesuch wurde am 09.05.2017 eingereicht.
Das Kolloquium fand am 30.01.2018 statt.

Der Prüfungsausschuss

Vorsitzender: Prof. Dr. Ferdinand Evers
Erster Gutachter: PD Dr. Andreas K. Hüttel
Zweiter Gutachter: Prof. Dr. Jascha Repp
weiterer Prüfer: Prof. Dr. Sergey Ganichev

Contents

1 Introduction 7

2 Carbon Nanotube Quantum Dots 11
- 2.1 Band structure of carbon nanotubes 11
  - 2.1.1 Characterization of carbon nanotubes in real-space 12
  - 2.1.2 Band structure of graphene 14
  - 2.1.3 Zone-folding approximation for carbon nanotubes 15
  - 2.1.4 Beyond the zone-folding approximation 18
- 2.2 Bulk transport in carbon nanotubes 20
  - 2.2.1 Room-temperature characterization 20
  - 2.2.2 Conditions for ballistic transport 22
- 2.3 Quantized transport in carbon nanotubes 23
  - 2.3.1 Metallic and quantum Coulomb blockade 23
  - 2.3.2 Conditions and classifications of quantized transport 24
  - 2.3.3 A carbon nanotube as a quantum dot 25
- 2.4 Quantum dot spectroscopy 28
- 2.5 Transport in the intermediate and open regime 30
  - 2.5.1 Classification 30
  - 2.5.2 Co-tunneling and Kondo effect 31
  - 2.5.3 The Kondo effect in carbon nanotube quantum dots 34
  - 2.5.4 Fabry-Pérot regime 35

3 Overgrowth fabrication and measurement setups 37
- 3.1 Metallization 37
  - 3.1.1 Bond pads and outer leads 38
  - 3.1.2 Inner structures 39
- 3.2 Growth of carbon nanotubes 42
  - 3.2.1 Catalyst deposition 42
  - 3.2.2 Chemical vapor deposition 44
- 3.3 Preselection and statistics 44

3.4 Low-temperature setup: the dilution cryostat 47
3.5 Measurement setups 50
  3.5.1 dc cable filtering 50
  3.5.2 Voltage-bias setup 52
  3.5.3 Current-bias setup 52
  3.5.4 Mechanic setup 53

4 Transport spectroscopy of an ultraclean CNT-QD 55
4.1 Localization of transport regimes and band gap 56
  4.1.1 Transport regimes 56
  4.1.2 Band gap 56
4.2 Hole transport regime 58
4.3 Strong Coulomb blockade regime 60
4.4 Intermediate transport regime 64
4.5 Strong coupling regime 67
4.6 Temperature dependence of the Kondo correlation 70

5 Mechanical charge detection 73
5.1 Continuum response of the CNT resonator 73
  5.1.1 General differential equation and mechanisms 74
  5.1.2 Parameters for a CNT resonator 75
  5.1.3 Detection mechanism 77
  5.1.4 Calibration of the setup to linear resonator response 78
5.2 Sensitivity to charge transitions in the quantum dot 80
5.3 Model for the average charge on a quantum dot 81
5.4 Fitting pre-existing data 86
5.5 Hole side, mixed valence regime and Fabry-Pérot interferometry 92
5.6 Low electron numbers regime 94
5.7 Strong coupling regime 96
5.8 Temperature dependence of the Kondo peak 100

6 Optimization of molybdenum rhenium alloys 103
6.1 Co-sputtered MoRe films 104
  6.1.1 Resulting alloys 104
  6.1.2 Influence of CNT growth environment 106
  6.1.3 dc characterization 108

6.2 MoRe films of premixed targets . . . 110
  6.2.1 XPS properties of the pristine films . . . 110
  6.2.2 CVD influence on the film properties . . . 112
  6.2.3 dc characterization . . . 114

7 Low temperature transport in MoRe-CNT devices 115
7.1 Co-sputtered MoRe-CNT device . . . 116
  7.1.1 Characterization at base temperature . . . 116
  7.1.2 Current-bias measurement . . . 118
7.2 Premixed MoRe-CNT device . . . 120
  7.2.1 Characterization at base temperature . . . 120
  7.2.2 Quantum dot spectroscopy . . . 122

8 Development of nanotube transfer techniques 125
8.1 Starting point and motivation . . . 125
8.2 Building up a new fabrication process . . . 126
8.3 Characterization of the transferred nanotubes . . . 130
8.4 Low temperature measurements . . . 132
  8.4.1 Niobium device . . . 132
  8.4.2 MoRe device . . . 134

9 Conclusion and outlook 137

A Fabrication methods, techniques and parameters 143
A.1 Wafer material preparation . . . 143
A.2 Cleaning . . . 144
A.3 Optical lithography . . . 145
A.4 Electron Beam Lithography . . . 146
A.5 Metal Evaporation setup I: Univex 450A . . . 149
A.6 Metal Evaporation setup II: Orion . . . 150
A.7 Lift-off . . . 154
A.8 Reactive ion etching (RIE) . . . 155
A.9 Carbon nanotube growth catalyst . . . 157
A.10 Catalyst Deposition and Lift-off . . . 159
A.11 Setup for chemical vapor deposition and growth process . . . 160
A.12 Preparation and bonding . . . 161

B Device fabrication recipes **163**
B.1 Platinum sample 163
B.2 Co-sputtered MoRe sample 166
B.3 Premixed MoRe sample 168

Bibliography **171**

Acknowledgments **189**

Curriculum Vitae **191**

Chapter 1

Introduction

Since at least the experiment by Millikan on the speed measurements of ionized oil drops in an electric field, effects due to single electron charging are known and proven [Millikan, 1911]. In solid metallic grains, single electron tunneling was studied in the 1950s, followed by the development of the related transport theory in the 1970s [Gorter, 1951; Kulik and Shekhter, 1975].
With the aid of miniaturization techniques developed in the 1980s as e.g. lithography, molecular-beam epitaxy, and thin-film deposition, devices could be created exhibiting controlled single electron tunneling, for example in an aluminum island as shown in [Fulton and Dolan, 1987]. From the side of semiconductor technology, highly conducting interfaces in heterostructures can be further confined down to the nanometer-scale. In [Reed et al., 1988], first transport measurements at cryogenic temperatures were reported showing resonant tunneling currents through semiconductor nanostructures, later theoretically described in [Glazman and Shekhter, 1989]. Since that time, such small islands exhibiting discrete states are denoted as quantum dots.

In contrast, due to their cylindrical shape with diameters in the nanometer-range, carbon nanotubes are conductors confined by nature. The thickness of these carbon cylinders is determined by the layers of graphene which are concentrically rolled up, see [Saito et al., 1998; Castro Neto et al., 2009]. The tubes are denoted as single-walled or multi-walled carbon nanotubes created by rolling up either one single- or a multi-layer graphene sheet. By means of transmission electron microscopy (TEM), multi-walled carbon nanotubes, short MWCNTs, were depicted first in [Radushkevich and Lukyanovich, 1952]. Forty years later, [Iijima, 1991] rediscovered CNTs of even only two-layer-walls. Soon after, the growth of single-walled carbon nanotubes was reported almost at once in [Iijima and Ichihashi, 1993; Bethune et al., 1993].
In [Kong et al., 1998b], a fabrication method is presented to achieve individual SWCNT on

a substrate. Here, a mixture of catalytic active material containing iron, molybdenum, and alumina is deposited onto small lithographically defined areas on a silicon substrate. After being exposed to a chemical vapor deposition (CVD) process using methane CH_4, the substrate contains single-walled carbon nanotubes grown outwards from the catalyst areas. Localizing individual tubes on the substrate by means of scanning electron microscopy (SEM) is a necessary step before contacting by metallic electrodes. Low-temperature transport in such CNT-devices is experimentally characterized e.g. in [Tans et al., 1997; Nygård et al., 1999; Liang et al., 2001]. Regarding clean carbon nanotubes, the fabrication process was optimized by performing the growth step at last. The hereby obtained SWCNTs are suspended over prefabricated electrodes, untouched by further lithography, imagining or even interactions with the substrate material. Soon, this overgrowth method lead to measurements on suspended single-walled carbon nanotube quantum dots revealing also the very first electron transition, as e. g. published in [Cao et al., 2005].
In addition, suspended carbon nanotubes act as nano-electromechanical system (NEMS), which was reported first in [Sazonova et al., 2004]. The lowermost, transversal vibrational mode is detected in the MHz range with a resonance frequency depending on the suspended CNT-length L. In the vacuum at cryogenic temperatures, such NEMS exhibit quality factors exceeding 10^5, see [Hüttel et al., 2009; Schmid et al., 2012; Moser et al., 2014]. Especially in ultraclean devices in the quantum dot regime, single-electron transitions appear as a resonance frequency dip, as shown first in [Steele et al., 2009b; Lassagne et al., 2009] and later among others also in [Benyamini et al., 2014].

At University of Regensburg, the overgrowth technique is used since 2010 to fabricate suspended clean carbon nanotube devices, see [Schmid, 2010]. The results shown in the present thesis expand on that experience and knowledge to establish quantum dots in clean and suspended CNTs. By using the behavior of the vibrational resonance frequency to probe single-electron transitions, it is shown that especially the Kondo effect [Kondo, 1964] has an influence on the transport through a carbon nanotube quantum dot but not on the vibrational properties. This detection scheme reveals the charge distribution in Kondo-correlated quantum dots and confirm the observations shown formerly in [Sprinzak et al., 2002].
The second part of this thesis deals with the optimization of the superconducting alloy molybdenum rhenium [Lerner and Daunt, 1966; Postnikov et al., 1977; Seleznev et al., 2008] in combination with carbon nanotube growth on it. It shows the results on examinations of molybdenum rhenium alloys regarding composition, the influence of CNT growth process, and its superconducting properties as already published for co-sputtered films in

[Götz et al., 2016]. Furthermore, sputtered films originating from premixed targets are investigated in the same manner and evaluated. The most suitable alloy for the overgrowth process is found, and then patterned to contact electrodes for suspended carbon nanotubes. Results on low temperature measurements of MoRe-CNT devices fabricated by both sputtering techniques are shown as well in this thesis. Even though superconducting transport features in these devices are not observed, it is proven that clean and suspended carbon nanotube quantum dots on molybdenum rhenium alloys are established.

Supercurrents through CNTs contacted after growth by niobium leads are reported in [Pallecchi et al., 2008]. An alloy out of MoRe already served as contact electrodes to suspended carbon nanotubes exhibiting supercurrents as shown in [Schneider et al., 2012], in addition to pure rhenium [Keijzers, 2012].

Thereafter, a summary concerning a new attempt for CNT device fabrication is placed within this thesis: the carbon nanotube is grown on an extra chip and afterwards transferred to a chip containing electrodes. First low temperature characterization measurements of such devices are also depicted.

Following this introduction, this thesis is divided into eight chapters: chapter 2 contains the theoretical background necessary to understand quantum dot transport in carbon nanotubes. It is followed by chapter 3 dealing with the optimization of fabricating overgrown CNT devices. The cryogenic measurement setup is also described within this chapter. Chapter 4 shows the results on low temperature transport through a clean carbon nanotube quantum dot, followed by its mechanical characterization in chapter 5. Chapter 6 and chapter 7 deal with material optimization for MoRe and characterization of respective CNT devices. Chapter 8 summarizes the progress on the carbon nanotube stamping attempts at the University of Regensburg. Finally, chapter 9 reports on the most important results of the previous chapters, and especially gives an outlook on future stamping technique trends.

Appendix chapter A states the applied fabrication setups, techniques, and procedures, whereas appendix chapter B lists detailed recipes of the main three devices. At the end of this thesis, bibliography, acknowledgments, a short curriculum vitae, and the affirmation are placed.

Chapter 2

Carbon Nanotube Quantum Dots

This chapter contains basic theoretical background needed to discuss quantum dots in carbon nanotubes.

Starting with a discussion of the structure of a CNT in section 2.1, which includes information about chirality and band gap size, a classification of all nanotube types is obtained. This enables a prediction of the electrical transport behavior when contacted to leads and manipulated by a global back gate, as depicted in section 2.2. This section also deals with the conditions for ballistic transport as given in the low temperature limit.

In section 2.3, a classification of quantum dots is given and conditions for Coulomb blockade transport are stated. In addition, the characteristic quantities of a carbon nanotube quantum dot are defined. It is followed by section 2.4, which describes the experimental determination of these quantities.

By increasing the coupling between dot and lead, additional effects appear in transport measurements. This is the content of the last section 2.5 of this chapter. It includes a description of the situation when the barriers completely disappear leading to pure ballistic transport at low temperatures.

2.1 Band structure of carbon nanotubes

In contrast to rather randomly fabricated and observed carbon nanotubes, [Radushkevich and Lukyanovich, 1952; Iijima, 1991], both multi-walled as well as single-walled carbon nanotubes (MWCNTs and SWCNTs) can be nowadays synthesized in a reproducible way, [Iijima and Ichihashi, 1993; Bethune et al., 1993; Kong et al., 1998b; Kong et al., 1998a]. Since this thesis focuses on the examination of SWCNTs, only this type is discussed in the following. A single-walled carbon nanotube is equivalent to one rolled-up strip taken from the two-dimensional honeycomb of carbon atoms that makes up a graphene sheet, see [Charlier et al., 2007; Laird et al., 2015].

2.1.1 Characterization of carbon nanotubes in real-space

In graphene, the two-dimensional molecular lattice is formed by the two basis vectors

$$\vec{a}_1 = \left(\frac{\sqrt{3}}{2}, +\frac{1}{2}\right) a \text{ and } \vec{a}_2 = \left(\frac{\sqrt{3}}{2}, -\frac{1}{2}\right) a \ . \tag{2.1}$$

In order to have a unique description of a SWCNT, a so-called chiral vector $\vec{C}$ is defined. It connects the lattice sites on opposite sides of a graphene strip, which are superposed after "rolling it up" into a carbon nanotube. In terms of the graphene basis vectors according to eq. 2.1, $\vec{C}$ is expressed by

$$\vec{C} = n\vec{a}_1 + m\vec{a}_2 \ . \tag{2.2}$$

By definition, the tuple (n,m) consists of two integers, and m is restricted by the condition $-n/2 < m \leqslant n$ to exclude that the same structure is labeled several times. The tuple (n,m) is sufficient to describe one certain type of SWCNT. The unit cell of a SWCNT is spanned by $\vec{C}$ and the translational vector $\vec{T}$, which is defined by

$$\vec{T} = t_1\vec{a}_1 + t_2\vec{a}_2 = \frac{2m+n}{\gcd(2m+n, 2n+m)}\vec{a}_1 - \frac{2n+m}{\gcd(2m+n, 2n+m)}\vec{a}_2 \ , \tag{2.3}$$

with gcd being the greatest common divisor of the two arguments.

As an alternative, a CNT can be specified by its diameter d and chiral angle θ. d results from the circumference of the nanotube given by the length of the chiral vector, therefore

$$|\vec{C}| = a\sqrt{n^2 + nm + m^2} \Rightarrow d = |\vec{C}|/\pi \ . \tag{2.4}$$

θ is the angle between $\vec{C}$ and $\vec{a}_1$, it follows:

$$\cos(\theta) = \frac{\vec{C} \circ \vec{a}_1}{|\vec{C}| \cdot |\vec{a}_1|} \ , \tag{2.5}$$

$$\theta = \arccos\left(\frac{2n+m}{2\sqrt{n^2 + nm + m^2}}\right) = \arctan\left(\frac{\sqrt{3}m}{2n+m}\right) \ , \tag{2.6}$$

where $-\pi/6 < \theta \leqslant \pi/6$.

Two special classes are zig-zag-($m = 0$) and armchair-($n = m$) nanotubes. These denominations are chosen due to the arrangement of atoms along a cut normal to the nanotube axis. All others are called chiral nanotubes because of the twist of the molecular arrangement along its axis. An example for creating a CNT out of graphene and the resulting classifications are plotted in Figure 2.1.

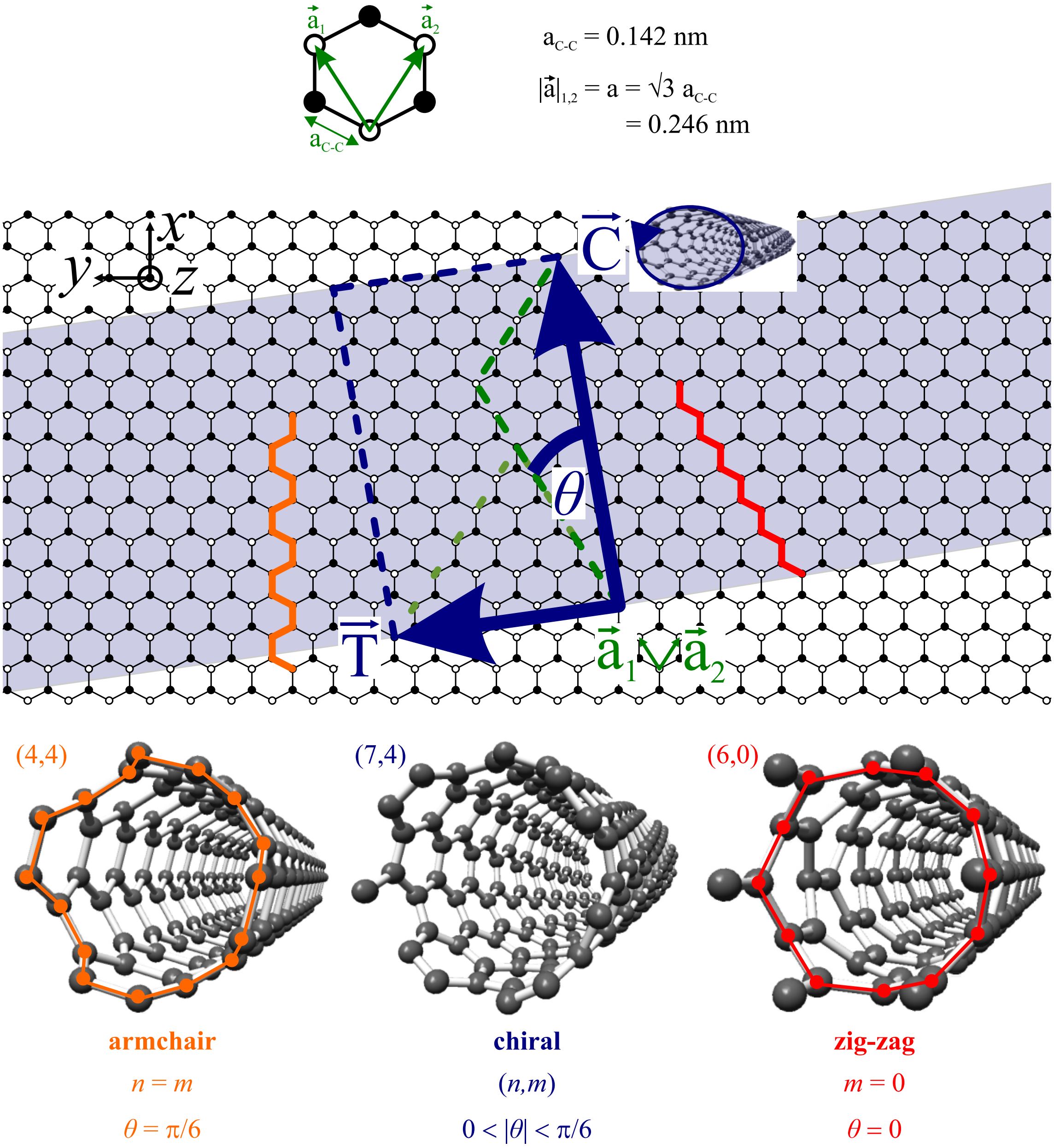

Figure 2.1: Deriving the structure of a carbon nanotube from a graphene sheet: the two basis vectors $\vec{a}_{1,2}$ have lengths $\sqrt{3}a_{\mathrm{C-C}}$ as a function of the bond length $a_{\mathrm{C-C}}$ (top). The chiral vector $\vec{C}$, for this example $(n,m) = (7,4)$, is drawn into a graphene sheet. The unit cell of a CNT is marked by the dashed blue lines, and spanned by $\vec{C}$ and the translational vector $\vec{T}$, here $(t_1,t_2) = (5,-6)$. The chiral angle for this example is $\theta \approx 21.05°$ (further definitions see text). The CNT created by rolling the shaded strip up is sketched in the inset, to visualize the embracing meaning of $\vec{C}$. Below, examples for the three classes of CNTs are plotted; colorized intersections of armchair (orange) and zig-zag (red) edges, as found in the graphene sheet, are indicated in the nanotubes. The CNT segments were generated using *Nanotube Modeler* (©, JCrystal Soft, 2017).

2.1.2 Band structure of graphene

In a free carbon atom, six electrons occupy the configuration $1s^2 2s^2 2p^2$. The second shell consists of a s-orbital and three p-orbitals, namely p_x, p_y, and p_z. Since each orbital can house two electrons with different spin, only four of eight states in the second shell are occupied.

For graphene and carbon nanotubes, sp^2-hybridization takes place among 2s-, $2p_x$-, and $2p_y$-orbitals. However, the $2p_z$ orbital, which is oriented perpendicular to the plane does not participate in the hybridization because of its odd parity under z-inversion (in contrast to the other $2p_{x,y}$-orbitals). Further hybridization across neighboring atoms in graphene forms a bonding band σ and an antibonding band σ^* out of all sp^2-hybridized orbitals. Hybridization between neighboring $2p_z$ orbitals forms bonding and antibonding bands denoted as π and π^*. Compared to σ- and σ^*-bands, π-bands exhibit a smaller bonding energy. In undoped graphene, the bonding bands are exactly filled with three electrons occupying the σ- and one the π-band per atom. Since the σ-band remains filled at all times, it does not participate in transport. The electrical behavior of nanotubes as well as of graphene is therefore determined by the properties of the π- and π^*-bands.

The hexagonal Brillouin zone of graphene is spanned by two basis vectors $\vec{b}_1$ and $\vec{b}_2$. Both fulfill the orthogonality condition $\vec{b}_i \circ \vec{a}_j = 2\pi\delta_{ij}$ with respect to the real-space basis vectors $\vec{a}_j$ from equation 2.1. It follows therefore

$$\vec{b}_1 = \left(\frac{1}{\sqrt{3}}, +1\right) \cdot \frac{2\pi}{a} \quad \text{and} \quad \vec{b}_2 = \left(\frac{1}{\sqrt{3}}, -1\right) \cdot \frac{2\pi}{a} \quad . \tag{2.7}$$

The corners of the k-space hexagon are labeled as K and K', see Figure 2.2(b). Since the three K, respectively three K' points are connected by reciprocal lattice vectors $\vec{b}_{1,2}$, they correspond to equivalent electronic states according to Bloch's theorem. The two points on the k_y-axis are given by:

$$\vec{K} = \frac{\vec{b}_2 - \vec{b}_1}{3} = (0, -1) \cdot \frac{4\pi}{3a} \quad \text{and} \quad \vec{K}' = -\frac{\vec{b}_2 - \vec{b}_1}{3} = (0, 1) \cdot \frac{4\pi}{3a} \quad , \tag{2.8}$$

Even though there is no band gap, π- and π^*-bands touch only at K and K'. The Fermi level E_F intersects the band structure at these points (for $T = 0\,\mathrm{K}$) and the energy dispersion is thus linear around K and K'. Hence, undoped graphene is neither a true metal nor a true semiconductor, but a semimetal.

The energy dispersion relation for graphene is according to [Saito et al., 1998]:

$$E_{\mathrm{gr}}^{\pm}(k_x, k_y) = \pm\gamma_0 \left[1 + 4\cos\left(\frac{\sqrt{3}k_x a}{2}\right)\cos\left(\frac{k_y a}{2}\right) + 4\cos^2\left(\frac{k_y a}{2}\right)\right]^{1/2} \quad . \tag{2.9}$$

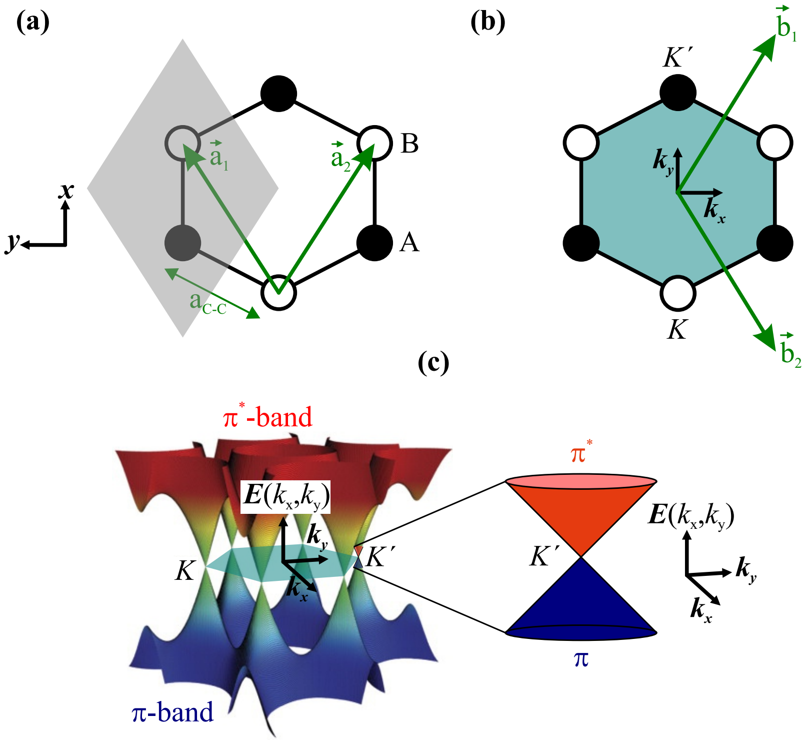

Figure 2.2: The reciprocal lattice of graphene. **(a)** The basis vectors of the real-space lattice. The gray-shaded area is the unit cell of the graphene lattice, which consists of two sublattices A and B. **(b)** In the reciprocal space, the first Brillouin zone exhibits also a hexagonal shape with points denoted as K and K' at the corners. The two corresponding basis vectors $\vec{b}_{1,2}$ are sketched. **(c)** The energy dispersion $E^{\pm}_{\mathrm{gr}}(k_x, k_y)$, mapped as a 3d-plot. The gray-green shaded 2d-area (c. f. **(b)**) serves as orientation where π- and π^*-band intersect each other: at these points for valence and conduction band, K, K', the dispersion can be approximated as a double cone as sketched on the right. The 3d-plot is taken from [Katsnelson, 2007]. For further definitions and relations see the text.

Here, $+$ denotes for the conduction π^*-band and $-$ the valence π-band. $\gamma_0 = (2.7 \pm 0.1)\,\mathrm{eV}$ is the overlap energy, see [Saito et al., 1998]. The energy dispersion is plotted in Figure 2.2(c).

2.1.3 Zone-folding approximation for carbon nanotubes

The graphene band structure as shown in subsection 2.1.2 has to be modified for carbon nanotubes due to the periodic boundary condition originating from "rolling up" the graphene sheet. This modification is also known as zone-folding approximation. The introduced condition is $\vec{k} \circ \vec{C} = 2\pi p$, where p is an integer. The component of $\vec{k}$ perpendicular to the nanotube axis becomes

$$k_\perp = \frac{2p}{d} = \frac{2\pi p}{|\vec{C}|} \quad . \tag{2.10}$$

The allowed $\vec{k}$-values correspond to a series of lines in reciprocal space, known as quantization lines and running at an angle $\pi/2+\theta$ from the k_x-axis. Thus, the distance between such two quantization lines is of $\Delta k_\perp = 2/d = 2\pi/|\vec{C}|$.
In contrast, the dispersion along the nanotube axis direction, along $\vec{T}$, as a function of $k_{||}$, remains continuous. Regarding the dispersion around the Dirac points K and K', by writing $\vec{k} = \vec{K} + \vec{\kappa}$ or $\vec{k} = \vec{K}' + \vec{\kappa}$ and defining $E_\mathrm{F} = 0$, the energy dispersion along the nanotube axis, $E(\kappa_{||})$ is a cut along the quantization lines of the two-dimensional graphene dispersion relation, see Figure 2.3. With these restrictions, two messages are obtained: if the energetically lowest quantization lines for $k_\perp$ intersect the Dirac points, $E(\kappa_{||})$ is linear near $\kappa_{||} = 0$ resulting in a zero band gap and thus a metallic nanotube, see Figure 2.3(c). Consequently, the zone folding-approximation delivers the condition for a metallic nanotube as function of the chiral indices:

$$\vec{K} \circ \vec{C} = 1/3 \cdot (n-m) \cdot 2\pi \overset{\text{eq. 2.10}}{=} 2\pi p \quad \Leftrightarrow \quad (n-m) = 3p \quad . \tag{2.11}$$

If the lines miss the Dirac points by $\Delta\kappa_\perp$, the dispersion for $E(\kappa_{||})$ results in hyperbola for the π^*- and π-bands which are separated by a band gap

$$E_\mathrm{G} = 2\hbar v_\mathrm{F} \Delta\kappa_\perp = 4/3\hbar v_\mathrm{F} \cdot d^{-1} \approx 700\,\mathrm{meV}/d(\mathrm{nm}) \quad , \tag{2.12}$$

and hence a semiconducting nanotube, see Figure 2.3(d). The energy dispersion for a semiconducting CNT is [Zhou et al., 2005]

$$E^\pm(\kappa_{||}) = \pm\sqrt{\hbar^2 v_\mathrm{F}^2 \kappa_{||}^2 + E_\mathrm{G}^2/4} \quad , \tag{2.13}$$

with $v_\mathrm{F} = \hbar^{-1} \cdot \nabla_{\vec{k}} E$ being the Fermi velocity. The effective mass of a CNT can be derived from the curvature of equation 2.13 and is of

$$m_\mathrm{eff} = \hbar^2 \cdot \left(\frac{\mathrm{d}^2 E^\pm(\kappa_{||})}{\mathrm{d}\kappa_{||}^2} \right)^{-1} \approx \frac{E_\mathrm{G}}{7.3\,\mathrm{eV}} \cdot m_\mathrm{e} \quad , \tag{2.14}$$

where m_e is the free electron mass. The experimentally determined band gap energies are in the range of $E_\mathrm{G} \approx 10\ldots100\,\mathrm{meV}$, see e. g. [Cao et al., 2005]. According to equation 2.12, such small band gap values would result in CNT diameters ranging from $d = 7\ldots70\,\mathrm{nm}$.

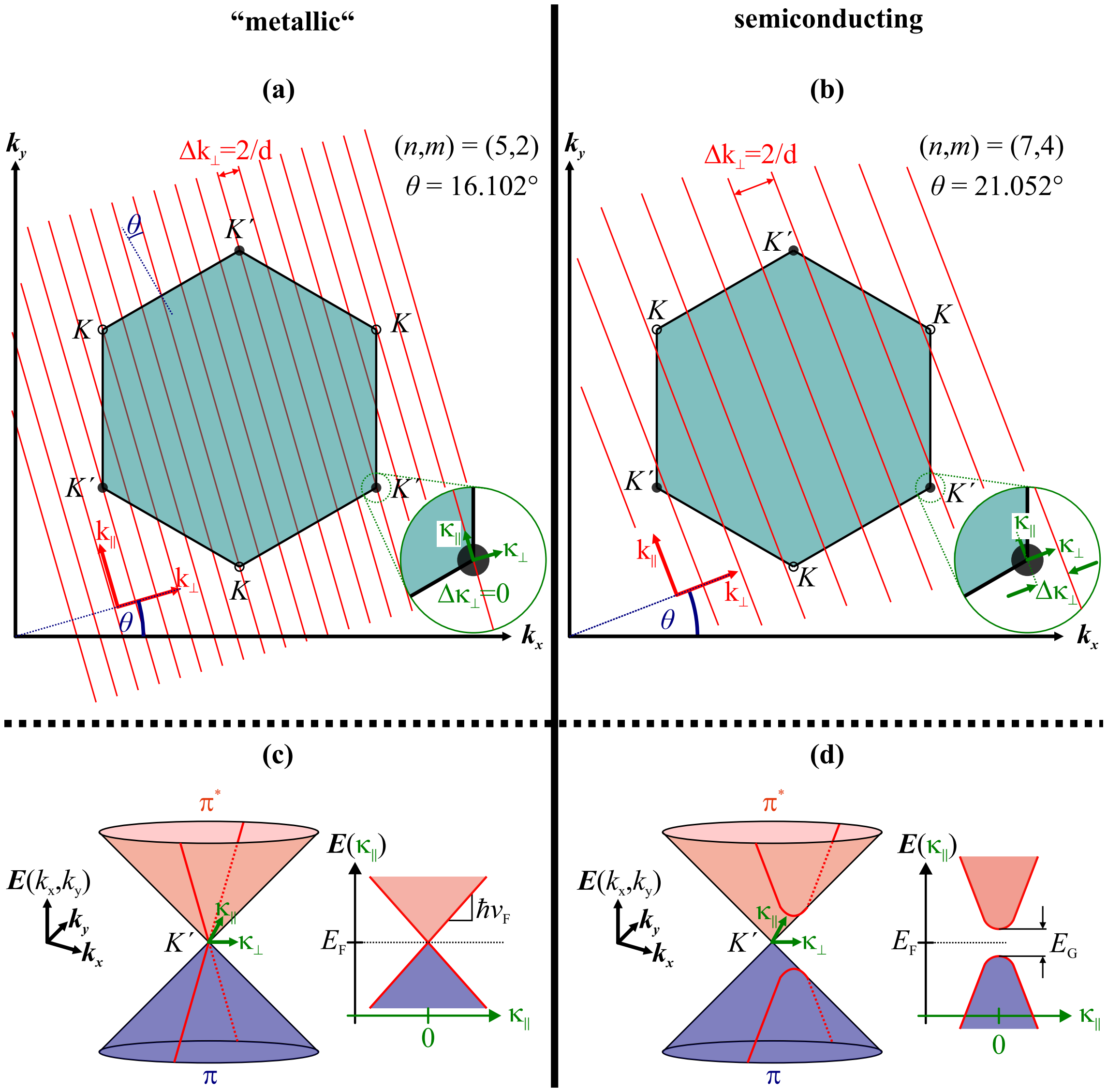

Figure 2.3: The results on the zone-folding approximation. **(a)** The quantization lines intersect the corners K, K', this results here in a metallic nanotube. The inset shows a zoom at K', where $\Delta\kappa_\perp = 0$. Note that the example is a chiral nanotube. **(b)** Example for a semiconducting nanotube; the quantization lines are shifted by $\Delta\kappa_\perp$. The $k_{||}$ $(k_\perp)$-axis corresponds to the motion along(around) the CNT. In **(c)** and **(d)**, the resulting dispersions for the lowest energy 1d band close to K' are sketched. In **(d)**, $\Delta\kappa_\perp$ is the origin of the band gap E_G. E_F is indicated for an undoped CNT at $T = 0\,\mathrm{K}$. This figure was created following [Laird et al., 2015].

CNTs which exhibit such large diameters are structurally unstable and do not exist. As will be shown in subsection 2.1.4, even nanotubes classified as metallic according to equation 2.11, show a small band gap in transport measurements which originates from additional perturbations in the band structure of carbon nanotubes.

2.1.4 Beyond the zone-folding approximation

Additional perturbations in the band structure are the overlap between adjacent electron orbitals, i. e., deformation of the carbon bonds. One unavoidable example for this is the curvature introduced by rolling up the graphene sheet. It leads to two effects on the CNT band structure [Blase et al., 1994]. The first one is a small renormalization of the Fermi velocity v_F by at most a few percent and is not significant for experiments. The second effect is the displacement of the Dirac points in reciprocal space away from K and K' and breaking the three-fold symmetry in the first Brillouin zone, see also [Kane and Mele, 1997; Izumida et al., 2009].

This shift is represented in Figure 2.4 by a displacement vector $\Delta\vec{\kappa}^{\mathrm{cv}}$. Semiconducting nanotubes exhibit a $|\Delta\vec{\kappa}^{\mathrm{cv}}|$ much smaller than the offset from the zone-folding approximation $\Delta\kappa_{\perp}$. In nominally metallic nanotubes fulfilling equation 2.11, the shift of the Dirac cones relative to the quantization lines introduces a band gap as

$$E_{\mathrm{G}} = 2\hbar v_{\mathrm{F}} \Delta\kappa_{\perp}^{\mathrm{cv}} = \frac{\hbar v_{\mathrm{F}} a_{\mathrm{CC}}}{2d^2} \cdot \cos 3\theta \approx \frac{40\,\mathrm{meV}}{d(\mathrm{nm})^2} \cdot \cos 3\theta \tag{2.15}$$

with $\kappa_{\perp}^{\mathrm{cv}}$ being the component of $\Delta\vec{\kappa}^{\mathrm{cv}}$ perpendicular to the nanotube axis. The curvature-induced band gap according to equation 2.15 is always smaller than the gap originating from zone-folding, see equation 2.12, and depends on the chiral angle θ.

For armchair nanotubes ($\theta = \pi/6$, see Figure 2.1) follows $\cos 3\theta = 0$, resulting in $E_{\mathrm{G}} = 0$. If no other perturbation is applied, these are the only nanotubes expected to be truly metallic, see also Figure 2.4(b).

A further source of a possible perturbation is strain, which also depends on nanotube chirality [Heyd et al., 1997]. An uniaxial strain ξ (units %) results in a Dirac point displacement in the same direction, and a band gap

$$E_{\mathrm{G}} = \frac{2\hbar v_{\mathrm{F}}}{a_{\mathrm{CC}}} \cdot \frac{12\varsigma}{1+6\varsigma} \cdot (1+\lambda)\xi \cos 3\theta \approx 51\,\mathrm{meV} \cdot \xi(\%) \cdot \cos 3\theta \ , \tag{2.16}$$

where $\lambda \approx 0.2$ is the Poisson ratio and $\varsigma \approx 0.066$ is a parameter related to the carbon-carbon bond force constants [Huang et al., 2008].

A third perturbation due to torsional strain γ (units °/µm) is reported in [Yang and Han, 2000], leading to a band gap

$$E_{\mathrm{G}} = 2\hbar v_{\mathrm{F}} \gamma \sin 3\theta \approx 0.018\,\mathrm{meV} \cdot \gamma(^{\circ}/\mu\mathrm{m}) \cdot \sin 3\theta \ . \tag{2.17}$$

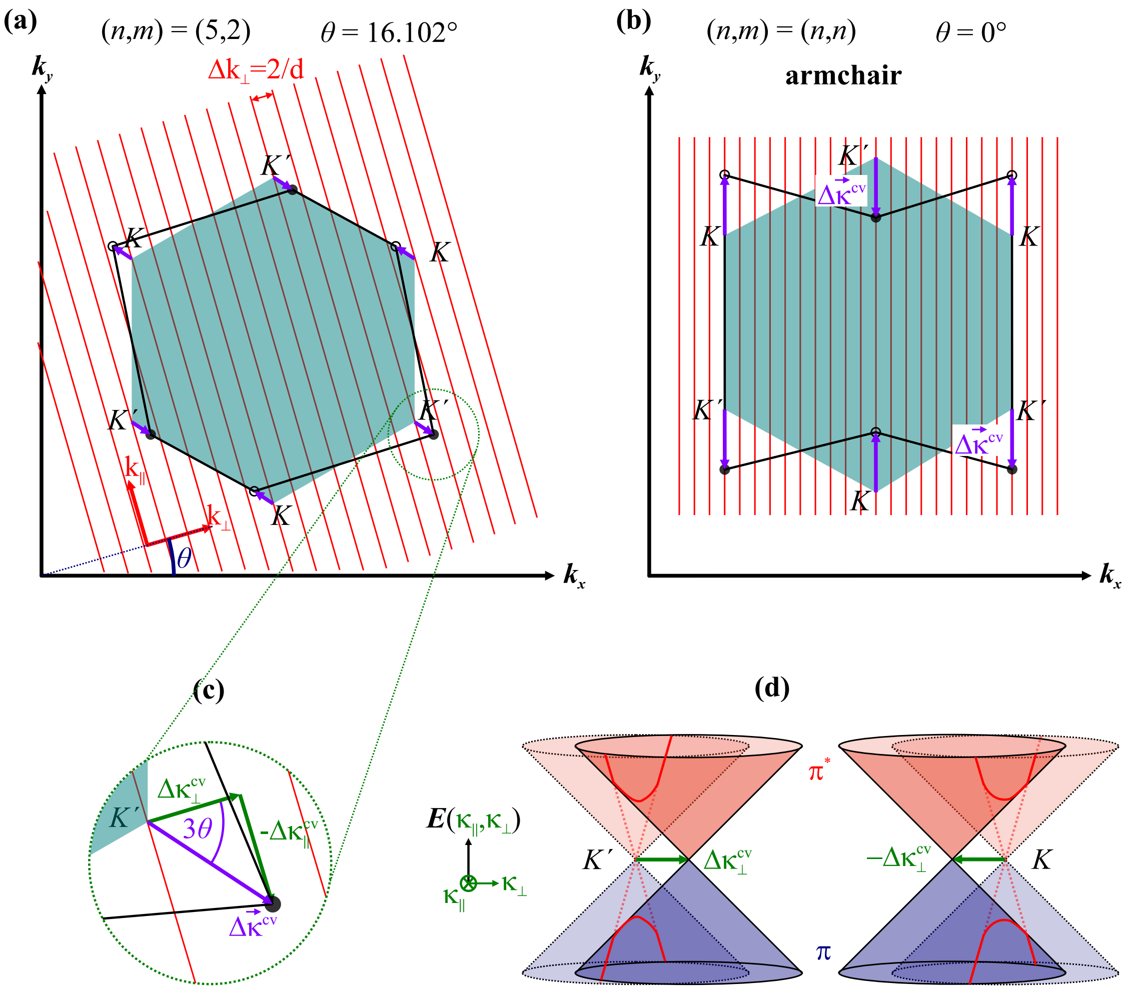

Figure 2.4: The band gap introduced by the CNT-curvature. **(a)** Impact on the originally metallic CNT from 2.2**(a)**: the corners of the first Brillouin zone shift due to $\Delta\vec{\kappa}^{\mathrm{cv}}$. For time reversal symmetry arguments, it is of opposite sign at K and K', see [Castro Neto et al., 2009]. The vector can be separated into a parallel and perpendicular component, as shown in **(c)**. Note that $|\Delta\vec{\kappa}^{\mathrm{cv}}| < \Delta\kappa_\perp < \Delta k_\perp$, since the curvature-induced gap is much smaller than the one originating from the zone-folding approximation. The shift of the corners leads to a band gap as sketched in **(d)**. **(b)** shows the effect on armchair nanotubes: since the curvature induced shift has only an effect on the parallel component of $\vec{k}$, respectively $\vec{\kappa}$, the bands can still intersect at the corners. This figure was created following [Laird et al., 2015].

Armchair nanotubes are insensitive to uniaxial strain but most sensitive to torsional strain, while for zig-zag-nanotubes the opposite statements are the case. Nanotube bending has no first-order effects on the band gap [Kane and Mele, 1997].

type	chiral indices	equation (2.11)	band gap dependence
metallic	(n,n)	$n-n=0$	no gap
small-gap	(n,m)	$n-m=3p$	$\propto 1/d^2$
large-gap	(n,m)	$n-m\neq 3p$	$\propto 1/d$

Table 2.1: Overview of carbon nanotube types.

2.2 Bulk transport in carbon nanotubes

It is rather difficult determining the chirality of nanotubes without any influence on its structural purity. For example, a high-energy electron-beam of the scanning electron microscope can affect the structure of the nanotube, and in general, it gets doped by environmental atoms or molecules like amorphous carbon in the setup chamber. Therefore, preselection processes which can damage the structure of the CNT must be excluded.

Electronic characterization of possible devices at room-temperature allows to determine the overall type of the nanotube as given in the Table 2.1.

2.2.1 Room-temperature characterization

Single-walled carbon nanotubes suspended over prefabricated contacts can be probed electrically even at room temperature, see Figure 2.5(a). By varying the gate voltage V_{g} at a constant and small bias $V_{\mathrm{sd}} \approx$ mV, band gaps down to a size of $E_{\mathrm{G}} \approx k_{\mathrm{B}}T \approx 26\,\mathrm{meV}$ can be detected by the measured current I through the device. Here, V_{g} shifts the energy levels respectively the bands up or down and therefore tunes the position of the gap relative to E_{F}. By tuning E_{F} into the band gap, a drop or even a full suppression of the current I can be induced.

The minimal room-temperature resistance of the device is determined by the bias divided through the current measured in the open regime at large negative V_{g}. Hence, devices exhibiting a current drop as well as a resistance between $10\ldots60\,\mathrm{k\Omega}$ are identified as small-gap nanotubes, see Figure 2.5(c). In contrast, devices having a clear current suppression over a large gate range are large-gap nanotubes, see Figure 2.5(b). In addition to that, their resistance ranges often above $100\,\mathrm{k\Omega}$. Devices which show a constant I as function of V_{g} in combination with a resistance of about $10\ldots30\,\mathrm{k\Omega}$ are identified as (quasi-)metallic, see Figure 2.5(d).

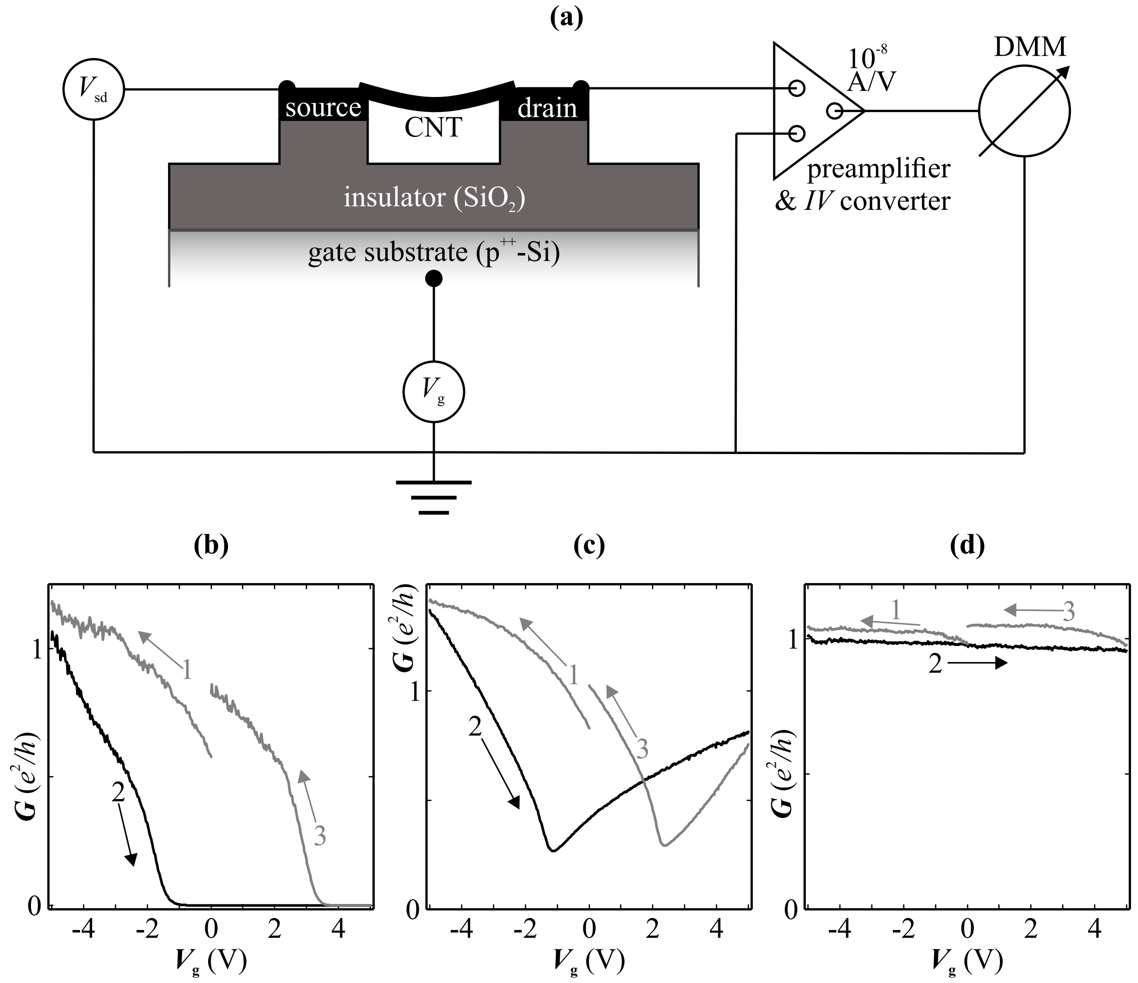

Figure 2.5: Room temperature setup to probe a suspended CNT, and three typical $G\left(V_g\right)$-characteristics. **(a)** Measurement setup: Two voltage supplies are connected to the back gate substrate, and to the source, respectively. The current I through the device is amplified and converted to a voltage signal which is read out by a subsequent digital multimeter. **(b)** Trace of a large-gap nanotube, **(c)** of a small-gap CNT, and **(d)** of a (quasi-)metallic device. **(b)**-**(d)** The measured current is divided by the bias voltage V_{sd} and plotted in units of e^2/h. The typical hysteretic behavior of sweep sequences is also illustrated. Possible explanations for this effect are stated in [Kim et al., 2003].

Of course, the band gap size could be of $E_G \ll k_B T$. The absence of a gate dependence of I can also be attributed to several nanotubes contributing to the transport, either several single CNTs or bundles of nanotubes being suspended between the electrodes. In this case, the nanotubes are regarded as a parallel circuit in between the electrodes and the current splits up due to Kirchhoff's mesh rule [Kirchhoff, 1845]. Therefore, each nanotube is screened from the gate by turns. In addition, metallic nanotubes are rare by nature.

Consequently, it is very difficult to detect and determine metallic carbon nanotubes at room temperature. These statements are in well agreement with own experiences.

2.2.2 Conditions for ballistic transport

The characteristic dimensions of a nanotube device are diameter d and length of the suspended nanotube part L, which is in this thesis $\lesssim 1.2\,\mu\mathrm{m}$. The electron mean free path L_m of single-walled carbon nanotubes on a $\mathrm{SiO_2}$ substrate was determined in [Purewal et al., 2007]. At room temperature, all examined nanotubes exhibit $L_\mathrm{m} \lesssim 1\,\mu\mathrm{m}$. The electron mean free path was observed to increase with decreasing temperature up to several μm at $T \approx 10\,\mathrm{K}$ for small-gap CNTs.

This means that only cryogenic temperatures really provide a ballistic transport regime in mesoscopic devices based on single-walled carbon nanotubes. The requirement for ballistic transport, $L_\mathrm{m} \gg L, d$, is then fulfilled [Datta, 1997]. Charge transport through the nanotube takes place without backscattering or dissipation. Due to the structure of carbon nanotubes in reciprocal space (see subsection 2.1.2), the maximum possible value for conductance, respectively the minimum resistance value is given by

$$G_\mathrm{max} = 4e^2/h \approx 1.55 \cdot 10^{-4}\,\mathrm{S} \;\;\Leftrightarrow\;\; R_\mathrm{min} = \frac{R_\mathrm{K}}{4} \approx 6.45\,\mathrm{k\Omega} \;, \tag{2.18}$$

with R_K being von Klitzing's constant [von Klitzing et al., 1980]. The upper restriction of the conductance comes from the limitation to e^2/h for each subband. The Pauli principle leads to reflection of incoming electrons if a conducting state is occupied [Imry, 2002]. Regarding the reciprocal lattice of carbon nanotubes in Figure 2.3, the two degenerate subbands are located at K and K', each providing two possible spin-states. This leads to the factor 4 in equation 2.18.

The measured resistances of the devices are usually higher than R_min. The main reasons for this observation are due to the metal-nanotube interfaces: either a highly resistive Schottky barrier or an ohmic contact are existent, depending on the work function difference between metal and nanotube, and the intrinsic doping state of the CNT alone. For a detailed description, see subsection 10.4.2 and Figure 10.27 in [Hunklinger, 2007]. In the case of an ohmic contact, charge carriers accumulate at the nanotube side of the interface, leading to (locally) doping.

For $V_\mathrm{g} < 0\,\mathrm{V}$, holes are accumulated in the suspended CNT part because of the field effect. For consequence, the device resistance is only determined by both interfaces. In contrast, for $V_\mathrm{g} > 0\,\mathrm{V}$, the conduction band of the suspended nanotube is bent below the Fermi level because of electron accumulation. For consequence, p-n-junctions are established next to contacts. These are the tunneling barriers which limit the conductance at the electron transport side. The probability for electrons to enter or leave the nanotube is proportional to the tunneling rates denoted as $\Gamma^{\pm}_{\mathrm{s,d}}$. If the conduction band exhibits discrete states, the transport is quantized, see the next section.

2.3 Quantized transport in carbon nanotubes

As shown in section 2.1, a carbon nanotube exhibits a band structure which is already confined by level quantization in the $k_{\perp}$-direction. This results in predictable room-temperature bulk transport properties depending on the size of the band gap. Further confinement is realized by the reduction of the mean occupation of the subbands, i. e. lowering the temperature to circa $\gtrsim 10\,\mathrm{K}$, until reaching the conditions for ballistic transport as described in section 2.2. Due to this unique characteristics in combination with temperatures $\ll 10\,\mathrm{K}$, the confined transport in carbon nanotubes can be further reduced to the Coulomb blockade regime, as experimentally shown first in [Tans et al., 1997].

2.3.1 Metallic and quantum Coulomb blockade

In [Gorter, 1951; Kulik and Shekhter, 1975], the circumstances under which Coulomb charging becomes important are discussed first. In [Kulik and Shekhter, 1975], the system consists of a small metallic particle acting as an island coupled by tunnel interactions to the leads. The charge on this island is quantized in terms of elementary charge, $N \cdot e$. An additional extra charge carrier tunneling to the island changes the electrostatic potential by the charging energy e^2/C_{Σ}. Such an island has a spatial quantization energy level separation $\Delta\varepsilon$ usually smaller than the thermal energy $k_{\mathrm{B}}T$ and a charging energy $E_{\mathrm{C}} = e^2/C_{\Sigma}$ with C_{Σ} being the capacitance of the island to its whole environment. As consequence, the charging energy E_{C} becomes important when exceeding the thermal energy $k_{\mathrm{B}}T$. If discreteness of the energy spectrum of the island can be ignored, the system is in the "classical Coulomb blockade" regime, see [Beenakker, 1991] and Table 2.2 (I). Transport measurements on metallic islands devices were performed first in [Fulton and Dolan, 1987; Grabert and Devoret, 1993; Ralph et al., 1995]. Here, a metallic aluminum-island is contacted by two aluminum electrodes.

With a low density of states n_{s} in the island, the Fermi wavelength also reduces according to $\lambda_{\mathrm{F}} = \sqrt{2\pi n_{\mathrm{s}}}$. Consequently, the energy level separation $\Delta\varepsilon$ of the island reaches the same order of magnitude as E_{C}. This can be realized in the two-dimensional electron gas (2DEG) at the interface of semiconductor heterostructures like GaAs/(Al,Ga)As. The confinement in the xy-plane is realized by placing additional top gates on the heterostructure creating potential layers. For examples, see [Sprinzak et al., 2002; Hüttel, 2005]. A small confined region in between two contact structures can also otherwise be realized, for example by etching a nanowire out of a heterostructure. Even a small "drop" on a semiconductor surface is another possibility. Due to the creation of quantum states in the small islands, such devices are called quantum dots, see [Kouwenhoven et al., 1997].

2.3.2 Conditions and classifications of quantized transport

In addition to charging energy E_C condition for observing Coulomb blockade, charge has to be localized on either electrodes or on the dot. This means that the tunneling barriers should be sufficiently high. The typical time to charge or discharge a dot, $\Delta t = R_\mathrm{t} \cdot C_\Sigma$, and the expression of the charging energy must fulfill Heisenberg's uncertainty relation, see [Heisenberg, 1927], as follows

$$\Delta E \cdot \Delta t = e^2/C_\Sigma \cdot R_\mathrm{t} C_\Sigma = e^2 \cdot R_\mathrm{t} > h \quad \Leftrightarrow \quad R_\mathrm{t} > R_\mathrm{K} \ . \tag{2.19}$$

The two conditions for observation of Coulomb blockade in quantum dots can be expressed in the following:

$$R_\mathrm{t} \gg R_\mathrm{K} = h/e^2 \qquad \text{Tunneling resistance condition,} \tag{2.20}$$

$$e^2/C_\Sigma \gg k_\mathrm{B} T \qquad \text{Charging energy condition.} \tag{2.21}$$

	transport properties	limitations
(I)	Classical Coulomb blockade thermal broadening, metallic island	$\hbar\Gamma, \Delta\varepsilon \ll k_\mathrm{B}T \ll e^2/C_\Sigma$
(II)	Quantum Coulomb blockade thermal broadening, discrete quantum levels	$\hbar\Gamma \ll k_\mathrm{B}T \ll \Delta\varepsilon \lesssim E_\mathrm{C}$
(III)	Quantum Coulomb blockade lifetime broadening defines curve shape, discrete quantum levels	$k_\mathrm{B}T \ll \hbar\Gamma \ll \Delta\varepsilon \lesssim E_\mathrm{C}$

Table 2.2: Transport regimes for Coulomb blockade. In addition, the conditions from equations 2.20 and 2.21 are required.

The transport through quantum dots is classified into two further regimes: either where thermal broadening is larger or smaller than the lifetime broadening $\hbar\Gamma$ of the quantum dot levels, see Table 2.2, cases (II) and (III).

2.3.3 A carbon nanotube as a quantum dot

Fabricating a carbon nanotube quantum dot is the next step forward regarding miniaturization progress: by simply connecting the nanotube with electrodes on both sides of the trench, a lateral quantum dot is created if the abovementioned requirements are fulfilled. The energy levels can be tuned by a global back gate V_g. Quantum dot measurements in an as-grown suspended single-walled carbon nanotube device are reported among others in [Cao et al., 2005]. Here, the typical four-fold-degeneracy of the carbon nanotube was revealed as also on CNT contacted even after growth, see [Liang et al., 2002; Sapmaz et al., 2006].

The quantum dot charge changes by an integer while the gate voltage induces an effective continuous or control charge q_c. By sweeping V_g, the build up of the induced charge will be compensated in periodic intervals by tunneling of discrete charges onto the quantum dot.

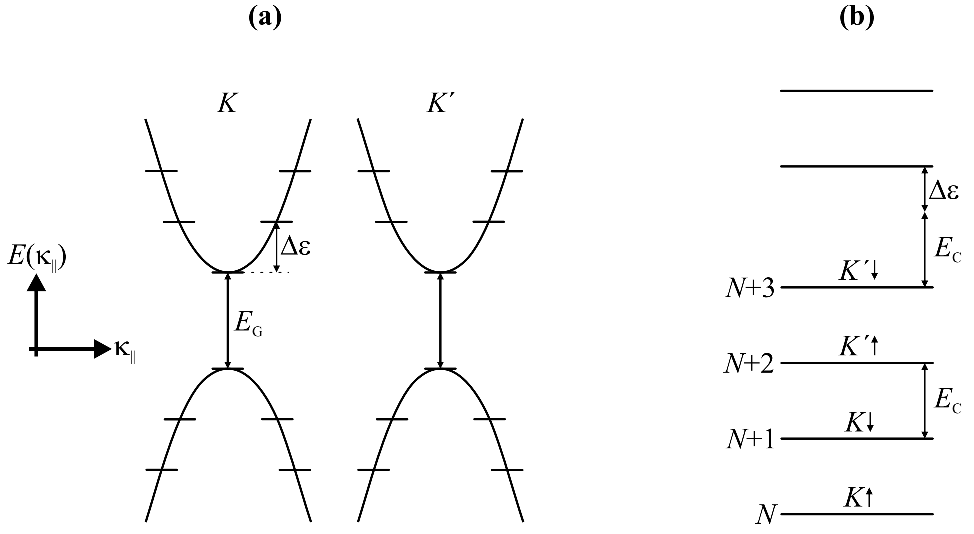

Figure 2.6: The quantized states in a CNT quantum dot neglecting spin-orbit interaction, considering degenerate K and K' energy levels, and using the constant interaction model. **(a)** Lowest transversal subbands, as already introduced in Figure 2.3, here at K and K'. Since each state can house two electrons with different spins, one conduction channel is four-fold degenerated. **(b)** The energy which has to be paid for each electron entering the quantum dot is E_C; for every fourth electron it is increased by the level separation $\Delta\varepsilon$ since one four-fold degenerate channel is fully occupied and the subsequent electron enters the next one. Further descriptions see text.

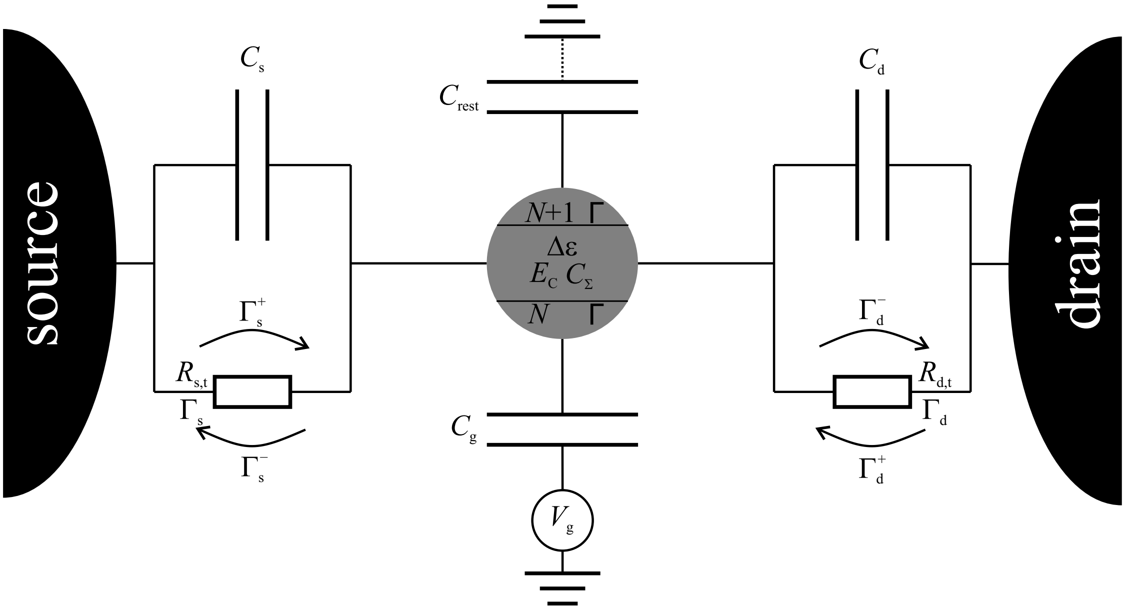

Figure 2.7: Circuit diagram of a quantum dot including all characteristic quantities. The island exhibiting quantized states is depicted in the middle. The coupling to source and drain is sketched as a parallel circuit of capacitances C_s, C_d and tunnel barriers with rates $\Gamma_\mathrm{s}^\pm$ and $\Gamma_\mathrm{d}^\pm$. C_rest is the total capacitive coupling from the carbon nanotube quantum dot to all parallel connected elements which are connected to ground: for example all metallic elements in the cryostat, bond wires of another device, or the outer wire of the opened antenna.

The interaction between charge induction and discrete compensation becomes visible as Coulomb oscillations in an $I\left(V_\mathrm{g}\right)$-measurement at low temperatures.

The typical setup for characterizing a carbon nanotube quantum dot is sketched in Figure 2.7. It also serves as a general model for quantum dots by replacing the nanotube by another arbitrary island. Besides the tunneling rates $\Gamma_\mathrm{s,d}^\pm$ and the lifetime broadening of the quantum dot level $\hbar\Gamma$, the capacitive couplings to source, drain and gate, C_s, C_d, C_g are now defined. The relation to the total capacity of the quantum dot is given by

$$C_\Sigma = C_\mathrm{s} + C_\mathrm{g} + C_\mathrm{d} + C_\mathrm{rest} \quad . \tag{2.22}$$

C_rest is here the capacitance of the nanotube to the rest of its environment. Conversion factors between the capacitances are defined as:

$$\alpha_\mathrm{g} := \frac{C_\mathrm{g}}{C_\Sigma} \quad \text{and} \quad \alpha_\mathrm{s} := \frac{C_\mathrm{s}}{C_\Sigma} \quad . \tag{2.23}$$

The Fermi levels of source and drain are displaced as a function of the applied bias voltage V_sd, as follows

$$-e \cdot V_\mathrm{sd} = \mu_\mathrm{s} - \mu_\mathrm{d} \quad . \tag{2.24}$$

The potential of the quantum dot is given by

$$\Phi_{\mathrm{dot}} = \frac{Q}{C_\Sigma} + \frac{C_\mathrm{s}}{C_\Sigma} \cdot V_\mathrm{sd} + \frac{C_\mathrm{g}}{C_\Sigma} \cdot V_\mathrm{g} \quad . \tag{2.25}$$

The classical electrostatic energy is then:

$$U(N) = \int_0^{-Ne} \Phi_{\mathrm{dot}}\, \mathrm{d}Q \overset{\text{eqs. 2.25,2.23}}{=} \frac{(Ne)^2}{2C_\Sigma} - \left(\alpha_\mathrm{s} V_\mathrm{sd} + \alpha_\mathrm{g} V_\mathrm{g}\right) \cdot Ne \quad . \tag{2.26}$$

In the so-called "constant interaction model", see [Glazman and Shekhter, 1989; Averin et al., 1991; Korotkov et al., 1990; Meir et al., 1991], the total energy of the quantum dot, E_{dot}, is assumed to be the sum of the classical electrostatic energy $U(N)$ and the quantum mechanical energy of all electrons $i = 1...N$ occupying single particle levels with energies ε_i in the quantum dot:

$$E_{\mathrm{dot}} = \sum_{i=1}^{N} \varepsilon_i + \frac{(Ne)^2}{2C_\Sigma} - \left(\alpha_\mathrm{s} V_\mathrm{sd} + \alpha_\mathrm{g} V_\mathrm{g}\right) \cdot Ne \quad . \tag{2.27}$$

The chemical potential of the quantum dot level, loaded with N electrons, is then defined as

$$\mu_{\mathrm{dot}}(N) := E_{\mathrm{dot}}(N) - E_{\mathrm{dot}}(N-1) = \varepsilon_N + \frac{e^2}{2C_\Sigma} \cdot (2N-1) - e\left(\alpha_\mathrm{s} V_\mathrm{sd} + \alpha_\mathrm{g} V_\mathrm{g}\right) \quad . \tag{2.28}$$

If one additional electron enters the quantum dot, the chemical potential changes from $\mu_{\mathrm{dot}}(N)$ to $\mu_{\mathrm{dot}}(N+1)$, where the charging energy appears in the following:

$$\mu_{\mathrm{dot}}(N+1) - \mu_{\mathrm{dot}}(N) = \varepsilon_{N+1} - \varepsilon_N + \frac{e^2}{C_\Sigma} \quad ,$$

assuming that the coupling capacitances are constant. The difference $\varepsilon_{N+1} - \varepsilon_N$ is the same as the quantum energy level separation $\Delta\varepsilon$, see Table 2.2.

Transport through the quantum dot is only possible, if the potential μ_{dot} lies in the so-called "bias-window" which is opened by the bias voltage V_sd. Furthermore, for $T = 0\,\mathrm{K}$, the occupation in the leads follows step functions. The positions where the single-electron tunneling (SET)-state changes to Coulomb blockade is therefore $\mu_{\mathrm{dot}} = \mu_\mathrm{s}$ and $\mu_{\mathrm{dot}} = \mu_\mathrm{d}$. With equation 2.24 and 2.28 one can write

$$\mu_\mathrm{d} = \varepsilon_N + \frac{e^2}{2C_\Sigma} \cdot (2N-1) - e\left(\alpha_\mathrm{s} V_\mathrm{sd} + \alpha_\mathrm{g} V_\mathrm{g}\right) \quad ,$$
$$\mu_\mathrm{d} = \varepsilon_N + \frac{e^2}{2C_\Sigma} \cdot (2N-1) - e\left((\alpha_\mathrm{s} - 1) V_\mathrm{sd} + \alpha_\mathrm{g} V_\mathrm{g}\right) \quad .$$

The upper two conditions are rewritten using equation 2.23 and simple equivalent transformations to

$$C_\mathrm{s}V_\mathrm{sd} + C_\mathrm{g}V_\mathrm{g} = \frac{C_\Sigma}{e}\cdot\left(\varepsilon_N - \mu_\mathrm{d} + \frac{e^2}{2C_\Sigma}\cdot(2N-1)\right) \quad , \tag{2.29}$$

$$-(C_\Sigma - C_\mathrm{s})V_\mathrm{sd} + C_\mathrm{g}V_\mathrm{g} = \frac{C_\Sigma}{e}\cdot\left(\varepsilon_N - \mu_\mathrm{d} + \frac{e^2}{2C_\Sigma}\cdot(2N-1)\right) \quad . \tag{2.30}$$

2.4 Quantum dot spectroscopy

The Coulomb oscillations of a quantum dot system can be probed by an $I\left(V_\mathrm{g}\right)$-measurement at constant V_sd, as described in subsection 2.3.3. A principal measurement setup is depicted in Figure 2.5(a). With an additional V_sd variation, the resonance condition of the quantum dot level with at least one lead potential according to equations 2.29, 2.30 can be revealed. With measuring the current I through the quantum dot as a function of V_sd at constant V_g, then repeating the same $I\left(V_\mathrm{sd}\right)$-measurement at the next V_g-value etc., the $I\left(V_\mathrm{sd}, V_\mathrm{g}\right)$-dependence can be mapped as a two-dimensional plot as shown in Figure 2.8. The Coulomb blockade regions are clearly separated from the conducting SET-regions. The diamond shaped CB-regions are labeled with the number N of trapped electrons. Furthermore, the two slopes of the CB diamond edges are defined as shown in Figure 2.8(b). Out of the measurement, $\lambda_{1,2}$ can be extracted in the following:

$$\lambda_1 := \frac{\Delta V_\mathrm{sd,1}}{\Delta V_\mathrm{g} - \Delta V_\mathrm{g,1}} = \frac{\Delta V_\mathrm{sd,2}}{\Delta V_\mathrm{g,2}} < 0 \quad , \tag{2.31}$$

$$\lambda_2 := \frac{\Delta V_\mathrm{sd,1}}{\Delta V_\mathrm{g,1}} = \frac{\Delta V_\mathrm{sd,2}}{\Delta V_\mathrm{g} - \Delta V_\mathrm{g,2}} > 0 \quad . \tag{2.32}$$

These slopes define linear functions in the V_sd-V_g plane following the conditions 2.29 and 2.30. Since N is constant in one diamond, the right-hand sides of these both equations can be regarded as constant. Consequently, $V_\mathrm{sd}(V_\mathrm{g})$ at the edges of the CB region is:

$$2.29 \Rightarrow \frac{\mathrm{d}V_\mathrm{sd}}{\mathrm{d}V_\mathrm{g}} = -\frac{C_\mathrm{g}}{C_\mathrm{s}} < 0 \quad ,$$

$$2.30 \Rightarrow \frac{\mathrm{d}V_\mathrm{sd}}{\mathrm{d}V_\mathrm{g}} = \frac{C_\mathrm{g}}{C_\Sigma - C_\mathrm{s}} > 0 \quad .$$

By comparison with the experimentally extracted $\lambda_{1,2}$ from equations 2.31 and 2.32, one obtains the relations:

$$\lambda_1 = \frac{\Delta V_\mathrm{sd,1}}{\Delta V_\mathrm{g} - \Delta V_\mathrm{g,1}} = \frac{\Delta V_\mathrm{sd,2}}{\Delta V_\mathrm{g,2}} \equiv -\frac{C_\mathrm{g}}{C_\mathrm{s}} \quad , \tag{2.33}$$

$$\lambda_2 = \frac{\Delta V_\mathrm{sd,1}}{\Delta V_\mathrm{g,1}} = \frac{\Delta V_\mathrm{sd,2}}{\Delta V_\mathrm{g} - \Delta V_\mathrm{g,2}} \equiv \frac{C_\mathrm{g}}{C_\Sigma - C_\mathrm{s}} \quad . \tag{2.34}$$

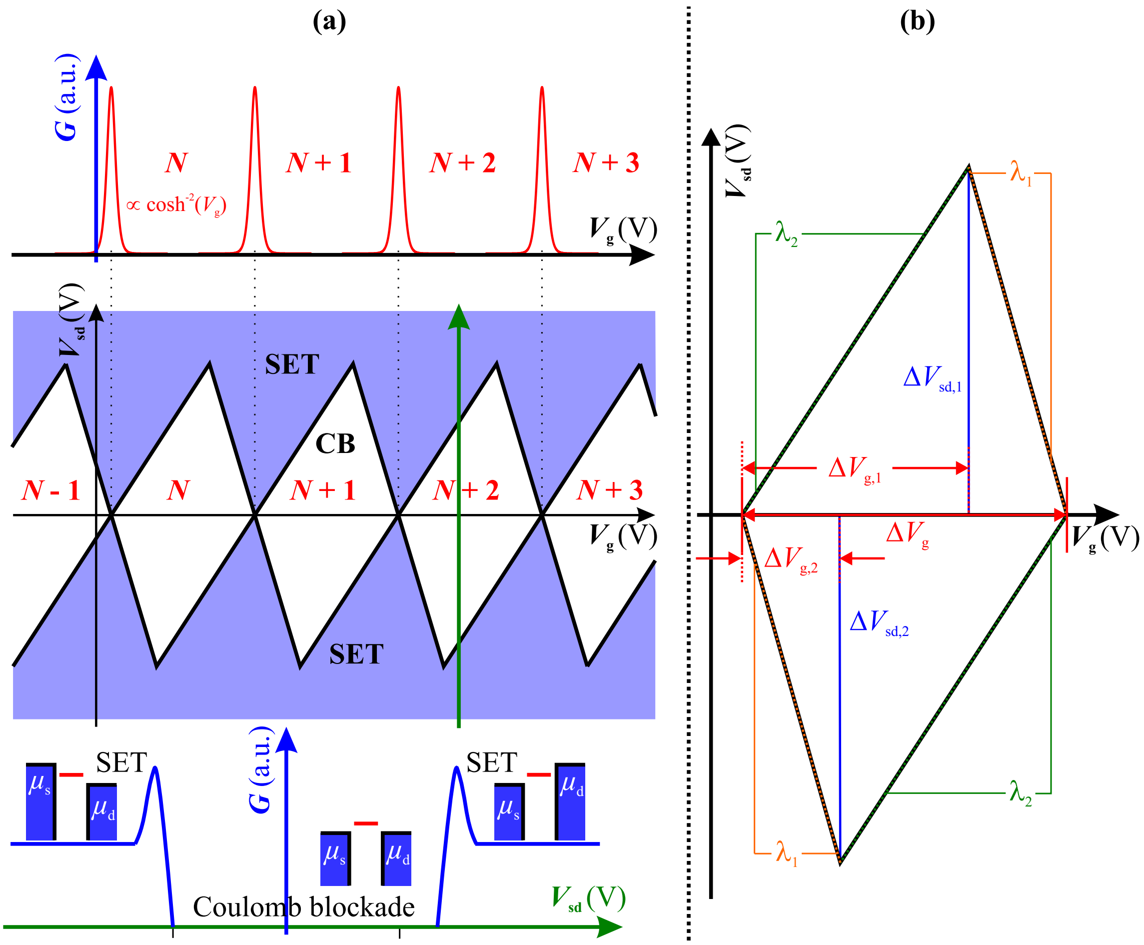

Figure 2.8: Quantum dot spectroscopy. **(a)** Center panel: stability diagram. The regions with a measurable current through the quantum dot are blue-shaded. The differential conductance is hence defined as $G \equiv \mathrm{d}I/\mathrm{d}V_{\mathrm{sd}}$. The Coulomb blockade (CB) regions exhibit a characteristic diamond-shape. Below, a $G\left(V_{\mathrm{sd}}\right)$-linetrace is sketched in which the transitions between conducting and insulating state is indicated. Above, the Coulomb-oscillations are sketched in a $G\left(V_{\mathrm{g}}\right)$-trace for zero bias. **(b)** Quantities which define the CB diamond geometry in the V_{sd}-V_{g} plane, see the text.

From these relations, the characteristic conversion factors and capacitances of the quantum dot are obtained:

$$\alpha_{\mathrm{g}} = \frac{1}{\left|\frac{1}{\lambda_1}\right| + \left|\frac{1}{\lambda_2}\right|} \quad , \tag{2.35}$$

$$\alpha_{\mathrm{s}} = \left|\frac{1}{\lambda_1}\right| \cdot \alpha_{\mathrm{g}} \quad , \tag{2.36}$$

$$C_{\mathrm{g}} = \frac{e}{\Delta V_{\mathrm{g}}} \quad , \tag{2.37}$$

$$C_{\mathrm{s}} = \left|\frac{1}{\lambda_1}\right| \cdot C_{\mathrm{g}} \quad , \tag{2.38}$$

$$C_{\Sigma} = \frac{C_{\mathrm{g}}}{\alpha_{\mathrm{g}}} \quad . \tag{2.39}$$

The stability diagrams obtained by quantum dot spectroscopy deliver all characteristic quantities of each probed quantum dot level.

2.5 Transport in the intermediate and open regime

Up to now, low-temperature transport through carbon nanotube quantum dots was only discussed in terms of first-order tunneling events. This section deals with higher-order tunneling processes leading to additional features in quantum dot spectroscopy. These effects are commonly known as co-tunneling due to simultaneous tunneling of two or more electrons. A special case where the electron-spin has to be taken into account is the Kondo effect. Originally proposed by Jun Kondo in 1964, the effect explains the resistance minimum in dilute magnetic alloys at low temperatures [Kondo, 1964]. The model describes the electron scattering from a localized magnetic impurity, which leads to an increase in the resistance below a characteristic Kondo-temperature T_{K}. Including the Anderson model, [Anderson, 1961], the theoretical description of this phenomenon was completed by Wilson's renormalization method [Wilson, 1975].

In semiconductor quantum dots, the Kondo effect was observed first by [Goldhaber-Gordon et al., 1998b; Cronenwett et al., 1998]. In comparison to bulk metals, the dot level is the analogon to the magnetic impurity if it exhibits an odd occupation number N.

An additional density of states leads to an even larger coupling between dot and leads, opening the tunneling barriers up. The transport is described via the wave-particle duality of the charge carriers; we obtain a behavior of an electron waveguide equivalent to a Fabry-Pérot interferometer. This transport regime was measured first in semiconductor quantum dot devices in [Johnson et al., 1992].

2.5.1 Classification

Regarding cases (II) and (III) in Table 2.2 in subsection 2.3.2, only charging effects due to Coulomb blockade dominate transport through the quantum dot. As soon as the tunnel barriers become more transparent, the tunnel rates onto and off the dot increase. This results in an increased lifetime broadening Γ, since this is a function of all tunnel rates. Note that the conditions for thermal broadening are still valid in order to be in the quantized transport regime (see equations 2.20, 2.21 in subsection 2.3.2). Hence, two further cases for the transport through dots can be defined, see Table 2.3:

	transport	tunneling resistance	limitation
(IV)	Intermediate regime	$R_t \gtrsim R_K$	$\hbar\Gamma \lesssim E_C$
(V)	Open regime	$R_t \lesssim R_K$	$\hbar\Gamma \gg E_C$

Table 2.3: Transport regimes through quantum dots with enhanced tunneling. The tunneling condition from equation 2.20 is softened or even lifted but charging condition following equation 2.21 stays valid. Adapted from [Sapmaz, 2006; Schmid, 2010].

For case (IV), charging effects are still important but higher-order tunneling effects also appear. Co-tunneling and the Kondo effect are stated as examples. If case (V) is present, the system is open and in the Fabry-Pérot regime.

2.5.2 Co-tunneling and Kondo effect

In quantum dots with an enhanced tunnel coupling to the leads, additional tunnel currents are measured in the originally insulating Coulomb blockade regime. These signatures are attributed to co-tunneling transport and are observed in a semiconductor quantum dot in [De Franceschi et al., 2001] for example.

In Figure 2.9, the tunnel current signatures in a Coulomb diamond and the underlying mechanisms are qualitatively sketched.

In principle, co-tunneling can be classified into two categories: on the one hand an elastic process after which the total energy of the dot is the same as before and on the other hand an inelastic process where it leaves the dot in an excited state. In Figure 2.9(b), the left and middle situations display elastic co-tunneling processes: as can be seen, $V_{sd} \simeq 0$, and an electron can tunnel into the dot to an unoccupied level which is close to, but not in the bias window (left situation). The energy difference between level and the (lead-)electron is coupled to the lifetime of this "virtual occupied" level over Heisenberg's uncertainty relation, see equation 2.19. The elastic process sketched in the middle picture happens when an electron tunnels from an occupied dot level far below μ_s, μ_d to a lead. The free dot state is immediately occupied by another electron originating from the other lead. Since the dot's energetic state remains after these events, the processes are denoted as elastic co-tunneling.

(a)

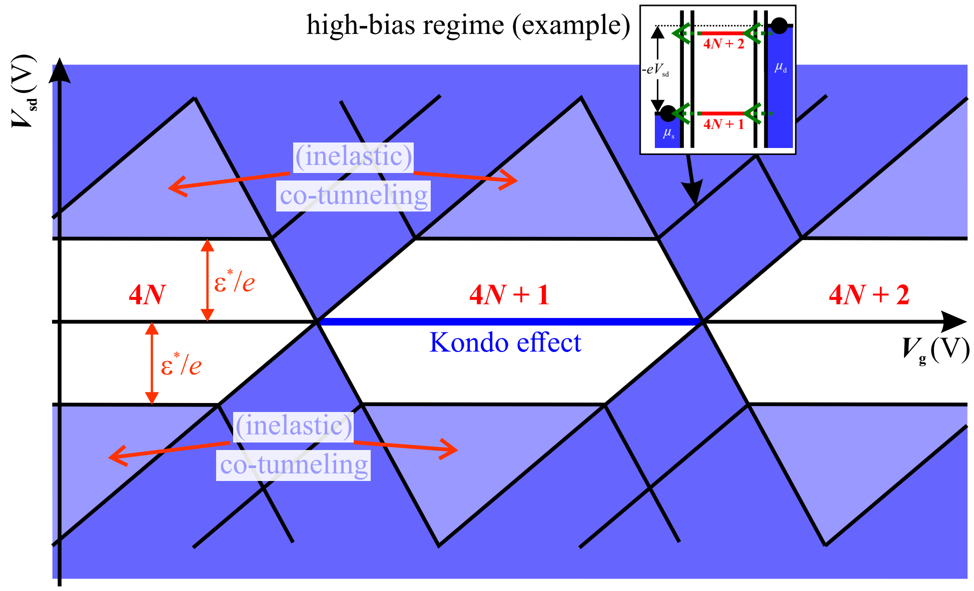

(b) Co-tunneling processes

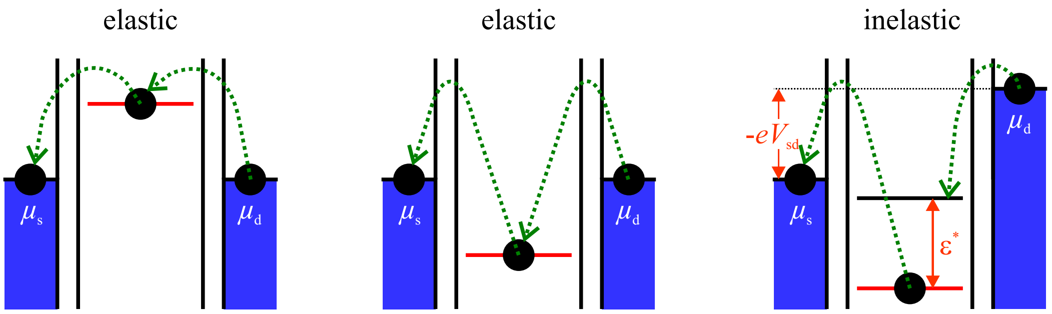

(c) Kondo effect

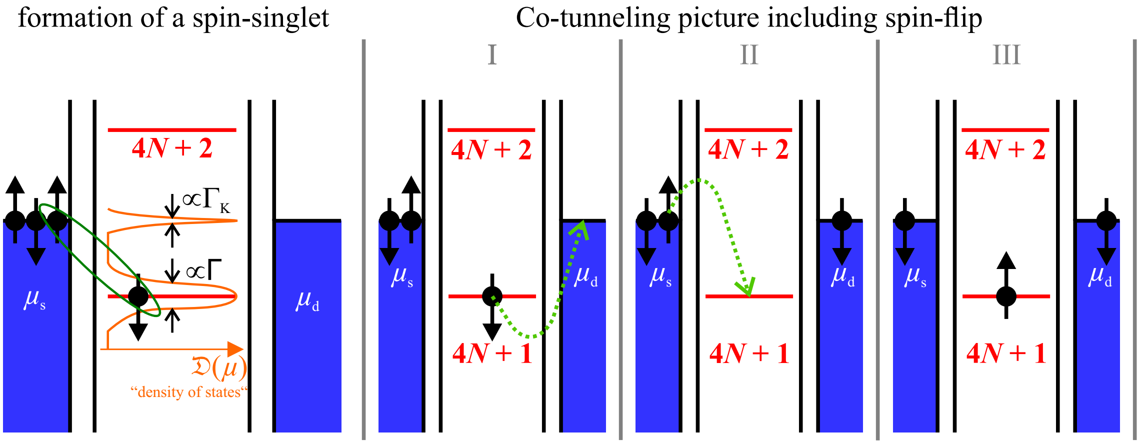

Figure 2.9: Co-tunneling and Kondo effect in quantum dots. **(a)** An example stability diagram including additional signatures in conductance. **(b)** Three possible co-tunneling processes. **(c)** The Kondo effect. The spin-singlet formation is indicated left. A simplified co-tunneling picture describes the measured zero-bias conductance.

Inelastic co-tunneling occurs when a dot-electron tunnels into a lead, and the following electron does not occupy the free state in the dot but another separated by ε^*. The threshold condition for this inelastic process is $|V_{\mathrm{sd}}| = \varepsilon^*/e$, and therefore it only appears for a finite bias voltage. The onset voltage is not or only weakly affected by V_{g}. At the edge of the Coulomb blockade diamond, it connects to the onset of the single-electron tunneling in the conducting regime. Here, more than one dot level is situated in the bias-window and participates in the transport. This regime is denoted as high-bias regime, see [Laird et al., 2015]. This may be both an excited level ε^* and the next quantum dot levels.

Figure 2.9(c) describes the Kondo effect in quantum dots: at $V_{\mathrm{sd}} \simeq 0$ conductance is enhanced in the Coulomb blockade. Using the co-tunneling picture, the effect can be described in three steps. At first, the electron from a dot level exhibiting an unpaired spin state (odd N) tunnels to the (right) lead (I). The free level as an intermediate state (II) gets then occupied by an electron with opposite spin (III). It can be assumed that the virtual state on the dot at zero bias (see left picture) forms out because of the formation of a spin singlet between the localized electron on the dot and unlocalized electrons with opposite spin in the lead. The resonance width of the Kondo dot level Γ_{K} is typically much smaller than the tunnel rate induced level broadening Γ. The conductance behavior of a Kondo-degenerated quantum dot level as a function of temperature is examined and theoretically discussed in [Goldhaber-Gordon et al., 1998a]. Sweeping the gate voltage V_{g}, a "ridge" in conductance oscillations confining the odd quantum dot level is expected and in the blockade a measurable current is detected. A co-tunneling feature in this region can be excluded by regarding the lower and the next higher dot level with even occupation numbers $N \pm 1$. Here, no current-flow is detected in the middle of the blockade diamond. The Kondo-temperature T_{K} can be determined out of gate-sweeps for several temperatures T following

$$G(T) = G_0 \cdot \left(\frac{T_{\mathrm{K}}^{*2}}{T^2 + T_{\mathrm{K}}^{*2}} \right) \quad , \tag{2.40}$$

with $T_{\mathrm{K}}^* = T_{\mathrm{K}} / \sqrt{2^{1/s} - 1}$ and $s \approx 0.22$ being a fitting parameter for the spin-1/2-Kondo effect. A bias-(V_{sd}-)sweep in the middle an odd-numbered Kondo-degenerated quantum dot level exhibits a peak at $V_{\mathrm{sd}} = 0$; its width is directly proportional to T_{K} and can be fitted to a universal Lorentzian curve [Kretinin et al., 2012] leading to the relation

$$\Delta V_{\mathrm{sd}} = V_{\mathrm{sd}}^{+}\left(\frac{2}{3} G_0\right) - V_{\mathrm{sd}}^{-}\left(\frac{2}{3} G_0\right) = \frac{2 k_{\mathrm{B}} T_{\mathrm{K}}}{e} \quad , \tag{2.41}$$

with G_0 being the maximum conductance at $V_{\mathrm{sd}} = 0$. ΔV_{sd} is here the width of the conductance peak defined as the difference between positive and negative bias-voltage $V_{\mathrm{sd}}^{\pm}$ for which the conductance is two-third of G_0.

2.5.3 The Kondo effect in carbon nanotube quantum dots

Especially for carbon nanotube quantum dots, an orbital Kondo effect can appear as observed and described first in [Jarillo-Herrero et al., 2005b]. Besides the $SU(2)$-Kondo (spin), an additional $SU(2)$-Kondo (orbital) can appear in CNT quantum dots. Furthermore, the $SU(4)$-Kondo, i. e. a combination of both is also possible, as depicted in Figure 2.10. The orbital Kondo effect considers the KK' degeneracy of the CNT band structure: the state of the dot level changes to the other orbital after tunneling events.

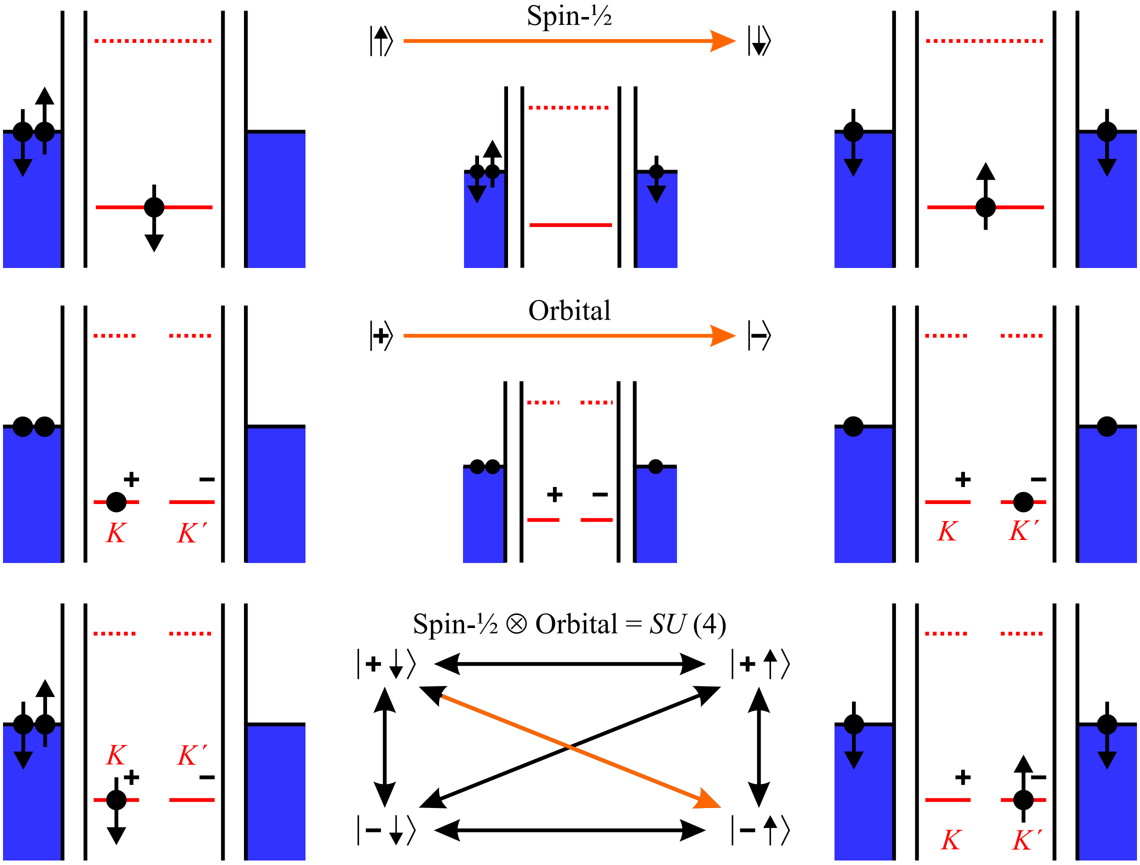

Figure 2.10: Kondo effect in carbon nanotube quantum dots: above, the already introduced Kondo-Spin-1/2 effect, see also Figure 2.9**(c)**. In the middle, the difference between K and K' valleys in the CNT quantum dot is considered. Both transitions being mixed up result in the so-called $SU(4)$-Kondo effect. The transitions are sketched below. Adapted from [Jarillo-Herrero et al., 2005b].

The $SU(4)$-Kondo can occur in nanotubes exhibiting a broken spin and orbital degeneracy due to curvature induced spin-orbit coupling and valley mixing. Then, if the degeneracy is weakly broken, i. e. on an energy scale comparable to $k_B T_K$, inelastic Kondo peaks at finite V_{sd} are also detected, see [Cleuziou et al., 2013; Schmid et al., 2015a]. The latter publication shows a detailed experimental as well as theoretical analysis of a quantum dot level exhibiting a Kondo-enhanced conductance peak around $V_{\mathrm{sd}} \simeq 0$ plus satellites separated from the center by an energy amount Δ_{sat}. By examination of the peak shape as a function of temperature, its origin in the Kondo effect can be confirmed. By applying an external B-field perpendicular to the nanotube axis, the four energy levels are resolved due to Zeeman-splitting $g\mu_{\mathrm{B}}B_{\perp}$. In contrast, the response to an external applied parallel magnetic field having an influence on the orbital magnetic momentum of the CNT is described in [Kuemmeth et al., 2008]. Performing such experiments on carbon nanotube quantum dots enable the calculation of $\Delta_{\mathrm{KK}'}$ and Δ_{SO}, as stated in [Schmid et al., 2015a]. Similar experiments which split the Kondo-peak in the Coulomb diamond due to external B-fields are demonstrated in quantum dot devices in which the carbon nanotube was contacted subsequent to the growth, see [Jarillo-Herrero et al., 2005a; Gaass et al., 2011].

2.5.4 Fabry-Pérot regime

This subsection deals with the case (V) in Table 2.3: because of an enlarged tunneling rate, the lifetime broadening energy $\hbar\Gamma$ exceeds the charging energy E_{C}. The system is hence open even though fulfilling the charging energy condition, see equation 2.21.

The conditions for ballistic transport, as described in subsection 2.2.2 are still valid. In addition to the requirement for the electron mean free path $L_{\mathrm{m}} > L$, also the coherence length L_{ϕ} is larger than the nanotube length L. Therefore, the wave-nature of an electron traveling through the nanotube has to be taken into account. Scattering at the metal-nanotube interface leads to interference of right- and left-moving electron waves, in analogy to an optical Fabry-Pérot interferometer, see [White and Todorov, 2001].

The electrons propagating in the carbon nanotube "cavity" can be thereby described by plane electron waves. Fabry-Pérot interference between a directly transmitted wave with waves circulating one or multiple times in the cavity produces the oscillation patterns of the transport measurements as depicted in [Liang et al., 2001; Liang et al., 2002; Grove-Rasmussen et al., 2007]. According to [Dirnaichner, 2017], the resonance condition in terms of the phase ϕ acquired upon one roundtrip and for one channel reads

$$\phi\left(V_{\mathrm{g}},V_{\mathrm{sd}}\right) \equiv \left|\phi^{\mathrm{dir.}}\left(V_{\mathrm{g}},V_{\mathrm{sd}}\right) - \phi^{\mathrm{rnd.}}\left(V_{\mathrm{g}},V_{\mathrm{sd}}\right)\right| = \left|k_{\mathrm{l}}\left(V_{\mathrm{g}},V_{\mathrm{sd}}\right) - k_{\mathrm{r}}\left(V_{\mathrm{g}},V_{\mathrm{sd}}\right)\right| \cdot L \overset{!}{=} 2\mathfrak{n}\pi \quad ,$$

where k_{l} and k_{r} are the wave vector components parallel to the nanotube axis of the left, respectively right moving electrons, L is the length of the suspended CNT, and $\mathfrak{n}$ is an integer. With an approximately linear dispersion relation in the vicinity of the Dirac point (see section 2.1), a relation between length L and energy difference $\Delta E\left(\Delta V_{\mathrm{g}},\Delta V_{\mathrm{sd}}\right)$ corresponding to one oscillation period is obtained as follows

$$\Delta\phi\left(\Delta V_{\mathrm{g}},\Delta V_{\mathrm{sd}}\right) = |\Delta k_{\mathrm{l}} - \Delta k_{\mathrm{r}}|\, L \simeq \frac{2L}{\hbar v_{\mathrm{F}}}\Delta E\left(\Delta V_{\mathrm{g}},\Delta V_{\mathrm{sd}}\right) \simeq 2\pi \ . \tag{2.42}$$

Note that the energy difference is here a function of a change in the bias voltage V_{sd}, a change in the gate voltage V_{g}, or a change in both. Using the Fabry-Pérot formalism, the transmission amplitude for one spin-degenerate channel is

$$\mathfrak{T}\left(V_{\mathrm{g}}\right) = 2\cdot\frac{|\mathfrak{T}_{\mathrm{s}}|^2|\mathfrak{T}_{\mathrm{d}}|^2}{1-2|\mathfrak{R}_{\mathrm{s}}||\mathfrak{R}_{\mathrm{d}}|\cos\left[\Delta\phi\left(V_{\mathrm{g}},L\right)\right]+|\mathfrak{R}_{\mathrm{s}}|^2|\mathfrak{R}_{\mathrm{d}}|^2} \ , \tag{2.43}$$

where $V_{\mathrm{sd}} = 0$ and $\mathfrak{T}_{\mathrm{s}},\mathfrak{R}_{\mathrm{s}}$, respectively $\mathfrak{T}_{\mathrm{d}},\mathfrak{R}_{\mathrm{d}}$ are the transmission and reflection coefficients at the source-, and drain-interface.

Since the tunneling resistance condition according to equation 2.20 is lifted in the open regime, a conductivity of at least $\gtrsim 1\,e^2/h$ is expected for Fabry-Pérot transport regime. Note that possible interface resistances are not considered within this assumption. The conductance oscillations are determined by the transmission amplitude $\mathfrak{T}$, see equation 2.43, but never exceed $G_{\mathrm{max}} = 4e^2/h$ according to subsection 2.2.2.

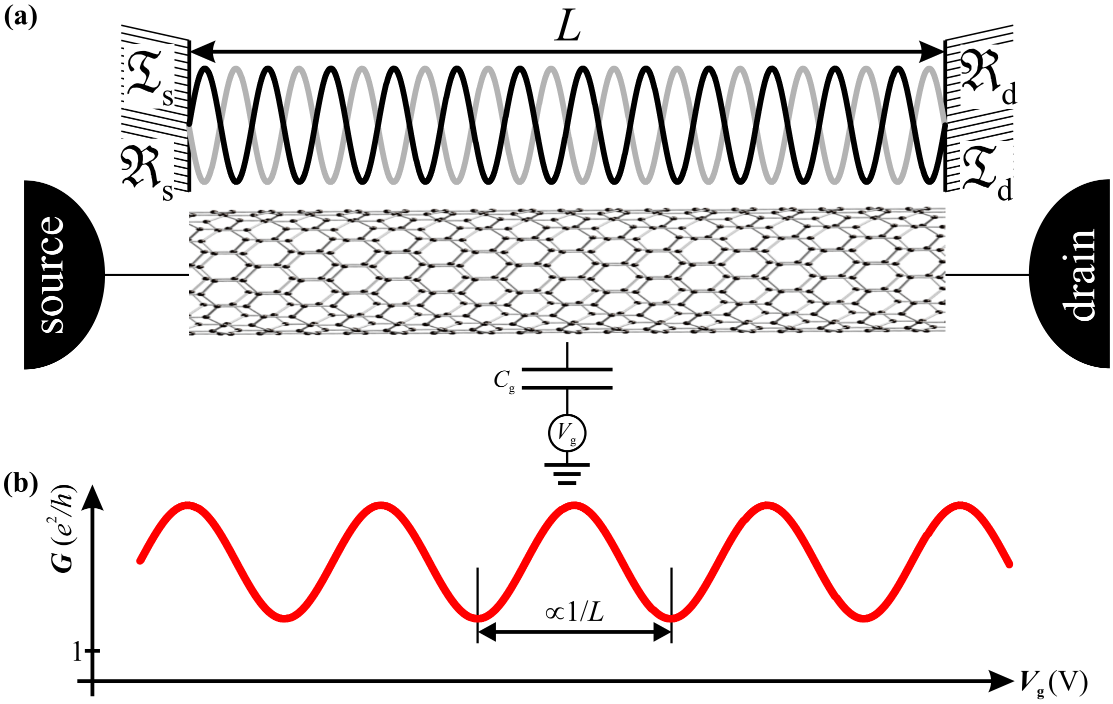

Figure 2.11: For the conductance in the Fabry-Pérot regime of a carbon nanotube based device. **(a)** is a circuit diagram in the open-dot regime. The tunneling barriers are now replaced by metal-nanotube interfaces exhibiting a reflection and a transmission probability $\mathfrak{R}$, $\mathfrak{T}$ each. In **(b)**, the resulting $G\left(V_{\mathrm{g}}\right)$-trace is sketched. The sequence of the extrema in conductance is according to equation 2.42 a measure for the length of the suspended CNT.

Chapter 3

Overgrowth fabrication development and measurement setups

The overgrowth fabrication technique was established at the University of Regensburg over the last couple of years, see [Schmid, 2010; Kugler, 2013; Schupp, 2014]. It is based on the selective placement of catalytic material on a chip with prefabricated metal structures which are used as bond pads, as leads, and electrodes. Since CVD growth takes place as the last fabrication step, ultraclean and suspended CNT devices are obtained reliably [Kong et al., 1998b; Cao et al., 2005; Steele et al., 2009b; Schmid, 2015]. After preselection at the probe station, low-temperature measurements are carried out in the vacuum of a dilution cryostat with base temperature of about 15 mK.

In this chapter, the improvement of the group's overgrowth fabrication technique is described. It also deals with the modification of the fabrication process which results in a higher yield of suspended clean single-walled carbon nanotube devices. The clean room techniques, metal evaporation parameters, and CVD growth recipes can be found in appendix A. Furthermore, detailed recipes of certain devices are stated in appendix B. Statistics of all tested possible devices on each chip during the preselection step at room temperature are included in this chapter. The circuit diagrams which are depicted in this chapter also apply to low-temperature experiments evaluated in the next chapters.

3.1 Metallization

Since metallized structures on the chip have to withstand the CNT growth conditions, the choice of possible elements or alloys is very limited. Since [Schmid, 2010], it is commonly known that only platinum and rhenium are suitable metallic elements. In addition, alloys of rhenium and molybdenum are used and optimized in the present thesis, see also [Stiller et al., 2013; Götz et al., 2016; Blien et al., 2016]. The optimization of MoRe alloys concerning composition, growth condition influence, and superconducting properties is described in detail in chapter 6.

Metallization starts with a clean and quadratic piece of the p^{++}-Si/SiO$_2$ wafer of several millimeters edge length. The substrate of such a chip is highly boron-doped so that it is still conductive in the millikelvin temperature range and can be used as a global back gate. The substrate is capped by a 500 nm thick insulating thermal SiO$_2$ layer upon which the metallization takes place.

3.1.1 Bond pads and outer leads

In Figure 3.1(a), the optical mask for fabrication of one single chip is plotted. Usually, four chips are simultaneously metallized and afterwards separated to fit into standard chipcarriers. One chip is named using two capital letters, as e. g., "AA". It contains 25 arrays of six bond pads plus outer leads each. They are denoted from "11" to "55". After the second metallization step for the inner structures (see subsequent subsection), each array houses two possible devices. Hence, a device is later called according to its exact address on the chip, for example "BC_12_Left".

After optical lithography, the bare surface of SiO$_2$ on the chips is etched by reactive ion etching (RIE). The etch depth must be adapted to the thickness of the metal layer which is evaporated next. This is titanium of about five to ten nanometers, followed immediately by platinum in order to have a total layer thickness of about 100 nm. Titanium is evaporated to achieve a lower base pressure in the evaporation chamber and a better adhesion to the SiO$_2$, thick platinum withstands CVD conditions and also serves as a suitable sticking material to the aluminum bond wire. The resulting step between outer leads and the pristine SiO$_2$ surface must not exceed the thickness of the inner structures which is about 50 nm, see Figure 3.1(b).

By burying the bond pads and outer leads into the insulating layer, higher metal layer thicknesses can be realized. This stabilizes the pads for bonding and improves the edges to the thinner inner structures at once.

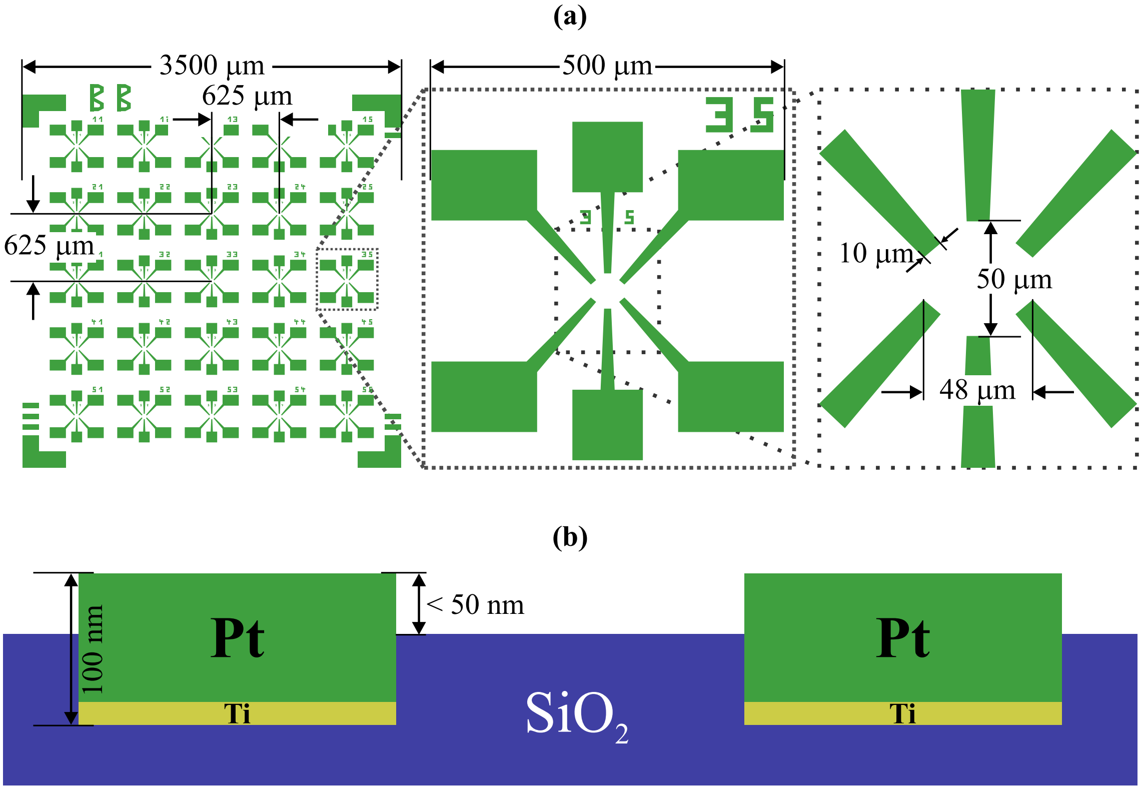

Figure 3.1: Metallization of bond pads and outer leads. **(a)** Optical mask including dimensions; from left to right: one chip, a device array, and the reserved area for the inner structures. **(b)** Horizontal cut after the first metallization step has finished.

3.1.2 Inner structures

As "inner structures", we henceforth denote all smaller leads and electrodes that are now in the next step added to the optically patterned structure. The patterning is here done by electron beam lithography (EBL), the masks are depicted in Figure 3.2(a). After the reactive ion etching procedure, which also deepens the trench in between both electrodes, the chips are ready for proximate fabrication steps.

Two different fabrication recipes for inner structure metallization were used: either the direct one in which the electrodes are defined in one EBL step, evaporation, lift-off, and subsequent reactive ion etching, or where metallization and definition were separated into two lithography steps.
The corresponding fabrication principles are sketched in Figure 3.2(b). Here, the first recipe is shown schematically above: after patterning by EBL, lift-off is performed and the chip is exposed to the trench-etching RIE procedure. Following the second recipe, a

square is defined in the middle of each device array, the metal or alloy is deposited, and lifted off resulting in better surface properties in the middle; the bent edges as well as the splinters from the lift-off are situated outside at the edge of the square. In the subsequent EBL, an etching mask is defined. By means of RIE using a SF_6/Ar-plasma, the bare metal is removed whereas the PMMA-protected electrode and lead geometry stays. In the same step, the trench in between electrodes is deepened using CHF_3/O_2-plasma for SiO_2 etching. In this last etching sequence, the on-chip metal serves as mask since it is not or only weakly attacked by the trifluorine-oxygen plasma. This is the same trench-etching procedure which is also used in the first recipe.

A small partial pressure of oxygen is added to CHF_3 in order to avoid deposition of organic residues on the chip surface. This happens for longer etching durations, and results in an overall shortcut after CVD where carbon adsorbs on the organic material and forms a conductive layer of several hundreds of nanometer thickness. This effect was also observed in [Keijzers, 2012; Schupp, 2014; Steger, 2015].

The single chips are cut from the large one by scratching with a diamond scribe and breaking. The metallized surface is protected by an optical resist, which is stripped afterwards in hot acetone, also removing the dust from breaking.

By means of atomic force microscopy (AFM), two pairs of electrode strips are compared in Figure 3.2(c): the left ones have been undergone the first fabrication recipe whereas the right ones the second. The fabrication parameters are otherwise chosen to be the same. The applied EBL masks are shown in panel 1 and 2 of Figure 3.2(a), exhibiting the same range of dimensions for trench and electrode widths. Both electrode structures consist of co-sputtered $Mo_{20}Re_{80}$. Especially for co-sputtered structures, metal edges turn upwards during lift-off, as can be seen in the left horizontal linecut in Figure 3.2(c). Furthermore, lift-off splinters are deposited onto the electrode surface. In contrast, the electrode surface on the right-hand side micrograph are comparably flat. The larger height difference to the substrate is due to the final RIE trench-etching procedure. The characteristic average, and root-mean-square roughness R_a, and R_q, are more than four times smaller here compared with the lift-off first recipe.

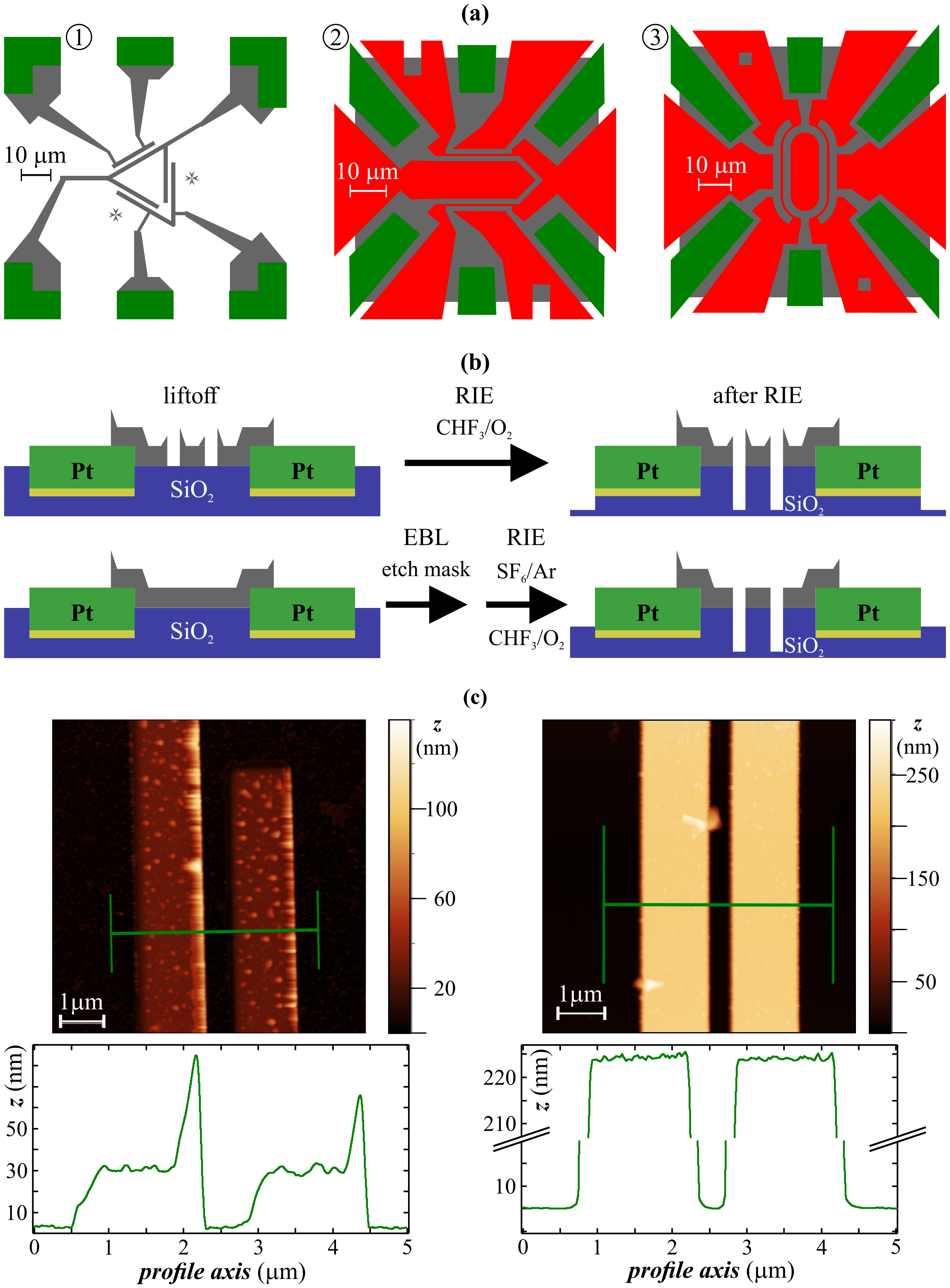

Figure 3.2: Metallization of the inner structures. **(a)** EBL masks: left one (panel 1) is designed for direct lift-off, the middle and the right one (panels 2 and 3) for the second, more complex recipe. **(b)** Fabrication principles following the first (up), and the second recipe (below). **(c)** AFM micrographs and linecuts for comparison of both recipes. Further explanations see text.

3.2 Growth of carbon nanotubes

The CNT growth procedure is optimized to obtain few, but clean and defect-free single-walled carbon nanotubes. The technique was developed by [Kong et al., 1998b], and is applied in this thesis. The methane-CVD growth is supported by a special catalyst mixture. An additional publication from the same author, [Kong et al., 1998a], deals with results using other catalysts types, as e. g. cobalt oxide, also regarding the yield of bundles and multi-walled nanotubes. The mixture used here, however, turns out to be the best one for individual-SWCNT growth in a hot methane-hydrogen atmosphere. Furthermore, since then, it has been used nearly exclusively for transport measurements, see [Cao et al., 2005; Sapmaz et al., 2006; Steele et al., 2009a; Gaass et al., 2011; Eichler et al., 2013; Häkkinen et al., 2015].

3.2.1 Catalyst deposition

The catalyst mixture consists of nanoparticular iron nitrate nonahydrate $Fe(NO_3)_3 \cdot 9H_2O$ and molybdenyl acetylacetonate $MoO_2(acac)_2$. A significant amount of alumina Al_2O_3-nanopowder is added in order to provide a large specific surface area which is necessary for catalytic chemical vapor deposition. The mixture of all these three materials is stored in methanol or isopropanol suspension. The exact amounts of all ingredients is given in the appendix section A.9.

Once again, EBL is carried out for defining small areas in the middle of the device arrays on the metallized chips. For this special deposition and lift-off process, a double-layer of PMMA of more than 400 nm thickness is chosen. It keeps the elevated metallized structures and the SiO_2 surface clean, especially at the edges. The areas reserved for the catalyst are of about 10 to 15 μm^2 size, and the distance from their edges to the middle of the trenches is in the range of 6 to 7 μm.

After development, the catalyst in the suspension is drop-cast onto the chip, and the solvent is dried off. The surplus catalyst material is removed by a lift-off procedure in stirred hot acetone. Then, the catalyst mixture remains only at the desired and predefined areas in the middle of each device array.

The dimensions of the catalyst areas are larger compared to other fabrication procedures, for example in [Keijzers, 2012; Schneider, 2014]. In contrast to the fabrication recipes there, the catalyst is deposited onto the etched SiO_2. When using the double-layer PMMA, the height of the mixtures is more than 300 nm. It is assumed that only CNTs growing out from the upper ranges of the mixture are able to fall over both contacts.

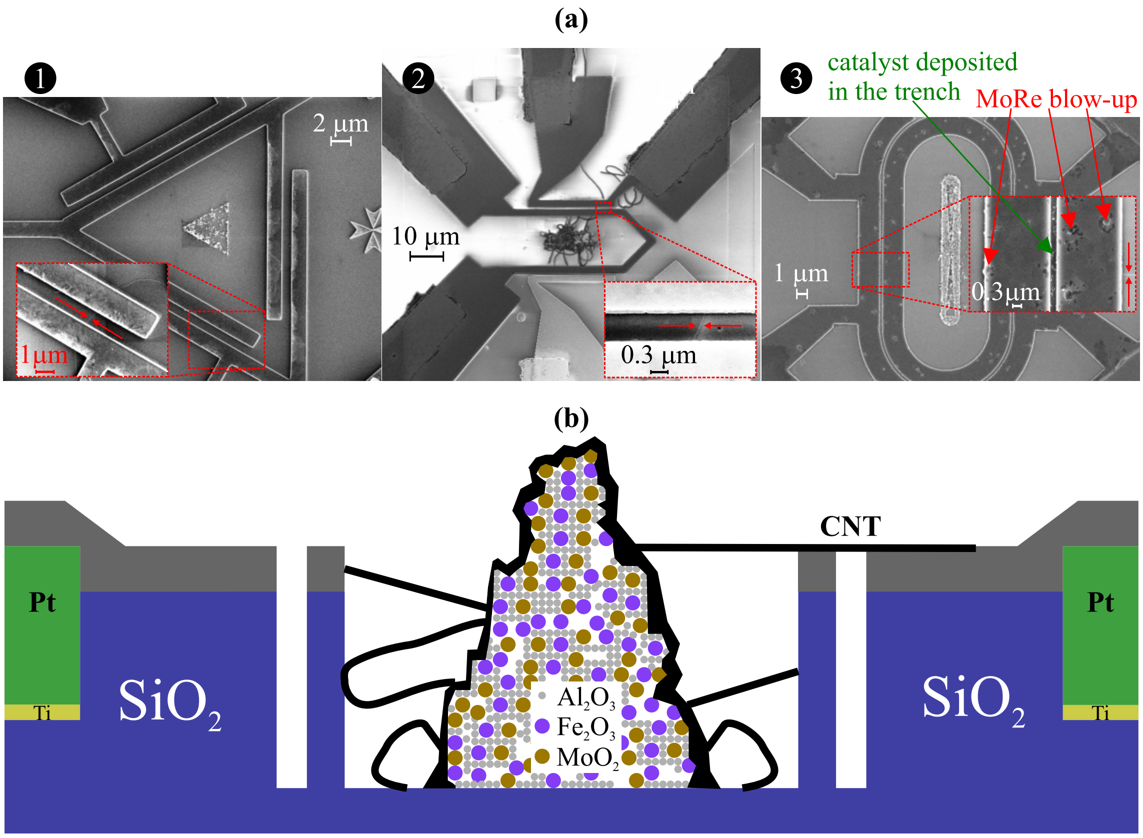

Figure 3.3: Catalyst deposition and CNT growth. **(a)** SEM micrographs of three devices after growth step. In the middle of each micrograph, the area with the deposited catalyst mixture can be made out. The insets show suspended nanotubes (panels 1 and 2), and a CNT which stopped growing at the inner mesa edge (panel 3). They can be found in between the opposite red arrowheads. A too-thin PMMA-layer results in a failed catalyst lift-off procedure, and also catalyst particles can be found in the trench (panel 3). **(b)** Schematic linecut of a device after growth emphasizing the impact of the height differences between catalyst mixture and electrodes. After growth, the catalyst mixture is completely covered with amorphous carbon, which is indicated as a black layer. Some CNTs are not longer than few micrometers, others grow out from layers which are not high enough, and one CNT is successfully overgrown.

This means that the first 200 nm high layer of catalyst mixture does not effectively contribute to the growth yield. Here, this value is the elevation of the electrodes from the surface.

By means of SEM, this assumption is verified: lots of nanotubes seem to stop growing when reaching the inner edge of the elevated electrode mesa, see Figure 3.3(a), panel 3. Indeed, these nanotubes grow out from catalyst segments below the electrode level. On the one hand, this particularity in fabrication leads to less yield, on the other hand contamination of the metallized structures due to catalyst mixture and growth residues is completely avoided.

3.2.2 Chemical vapor deposition

The growth procedure can be divided into three parts: the heating up sequence, the actual growth step, and the cooling down sequence. During heating up, the quartz tube is flushed with argon and hydrogen. In [Kong et al., 1998a], it is stated that the catalyst ingredient iron nitrate nonahydrate decomposes to Fe_2O_3 after heating up in pure Ar flow to $1000\,^{\circ}C$, which was verified by XPS. The same decomposition to MoO_2 is expected for molybdenyl acetylacetonate. The small amount of H_2 flow is added in order to reduce the surface of the electrodes as well as of the catalytic active material.

During the growth step, the argon flow is stopped and the methane valve is opened. The flow rate ratio between CH_4 and H_2 is of $1:2$. The growth duration, i. e. as long as the methane valve is open, varies between 10 to 20 min. The nanotubes are expected to fall over reduced and clean surfaces of the electrodes providing a good electrical contact.

After growth has finished, the CNT including the chips is cooled down to room-temperature again under the same Ar/H_2-environment as for the heating up sequence.

3.3 Preselection and statistics

The growth yield is analyzed using a probe station and following the setup as shown in Figure 2.5(a) in subsection 2.2.1: depending on the measured current through a device after being contacted, the bias V_{sd} is increased to $1 \ldots 3\,\mathrm{mV}$, and the sensitivity of the amplifier is set to 10^{-7} or even $10^{-8}\,\mathrm{A/V}$. Then, the gate voltage V_g is swept in three sequences, usually from 0 V to negative V_g-values, then to the positive gate range traversing 0 Volts, and finally back to 0 V again. The exact current-minimum for a small-gap nanotube depends on the contact electrode material. For the overgrowth fabrication method, this is in the present thesis platinum and molybdenum-rhenium alloys. The device is tested at the same time regarding leakages to the back gate substrate. Such parasitic conductance can originate from overall organic material deposition due to RIE, a bad catalyst lift-off or destruction of the bond pads when being scratched by the needles of the probe station. Thanks to thicker metal layers, especially the latter failure was step by step excluded.

Furthermore, hysteresis of the $I\left(V_g\right)$ characteristics due to sweeping directions is also recorded. It turns out, that this effect can be attributed to adsorbates on the nanotube as well as on the underlying SiO_2, changing the relative permittivity ε_r; this hysteresis is less dominant in the vacuum of the dilution cryostat, which is in rather good agreement with

[Kim et al., 2003]. Hysteresis and its prevention for CNT field-effect transistors are of particular interest for industrial applications, among others see [Pascal-Levi et al., 2014; Park et al., 2017].

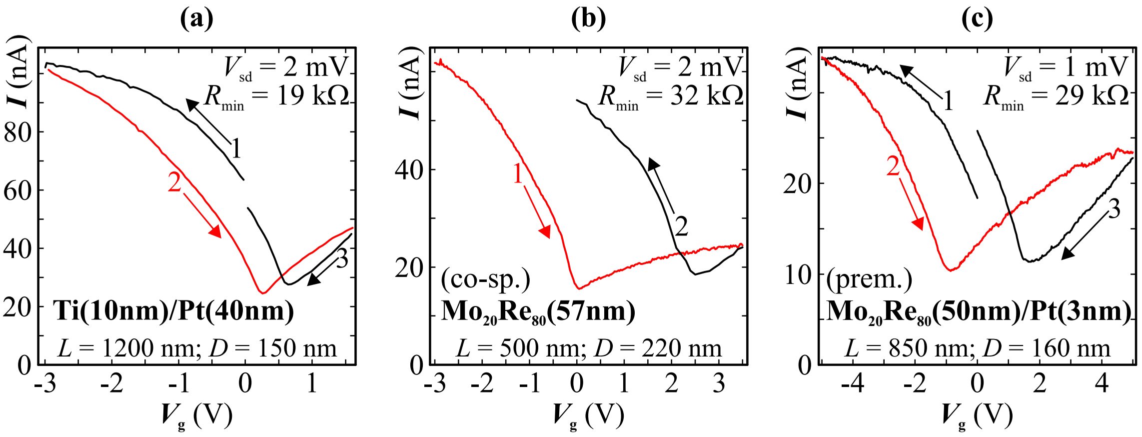

Figure 3.4: Room-temperature gate voltage V_g dependence of the current I, in the CNT devices later examined and evaluated in this thesis. The device parameters as electrode materials and layer thicknesses, trench length L, and trench depth D is stated. The applied bias voltage V_{sd}, and resistance for largest negative V_g are specified above right. All three devices are determined as small-gap CNTs. **(a)** CNT-platinum device "54 short". **(b)** CNT-cosputtered-MoRe device "32 up". **(c)** CNT-premixed-MoRe device "45 right".

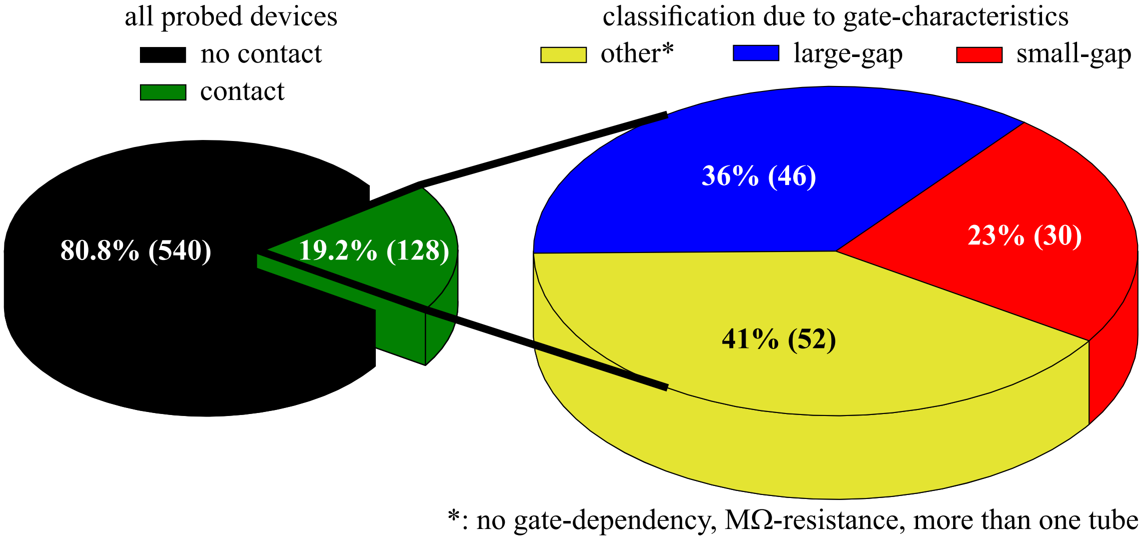

Figure 3.5: Overgrowth-fabrication yield. Statistics of the room-temperature characterization of all probed CNT devices. The percentages and total numbers in braces are noted inside of the circular charts.

The room-temperature characteristics of the three devices examined at cryogenic temperatures and evaluated in the present thesis are plotted in Figure 3.4. Obviously, the minimum of the current appears at different V_g-values for the different electrode materials.
Since all possible devices on the chips are probed in this step, an evaluation regarding the yield of the overgrowth fabrication is reasonable at this point. The statistic includes all chips which show at least one large-gap-CNT device. Chips exhibiting only gate-independent characteristics are not considered because the growth of individual nanotubes was not successful; by means of SEM more than one individual suspended CNT is often observed which can be attributed to a too large amount of catalyst at each device array. Chips with no single current signature are also excluded from the statistics due to fabrication errors, which were only found at the probe station; possible reasons may have been that a catalyst suspension was out of date or that CVD growth was not successful due to contamination of the gas lines etc.
The result of the evaluation is plotted as two pie charts in Figure 3.5: on the left-hand chart, all probed devices are plotted; the percentage of contact in between two electrodes of a potential device is 19 %. This part is further analyzed on the right-hand chart: large-gap, and a small-gap behavior as well as other findings. The latter includes all devices exhibiting gate-independent $I\left(V_g\right)$-behavior or high resistances in the MΩ-range. Note that all possible metallic nanotubes are included in this part as well, but disregarded in the following. Furthermore, the growth of multi-walled CNTs cannot be entirely excluded, which is considered in this subfraction as well. Other origins for these signatures can be bundles of nanotubes or amorphous carbon on undesired catalyst residues in the trench, as shown in panel 3 of Figure 3.3(a). It turns out that the total percentage of feasible devices is 11.4 %, consisting of 4.5 % of small-gap and 6.9 % large-gap nanotubes.

After precharacterization at the probe station, the chips are glued into standard chipcarriers using two-component silver epoxy as adhesive between substrate and inner plane of the chipcarrier. This plane is connected to one pin at the edge, and thus to the p^{++}-Si substrate of the chip.
The most promising devices, preferably small-gap CNTs, are bonded using aluminum wires. Since each electrode is connected to two different bond pads, a four-terminal connection to the nanotube is realized by bonding all four bond pads.
The rather small fabrication yield is compensated by the amount of devices which can be examined at once within one cool-down of the cryostat: having in mind, that only three (4-terminal) or nine (2-terminal bonding) at maximum can be simultaneously examined at low-temperatures, it is rather easy to preselect the most-promising devices.

Unfortunately, bonding can further damage or even destroy devices. It is observed that again a significant amount of nanotubes are lost in between probe station characterization and integration into the cryostat insert.

3.4 Low-temperature setup: the dilution cryostat

Low-temperature techniques and basics are described in detail in [Enss and Hunklinger, 2000; Balshaw, 2001; Ventura and Risegari, 2008; Strunk, 2010], among others.

This section summarizes principles of the dilution cryostat used in the present thesis for low-temperature measurements.

This device is designed and installed by Oxford Instruments. The first part of the system is a cylindrical dewar "IntegraAC cryostat", with three volumes: an outer vacuum chamber (OVC), a tank for liquid nitrogen, and a tank intended for liquid helium. A magnet coil is built in the latter volume, and an external insert can be integrated into the helium bath. After pumping the OVC, the outer and inner tanks are filled with liquid N_2 respectively liquid He. Then the dewar is said to be cold. It can keep its state as long as the cryogenic liquids are refilled regularly.

An external rack contains controllers for cryogenic liquid level measurements, and for the magnet coils. In the following, the whole "Kelvinox400HA" insert and its single parts are described. A computer in a second rack controls thermometry, heaters, and the dilution circuit. The ^{3}He/^{4}He-storage tank is also placed in this rack. A pumping rack contains both pumps for the dilution circuit, and an additional pump is intended for pumping the 1 K-pot. Since these parts are not inserted into the helium bath of the cryostat, "insert" henceforth only denotes the part of this system which is described in the subsequent paragraph.

This "insert" - see Figure 3.6(b) - contains the 1 K-pot, the dilution unit, sorption coal, and all electronic lines for thermometry, heaters, measuring lines for ac as well as dc measurements plus sample holders, and a can which separates all inner elements from the helium bath. It is fixed by 24 screws of stainless steel with an indium flange in between, so that the tight volume inside can be also pumped being denoted as "inner vacuum chamber" IVC. For clarity, this can, which mostly consists of brass, is not shown in the picture of the insert in Figure 3.6(b).

Connections for cabling and vacuum lines are welded onto the top of the insert. In addition, the cabling sockets are fixed vacuum-tight.

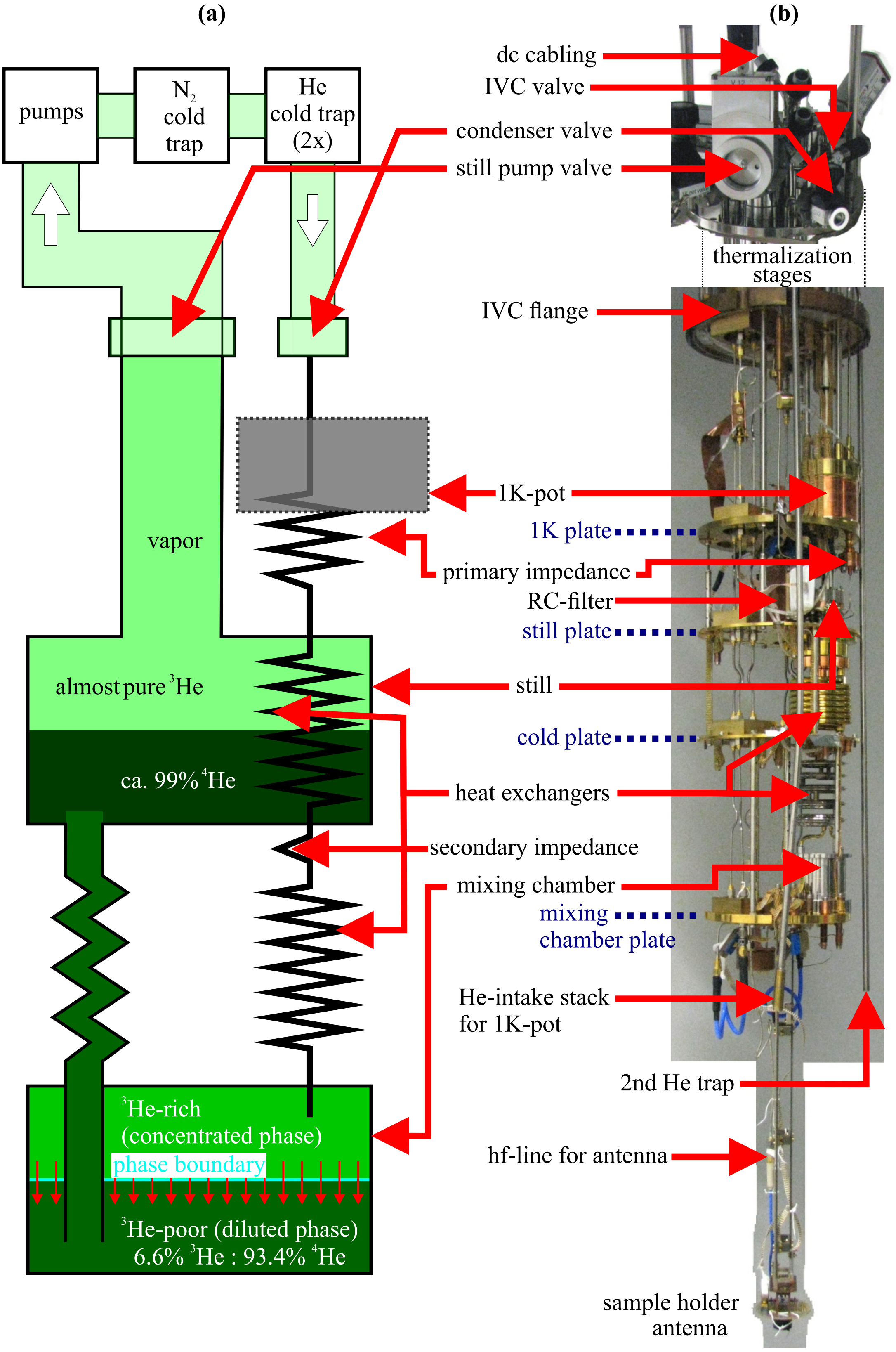

Figure 3.6: **(a)** Sketch of the dilution circuit and **(b)** Insert part of the "Kelvinox400HA" system. The lineup of both subfigures explains the operating principle of the dilution cryostat and the location of the single elements in the setup. For further explanations see the text.

Regarding the sketch in Figure 3.6(a), the operating principle of cooling down to the millikelvin range in dilution cryostats is as follows: a gaseous mixture of both helium isotopes, ^{3}He/^{4}He, is pumped into the cryostat. As soon as being in thermal contact to the 1 K-pot, the mixture starts condensing. At a temperature of about 880 mK, the mixture starts to split up into two liquid phases; these are a ^{3}He-rich phase and a ^{3}He-poor phase exhibiting a volume ratio of approximately 6.6 % : 93.4 % of ^{3}He : ^{4}He which is situated below because of its higher density. The phase boundary is located in the mixing chamber. The process for a ^{3}He-atom to cross the boundary into the dilute phase is endothermic and removes energy from the environment of the mixing chamber. This is the effective cooling, depending on the phase boundary area and the cooling power.

Of course, this solving process ends up when reaching its equilibrium and no cooling takes place anymore. By removing ^{3}He liquid from the dilute phase, the "evaporation" process across the phase boundary is maintained. This is realized by pumping the dilute liquid of ^{3}He/^{4}He to the still which is at a temperature of about 700 mK. In the still, almost only ^{3}He vaporizes because of the higher vapor pressure. The gaseous ^{3}He is pumped out from the still and from the insert by a series of turbo pump and rotary vane pump outside the cryostat at room temperature. On the other side of the rotary vane pump, the gas is first cleaned from impurities by a nitrogen cold trap, followed by a ^{4}He-trap in the dewar, and a second ^{4}He-trap at the insert. After being cleaned and cooled to ^{4}He-temperatures, the gas reenters the dilution circuit part of the insert, and condenses at the 1 K-pot. The liquid drips into the mixing chamber, adding to the concentrated ^{3}He-phase.

As an additional remark, the cooling from 1 K to the critical temperature for phase separation is provided by the thermal contact to the still. Temperatures of about 10 mK below the mixing chamber plate are realized in the present dilution cryostat. This state can be maintained as long as the dilution circuit is running, the 1 K-pot is full and can be pumped, and enough liquid ^{4}He is in the tank of the dewar.

3.5 Measurement setups

This section deals with the circuit diagrams and electronic setup used for all experiments in the dilution cryostat described in section 3.4. Note that the size of the resistors and capacitors in the voltage divider as well as for the low-pass filter should be adapted to its usage. For that reason, especially the device-resistance range has to be taken into account. The measurements are performed using lab::Xpress scripts. Here, each device is controlled via setting and sweeping parameters, for example voltages for V_{sd}- and V_{g}-supplies, frequency as well as nominal power at the rf-generator. Simultaneously, measured quantities as, e. g., voltage drop or converted current are recorded. The measurement data is saved in files having predefined columns for set and measured quantities each.

3.5.1 dc cable filtering

The dc cabling runs through several filtering stages as depicted schematically in Figure 3.7. The location of the filtering stages in the cryostat as well as outside is also indicated. In first measurements, the series resistance was dominated by a $10\,\mathrm{k\Omega}$ resistor at the breakout box, but these resistors were removed later. The final dc cable filtering takes place at two stages: the first one is a RLC low-pass filter at room-temperature, which is directly connected to the insert at the dc cabling socket (see Figure 3.6). The LC low-pass filtering is modified by an additional resistor at the capacitor in order to avoid resonant amplification. The second RC filter is mounted at the still plate, i. e. , at approximately $700\,\mathrm{mK}$; it is a series of two single RC-filter elements having a dc resistance of $2.02\,\mathrm{k\Omega}$ in total. This RC filter contributes the main parts of the total dc line resistance of $2.1\,\mathrm{k\Omega}$.

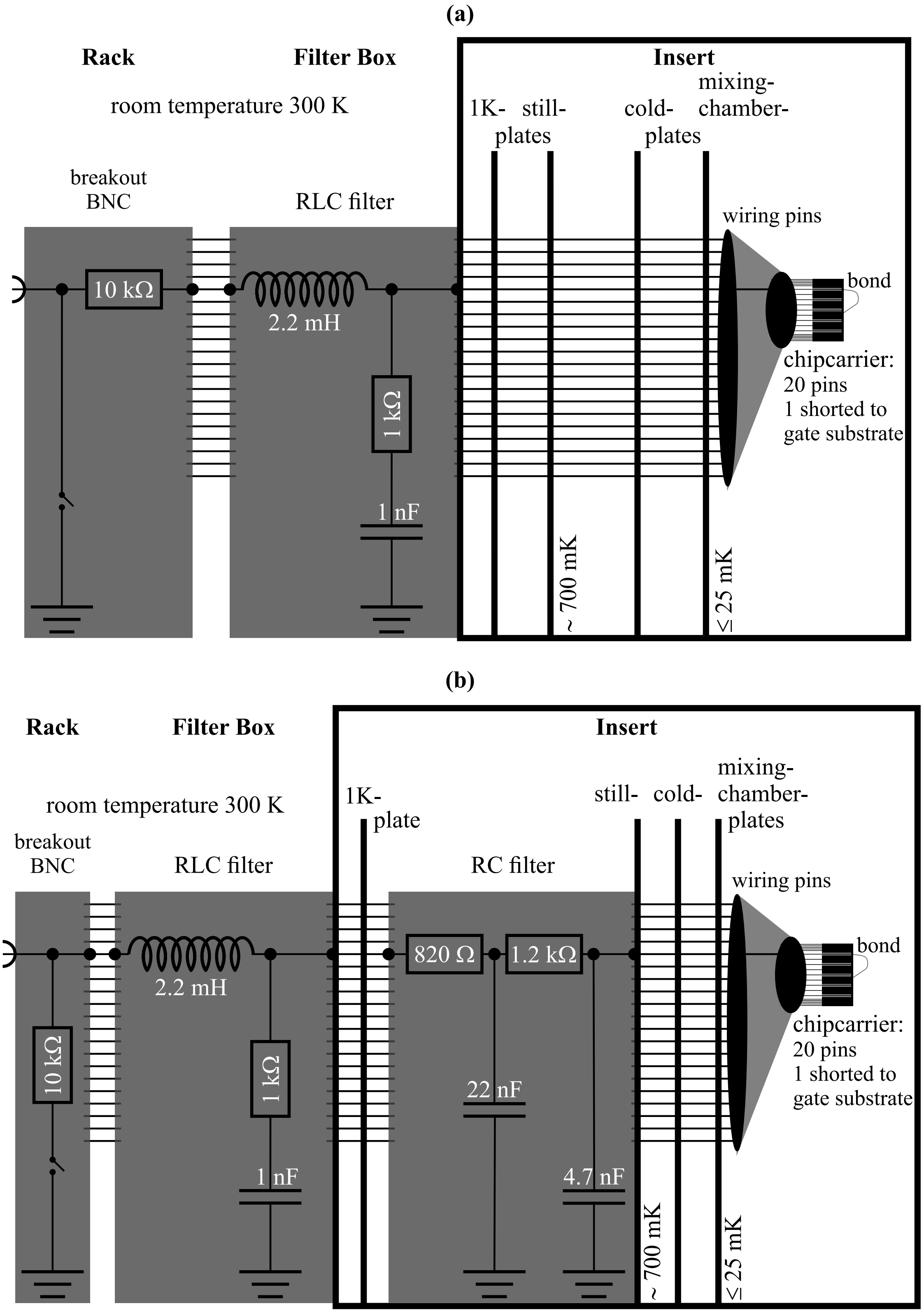

Figure 3.7: Filtering in the dc cabling. The setup **(a)** was step by step modified to **(b)**. The measurement data evaluation takes the serial resistance into consideration. The thick black lines indicate here the insert and the temperature stages, as denoted in section 3.4 and depicted in Figure 3.6(b).

3.5.2 Voltage-bias setup

This setup is used for quantum dot spectroscopy as well as single traces for constant V_{sd} or V_{g}. The circuit diagram can be seen in Figure 3.8.

As already indicated in Figure 2.8, section 2.4, regarding quantum dot spectroscopy, and in agreement with equation 2.24, electrons are regarded as charge carriers. Therefore, by applying a positive bias at the V_{sd}-supply, electrons are pulled from the source into the supply and μ_{s} is shifted below μ_{d} by $-eV_{\mathrm{sd}}$. For the opposite case, it is $\mu_{\mathrm{s}} - \mu_{\mathrm{d}} = eV_{\mathrm{sd}}$ for $V_{\mathrm{sd}} < 0$. Since the technical current has the inverse direction of the electron movement, a positive current is measured for positive bias and vice versa, see also [Thijssen and van der Zant, 2008].

The bias supply is connected to the device in the cryostat over a voltage divider at the breakout box. The current read-out takes place over a preamplifier and current-voltage converter plus digital multimeter. In order to obtain the differential conductance G in units of e^2/h out of the dc current, each $I\,(V_{\mathrm{sd}})$-linetrace is numerically smoothed and derived first. Then, each data point is multiplied by a factor of $h/e^2 \cdot 1/V_{\mathrm{sd,res}}$, where $V_{\mathrm{sd,res}}$ is the constant step width in between each bias value after the voltage divider.

The gate voltage supply connects to the global back gate substrate on the chip with an additional low-pass filter at the breakout box.

The setup can be upgraded by a lock-in-amplifier (LIA) which supplies an additional small ac signal to the voltage bias. The ac voltage read-out takes place after the preamplifier/current-voltage converter. To obtain G in units of e^2/h, the measured ac current is multiplied by $h/e^2 \cdot 1/V_{\mathrm{ac}}$.

3.5.3 Current-bias setup

In Figure 3.9, the circuit diagram for a current-bias setup is sketched. For this setup, a LIA is commonly used for readout. The dc current is biased by a voltage supply plus series resistor, and superimposed with a small ac current from the LIA output in combination with another significantly higher series resistor. The biased current is running through the input dc line to the device including bond wire, leads, CNT and back over the opposite lead, bond wire and dc line to the second BNC terminal at the breakout box which is set to ground. The voltage drop over the CNT is measured as follows: two further leads to the nanotube connect to a voltage preamplifier. This connects to the LIA. This way, the differential voltage drop over the CNT is measured and simultaneously the differential resistance dR can be recorded. The gate supply is connected to the nanotube as stated before.

3.5.4 Mechanic setup

In addition to the voltage bias measurement setup described above, an open-ended coaxial cable is placed above the chip carrier and serves as an antenna for driving the CNT. A radio frequency (rf-)supply is connected to the cable. The nominally supplied power of the electromagnetic signal is set by the rf supply in terms of "decibel milliwatt" (dBm), in reference to a 50 Ω resistor. The emitted power at the open-end of the coaxial cable and irradiated to the carbon nanotube device is hence proportional the nominal set power at the rf supply. In order to remove room-temperature noise, additional damping elements are mounted at the rf sockets on top of the insert. These are placed next to the dc cabling sockets, which can be seen in Figure 3.6(b).

An amplitude-modulated-(AM-)signal is created by connecting the low-frequency-LIA-output to the modulation input of the rf generator.

The readout of the current, and the shifts due to resonant actuation of the nanotube takes place after the preamplifier/current-voltage converter by the dc multimeter and/or by the LIA, see Figure 3.10.

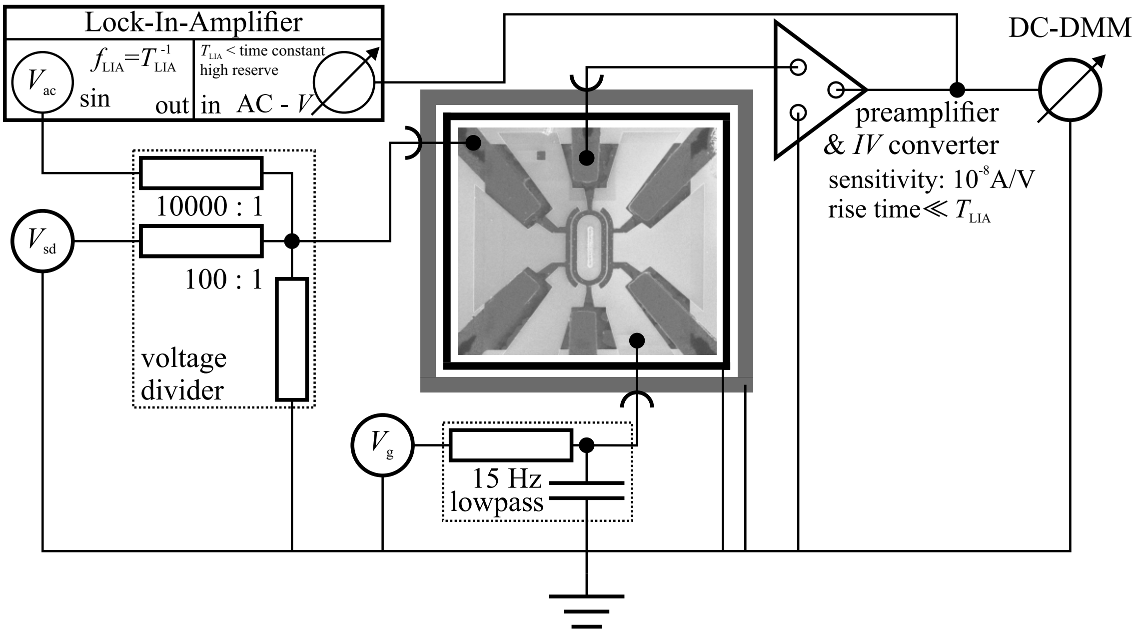

Figure 3.8: Voltage-bias setup. The breakout box is indicated as a gray line, and the insert as a black line surrounding the chip respectively the device. The two additional terminals to the device which are not used are either not bonded or set to float at the breakout box. Further descriptions see subsection 3.5.2.

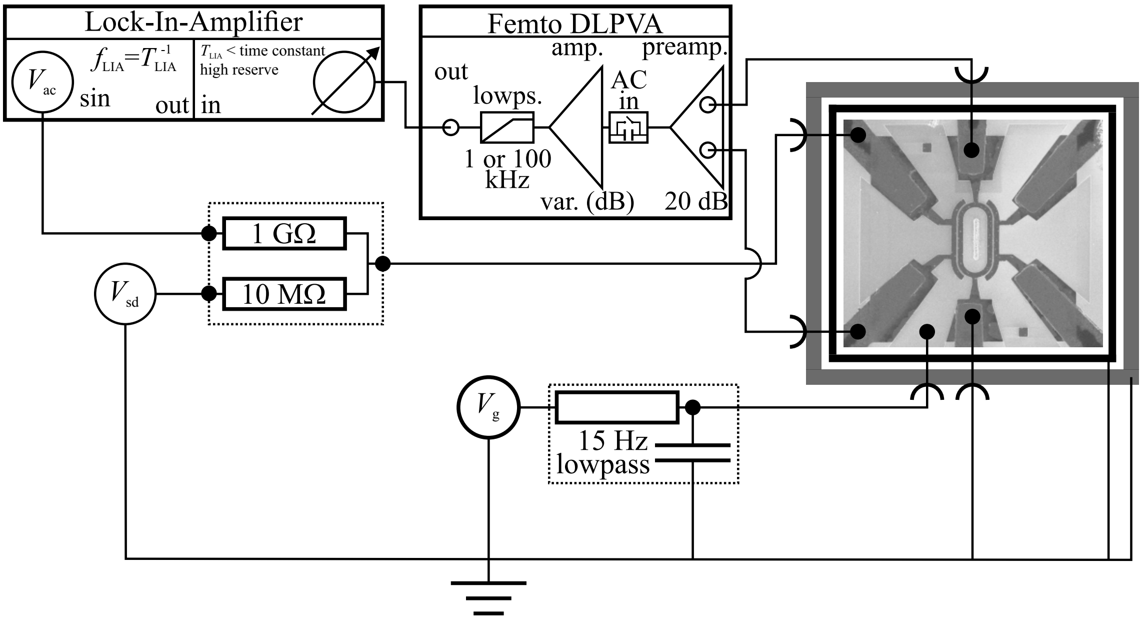

Figure 3.9: Current-bias setup using four terminals of the device. Current-line and voltage probes are chosen to be crossed, as indicated. Further descriptions see subsection 3.5.3.

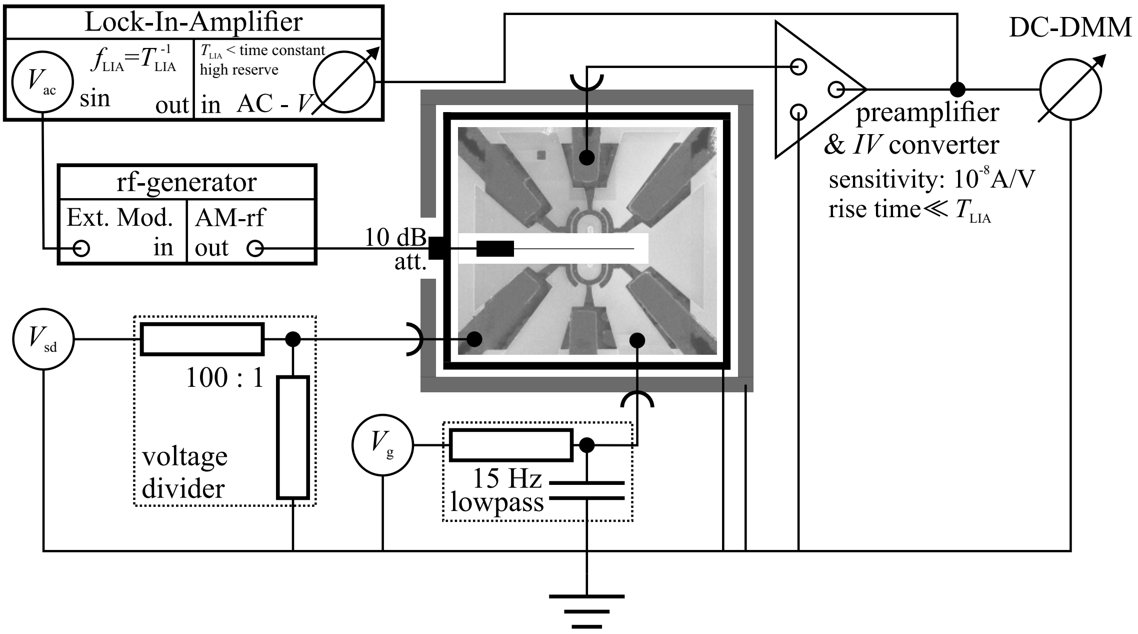

Figure 3.10: The em-wave is fed into the cryostat and irradiated contact-free onto the device. Further descriptions see subsection 3.5.4.

Chapter 4

Transport spectroscopy of an ultraclean carbon nanotube quantum dot

In this chapter, a detailed transport spectroscopy measurement of an ultraclean carbon nanotube quantum dot is presented and evaluated. All transport regimes which are described in chapter 2 are observed. The regular pattern of Coulomb oscillations, the observation of the first electron and hole transitions confirm the absence of contamination or defects.

The fabrication was performed as described in chapter 3, together with Felix Schupp, see [Schupp, 2014]. The electrode structure is similar to the EBL mask depicted in panel 1 of Figure 3.2(a). It consists of a 10 nm thick titanium sticking layer plus 40 nm platinum on top. The electrodes are separated by a trench of 1.2 µm width.

The growth took place under standard conditions for 20 min as last fabrication step. During precharacterization, the suspended small-gap nanotube on the device "54 short" was probed as depicted on the diagram of Figure 3.4(a). The detailed fabrication recipe is stated in section B.1 in appendix B.

The low-temperature measurements were carried out in the dilution cryostat which is presented in section 3.4, and including the first dc filtering setup, see Figure 3.7(a). The long-term base temperature for this cool-down is (15 ± 5) mK. All stability diagrams, i.e. $G\left(V_{\mathrm{sd}}, V_{\mathrm{g}}\right) \equiv \mathrm{d}I/\mathrm{d}V_{\mathrm{sd}}\left(V_{\mathrm{sd}}, V_{\mathrm{g}}\right)$ color-maps which are presented in this chapter are obtained using the voltage-bias setup as drawn in Figure 3.8, with dc current readout. The observed hysteresis of the V_{g}-sweep in Figure 3.4(a) reduces to few millivolts at 15 mK. This estimation is obtained by comparison of the first few Coulomb oscillations in $I\left(V_{\mathrm{g}}\right)$ measurements for both sweeping directions of V_{g}. This has to be considered when measurements are compared to each other, for example for electron N_{el} or hole N_{h} indexing.

4.1 Localization of transport regimes and band gap

4.1.1 Transport regimes

Figure 4.1 depicts a $G\left(V_g\right)$ measurement of the CNT quantum dot at base temperature: it zooms into the region around the band gap which is constricted in between the first electron and hole transition, $N_{\mathrm{el}} = N_{\mathrm{h}} = 1$. Since the first hole transition takes place at $V_g = +0.255\,\mathrm{V}$, the nanotube is intrinsically positively doped. This may be caused by the metal contacts setting the Fermi level E_{F} close to the valence band of the CNT, which is also observed for many other SWCNT-based quantum dot devices, among others see [Cao et al., 2005; Keijzers, 2012; Stiller et al., 2013; Schmid, 2015; Dirnaichner, 2017].

In contrast to the hole conduction side, the first Coulomb oscillations at the electron transport side are about an order of magnitude smaller. The separation in between these oscillation maxima is in the range of about 20 mV on the V_g axis. At about $N_{\mathrm{el}} = 12$, the oscillation minima in Coulomb blockade do not reach the noise level anymore, alternating in different absolute values for every second valley.

4.1.2 Band gap

The band gap of the nanotube and the first Coulomb blockade diamonds are mapped in the stability diagram of Figure 4.2. Unfortunately, the left border of the band gap is not recorded and has to be extrapolated for further evaluation. Nevertheless, this stability diagram confirms the rightness of the indexing stated in Figure 4.1: the very first Coulomb oscillation is probed at 360 mV, which is in well agreement with $N_{\mathrm{el}} = 1$ from Figure 4.1. By applying the same techniques as for determining E_{C} in Coulomb blockade spectroscopy, see section 2.4, the energetic size of the gap can be estimated. This is plotted in the diagrams on the right-hand side of Figure 4.2. The larger error bar for the band gap originates from the uncertainty of the extrapolation to the first hole transition. A band gap size of

$$E_{\mathrm{G}}^{\mathrm{CNT}} = (62.4 \pm 2.9)\ \mathrm{meV} \tag{4.1}$$

is evaluated. Note that the energy axis of the right diagram is labeled as $E_{\mathrm{add}} = E_{\mathrm{C}} + \Delta\varepsilon$. The size of $\Delta\varepsilon$ is not resolved, but for the quantized Coulomb blockade regime of $\Delta\varepsilon \lesssim E_{\mathrm{C}}$, see Table 2.2 in subsection 2.3.2.

The stability diagram gives also a first estimation of the bias and gate range of the electron diamonds. A detailed measurement is depicted in Figure 4.4 in section 4.3.

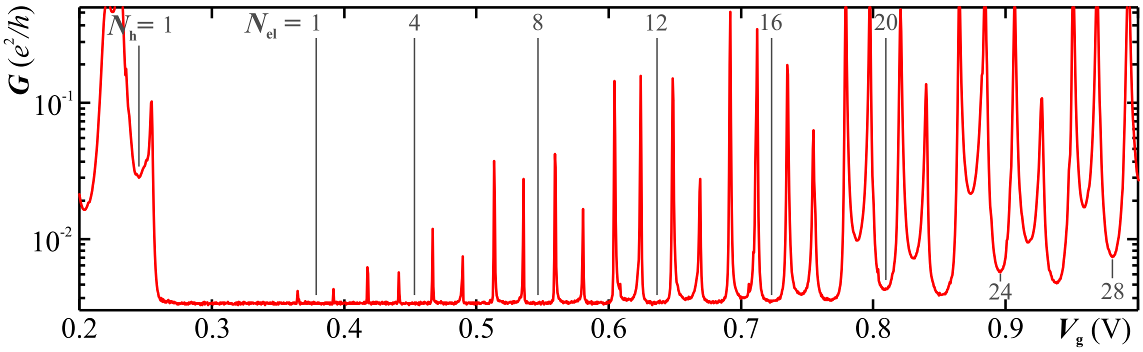

Figure 4.1: Different transport regimes in the same nanotube. Gate dependence of the conductance $G(V_g) = dI/dV_{sd}$. The bias voltage is set to $V_{sd} = -20\,\mu V$. The cryostat is at base temperature of circa 15 mK. The first hole transition, the band gap and the electron transport side starting from the first electron transition at 0.365 V is plotted. The conductance is plotted on a logarithm scale.

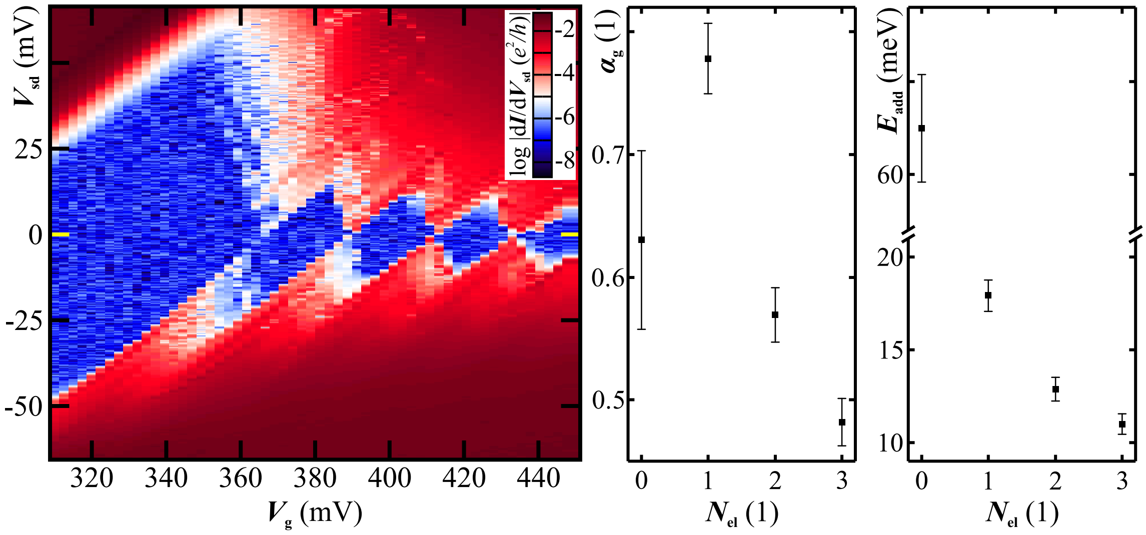

Figure 4.2: Stability diagram mapping the conductance on a logarithmic scale around the band gap and the first electron diamonds at base temperature. Following the method described in section 2.4, the size of the band gap as well as charging energies can be extracted and is plotted on the diagrams on the right-hand side.

4.2 Hole transport regime

The stability diagram of Figure 4.3(b) reveals the first hole transitions left-hand side of the band gap. Already at the fourth oscillation maximum, a conductance level $\gtrsim 1\,e^2/h$ is reached. For higher negative gate voltages, the oscillation minima saturate at about $0.5\,e^2/h$. This trend can be seen in Figure 4.3(a).

For consequence, only the first three conductance oscillations starting from the band gap can be attributed to single-hole tunneling alone. Then, the dot opens up and evolves to the the Fabry-Pérot regime.

In recent works, see [Dirnaichner et al., 2016; Dirnaichner, 2017], the periodicity of FP-oscillations is used to determine the length of the electron waveguide which is assumed to be equal to the suspended part of the CNT in between the electrodes. The result is a length of $L = 1240\,\mathrm{nm}$, which is in agreement with the EBL settings. Furthermore, the detailed analysis of the secondary interference pattern delivers a range of the chiral angle which is of

$$22^\circ \leqslant \theta < 30^\circ \quad . \tag{4.2}$$

This evaluation requires a stability diagram to larger negative V_g-values which is plotted in Figure 1(a) in [Dirnaichner et al., 2016]. The model of an "armchair-like" CNT is used, which exhibits a curvature-induced band gap. The basics leading to this classification are described in Figure 2.4(a) in subsection 2.1.4. Using this chiral angle range and the estimated band gap size from equation 4.1, the equation 2.15 delivers possible diameters of $d \leqslant 0.5\,\mathrm{nm}$. These unrealistic small values, see [Hedman et al., 2015], are a consequence of the observed band gap. According to [Deshpande et al., 2009], repulsive electron interaction at half filling leads to a enlarged Mott band-gap in armchair-like CNTs being proportional to $r^{-1.3}$. Evaluation of data recorded on this device in the Fabry-Pérot regime, by M. del Valle and A. Dirnaichner, see [Dirnaichner et al., 2016], results in a diameter of $d \simeq 2\,\mathrm{nm}$.

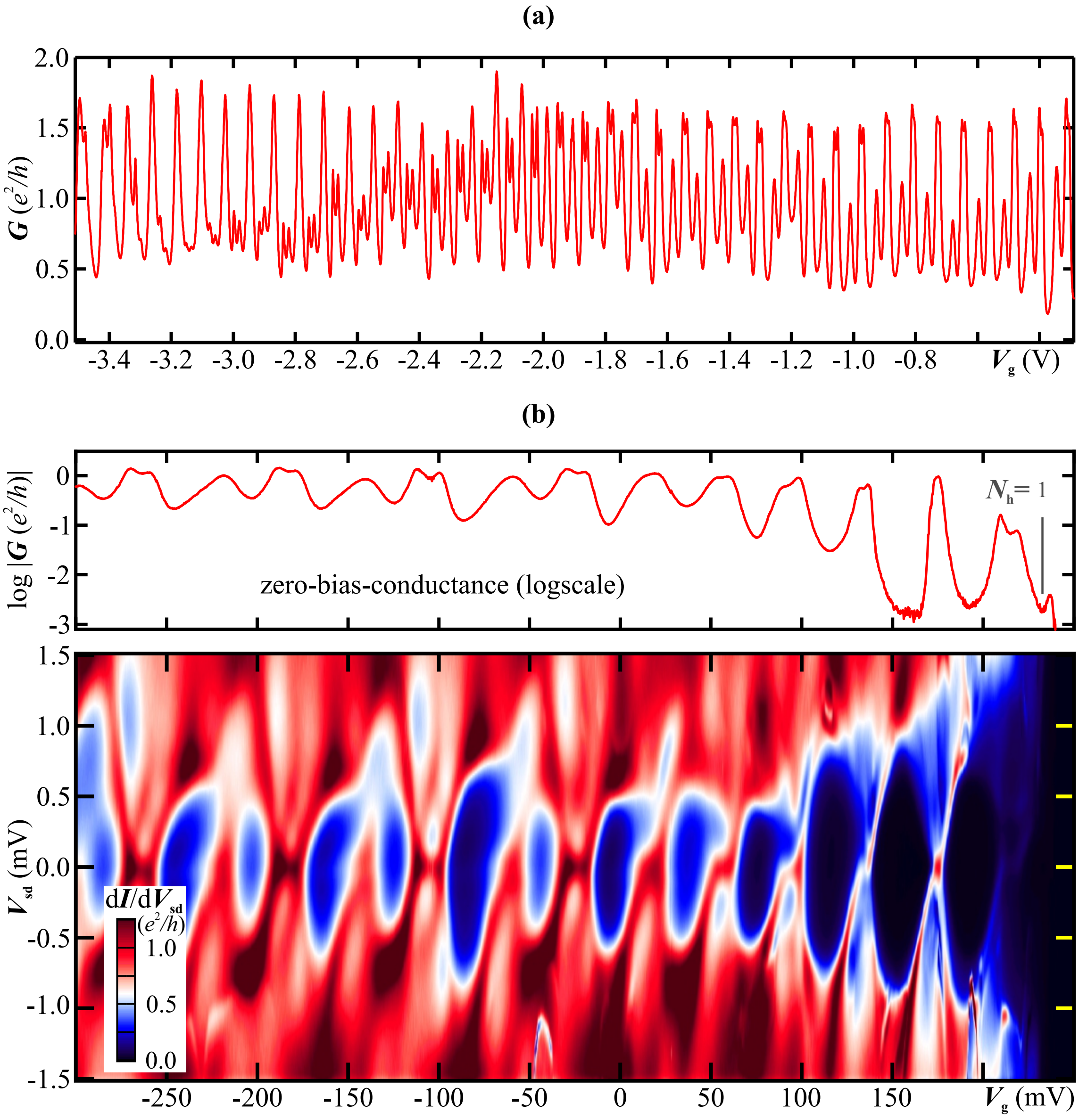

Figure 4.3: **(a)** $G\left(V_{\mathrm{g}}\right)$-plot at base temperature and a bias voltage of $-20\,\mu\mathrm{V}$, for negative gate voltages to $-0.3\,\mathrm{V}$. **(b)** Stability diagram of the hole transport side starting from $-300\,\mathrm{mV}$ into the band gap at base temperature. For a better orientation, the labels on the right-hand side V_{sd}-axis are colored yellow. A conductance-plot along the gate axis at zero bias is plotted above to reveal the first hole transition.

4.3 Strong Coulomb blockade regime

The conductance color maps in Figure 4.4 show the first thirty Coulomb diamonds at the electron transport side. Note that the oscillation for the first electron transition is not recorded in Figure 4.4(a), but extrapolation delivers a value which is in well agreement with the measured peak in the stability diagram of Figure 4.2 or the $G\left(V_\mathrm{g}\right)$-characteristic of Figure 4.1. Since the current as well as the differential conductance scale on small values, the color scale is chosen to be logarithmic for the very first eight electron diamonds. The tunnel barrier widths are broad, however the curve shape of the Coulomb oscillations is given by the lifetime broadening of the dot level states, $\hbar\Gamma$. In this gate region, the dot is in the quantum Coulomb blockade regime, see case (III) in Table 2.2.

The well defined diamond structure for each electron valley is accompanied by additional features as can be seen first at $N_\mathrm{el} = 4$ for negative bias. These features appear regularly for increasing electron numbers for negative as well as positive bias. They exhibit a characteristic oval shape preferably in the conducting region, but do also spread into each Coulomb blockade diamond, see also Figure 4.4(b). These signatures are an additional proof for a suspended and mechanically active carbon nanotube acting as quantum dot, see [Usmani, 2006; Steele et al., 2009b]. A recent publication, [Schmid et al., 2012], deals with the same observation in measurements of a comparable device. By performing the same measurement with the same device in a top-loading dilution refrigerator, where the CNT is immerged into the ^{3}He/^{4}He liquid, it is shown that these features do not appear in the stability diagrams anymore, see [Schmid et al., 2015b]. Significant for the present CNT is the appearance of these ovals already in the strong Coulomb blockade regime for low electron numbers.

The underlying effect is a strong feedback of the electron tunneling event on the mechanical system which generates mechanical oscillations and therefore a modification of the measured current through the dot, see also [Usmani, 2006].

The parallel lines in the conducting regions of the stability diagram, which are visible for example close to the third electron diamond are attributed to the confinement quantum level structure. The mechanism for the high-bias regime is described and sketched in Figure 2.9(a). Here, more than one state is in the bias window contributing to the overall current respectively conductance.

Furthermore, inelastic co-tunneling features become visible within the seventh electron diamond at first. The finite conductance within the blockade region (white colored on the $\log G$-scale) originates from the excited state which is energetically available when the threshold condition $e\left|V_\mathrm{sd}\right| \gtrsim \varepsilon^*$ is fulfilled, see also Figure 2.9(b) in subsection 2.5.2.

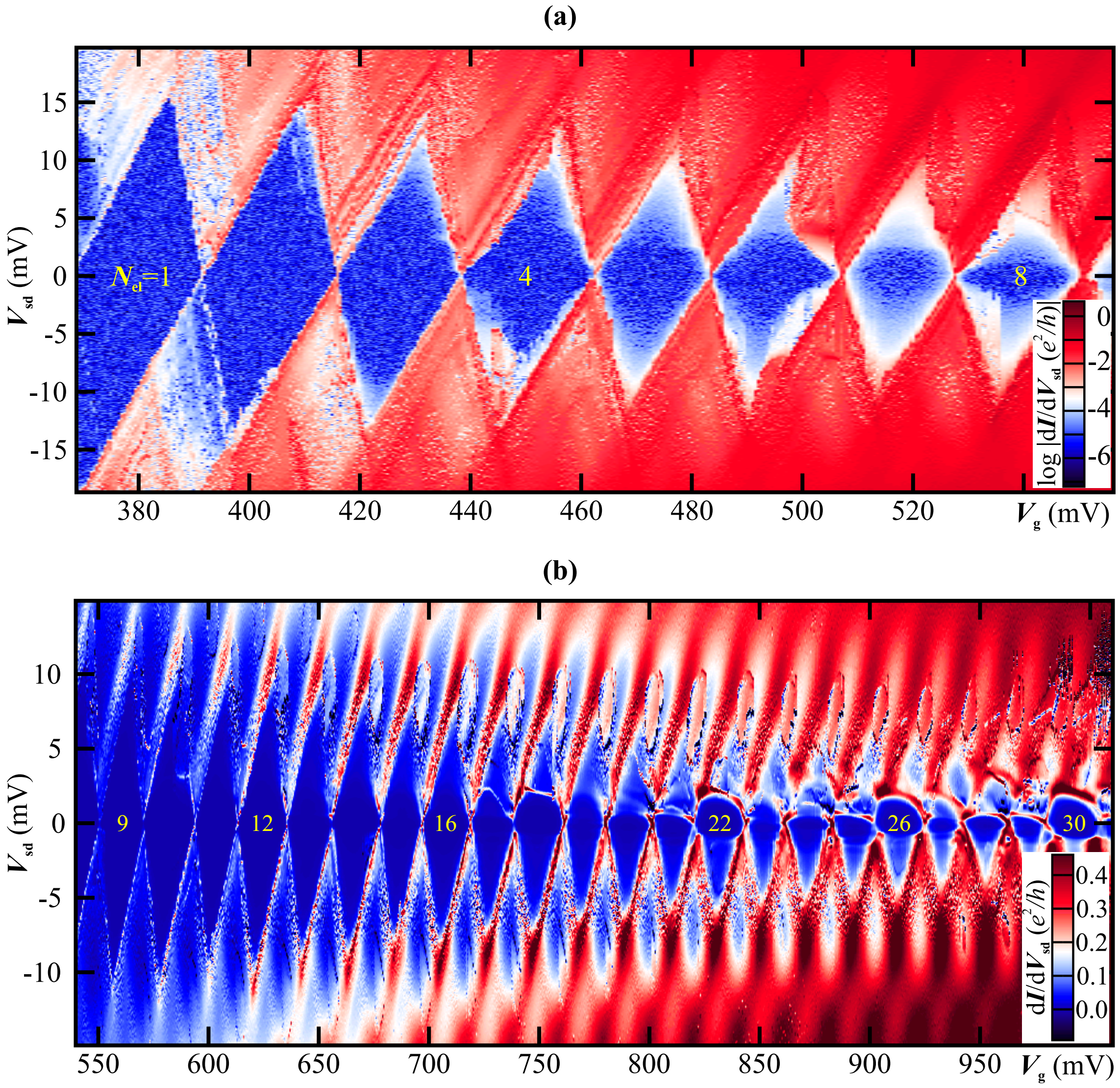

Figure 4.4: Stability diagram of the electron transport side right after the band gap. The measurement at base temperature using the voltage-bias setup (see Figure 3.8) is divided into two parts: **(a)** the conductance is plotted on the logarithm scale exhibiting the diamonds of the first eight electron transitions. **(b)** since the overall conductance increases with increasing N_{el}, the conductance scale is chosen in units of e^2/h.

Inelastic co-tunneling signatures in the conductance strengthen with increasing N_{el}, becoming visible on the G-color-scale in Figure 4.4(b) for each diamond beginning from $N_{\mathrm{el}} = 17$. Especially for positive bias, a distinct signature is observed. The sweeping direction from negative to positive bias may be a reason for this asymmetry. A pattern for every fourth electron diamond starting from $N_{\mathrm{el}} = 18$ can be made out, where the conductance threshold is more pronounced than for the others.

Spectroscopy on this quantum dot is performed and results in the estimation of $\alpha_\mathrm{g}, \alpha_\mathrm{s}$, $C_\mathrm{g}, C_\mathrm{s}, C_\Sigma$, and E_add for each of the first thirty electron diamonds. The dependencies as a function of N_el are plotted in Figure 4.5(a), (b), and (c). It can be seen that α_g decreases with increasing N_el, which is in contrast to the trend for α_s. The latter exceeds the gate conversion factor at $N_\mathrm{el} = 19$. A linear fit is performed revealing an intersection at $N_\mathrm{el} = 17$, linear fit parameters can be seen in Table 4.1.

The same intersection can be made out for C_g compared to C_s. C_Σ increases with increasing N_el in total, but an alternation between subsequent levels is also observed. The same alternation but more pronounced can be seen for the addition energy if the first two levels are neglected. This two-fold alternation is replaced by a four-fold alternation when inelastic co-tunneling arises significantly at $N_\mathrm{el} = 18$.

N_el range	$1\dots8$		$9\dots30$	
	slope	intercept	slope	intercept
α_g	-0.017 ± 0.003	0.636 ± 0.017	-0.007 ± 0.001	0.491 ± 0.231
α_s	0.008 ± 0.002	0.225 ± 0.010	0.009 ± 0.001	0.229 ± 0.020

Table 4.1: Linear parameters for fits in Figure 4.5(a); the conversion factors α_g and α_s.

N_el range	$3\dots8$	$9\dots16$	$20\dots30$
slope $(10^{-18}\,\mathrm{F}/1)$	0.375 ± 0.174	0.213 ± 0.162	0.757 ± 0.298
intercept $(10^{-18}\,\mathrm{F})$	11.07 ± 1.03	15.51 ± 2.21	6.87 ± 6.98

Table 4.2: Linear parameters for fits in Figure 4.5(b); The total capacity of the CNT quantum dot, C_Σ.

N_el range	$3\dots8$	$9\dots16$	$20\dots30$
slope (meV/1)	-0.340 ± 0.162	-0.124 ± 0.084	-0.193 ± 0.074
intercept (meV)	14.04 ± 1.01	10.27 ± 1.19	10.91 ± 1.82

Table 4.3: Linear parameters for fits in Figure 4.5(c); The energy needed to add the next electron to the quantum dot, E_add.

(a) ***Conversion factors*** α_g, α_s (1)

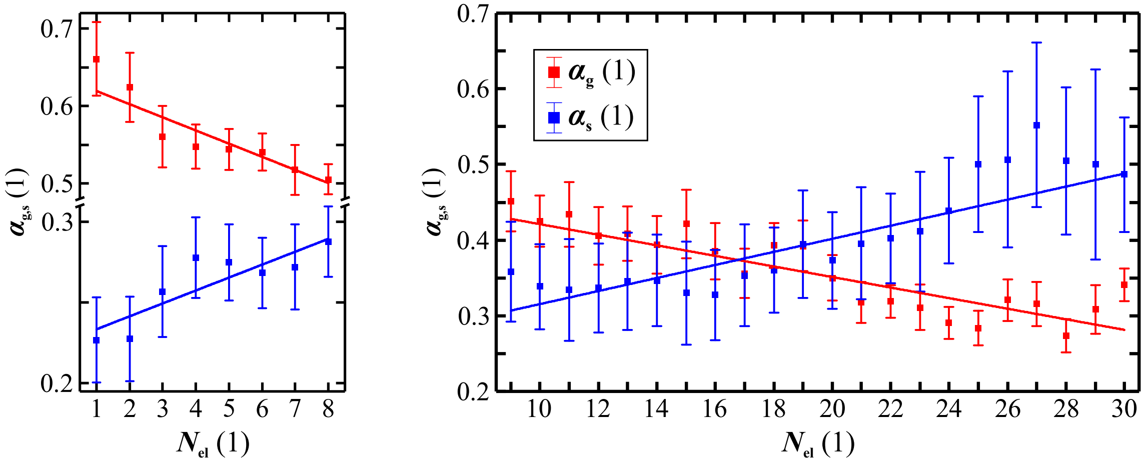

(b) ***Capacitive couplings*** C_g, C_s, C_Σ (10^{-18} F)

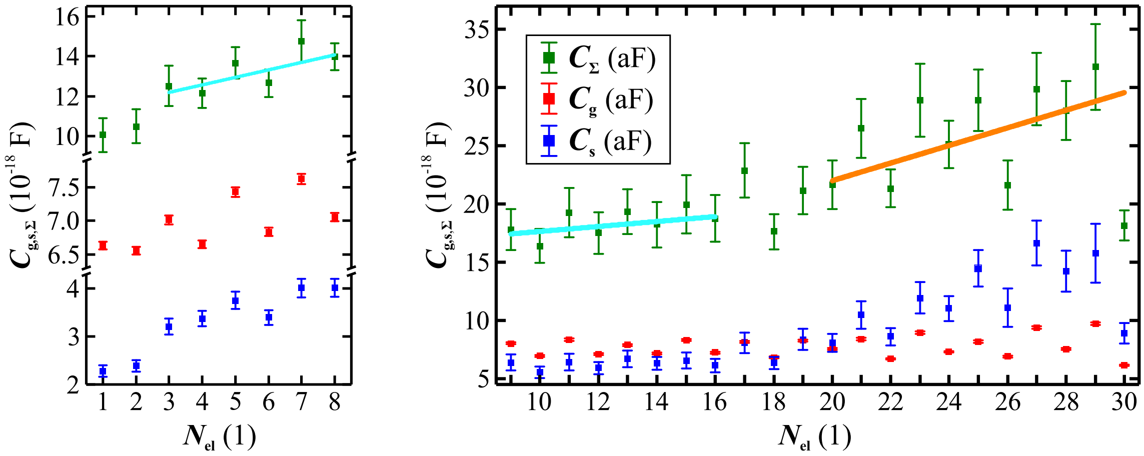

(c) ***Addition energy*** E_{add} (meV)

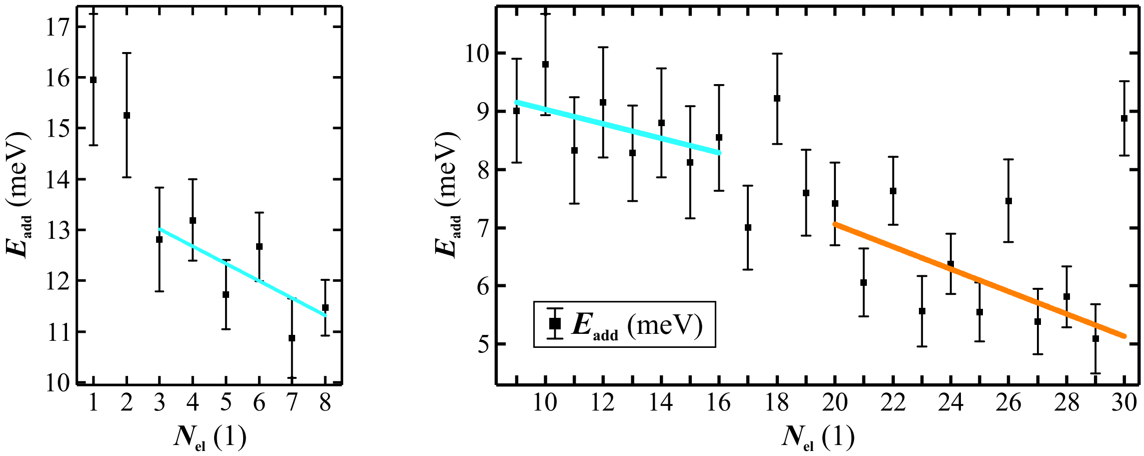

Figure 4.5: Spectroscopy of the stability diagrams of Figure 4.4. **(a)** Conversion factors α_g and α_s. **(b)** Capacitive coupling constants C_g, C_s, and C_Σ. **(c)** Addition energies needed to charge the dot with the actual electron.

The observed two-fold alternation has its origin in filling one orbital level with electrons exhibiting different spins. The four-fold alternation, which is observed at about $N_{\mathrm{el}} \approx 18$, is due to the filling of a four-fold degenerated shell - $(K\uparrow, K\downarrow, K'\uparrow, K'\downarrow)$ - with the first electron, see also Fig. 2.6. In addition to the charging energy E_{C}, the amount $\Delta\varepsilon$ has to be paid. According to [Makarovski et al., 2006], an electronic length of this CNT quantum dot is obtained using the relation $\Delta\varepsilon = \pi\hbar v_{\mathrm{F}}/L$. A mean value of $\Delta\varepsilon \approx 1.8967\,\mathrm{meV}$ is estimated regarding the difference of E_{add} between the levels 17,18, and 21,22, and 25,26, and resulting in $L = 873\,\mathrm{nm}$. In Figures 4.5(b) and (c), several linear fits for certain N_{el} ranges are performed, also in order to visualize the change from two-fold to four-fold shell filling. The parameters for the linear fits for C_{Σ} are stated in Table 4.2, and for E_{add} in Table 4.3. The slope for the C_{Σ} fits is larger for the $N_{\mathrm{el}} = 20\ldots30$ range. Furthermore, the slope for E_{add} fits is more steep for the $N_{\mathrm{el}} = 20\ldots30$ range. A more detailed analysis of the changing from two-fold to four-fold shell filling in carbon nanotube quantum dots is made in [Deshpande and Bockrath, 2008]. In contrast to other carbon nanotube quantum dots, it turns out that the shell filling as a function of electron numbers is shifted by 2. This is because of the first two electron states exhibiting other characteristics regarding degeneracy. The subsequent shell is filled with the first electron at $4N+2$, which is confirmed by the extracted E_{add} in Figure 4.5(c) for $N_{\mathrm{el}} = 18, 22, 26, 30$.
Since the diamond-like shape of the stability diagram becomes overlapped by co-tunneling and mechanical features for increasing N_{el}, the spectroscopy evaluation stops at this point. The dot is in the intermediate transport regime, according to Table 2.3, case (IV).

4.4 Intermediate transport regime

For orientation and completeness, the $G\left(V_{\mathrm{g}}\right)$ diagram of Figure 4.1 is continued in Figure 4.6. Indeed, all diagrams are extracted from one single measurement. As expected, the Kondo effect is observed in this regime. Stability diagrams at $N_{\mathrm{el}} \approx 80$ exhibit a clear and measurable zero-bias anomaly (ZBA) for odd N_{el}, see Figure 4.7. These peaks are overlapped by further elastic co-tunneling features. Nevertheless, distinct ZBAs taken from the middle of each odd-numbered valley can be attributed to the Kondo effect, see [Cleuziou et al., 2013; Schmid et al., 2015a] and also section 2.5.3. As mentioned there, the critical temperature T_{K} below which the Kondo effect establishes in quantum dots can be estimated regarding the line shape of zero-bias-anomaly following [Kretinin et al., 2012].

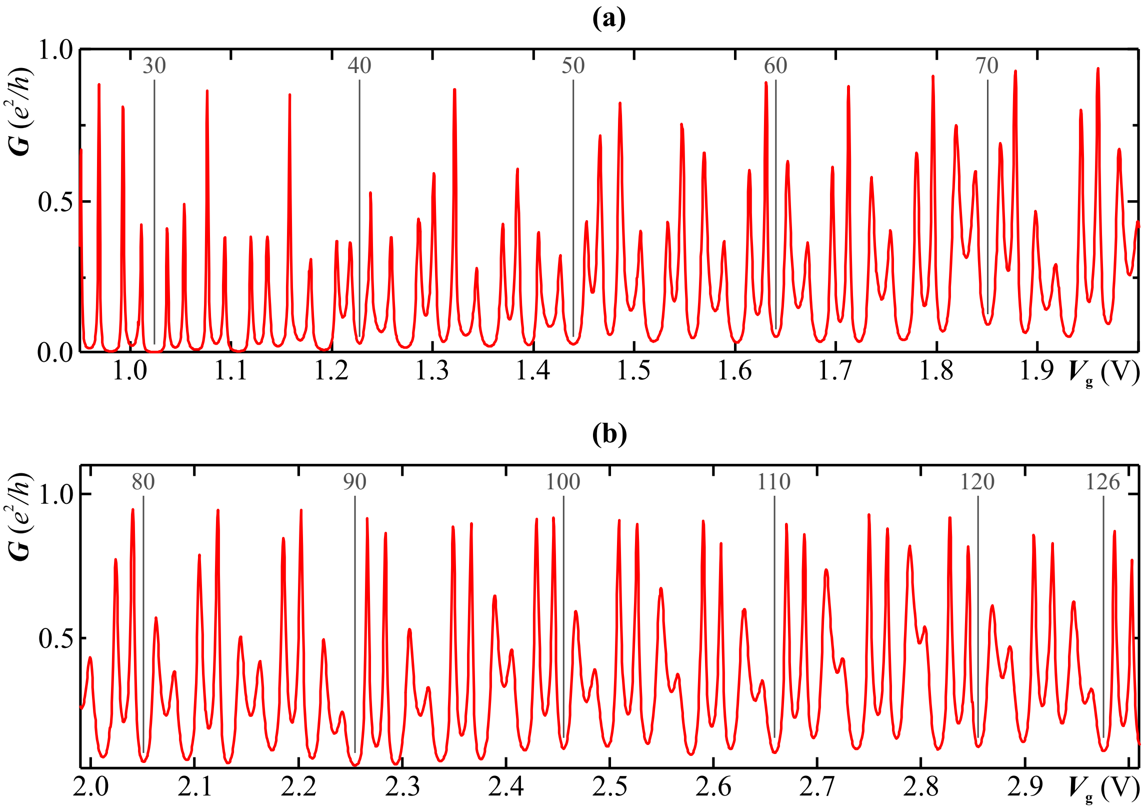

Figure 4.6: Continuation of the $G\left(V_g\right)$-plot of the CNT quantum dot including indexing. **(a)** The V_g-range right hand side of the stability diagram in Figure 4.4(b) is plotted. **(b)** Conductance as a function of V_g including upcoming Kondo ridges in each odd valley.

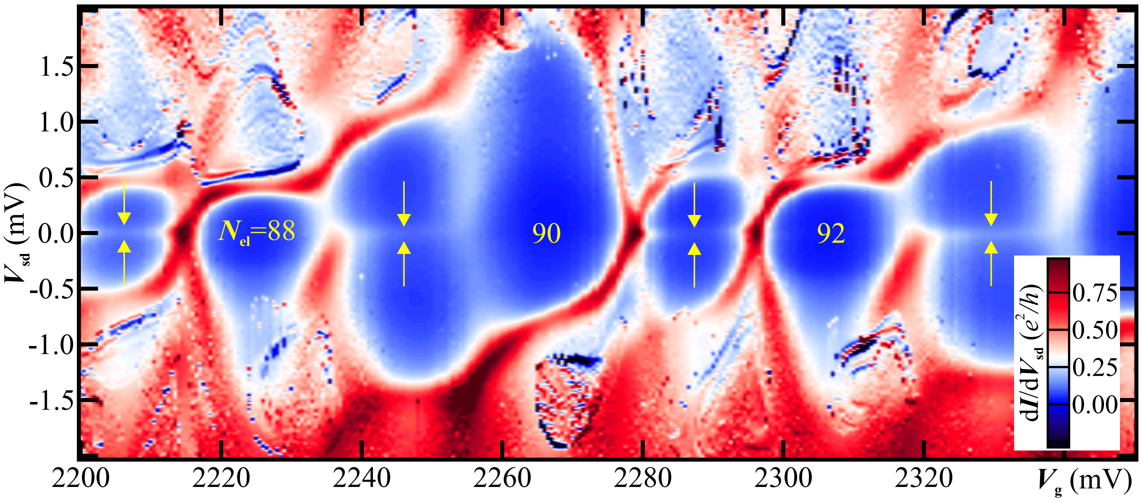

Figure 4.7: Stability diagram in the intermediate transport regime. The measurement is performed at base temperature using the voltage-bias setup, see Fig. 3.8. Kondo signatures in the odd valleys are marked with yellow arrows.

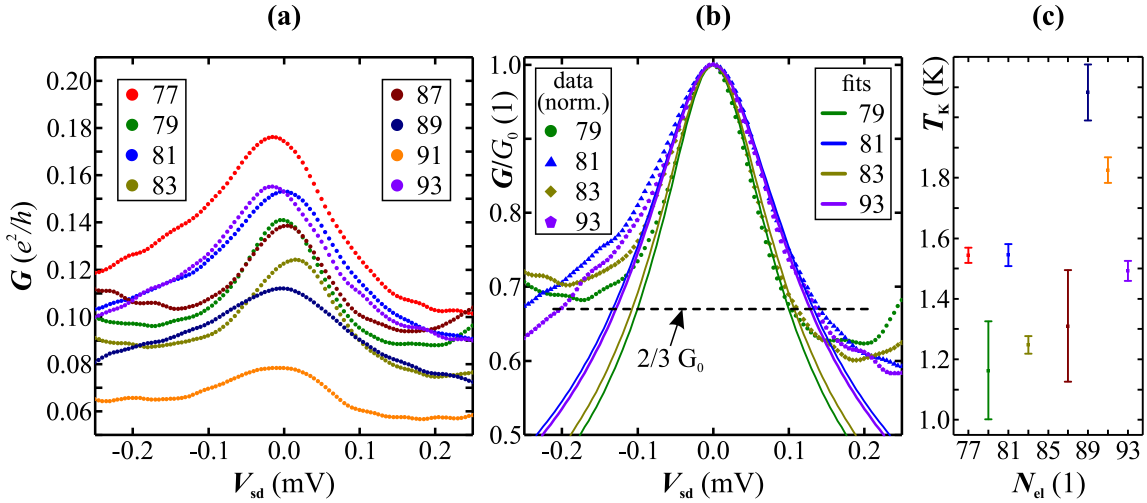

Figure 4.8: Estimation of T_K in the intermediate regime. **(a)** $G(V_{sd})$-plot taken from the middle of odd valleys, **(b)** Selection of normalized $G(V_{sd})$-lines offset to the maximum of the zero-bias anomaly. The related fits according to [Kretinin et al., 2012] are added, and the $2/3 \cdot G_0$ line is included for orientation. **(c)** Resulting Kondo temperatures as a function for each evaluated N_{el}.

The fitting formula,

$$\frac{G(T=0,T_K,V_{sd})}{G_0} = \left[1+\left(\frac{2^{\frac{1}{s}}-1}{\pi}\right)\left(\frac{eV_{sd}}{k_B T_K}\right)^2\right]^{-s} \tag{4.3}$$

is used for normalized data to its maximum conductance G_0. The exponent constant is set to $s = 0.32 \pm 0.01$, corresponding to equation (3) in [Kretinin et al., 2012]. The normalized bias trace has to be offset to this maximum such that $G(V_{sd} = 0) = G_0$. A possible source for errors is the zero-temperature approximation but it can be neglected as long as electron temperature T_{el} and base temperature of the cryostat are distinctly below T_K, i. e. $T_K \gg T_{el} \geq T_{base}$. This function delivers the Kondo temperature by simply extracting its width at $2/3 \cdot G_0$ which is equal to $2k_B T_K/e$.

The V_{sd}-traces extracted of the middle of each odd N_{el} valley from the stability diagrams as for Figure 4.7 are plotted in Figure 4.8(a). Normalized and offset data plus fits of certain traces can be seen in Figure 4.8(b). The resulting Kondo temperatures as a function of N_{el} plus error bars are traced in 4.8(c). The error bars are a consequence from the uncertainty of s. As can be seen, T_K of the dot ranges in between $1 \ldots 2\,$K.

Inelastic co-tunneling signatures in the intermediate region are still present like the conductance threshold for finite bias. It is observed furthermore, that transport features of mechanical activity arise preferably in regions where the CNT quantum dot is left in an excited state beyond the inelastic co-tunneling threshold. Regarding the color scale of Figure 4.7, mechanical activity locally causes a negative differential conductance $\mathrm{d}I/\mathrm{d}V_{sd}$.

Regarding the size of the regions with almost no conductance, the valleys for $4N+2$ are still larger than those for $4N$ which corresponds to a higher amount of energy to add the next electron. The shell filling from the previous section is hence still present.

4.5 Strong coupling regime

The conductance as a function of increasing gate voltage can be tracked in Figure 4.9: the pattern of Coulomb oscillations continues up to $N_{\mathrm{el}} \approx 200$. Indications of a Kondo ridge are observed the valleys for $4N+1$, whereas the other odd valley $4N+3$ is framed by two Coulomb peaks exhibiting the same shape. The conductance minima in these valleys are always smaller than for the previous others. Starting from $N_{\mathrm{el}} = 206$, this pattern changes: Coulomb peaks for $4N+2$ stepwise decrease, see blue dashes in Figure 4.9(b). They seem to vanish because of broadened $4N+3$ peaks. In addition, it can be seen that the Kondo ridge in the $4N+3$ valleys scales at a higher conductance level, whereas it apparently disappears in the $4N+1$ valleys.

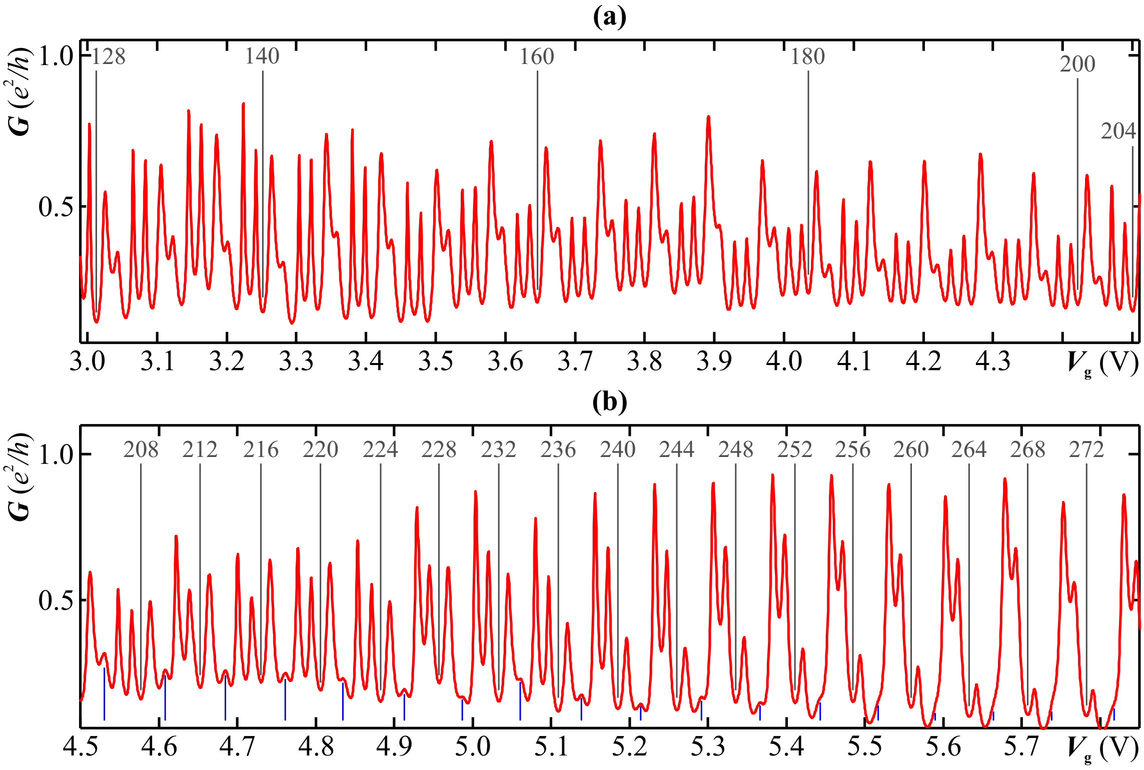

Figure 4.9: Continuation of the $G\left(V_{\mathrm{g}}\right)$-plot of the CNT quantum dot including indexing. **(a)** The subsequent V_{g}-range beyond 4.6(b) is plotted. **(b)** $G\left(V_{\mathrm{g}}\right)$ for $V_{\mathrm{g}} \gg 4.5\,\mathrm{V}$ with indexing of every valley for $4N$. Here, peaks for the $4N+2$ electron transitions are also marked with blue vertical dashes and also for orientation where these are supposed to be for numbers $N_{\mathrm{el}} \geqslant 254$.

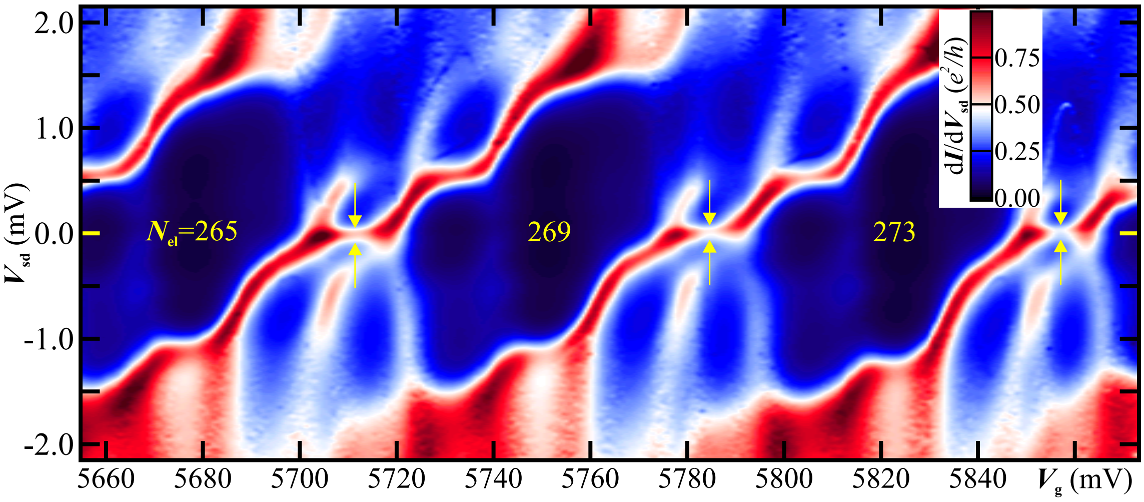

Figure 4.10: Stability diagram in the strong coupling transport regime at base temperature. Kondo signatures in the $4N+3$ valleys are marked, as well as the labels for $V_{sd} = 0$ in yellow color.

Also the stability diagram, see Figure 4.10 reveals an enhancement of the Kondo effect for $4N+3 = 267, 271, 275$, and a suppression for $4N+1 = 265, 269, 273$ valleys. As can be seen in Figure 4.11(b), the ZBAs scale indeed at a conductance level of about an order of magnitude smaller than those for $4N+3$. An unambiguous assignment of the $4N+1$-ZBAs to the Kondo effect cannot be made, by comparison with the $G(V_{sd})$-plots for the even valleys $4N$, see Figure 4.11(b): the conductance minima in the even valleys are higher than ZBA-maxima located in the odd valleys. A stability diagram measurement optimized to the lower conductance range for the $4N$ and $4N+1$ valleys, and exhibiting a higher bias resolution would have been necessary to clearly identify the Kondo signatures in the $4N+1$ valleys in the strong coupling regime. In contrast, the comparison between $G(V_{sd})$-characteristics for $4N+2$ and $4N+3$ valleys delivers a distinct difference in the conductance at $V_{sd} = 0\,\mathrm{V}$. The ridges here can be clearly attributed to the Kondo effect. The evaluation as described in section 4.4 results in T_Ks of about 1 K in this regime, see Figures 4.11(c) and (d).

The transport through the dot, beginning from $N_{el} = 227$, seems to be suppressed for one orbital state, and enhanced for the other since the pattern follows a two-fold alternation. The measurements on the present CNT quantum dot in this gate region (see Figures 4.9(b) and 4.10), hence reveal a transport pattern which cannot be completely attributed to the mixed-valence regime, as stated in [Makarovski et al., 2007]. Anyway, certain observations can be explained. Besides the Kondo anomaly at $V_{sd} = 0\,\mathrm{V}$ in the $4N+3$ valleys, this resonance reappears in the neighboring valleys at $V_{sd} \neq 0\,\mathrm{V}$. It is still the Kondo effect turning up as a non-zero bias anomaly in the quantum dot, see also [Borda et al., 2003; Le

Hur and Simon, 2003; Choi et al., 2005].

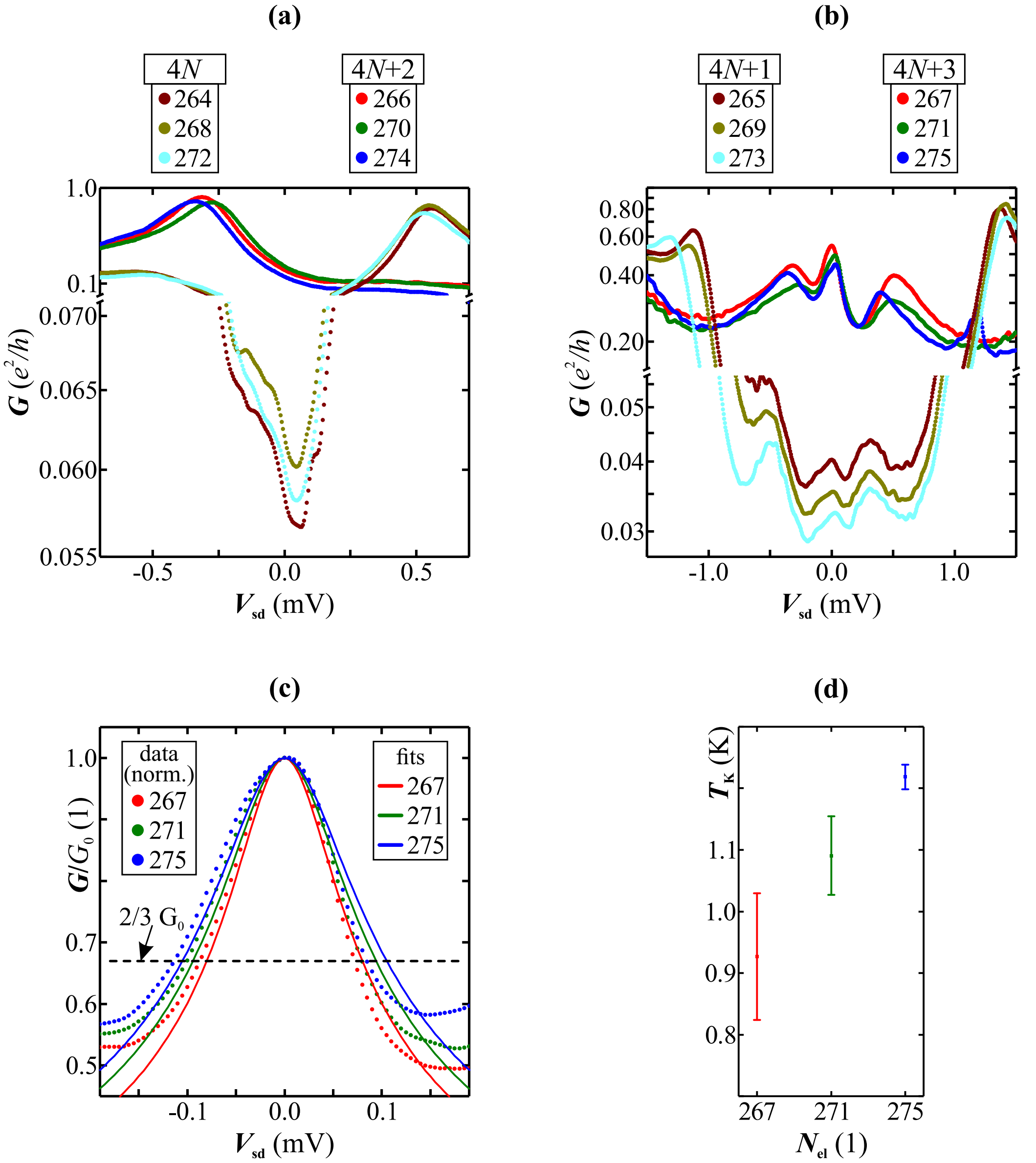

Figure 4.11: Estimation of T_K in the strong coupling regime. **(a)** $G\,(V_\mathrm{sd})$-plots taken from the middle of even valleys, **(b)** $G\,(V_\mathrm{sd})$-plots taken from the middle of odd valleys. **(c)** The three $4N+3$ normalized $G\,(V_\mathrm{sd})$-lines offset to the maximum of the zero-bias anomaly. The related fits according to [Kretinin et al., 2012] are added, and the $2/3 \cdot G_0$ line is included for orientation. **(d)** Resulting Kondo temperatures for $N_\mathrm{el} = 267, 271, 275$.

Furthermore, the conductance resonances still depend nonlinearly on V_g indicating the importance of electronic interactions in this regime. In addition to that, the amplitude of these oscillations is large, i. e. the difference between peak and subsequent valley conductance. These two observations clearly exclude the presence of Fabry-Pérot transport effects which exhibits an amplitude of ca. 10 % of the background, see [Makarovski et al., 2007].

4.6 Temperature dependence of the Kondo correlation

The region around $N_{\mathrm{el}} = 271$ is examined closer to obtain knowledge of the distorted transport spectrum in the strong coupling regime. The stability diagrams of Figure 4.12 show the behavior of the quantum dot as a function of temperature. The suppressed Coulomb blockade valley for $N_{\mathrm{el}} = 270$ starts to reestablish at 1.7 K. The dot is in the temperature broadened transport regime at 5.4 K -case (II) in Tab. 2.2- regarding the conductance scale of Figure 4.12(d) and the corresponding $G\left(V_{\mathrm{g}}\right)$ trace in Figure 4.13(a). The inelastic co-tunneling conductance threshold broadens for $T = 700\,\mathrm{mK}$ and $1700\,\mathrm{mK}$, and its maximum decreases. The stability diagram for $T = 1700\,\mathrm{K}$ still exhibits a Kondo-zero-bias peak even though the temperature is much higher than the predicted T_{K} in Figure 4.11(d) for $N_{\mathrm{el}} = 271$.

Following [Goldhaber-Gordon et al., 1998a], an alternative method is applied to estimate the Kondo temperature for $N_{\mathrm{el}} = 271$. The temperature dependence of the conductance for constant V_{g} is fitted to equation 2.40. G_0 is the extrapolated conductance at $T = 0\,\mathrm{K}$, and estimated to be close to the extracted values for $T = T_{\mathrm{base}}$. In Figure 4.13(a), $G\left(V_{\mathrm{g}}\right)$ characteristics taken from the stability diagrams of Figure 4.12 at $V_{\mathrm{sd}} = 0\,\mathrm{V}$ are plotted. The perpendicular dashed lines for certain V_{g} values intersect the data sets to be fitted to equation 2.40. Some of these functions are plotted in Figure 4.13(c), and extracted Kondo temperatures as a function of V_{g} are plotted in Figure 4.13(d). Obviously, T_{K} is more distributed compared to the other method, see Figure 4.11(d). This may be due to lack of data or even by the nature of this method, since T_{K} spreads in the same range in Figure 5(a) of [Goldhaber-Gordon et al., 1998a]. On the one hand, the method for determination of T_{K} according to [Kretinin et al., 2012] delivers more exact values but on the other hand only for one certain state of the dot. On the other hand, the ZBA spreads over the whole $4N+3$ valley, may it be enhanced by further elastic co-tunneling effects and resulting in higher critical temperatures. For conclusion, both methods deliver only a range for the appearance of the Kondo effect, which is determined to be in between $1 \ldots \approx 3\,\mathrm{K}$ for $N_{\mathrm{el}} = 271$. The V_{sd} sweeps as plotted in Figure 4.13(b) reveal a complete absence of the Kondo anomaly at 5.4 K.

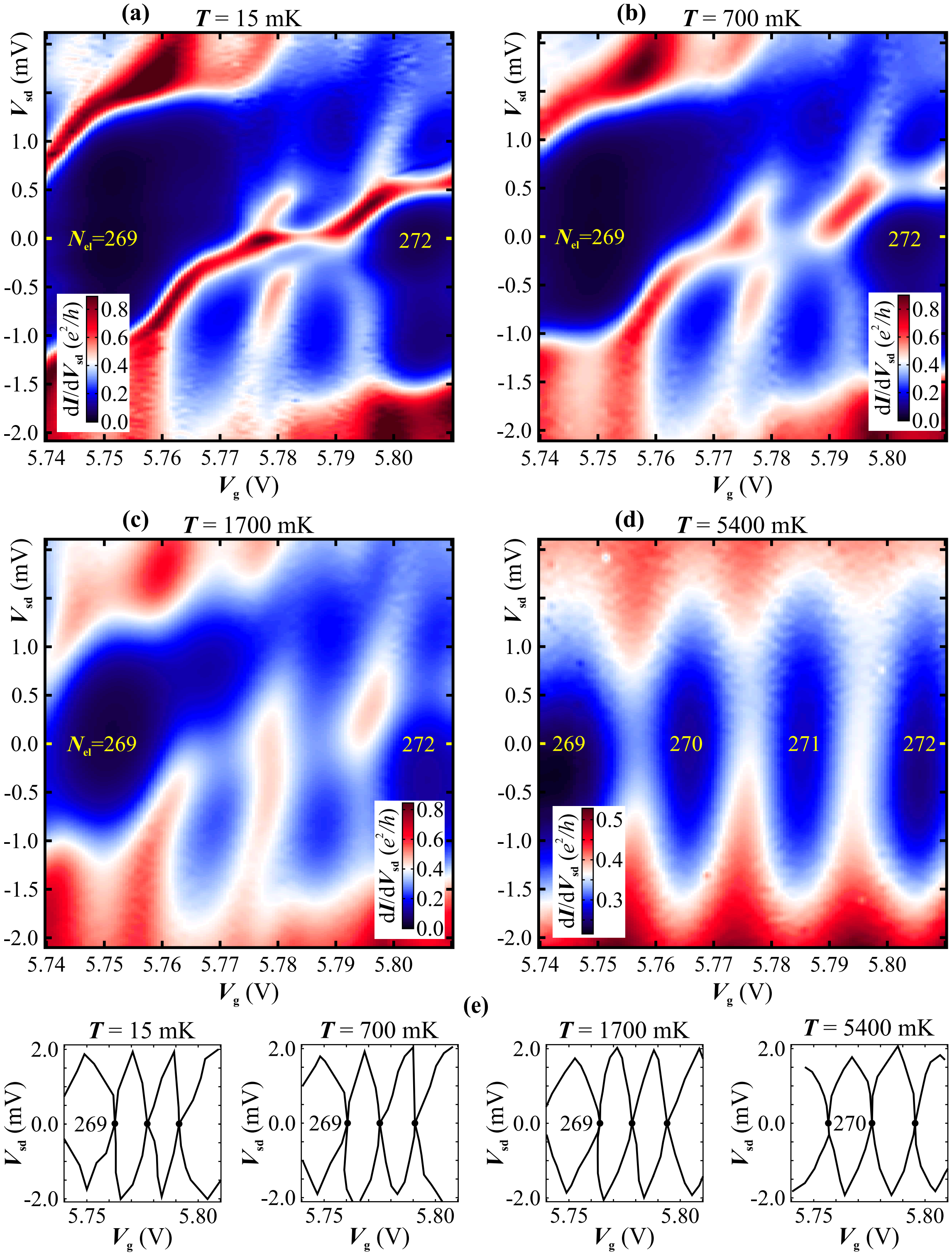

Figure 4.12: Stability diagrams around $N_{\mathrm{el}} = 271$. The measurements are performed at **(a)** base temperature, **(b)** at 700 mK, at **(c)** 1700 mK, and at **(d)** 5400 mK using the dc voltage-bias setup, see Figure 3.8. At high temperature clear strongly broadened Coulomb blockade oscillations emerge. **(e)** Edges of the Coulomb blockade areas in **(a)**-**(d)**.

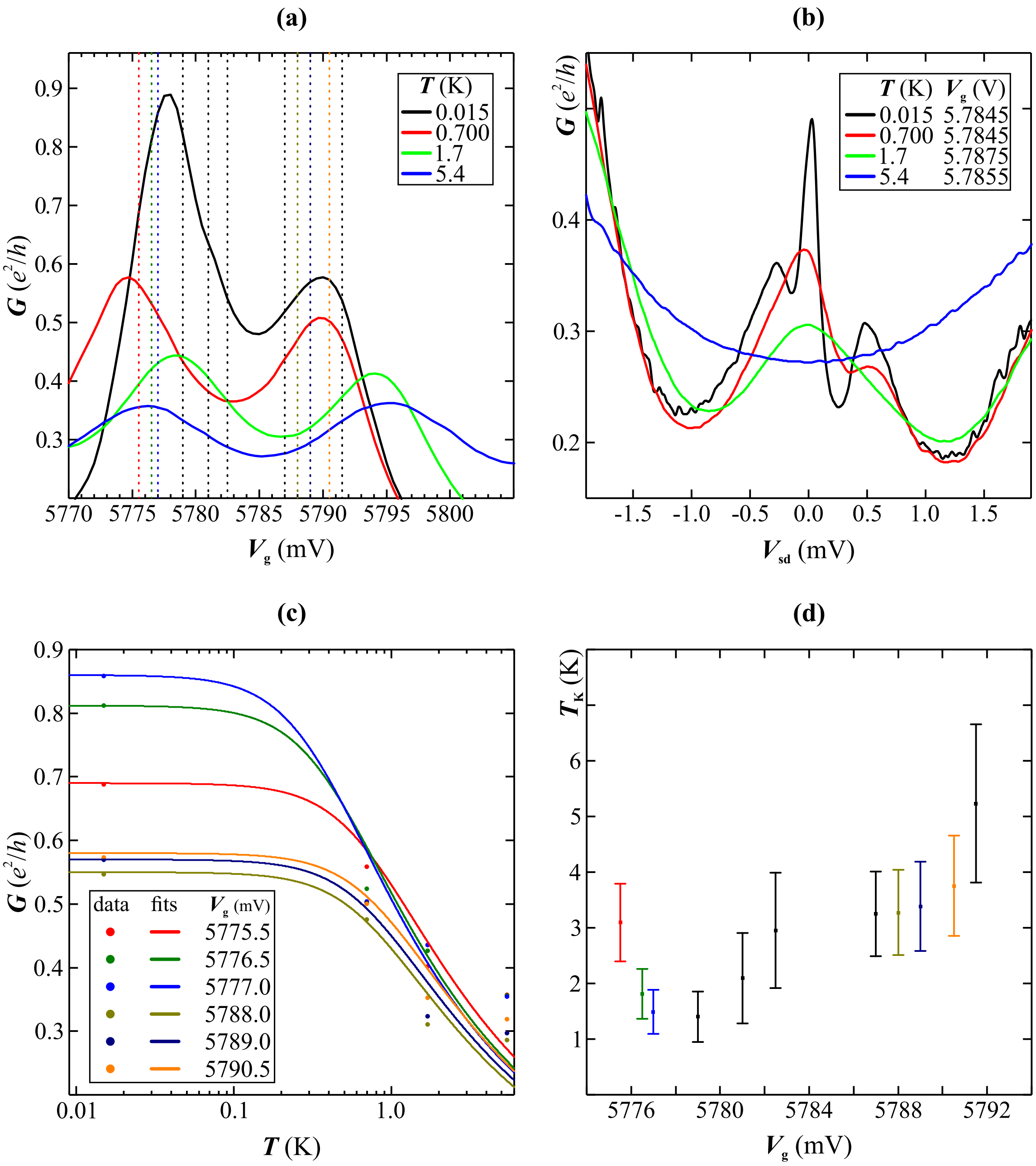

Figure 4.13: Temperature dependency of the $4N+3$-Kondo-degenerated valley at $N_{\mathrm{el}} = 271$. **(a)** Extracted zero-bias $G\left(V_{\mathrm{g}}\right)$-plots from the stability diagrams of Figure 4.12 and perpendicular dashed lines for further data extraction. **(b)** $G\left(V_{\mathrm{sd}}\right)$-plots extracted from the middle of the 271-valley of each stability diagram, see Figure 4.12. The (constant) V_{g} values for each plot is stated next to the temperature. **(c)** Corresponding fits according to equation 2.40 to the data extracted from **(a)**. **(d)** Resulting Kondo temperatures as a function of V_{g} including error bars.

Chapter 5

Mechanical charge detection

This chapter deals with measurements on nanomechanical phenomena at low-temperature performed on the suspended CNT device which has already been electrically characterized in chapter 4. The single-walled carbon nanotube is hereby driven contact-free by electromagnetic waves emitted by an external antenna which is placed few centimeters above in the cryostat. The measurement setup is depicted in Figure 3.10 and described in subsection 3.5.4. CNTs exhibit different types of vibrational modes; the three on the lowest energetic scale are radial-breathing (RBM), longitudinal, and the transversal bending modes. For detailed information, see [Hüttel et al., 2008]. The present nano-electromechanical system (NEMS) reveals two independent transversal modes. Their resonance frequency can be tuned by the global back gate V_g resulting in a well-defined resonator behavior. In the quantum dot regime, the local resonant behavior of the CNT is used to probe its own charging state, see [Steele et al., 2009b; Meerwaldt et al., 2012]. The model for the resonance frequency dependence on the single-electron tunneling event is extended to two quantum dot levels and applied to the strong coupling regime. It is shown that the resonator behavior is not affected by the Kondo effect and only sensitive to the charge on the dot.

5.1 Continuum response of the CNT resonator

Since its first detection in [Sazonova et al., 2004], even at room-temperature, the bending mode of a doubly-clamped carbon nanotube resonator is probed and modeled as a function of global back gate V_g. The setup is sketched in Figure 5.1. In order to model the continuum response of a resonator including a single-walled CNT, the picture of a cylindrical beam or string under tension is applied, see [Witkamp et al., 2006; Sapmaz, 2006].

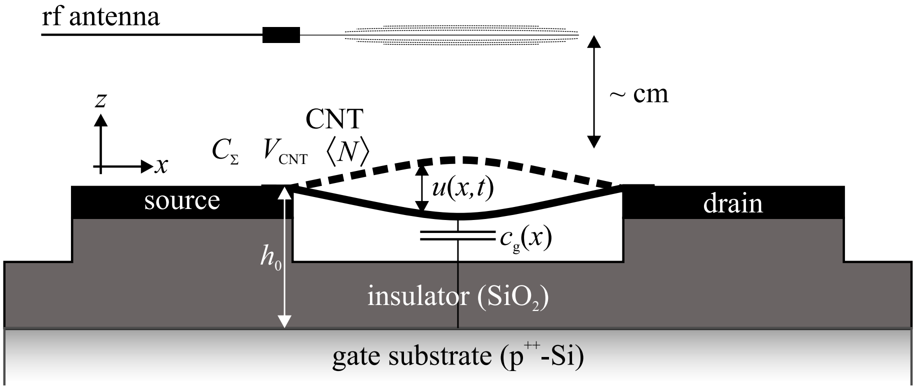

Figure 5.1: Model of a CNT doubly clamped at the source and drain electrode. The suspended part in between is driven by an antenna being placed close to the device. The characteristic parameters of the CNT in the Coulomb blockade regime, the total capacitive coupling to the environment C_Σ, and the average occupation number $\langle N\rangle$, are stated and needed later. At resonance, the displacement $u(x,t)$ amplitude is at its maximum. The readout scheme in the measurement setup is sketched in Figure 3.10 and described in subsection 3.5.4.

5.1.1 General differential equation and mechanisms

Following [Cleland, 2003], the Euler-Bernoulli beam equation reads

$$\rho A \frac{\partial^2 u}{\partial t^2} + \eta \frac{\partial u}{\partial t} + EI \frac{\partial^4 u}{\partial x^4} - T \frac{\partial^2 u}{\partial x^2} = F_{\text{ext}}(x,t) \quad . \tag{5.1}$$

It describes the displacement of the CNT $u(x,t)$ as a function of the position $x \in [0,L]$ along its axis at a time t. The product out of density ρ and cross section A is the linear mass density; it is the prefactor to the first term left-hand side, responsible for acceleration. The product of Young's modulus E and momentum of inertia I is denoted as bending rigidity. T is the tension in the nanotube. The damping parameter η is the prefactor of the displacement velocity $\frac{\partial u}{\partial t}$ and is neglected in the following. $F_{\text{ext}}(x,t)$ is the external driving force. Here, boundary conditions of the doubly-clamped beam are

$$u(0,t) = u(L,t) = \partial u/\partial x(0,t) = \partial u/\partial x(L,t) \equiv 0 \quad . \tag{5.2}$$

Two mechanisms can dominate the resonant response, either the bending rigidity or the tension, in which the other one can be neglected. In the case that bending rigidity is dominant, i. e. $T = 0$, the resonator acts as a beam, exhibiting the fundamental mode

$$f_0 = \frac{22.4}{2\pi L^2} \cdot \left(\frac{EI}{\rho A}\right)^{\frac{1}{2}} \quad . \tag{5.3}$$

In the opposite case, the resonator behaves like an also doubly-clamped string under tension. According to [Poot and van der Zant, 2012], this is the case when $T \gg EI/L^2$. The fundamental eigenfrequency reads

$$f_0 = \frac{1}{2L} \cdot \sqrt{\frac{T}{\rho A}} \quad . \tag{5.4}$$

Equation 5.1 for the case $F_{\text{ext}}(x,t) = 0$, and the boundary conditions from equation 5.2 are the starting point for further evaluation, see [Poot and van der Zant, 2012]. The tension consists of two parts: first the residual tension $T_0 = EA \cdot (L - L_0)/L_0$ of the string in absence of any displacement. The second contribution comes from the displacement of the nanotube. Since the displacement $u(x,t)$ is a sum of a stationary part u_{dc} and an much smaller oscillating part u_{ac}, a static term for the tension is obtained:

$$T_{\text{dc}} = T_0 + \frac{EA}{2L} \cdot \int_0^L \left(\frac{\partial u_{\text{dc}}}{\partial x'} \right)^2 \mathrm{d}x' \quad , \tag{5.5}$$

and equation 5.1 degrades to

$$EI \frac{\partial^4 u_{\text{dc}}}{\partial x^4} - T_{\text{dc}} \frac{\partial^2 u_{\text{dc}}}{\partial x^2} = 0 \quad . \tag{5.6}$$

The oscillating part u_{ac} gives an additional contribution T_{ac} to the tension which satisfies the equation of motion

$$\rho A \frac{\partial u_{\text{ac}}^2}{\partial t^2} + EI \frac{\partial^4 u_{\text{ac}}}{\partial x^4} - T_{\text{dc}} \frac{\partial^2 u_{\text{ac}}}{\partial x^2} = T_{\text{ac}} \frac{\partial^2 u_{\text{dc}}}{\partial x^2} \quad , \tag{5.7}$$

and delivers for the vibration-induced tension

$$T_{\text{ac}} = \frac{EA}{L} \cdot \int_0^L \left(\frac{\partial u_{\text{dc}}}{\partial x'} \frac{\partial u_{\text{ac}}}{\partial x'} \right) \mathrm{d}x' \quad . \tag{5.8}$$

5.1.2 Parameters for a CNT resonator

For single-walled carbon nanotubes, the bending rigidity EI is in the range of $10^{-24}\,\mathrm{Nm}^2$. Because of their high aspect-ratio, tension may overlap the influence of the bending rigidity.

The capacitance of a segment of the nanotube along its axis with respect to the gate substrate is

$$c_{\text{g}}(x) = \frac{2\pi\varepsilon_0}{\ln\left[\frac{2(h_0 - u(x))}{r}\right]} \approx \frac{2\pi\varepsilon_0}{\operatorname{arccosh}\left[\frac{h_0}{r}\right]} + \frac{2\pi\varepsilon_0}{\sqrt{h_0^2 - r^2}\operatorname{arccosh}^2\left[\frac{h_0}{r}\right]} \cdot u(x) \quad , \tag{5.9}$$

for $h_0 \gg u(x)$, see also Figure 5.1. For the capacitance between whole suspended CNT and substrate, one obtains

$$C_\mathrm{g} = \int_0^L c_\mathrm{g}(x')\mathrm{d}x' \ . \tag{5.10}$$

In the present case, the external force is a sum of electrostatic capacitive coupling and driving contribution from the emitted electromagnetic wave with $\omega = 2\pi f$, as follows

$$F_\mathrm{ext}(x,t) = F_\mathrm{dc} + F_\mathrm{ac} = \frac{1}{2}\frac{\partial c_\mathrm{g}}{\partial u}V_\mathrm{g}^2 + F_\mathrm{ac} = \frac{\pi\varepsilon_0 V_\mathrm{g}^2}{\sqrt{h_0^2 - r^2}\,\mathrm{arccosh}^2\left[\frac{h_0}{r}\right]} + F_\mathrm{rf}\cos(\omega t) \tag{5.11}$$

The antenna emits an electromagnetic wave into the cryostat; its amplitude is a function of the nominal power set by the rf-generator in combination with all dampening elements in the rf-line, and the emission characteristics of its tip. Thus, F_rf depends on the selected nominal rf-power. V_g has only an influence on the static force. In analogy to equations 5.6 and 5.7, the equation of motion for the CNT resonator can be separated into

$$EI\frac{\partial^4 u_\mathrm{dc}}{\partial x^4} - T_\mathrm{dc}\frac{\partial^2 u_\mathrm{dc}}{\partial x^2} = F_\mathrm{dc} \ , \tag{5.12}$$

$$-\omega^2 \rho A u_\mathrm{ac} + \mathrm{i}\omega\gamma u_\mathrm{ac} + EI\frac{\partial^4 u_\mathrm{ac}}{\partial x^4} - T_\mathrm{dc}\frac{\partial^2 u_\mathrm{ac}}{\partial x^2} - T_\mathrm{ac}\frac{\partial^2 u_\mathrm{dc}}{\partial x^2} = F_\mathrm{ac} \ . \tag{5.13}$$

Once again, the static tension consists of two parts: especially for CNTs, the residual tension T_0 originates from its clamping on the electrodes during CVD growth. In other words, the total length of the nanotube L_0 differs from the trench length L. The second contribution is a result of the back gate voltage V_g, which pulls the CNT toward the gate substrate [Witkamp et al., 2006] and elongates it.

Analytical solutions of the system of equations 5.5, 5.8, 5.12, and 5.13 are specified in [Sapmaz et al., 2003; Lefévre et al., 2005], and applied among others in [Hüttel et al., 2009]. In Figure 12(a) of [Poot and van der Zant, 2012], calculated $f_0\left(V_\mathrm{g}\right)$ curves for a SWCNT resonator of $L = 1\ \mu\mathrm{m}$ are plotted for three different residual tensions.

More often, a simple parabolic fit is nowadays applied to experimental data, see [Eichler et al., 2013]. In order to find the resonance frequency of a certain bending mode of the CNT resonator at arbitrary V_g, this has been also applied to the present device as can be seen in Figure 5.2. The overall parabolic $f_0\left(V_\mathrm{g}\right)$-dependence confirms that CNT resonators are mainly tuned by the induced static tension originating from the back gate voltage.

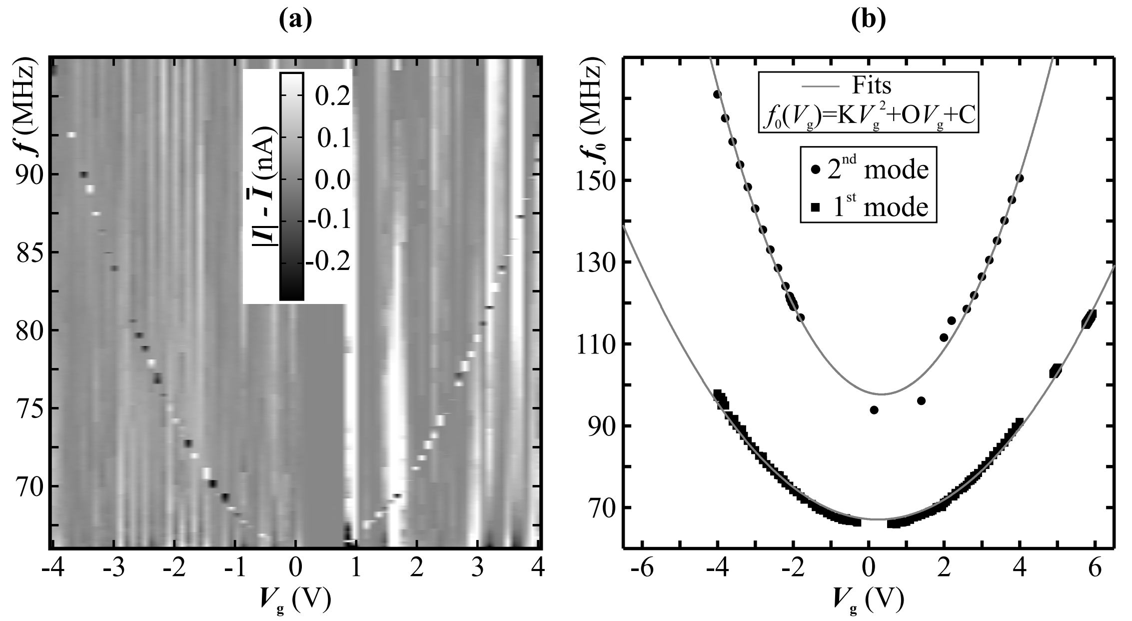

Figure 5.2: The CNT resonator response to external driving. **(a)** An exemplary measurement in which the frequency is swept for constant gate voltages. Experimental parameters are $V_{\mathrm{sd}} = -0.1\,\mathrm{mV}$, nominal rf-power $P_{\mathrm{rf}} = 2\,\mathrm{dBm}$, and $T = 15\,\mathrm{mK}$. It is the base temperature of the cryostat for the same cool-down as for the measurements presented in chapter 4. The current is measured and plotted in grayscale after subtracting its mean $\bar{I}$ for each f-sweep at constant V_{g}. At f_0, the current exhibits a distinct shift. **(b)** Extracted f_0 from several measurements as shown in (a). Two modes of the resonator observed and fitted. Parameters for the 1st mode: $\mathrm{C} = (67.20 \pm 0.09)$ MHz, $\mathrm{O} = (-0.76 \pm 0.03)$ MHz/V, and $\mathrm{K} = (21.58 \pm 0.01)\ \mathrm{MHz/V^2}$. Fitting parameters for the 2nd mode: $\mathrm{C} = (98.12 \pm 0.60)$ MHz, $\mathrm{O} = (-2.71 \pm 0.12)$ MHz/V, and $\mathrm{K} = (4.00 \pm 0.07)\ \mathrm{MHz/V^2}$.

5.1.3 Detection mechanism

In our setup, we use the measured dc current I to identify the resonance frequency f_0 of the vibrating CNT as discussed in [Hüttel et al., 2009]. On resonance, a nanotube segment oscillates with $u(t) = u_0 \cos(2\pi f_0 t)$, with a displacement amplitude u_0. This changes the overall gate capacitance over the time with amplitude $C_{\mathrm{g}}^{\mathrm{ac}} = (\mathrm{d}C_{\mathrm{g}}/\mathrm{d}u)u_0$. This contribution can be understood as if an effective ac gate voltage is applied, $V_{\mathrm{g}}^{\mathrm{ac,eff}} = V_{\mathrm{g}} C_{\mathrm{g}}^{\mathrm{ac}}/C_{\mathrm{g}}$. Obviously, this ac gate voltage oscillates at frequencies in the MHz-range, leading to additional currents on the same timescale. This timescale is not accessible in our detection setup, and only a time-averaged current is measured. A Taylor expansion leads to the time-averaged mechanically induced current

$$\langle I \rangle (u_0, V_{\mathrm{g}}) = I(V_{\mathrm{g}}) + \frac{u_0^2}{4} \left(\frac{V_{\mathrm{g}}}{C_{\mathrm{g}}} \frac{\mathrm{d}C_{\mathrm{g}}}{\mathrm{d}u} \right)^2 \frac{\partial^2 I}{\partial V_{\mathrm{g}}^2} + O(u_0)^4 \ . \tag{5.14}$$

As can be seen, the change in the measured dc current at f_0, $\Delta I = \langle I \rangle - I$ is proportional to the local curvature $\left(\partial^2 I / \partial V_\mathrm{g}^2\right)$ of the current, and also follows its sign. This is also observed in present measurements like in Figure 5.2(a).

The measurement setup can be improved by adding a Lock-In-Amplifier (LIA), as already mentioned in subsection 3.5.4 and sketched in Figure 3.10. Here, the rf-wave is amplitude-modulated by f_LIA. As a consequence, the external driving force is then proportional to $\sin(2\pi f t)\sin^2(\pi f_\mathrm{LIA} t)$. On resonance, the LIA measures the current shift without dc background. The shifts are smaller on the f-axis which originates from the resonator response being a convolution of external driving force and displacement of the harmonic oscillator with $F_\mathrm{ext} = 0$, see [Poot, 2009]. An additional advantage is that less power P_rf is needed to detect the current shift at f_0, see also Figure 5.3 in the next subsection. In the Coulomb blockade regime, the current through the CNT depends on the gate voltage in a strongly nonlinear way: whenever an electron enters the dot, the current changes strongly as a function of V_g. This leads to an enhanced curvature and therefore to an enhanced time-averaged current $\langle I \rangle$, see equation 5.14. This dependence leads to mechanical charge detection and will be examined precisely in the next section.

5.1.4 Calibration of the setup to linear resonator response

The response of the carbon nanotube resonator strongly depends on the power P_rf of the emitted rf-wave. It can be driven into non-linear regime in which $\langle I \rangle$ is distinctly enhanced at f_0. Here, the typical shape of the $I_\mathrm{dc}(f)$ plot is a broadened triangle around f_0. This response is suitable for a rough estimation of f_0 as a function of V_g, as applied in Figure 5.2(a), but not for detailed examination of the resonant response in smaller V_g ranges. Furthermore, a linear resonator response is required to estimate the Q-factor of the resonator. It is necessary to read out the dc current modification for a highly resolved $I(f)$ measurement at small radiation powers. After detecting f_0, the measurement is repeated for decreasing P_rf until no signal due to resonant driving is measured anymore. In the present case, such experiments are performed and evaluated in [Schupp, 2014], resulting in a quality factor of 10^4.

As mentioned in the last subsection, the response is convoluted if an AM-rf signal is emitted by the antenna. Nevertheless, the dc readout is still sensitive to the AM-rf signal at f_0 as can be seen in Figure 5.3(a) down to $-20\,\mathrm{dBm}$.

In contrast, the measured and converted I_LIA magnitude still exhibits a shift at $-26\,\mathrm{dBm}$ which is attributed to f_0. In total numbers, only a quarter of power is needed for lock-in detection.

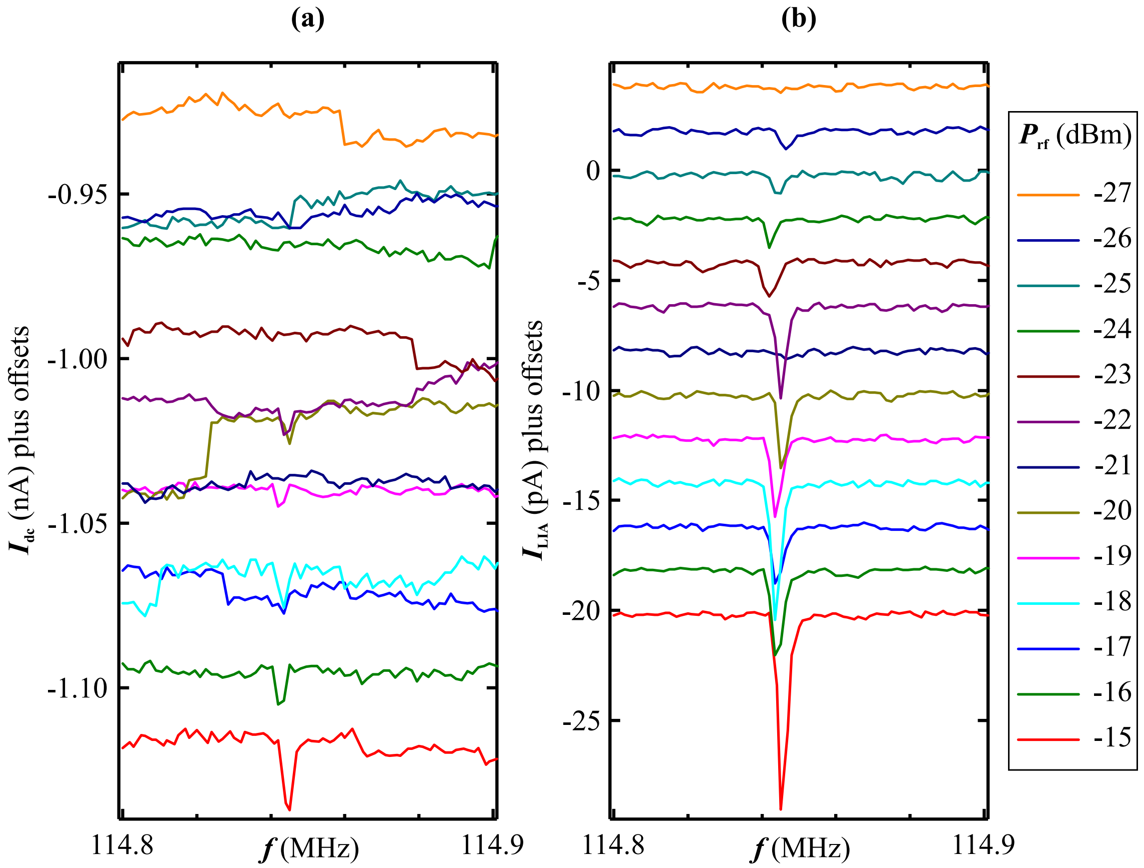

Figure 5.3: Calibration measurement for linear response driving at base temperature. The dc and ac current is measured during f-sweeps at different P_{rf} settings, starting from the lowest power. Such measurements are performed every time as preparation for a precise experiment spanning a nearby V_{g} range. The setup for nanomechanical measurements is applied, see Figure 3.10 in subsection 3.5.4 with AM driving, and readout. Comparable experimental parameters are chosen, this means $V_{\mathrm{sd}} = -0.1\,\mathrm{mV}$ at $V_{\mathrm{g}} = 5.77\,\mathrm{V}$. Lock-In output is $V_{\mathrm{ac}} = 0.650\,\mathrm{V}$, $f_{\mathrm{LIA}} = 137.36\,\mathrm{Hz}$ for external AM driving of the rf generator (step size $\Delta f = 1.5\,\mathrm{kHz}$). At the readout side, the current-voltage converter settings are $10^{-9}\,\mathrm{A/V}$ sensitivity at minimal rise time, $\lesssim 5\,\mu\mathrm{s}$. Lock-in input settings are 100 ms time constant, 10 mV sensitivity. The in-phase voltage signal X and quadrature component Y are converted to current magnitude I_{LIA}. The dc readout uses current-voltage converter and DMM. **(a)** I_{dc}, and **(b)** I_{LIA} for several power settings P_{rf} plotted for better visibility with offsets of 20 pA, respectively 2 pA between each f-sweep.

In the Coulomb blockade transport regime, the Q-factor and thus current shift of both detection schemes strongly changes even within a small V_{g} range. Hence, set power P_{rf} for gate-dependent experiments is usually chosen to be higher than mentioned above. However, it should not exceed the level for non-linear response.

Using the AM-rf input and readout, this is confirmed within a large range for P_{rf}. In the present case, a set power of $-18.5\,\mathrm{dBm}$ is chosen for next experiments.

5.2 Sensitivity to charge transitions in the quantum dot

A constant mechanical tension T_{dc}, and a small displacement $u(x)$ is assumed in the calculations included in this section. In addition, $u(x)$ is parallel to z. This is given within a small V_{g} range. First experiments to probe single-electron tunneling event via the resonant behavior of a suspended nanotube were carried out and published in [Steele et al., 2009b]. The calculations in this and the next sections are following the subsequent publication: [Meerwaldt et al., 2012].

Regarding the electrostatic force on the CNT in equation 5.11, eliminating the x-coordinate by eq. 5.10, and adding a voltage V_{CNT}, we obtain

$$F\left(z,V_{\mathrm{g}}\right)=\frac{1}{2}\frac{\mathrm{d}C_{\mathrm{g}}}{\mathrm{d}z}\left(V_{\mathrm{g}}-V_{\mathrm{CNT}}\right)^{2}\quad . \tag{5.15}$$

For the effective change of the mechanical spring constant follows

$$\begin{aligned}\Delta k\left(z,V_{\mathrm{g}}\right)&=-\frac{\mathrm{d}F\left(z,V_{\mathrm{g}}\right)}{\mathrm{d}z}=\\&=-\frac{1}{2}\left(V_{\mathrm{g}}-V_{\mathrm{CNT}}\right)^{2}\cdot\frac{\mathrm{d}^{2}C_{\mathrm{g}}}{\mathrm{d}z^{2}}-\frac{\mathrm{d}C_{\mathrm{g}}}{\mathrm{d}z}\left(V_{\mathrm{g}}-V_{\mathrm{CNT}}\right)\cdot\frac{\partial\left(V_{\mathrm{g}}-V_{\mathrm{CNT}}\right)}{\partial z}\end{aligned} \tag{5.16}$$

The voltage on the nanotube due to its charge, V_{CNT}, is calculated as a function of V_{g} in section 5.3. For its usage here, we have $V_{\mathrm{CNT}}=1/C_{\Sigma}\left(q_{\mathrm{c}}-e\langle N\rangle\right)$ with $q_{\mathrm{c}}=C_{\mathrm{g}}V_{\mathrm{g}}+C_{\mathrm{s}}V_{\mathrm{sd}}$ and $\langle N\rangle$ as the mean occupation number of the quantum dot. Due to the approximations stated at the beginning of this section (i. e. a small V_{g} range, and hence a small change of the CNT deflection), the first term in equation 5.16 is neglected. For the derivative in the second term follows

$$\begin{aligned}\frac{\partial\left(V_{\mathrm{g}}-V_{\mathrm{CNT}}\right)}{\partial z}&=\frac{\partial\left(V_{\mathrm{g}}-V_{\mathrm{CNT}}\right)}{\partial V_{\mathrm{g}}}\frac{\partial V_{\mathrm{g}}}{\partial z}=\frac{\partial\left(V_{\mathrm{g}}-V_{\mathrm{CNT}}\right)}{\partial V_{\mathrm{g}}}\frac{\partial V_{\mathrm{g}}}{\partial q_{\mathrm{c}}}\cdot\frac{\partial q_{\mathrm{c}}}{\partial z}=\\&=\frac{\partial\left(V_{\mathrm{g}}-V_{\mathrm{CNT}}\right)}{\partial V_{\mathrm{g}}}\frac{\partial V_{\mathrm{g}}}{\partial q_{\mathrm{c}}}\cdot\frac{\mathrm{d}C_{\mathrm{g}}}{\mathrm{d}z}V_{\mathrm{g}}=\frac{\partial\left(V_{\mathrm{g}}-V_{\mathrm{CNT}}\right)}{\partial V_{\mathrm{g}}}\frac{1}{C_{\mathrm{g}}}\cdot\frac{\mathrm{d}C_{\mathrm{g}}}{\mathrm{d}z}V_{\mathrm{g}}=\\&=\left(1-\frac{C_{\mathrm{g}}}{C_{\Sigma}}+\frac{e}{C_{\Sigma}}\frac{\partial\langle N\rangle}{\partial V_{\mathrm{g}}}\right)\frac{V_{\mathrm{g}}}{C_{\mathrm{g}}}\cdot\frac{\mathrm{d}C_{\mathrm{g}}}{\mathrm{d}z}=\\&=\frac{V_{\mathrm{g}}}{C_{\Sigma}}\left(\frac{C_{\Sigma}}{C_{\mathrm{g}}}-1+\frac{e}{C_{\mathrm{g}}}\frac{\partial\langle N\rangle}{\partial V_{\mathrm{g}}}\right)\cdot\frac{\mathrm{d}C_{\mathrm{g}}}{\mathrm{d}z}\quad .\end{aligned} \tag{5.17}$$

Combination of the second term in equation 5.16 and equation 5.17 results in

$$\Delta k\left(z,V_{\mathrm{g}}\right)=\frac{V_{\mathrm{g}}\left(V_{\mathrm{g}}-V_{\mathrm{CNT}}\right)}{C_{\Sigma}}\left(\frac{\mathrm{d}C_{\mathrm{g}}}{\mathrm{d}z}\right)^{2}\left(1-\frac{C_{\Sigma}}{C_{\mathrm{g}}}-\frac{e}{C_{\mathrm{g}}}\frac{\partial\langle N\rangle}{\partial V_{\mathrm{g}}}\right)\quad. \tag{5.18}$$

The resonance frequency for a harmonic oscillator fulfills the condition $\omega_0^2=k/m$. In the present case this can be rewritten to $k(V_{\mathrm{g}})=m\omega_0^2(V_{\mathrm{g}})$, and for the derivative follows

$$\frac{\partial k}{\partial V_{\mathrm{g}}}=m\cdot 2\omega_0(V_{\mathrm{g}})\cdot\frac{\partial\omega_0}{\partial V_{\mathrm{g}}}\quad. \tag{5.19}$$

In the restrictions stated above, the derivatives are replaced by absolute changes Δ and the expression for the resonance frequency shift due to single-electron tunneling is obtained:

$$\Delta\omega_0=\frac{V_{\mathrm{g}}\left(V_{\mathrm{g}}-V_{\mathrm{CNT}}\right)}{2m\omega_0 C_{\Sigma}}\left(\frac{\mathrm{d}C_{\mathrm{g}}}{\mathrm{d}z}\right)^{2}\left(1-\frac{C_{\Sigma}}{C_{\mathrm{g}}}-\frac{e}{C_{\mathrm{g}}}\frac{\partial\langle N\rangle}{\partial V_{\mathrm{g}}}\right)\quad. \tag{5.20}$$

The last term in the brackets has a negative sign leading to softening of the spring constant of the CNT resonator. It is proportional to the change of the average charge in the CNT quantum dot due to a charge transition. In other words, single-electron tunneling through the carbon nanotube leads to charge transport, and hence to a softened spring constant, and per consequence to a distinct dip in the resonance frequency ω_0, as observed in [Steele et al., 2009b; Lassagne et al., 2009; Meerwaldt et al., 2012; Benyamini et al., 2014].
A complete equation which also includes the overall linear dependence of ω as a function of V_{g} can be written as

$$\Omega_0\left(V_{\mathrm{g}}\right)=\Omega_0+\kappa\langle N\rangle\cdot V_{\mathrm{g}}+\Delta\omega_0\quad, \tag{5.21}$$

with $\kappa\langle N\rangle$ as linear slope which makes a step when a single electron transition takes place. For a complete description of the resonance frequency behavior of a CNT quantum dot resonator due to single electron transitions, calculations on V_{CNT} and respectively $\partial\langle N\rangle/\partial V_{\mathrm{g}}$ are performed from the transport side in the next section 5.3.

5.3 Model for the average charge on a quantum dot

In this section, a model is built for the voltage on a carbon nanotube quantum dot V_{CNT} and the average electron number on the quantum dot $\langle N\rangle$. It considers two non-interacting quantum dot levels energetically separated by a charging energy $-e\alpha_{\mathrm{g}}\Delta V_{\mathrm{g}}$. ΔV_{g} is the distance of the conductance peaks on the gate axis, $\Delta V_{\mathrm{g}}=V_{\mathrm{g},2}-V_{\mathrm{g},1}$ with $V_{\mathrm{g},2}>V_{\mathrm{g},1}$.
The electrochemical potential of the nanotube μ_{CNT}, as defined in equation 2.28, is simplified by $\alpha_{\mathrm{s}}V_{\mathrm{sd}}\approx 0$. In addition, since only small deviations from the peak positions at

the gate axis are regarded, it can be rewritten to $\mu_{\mathrm{dot}} = -e\alpha_{\mathrm{g}}\left(V_{\mathrm{g}} - V_{\mathrm{g},1/\mathrm{g},2}\right)$. The density of available states of both levels in the CNT quantum dot $\mathfrak{D}_{1/2}(\mu) \mapsto \mathfrak{D}_{1/2}(\mu - \mu_{\mathrm{dot}})$ exhibits a Lorentzian form. Regarding electrons, it is defined as

$$\mathfrak{D}_1(\mu) = \frac{\hbar\Gamma}{2\pi} \cdot \frac{1}{\left(\mu + e\alpha_{\mathrm{g}}(V_{\mathrm{g}} - V_{\mathrm{g},1})\right)^2 + \left(\frac{\hbar\Gamma}{2}\right)^2} \quad , \tag{5.22}$$

$$\mathfrak{D}_2(\mu) = \frac{\hbar\Gamma}{2\pi} \cdot \frac{1}{\left(\mu + e\alpha_{\mathrm{g}}(V_{\mathrm{g}} - V_{\mathrm{g},2})\right)^2 + \left(\frac{\hbar\Gamma}{2}\right)^2} \quad . \tag{5.23}$$

Γ is the the full width at half maximum of the levels, assumed to be equal, and given by the lifetime broadening. $\mathfrak{D}_{1/2}$ is hence defined in a way that its maximum is shifted by V_{g} relative to a reference potential. Using $\mu_{\mathrm{d}} = 0$ as reference potential, the peaks of $\mathfrak{D}_{1/2}$ are aligned with the drain potential for $V_{\mathrm{g}} = V_{\mathrm{g},1/\mathrm{g},2}$, as plotted in Figure 5.4(a).

As an example, assume that the initial gate voltage is set to zero. By increasing V_{g} (in positive direction), the "state ladder" (the quantum dot states in between the two leads) shifts lower and lower on the energy axis for μ. When reaching $V_{\mathrm{g}} = V_{\mathrm{g},1/\mathrm{g},2}$, the peak of $\mathfrak{D}_{1/2}$ is aligned with the Fermi edge of the drain lead, with the Fermi energy there defined as zero.

Formally, the tunneling rates between dot level and lead are obtained by integrating

$$\int_{-\infty}^{+\infty} \mathfrak{D}_{1/2}(\mu') \cdot \mathfrak{D}_{\mathrm{lead}}(\mu') f(\mu') \mathrm{d}\mu' \quad .$$

$f(\mu')$ is the Fermi distribution function of the lead electrons, which degrades to a step function for low temperatures, $\hbar\Gamma \gg k_{\mathrm{B}}T$. Therefore, the whole integrand is only non-zero up to the electrochemical potential of source or drain, μ_{s} or μ_{d}. Using an arbitrary μ for the lead potential and upper integration border, the integrand can be reduced to $\mathfrak{D}_{1/2}(\mu')\mathrm{d}\mu'$ leading to

$$\int_{-\infty}^{\mu} \mathfrak{D}_1(\mu')\mathrm{d}\mu' = \frac{1}{2} + \frac{1}{\pi} \cdot \arctan\left(\frac{2}{\hbar\Gamma}\left[e\alpha_{\mathrm{g}}\left(V_{\mathrm{g}} - V_{\mathrm{g},1}\right) + \mu\right]\right) \quad , \tag{5.24}$$

$$\int_{-\infty}^{\mu} \mathfrak{D}_2(\mu')\mathrm{d}\mu' = \frac{1}{2} + \frac{1}{\pi} \cdot \arctan\left(\frac{2}{\hbar\Gamma}\left[e\alpha_{\mathrm{g}}\left(V_{\mathrm{g}} - V_{\mathrm{g},2}\right) + \mu\right]\right) \quad . \tag{5.25}$$

The tunneling integral is also normalized, since

$$\int_{-\infty}^{\infty} \mathfrak{D}_{1/2}(\mu')\mathrm{d}\mu' \equiv 1 \quad . \tag{5.26}$$

There are four resulting tunneling rates between a specific dot level and leads: the tunneling rate from the source lead to the dot Γ_{s}^{+}, from the dot to the source Γ_{s}^{-}, from the dot

to the drain Γ_{d}^{-} and from the drain to the dot Γ_{d}^{+}, see also Figure 2.7. The width of the tunneling barriers between leads and dot is stated as prefactors a_{L}, respectively a_{R} to the tunneling integrals.
Regarding one level, for the drain side with $\mu_{\mathrm{d}} \equiv 0$ follows

$$\begin{aligned}\Gamma_{\mathrm{d},1}^{+}(V_{\mathrm{g}}) &= a_{\mathrm{R}} \int\limits_{-\infty}^{0} \mathfrak{D}_1(\mu')\mathrm{d}\mu' = \\ &= a_{\mathrm{R}} \left[\frac{1}{2} + \frac{1}{\pi} \cdot \arctan\left(\frac{2e}{\hbar\Gamma}\left[\alpha_{\mathrm{g}}\left(V_{\mathrm{g}} - V_{\mathrm{g},1}\right)\right]\right)\right] \quad , \end{aligned} \tag{5.27}$$

and

$$\begin{aligned}\Gamma_{\mathrm{d},1}^{-}(V_{\mathrm{g}}) &= a_{\mathrm{R}} \left[1 - \int\limits_{-\infty}^{0} \mathfrak{D}_1(\mu')\mathrm{d}\mu'\right] = a_{\mathrm{R}} \int\limits_{0}^{\infty} \mathfrak{D}_1(\mu')\mathrm{d}\mu' = \\ &= a_{\mathrm{R}} \left[\frac{1}{2} - \frac{1}{\pi} \cdot \arctan\left(\frac{2e}{\hbar\Gamma}\left[\alpha_{\mathrm{g}}\left(V_{\mathrm{g}} - V_{\mathrm{g},1}\right)\right]\right)\right] \quad . \end{aligned} \tag{5.28}$$

According to equation 2.24, the source potential is $\mu_{\mathrm{s}} = -eV_{\mathrm{sd}}$, leading to the tunneling rates at the source barrier:

$$\begin{aligned}\Gamma_{\mathrm{s},1}^{+}(V_{\mathrm{g}}) &= a_{\mathrm{L}} \int\limits_{-\infty}^{-eV_{\mathrm{sd}}} \mathfrak{D}_1(\mu')\mathrm{d}\mu' = \\ &= a_{\mathrm{L}} \left[\frac{1}{2} + \frac{1}{\pi} \cdot \arctan\left(\frac{2e}{\hbar\Gamma}\left[\alpha_{\mathrm{g}}\left(V_{\mathrm{g}} - V_{\mathrm{g},1}\right) - V_{\mathrm{sd}}\right]\right)\right] \quad , \end{aligned} \tag{5.29}$$

respectively

$$\begin{aligned}\Gamma_{\mathrm{s},1}^{-}(V_{\mathrm{g}}) &= a_{\mathrm{L}} \left[1 - \int\limits_{-\infty}^{-eV_{\mathrm{sd}}} \mathfrak{D}_1(\mu')\mathrm{d}\mu'\right] = a_{\mathrm{L}} \int\limits_{-eV_{\mathrm{sd}}}^{\infty} \mathfrak{D}_1(\mu')\mathrm{d}\mu' = \\ &= a_{\mathrm{L}} \left[\frac{1}{2} - \frac{1}{\pi} \cdot \arctan\left(\frac{2e}{\hbar\Gamma}\left[\alpha_{\mathrm{g}}\left(V_{\mathrm{g}} - V_{\mathrm{g},1}\right) - V_{\mathrm{sd}}\right]\right)\right] \quad . \end{aligned} \tag{5.30}$$

In contrast to [Meerwaldt et al., 2012], effects due to the height of the barriers are neglected. The tunnel coupling is determined by the overlap of the density of available states of the source or drain lead with that of the CNT is considered. We get for the net rates onto (Γ_1^{+}) and off the dot level (Γ_1^{-}):

$$\begin{aligned}\Gamma_1^{+}(V_{\mathrm{g}}) = \Gamma_{\mathrm{s},1}^{+}(V_{\mathrm{g}}) + \Gamma_{\mathrm{d},1}^{+}(V_{\mathrm{g}}) = \frac{a_{\mathrm{L}} + a_{\mathrm{R}}}{2} + \\ \frac{a_{\mathrm{L}}}{\pi} \cdot \arctan\left(\frac{2e}{\hbar\Gamma}\left[\alpha_{\mathrm{g}}\left(V_{\mathrm{g}} - V_{\mathrm{g},1}\right) - V_{\mathrm{sd}}\right]\right) + \frac{a_{\mathrm{R}}}{\pi} \cdot \arctan\left(\frac{2e}{\hbar\Gamma}\left[\alpha_{\mathrm{g}}\left(V_{\mathrm{g}} - V_{\mathrm{g},1}\right)\right]\right) \quad , \end{aligned} \tag{5.31}$$

$$\Gamma_1^-(V_g) = \Gamma_{s,1}^-(V_g) + \Gamma_{d,1}^-(V_g) = \frac{a_L + a_R}{2} - \\ \frac{a_L}{\pi} \cdot \arctan\left(\frac{2e}{\hbar\Gamma}\left[\alpha_g\left(V_g - V_{g,1}\right) - V_{sd}\right]\right) - \frac{a_R}{\pi} \cdot \arctan\left(\frac{2e}{\hbar\Gamma}\left[\alpha_g\left(V_g - V_{g,1}\right)\right]\right) \quad . \tag{5.32}$$

The same can be written for the second level by simply replacing $V_{g,1}$ by $V_{g,2}$, and a_L, a_R by b_L, b_R for the barrier widths.

With the assumption of two non-interacting dot levels in combination with only one dot level in the bias window, the current through the dot can be calculated using the relation

$$I\left(V_g\right) = e \cdot \frac{\Gamma_{s,1}^+\Gamma_{d,1}^- - \Gamma_{d,1}^+\Gamma_{s,1}^-}{\Gamma_1^+ + \Gamma_1^-} + e \cdot \frac{\Gamma_{s,2}^+\Gamma_{d,2}^- - \Gamma_{d,2}^+\Gamma_{s,2}^-}{\Gamma_2^+ + \Gamma_2^-} \quad . \tag{5.33}$$

As an example, see Figure 5.4(c). The mean occupation of a dot level as a function of gate voltage is given by

$$\left\langle N_1(V_g)\right\rangle = \frac{\Gamma_1^+(V_g)}{\Gamma_1^+(V_g) + \Gamma_1^-(V_g)} \quad , \tag{5.34}$$

$$\left\langle N_2(V_g)\right\rangle = \frac{\Gamma_2^+(V_g)}{\Gamma_2^+(V_g) + \Gamma_2^-(V_g)} \quad . \tag{5.35}$$

Starting from an arbitrary electron number N_0, this leads to a mean occupation $\langle N\rangle$ regarding two sequent charge transitions being located at $V_{g,1}$ and $V_{g,2}$:

$$\left\langle N(V_g)\right\rangle = N_0 + \left\langle N_1(V_g)\right\rangle + \left\langle N_2(V_g)\right\rangle = N_0 + \frac{\Gamma_1^+(V_g)}{\Gamma_1^+(V_g) + \Gamma_1^-(V_g)} + \frac{\Gamma_2^+(V_g)}{\Gamma_2^+(V_g) + \Gamma_2^-(V_g)} \tag{5.36}$$

According to [Meerwaldt et al., 2012], the definition of the control charge q_c is the charge that would be on the CNT in the absence of Coulomb blockade.

Since the drain lead is shorted to ground $V_d \equiv 0$, it is

$$q_c = C_g V_g + C_s V_{sd} = \alpha_g C_\Sigma V_g + \alpha_s C_\Sigma V_{sd} \quad . \tag{5.37}$$

Replacing Q in equation 2.25 by $-e\langle N\rangle$, an expression for the dot potential respectively voltage on the nanotube V_{CNT} is obtained as a function of mean occupation via

$$C_\Sigma V_{CNT} = q_c - e\left\langle N(V_g)\right\rangle \quad . \tag{5.38}$$

For the mean occupation taking two sequent charge transitions into account, this results in

$$V_{CNT}(V_g) = \frac{1}{C_\Sigma} \cdot \left(\alpha_g C_\Sigma V_g + C_\Sigma \alpha_s V_{sd} - e \cdot \left\langle N(V_g)\right\rangle\right) \quad . \tag{5.39}$$

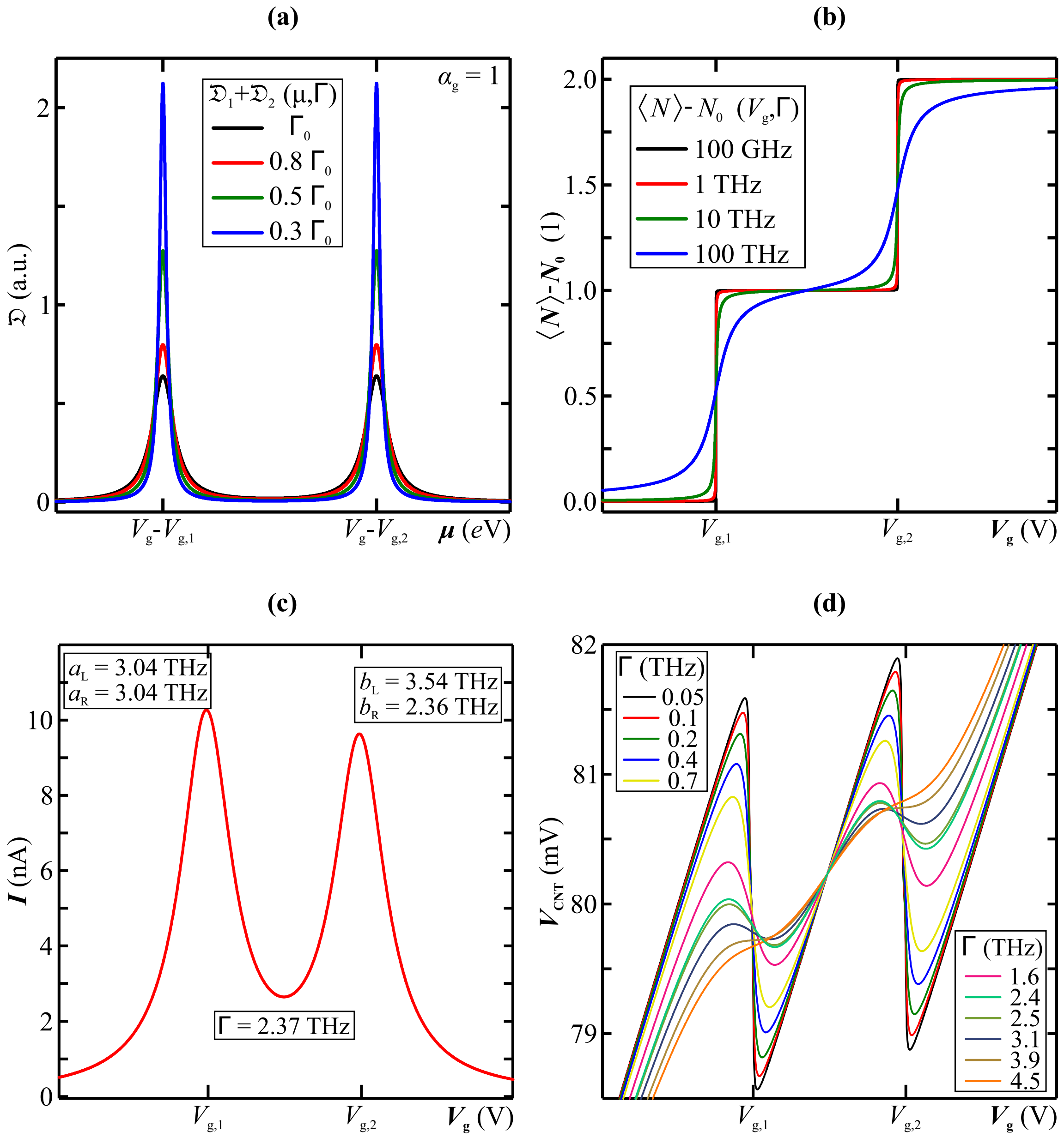

Figure 5.4: Modeling the average charge on a CNT. All parameters which are needed in addition to those which are not stated in the diagrams, can be found in Table 5.1 in section 5.4. **(a)** The density of available states $\mathfrak{D}(\mu,\Gamma)$ as a sum of equations 5.22 and 5.23. **(b)** The average charge $\langle N\rangle$ of the quantum dot as a function of V_g for several lifetime broadenings Γ using equation 5.36. It starts from $N_0 = 0$, the tunneling barrier widths are set to $a_L = a_R = b_L = b_R = 1$. **(c)** Calculation of the absolute current $|I|$ according to equation 5.33 using the parameters as stated in the diagram. **(d)** Resulting voltage V_{CNT} on the CNT using equation 5.40 for several Γ.

Expanding equation 5.39, one obtains

$$
\begin{aligned}
&V_{\mathrm{CNT}}(V_{\mathrm{g}}) = \alpha_{\mathrm{g}} V_{\mathrm{g}} + \alpha_{\mathrm{s}} V_{\mathrm{sd}} - \frac{e}{C_{\Sigma}} \cdot \left\langle N(V_{\mathrm{g}}) \right\rangle = \alpha_{\mathrm{g}} V_{\mathrm{g}} + \alpha_{\mathrm{s}} V_{\mathrm{sd}} - \frac{e}{\pi C_{\Sigma} \left(a_{\mathrm{L}} + a_{\mathrm{R}}\right) \left(b_{\mathrm{L}} + b_{\mathrm{R}}\right)} \cdot \\
&\cdot \Bigg\{ \left(a_{\mathrm{L}} b_{\mathrm{L}} + a_{\mathrm{L}} b_{\mathrm{R}} + a_{\mathrm{R}} b_{\mathrm{L}} + a_{\mathrm{R}} b_{\mathrm{R}}\right) \pi + \left(a_{\mathrm{L}} b_{\mathrm{L}} + a_{\mathrm{L}} b_{\mathrm{R}} + a_{\mathrm{R}} b_{\mathrm{L}} + a_{\mathrm{R}} b_{\mathrm{R}}\right) N_0 \pi \\
&\quad + a_{\mathrm{R}} \left(b_{\mathrm{L}} + b_{\mathrm{R}}\right) \arctan\left(\frac{2e}{\hbar\Gamma} \left[\alpha_{\mathrm{g}} \left(V_{\mathrm{g}} - V_{\mathrm{g},1}\right)\right] \right) + b_{\mathrm{R}} \left(a_{\mathrm{L}} + a_{\mathrm{R}}\right) \arctan\left(\frac{2e}{\hbar\Gamma} \left[\alpha_{\mathrm{g}} \left(V_{\mathrm{g}} - V_{\mathrm{g},2}\right)\right] \right) \\
&\quad + a_{\mathrm{L}} b_{\mathrm{L}} \arctan\left(\frac{2e}{\hbar\Gamma} \left[\alpha_{\mathrm{g}} \left(V_{\mathrm{g}} - V_{\mathrm{g},1}\right) - V_{\mathrm{sd}}\right] \right) + a_{\mathrm{L}} b_{\mathrm{R}} \arctan\left(\frac{2e}{\hbar\Gamma} \left[\alpha_{\mathrm{g}} \left(V_{\mathrm{g}} - V_{\mathrm{g},1}\right) - V_{\mathrm{sd}}\right] \right) \\
&\quad + a_{\mathrm{R}} b_{\mathrm{L}} \arctan\left(\frac{2e}{\hbar\Gamma} \left[\alpha_{\mathrm{g}} \left(V_{\mathrm{g}} - V_{\mathrm{g},2}\right) - V_{\mathrm{sd}}\right] \right) + a_{\mathrm{L}} b_{\mathrm{L}} \arctan\left(\frac{2e}{\hbar\Gamma} \left[\alpha_{\mathrm{g}} \left(V_{\mathrm{g}} - V_{\mathrm{g},2}\right) - V_{\mathrm{sd}}\right] \right) \Bigg\} .
\end{aligned}
\tag{5.40}
$$

5.4 Fitting pre-existing data

The model of sections 5.2 and 5.3 is applied here to a device which has already been characterized previously in many different ways, see [Schmid et al., 2012; Schmid et al., 2015a; Schmid et al., 2015b]. It is a single-walled CNT suspended in between 40 nm thick rhenium electrodes separated by a trench of 700 nm length. The underlying global back gate substrate is terminated with an insulating 300 nm thick SiO_2 layer. The evaluation is presented in [Schmid, 2015] and a first analysis of mechanical charge detection is performed in section 6.3. The model is applied to the intermediate transport regime in which Kondo anomalies as well as co-tunneling features appear in the stability diagrams.

The experiment was performed in the vacuum of a second dilution cryostat setup at a base temperature of about 30 mK. The same measurement setup as described in subsection 3.5.4 with dc readout was used. The data is plotted as a 2d color map in Figure 5.5. The continuous response of the resonator is increasing as a function of V_{g}. This dependence is approximated to be linear with respect to V_{g}. An exemplary $\Delta I\left(f\right)$ trace is plotted to identify f_0 in the panel right-hand side. f_0 is then read out by hands for all V_{g} values and multiplied by 2π to obtain ω_0. After subtracting the linear contribution denoted as $a + b \cdot V_{\mathrm{g}}$, the reduced resonance frequency $\tilde{\omega}_0 = \omega_0 - \left(a + b \cdot V_{\mathrm{g}}\right)$ is plotted against V_{g} as can be seen in the lower panel. The characteristic minima for each single electron transition, here from $\langle N \rangle = 40$ to 44, are now clearly visible. In the $I\left(V_{\mathrm{g}}\right)$ trace in the panel above, the Kondo effect for the odd valleys at $\langle N \rangle = 41; 43$ is revealed by the enhanced conductivity in contrast to the neighboring even ones.

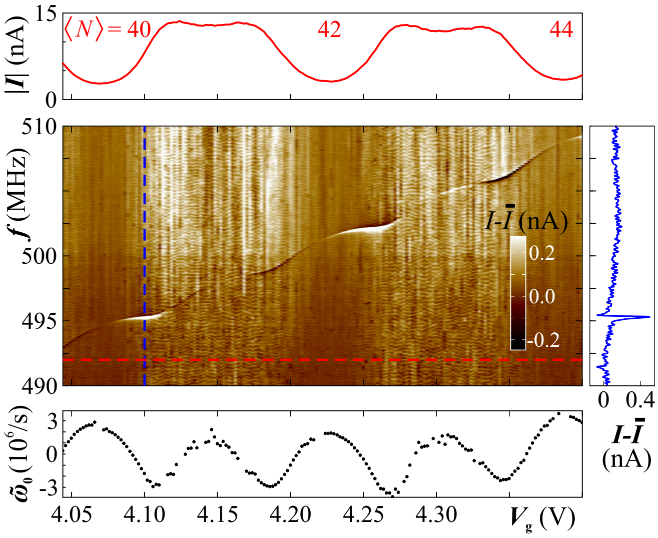

Figure 5.5: Charge detection in the Kondo regime, device "CB 3224". The frequency f of the driving rf signal (nominal power $P_{\mathrm{rf}} = -25\,\mathrm{dBm}$, step size $\Delta f = 10\,\mathrm{kHz}$) is swept for fixed V_{g}, and the dc current is measured for a constant bias of $V_{\mathrm{sd}} = -0.1\,\mathrm{mV}$. The color scale plot results from subtracting the mean value for each f sweep from each current data point. The panel above is the simultaneously recorded, and off-resonant absolute current $|I|(V_{\mathrm{g}})$ as a function of V_{g}. The data points are taken from the red dashed line as can be seen in the color map for constant $f = 492\,\mathrm{MHz}$. In addition, the electron number is indicated. The trace right-hand side plots the current $I - \bar{I}$ as a function of f, for constant $V_{\mathrm{g}} = 4.1\,\mathrm{V}$. The values for f_0 are extracted at the maximum of the current shift, converted to $\omega_0 = 2\pi f_0$, and its linear contribution $a + b \cdot V_{\mathrm{g}}$ is subtracted, leading to the data points as plotted in the lower panel.

The model is applied to the measurements as follows: first of all, quantities obtained from quantum dot transport spectroscopy in this region are included; these are device parameters as, e. g. α_{g}, α_{s}, C_{g}, C_{s}, C_{Σ}. The occupation numbers are obtained by counting the Coulomb oscillations in the $I\left(V_{\mathrm{g}}\right)$ characteristic starting from $N_{\mathrm{el}} = 1$, similar to the procedure outlined in chapter 4. The mean occupation $\langle N \rangle \left(V_{\mathrm{g}}\right)$ in the middle of each valley is set equal to the total occupation number N_{el}. The resonance frequency $\omega_0 = 2\pi f_0$ is taken from the measured data left-hand side of the first "dip". The height h_0 and length of the resonator L are taken from the fabrication recipe. $d = 2r = 0.9\,\mathrm{nm}$ is used as value for the diameter of the nanotube. The capacitive coupling of the resonator to the back gate is obtained by inserting these three quantities into equations 5.9, and 5.10 for the static case $u(x) = 0$. The obtained capacitance differs from the transport value C_{g} because of the length: the resonator length is about L, but the corresponding length of the nanotube which forms the quantum dot is much smaller. The comparison and the derivation of 5.10 at $z = h_0$ delivers an estimation for $\mathrm{d}C_{\mathrm{g}}/\mathrm{d}z$.

Nevertheless, this is one model parameter in the following calculations. The next one is the mass m of the resonator. For single-walled carbon nanotubes, it can be calculated according to [Laurent et al., 2010] as

$$m = \frac{10^{-3}}{1315} \cdot \pi L d \quad . \tag{5.41}$$

Due to the uncertainty in d and since not the whole nanotube moves equally, it serves only as an estimate of a model parameter for further calculations.

The tunneling barrier widths are obtained by fitting equation 5.33 to the related Coulomb oscillations from the $I\left(V_{\mathrm{g}}\right)$ traces. The result has to be adjusted having in mind that the Coulomb oscillations are strongly affected by the Kondo effect. Such a simulated current for $\langle N \rangle = 41$ without Kondo enhanced conductivity is plotted in Figure 5.4(c). The extremal gate values of the current fits $V_{\mathrm{g},1}$ and $V_{\mathrm{g},2}$ are thus different from the directly read out extremal values. $a_{\mathrm{L}}, a_{\mathrm{R}}, b_{\mathrm{L}}, b_{\mathrm{R}}$ are set as constants in the next calculations, and the obtained lifetime broadening Γ is an estimate for a model parameter.

The resonance frequency behavior (after subtraction of $a + b \cdot V_{\mathrm{g}}$) is then fitted to equation 5.21 with κ and Ω_0 as linear parameters. In a second fitting step, these are set as constants, with now $\mathrm{d}C_{\mathrm{g}}/\mathrm{d}z, m, \Gamma, C_{\Sigma}$ as model parameters as well as $V_{\mathrm{g},1}^{\mathrm{mech.}}$ and $V_{\mathrm{g},2}^{\mathrm{mech.}}$. The latter two parameters correspond to the minima of the $\Delta\omega_0$ dips, and thus the single electron charging. C_{Σ} has to be adjusted for the same reasons as C_{g} to the value obtained from equation 5.10: the length of the resonator, respectively the vibrating CNT is not equal to spatial dimension of the quantum dot in this charging state.

The results are plotted in Figure 5.6, showing the experimental data as well as resulting fits. The fits for the absolute current and mean occupation $\langle N \rangle$ implicate the obtained model parameters from the ω_0-fit. By comparison with the maxima in the $I\left(V_{\mathrm{g}}\right)$ trace, gate shifts are extracted directly from the measurements as stated in Figure 5.6 and in Table 5.2 and 5.4. All parameters for the calculations and fittings are listed in Tables 5.1 and 5.3. The extracted and calculated gate shifts can be found in Tables 5.2 and 5.4.

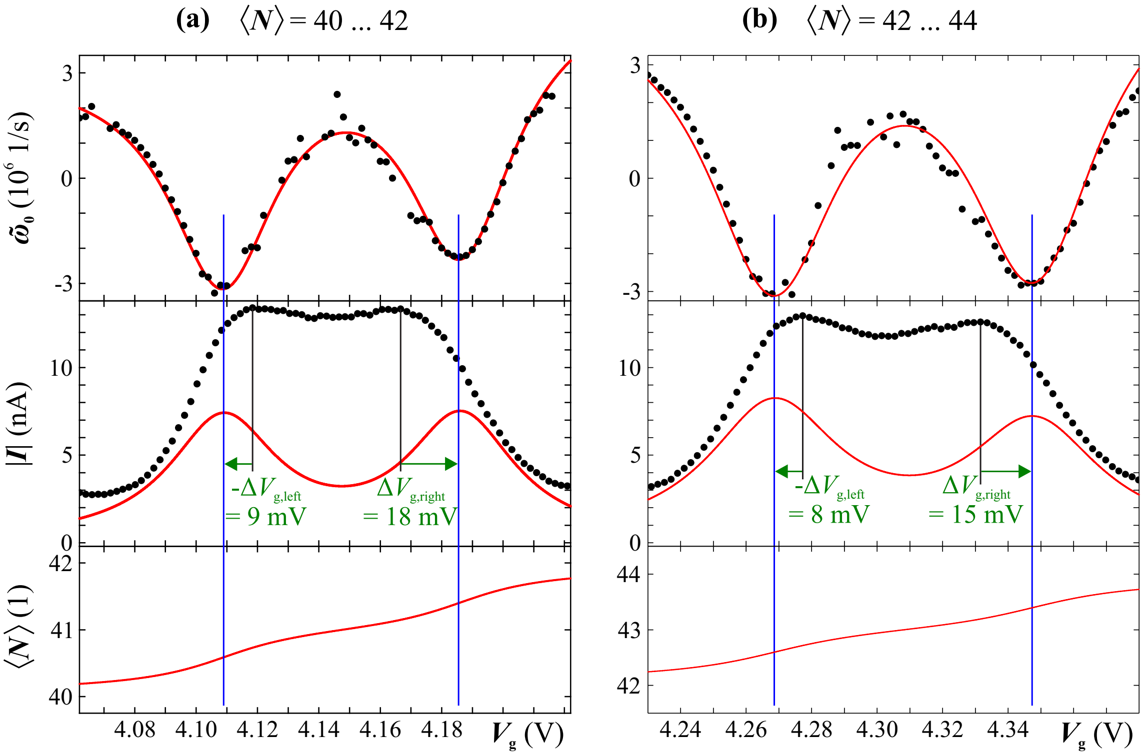

(a) $\langle N \rangle = 40 \ldots 42$ **(b)** $\langle N \rangle = 42 \ldots 44$

Figure 5.6: Resonance frequency evolution across current Kondo double peaks, around $\langle N \rangle = 41$ and $\langle N \rangle = 43$, **(a)** and **(b)**. All subplots of each column use the same V_g axis to make the experimentally obtained shifts visible. The corresponding fits are included as red lines. The lowest panel plots the mean occupation as a function of V_g, using the model parameters obtained from $\tilde{\omega}_0\left(V_\mathrm{g}\right)$ and $|I|\left(V_\mathrm{g}\right)$. All parameters are listed in Tables 5.1 and 5.3.

Device parameters			
α_g	0.05497	V_sd	$-0.1\,\mathrm{mV}$
α_s	0.30000	N_0	40
C_g	$2.41825\,\mathrm{aF}$	ω_0	$2\pi \cdot 494.31 \cdot 10^6\,1/\mathrm{s}$
C_s	$13.5195\,\mathrm{aF}$	L	$700\,\mathrm{nm}$
C_Σ	$44.3198\,\mathrm{aF}$	h_0	$340\,\mathrm{nm}$
Model parameters from $I\left(V_\mathrm{g}\right)$ measurement			
a_L	$3.192\,\mathrm{THz}$	Γ	$2.127\,\mathrm{THz}$
a_R	$3.157\,\mathrm{THz}$	$V_{\mathrm{g},1}$	$4.119\,\mathrm{V}$
b_L	$2.736\,\mathrm{THz}$	$V_{\mathrm{g},2}$	$4.173\,\mathrm{V}$
b_R	$3.928\,\mathrm{THz}$		
Model parameters from mechanical resonance detection			
κ	$3.22981 \cdot 10^5\,(\mathrm{Vs})^{-1}$	m	$1.247 \cdot 10^{-21}\,\mathrm{kg}$
Ω_0	$-23.4507 \cdot 10^6\,1/\mathrm{s}$	$\frac{\mathrm{d}C_\mathrm{g}}{\mathrm{d}z}$	$-5.852\,\mathrm{pF/m}$
C_Σ	$12.2188\,\mathrm{aF}$	$V_{\mathrm{g},1}^{\mathrm{mech.}}$	$4.109\,\mathrm{V}$
Γ	$3.549\,\mathrm{THz}$	$V_{\mathrm{g},2}^{\mathrm{mech.}}$	$4.187\,\mathrm{V}$

Table 5.1: Model and device parameters for the calculations around valley $\langle N\rangle = 41$.

$\langle N\rangle = 41$	Gate shifts	
	exp.	fits
Left: $V_{\mathrm{g},1}^{\mathrm{mech.}} - V_{\mathrm{g},1}$	$-9\,\mathrm{mV}$	$-9.7\,\mathrm{mV}$
Right: $V_{\mathrm{g},2}^{\mathrm{mech.}} - V_{\mathrm{g},2}^{\mathrm{tran.}}$	$18\,\mathrm{mV}$	$13.9\,\mathrm{mV}$

Table 5.2: Extracted and calculated gate shifts $\langle N\rangle = 41$.

Device parameters			
α_g	0.04653	V_{sd}	$-0.1\,\text{mV}$
α_s	0.35518	N_0	42
C_g	$2.36095\,\text{aF}$	ω_0	$2\pi \cdot 501.46 \cdot 10^6\,1/\text{s}$
C_s	$18.1848\,\text{aF}$	L	$700\,\text{nm}$
C_Σ	$50.736\,\text{aF}$	h_0	$340\,\text{nm}$
Model parameters from $I\left(V_g\right)$ measurement			
a_L	$3.329\,\text{THz}$	Γ	$2.137\,\text{THz}$
a_R	$3.480\,\text{THz}$	$V_{g,1}$	$4.279\,\text{V}$
b_L	$2.628\,\text{THz}$	$V_{g,2}$	$4.336\,\text{V}$
b_R	$3.252\,\text{THz}$		
Model parameters from mechanical resonance detection			
κ	$3.78513 \cdot 10^5\,(\text{Vs})^{-1}$	m	$1.236 \cdot 10^{-21}\,\text{kg}$
Ω_0	$-11.7483 \cdot 10^6\,1/\text{s}$	$\frac{\mathrm{d}C_g}{\mathrm{d}z}$	$-7.620\,\text{pF/m}$
C_Σ	$16.2796\,\text{aF}$	$V_{g,1}^{\text{mech.}}$	$4.269\,\text{V}$
Γ	$3.423\,\text{THz}$	$V_{g,2}^{\text{mech.}}$	$4.349\,\text{V}$

Table 5.3: Model and device parameters for the calculations around valley $\langle N \rangle = 43$.

$\langle N \rangle = 43$	Gate shifts	
	exp.	fits
Left: $V_{g,1}^{\text{mech.}} - V_{g,1}$	$-8\,\text{mV}$	$-9.3\,\text{mV}$
Right: $V_{g,2}^{\text{mech.}} - V_{g,2}^{\text{tran.}}$	$15\,\text{mV}$	$12.9\,\text{mV}$

Table 5.4: Extracted and calculated gate shifts $\langle N \rangle = 43$.

5.5 Hole side, mixed valence regime and Fabry-Pérot interferometry

The transport mechanism in the Fabry-Pérot regime is based on the continuous reflection or transmission of charge carriers at the metal-CNT-interfaces, see subsection 2.5.4. Therefore, since the dot is open, no discrete dips of f_0 as a function of V_g due to charge quantization are expected.

Figure 5.7(a) is a stability diagram in the negative V_g range around $\lesssim -2\,\mathrm{V}$ confirming the presence of Fabry-Pérot interferometry within this transport regime. Indeed, the overall conductance range is in between $0.5\,e^2/h \leq G \leq 2\,e^2/h$. However, single charging effects still appear typically attributed to the intermediate regime, see Table 2.2. Zero-bias-anomalies at $V_\mathrm{g} \approx -1.96\,\mathrm{V}$; $-1.88\,\mathrm{V}$; $-1.80\,\mathrm{V}$ indicate the presence of the Kondo effect. In contrast to Figure 3(a) in [Grove-Rasmussen et al., 2007], where exclusively Fabry-Pérot transport regime is plotted, the stability diagram in Figure 5.7(a) of the present CNT quantum dot reveals an intermediate, mixed valence regime in combination with Fabry-Pérot transport. In [Dirnaichner et al., 2016], the transport in this gate voltage range was classified in the same way.

Figure 5.7(b) shows a measurement on mechanical resonance detection in this transport regime. The corresponding $I\left(V_\mathrm{g}\right)$ trace can be seen in the top panel. The resonant behavior of the resonator as a function of V_g can be tracked in the middle panel. A pattern due to single charging effects as observed in Figure 5.5 is expressed by locally slightly different decreasing of f_0. The read-out reduced resonance frequencies $\tilde{\omega}_0$ are plotted as a function of V_g in the panel below: dips are marked as green vertical lines and extended to the $I\left(V_\mathrm{g}\right)$ trace above. Indeed, the dips can be attributed to single charging effects but do not distinctly appear anymore in this transport regime; it is difficult to extract the minimum of $\tilde{\omega}_0$. Charge detection using nanomechanical properties of the CNT resonator in this intermediate regime is hence rather difficult. Due to the nature of an exclusively Fabry-Pérot transport regime, mechanical charge detection is not practicable at all. Measurements on mechanical resonance as a function of V_g do not exhibit characteristic dips, see also [Meerwaldt, 2013; Schmid, 2015].

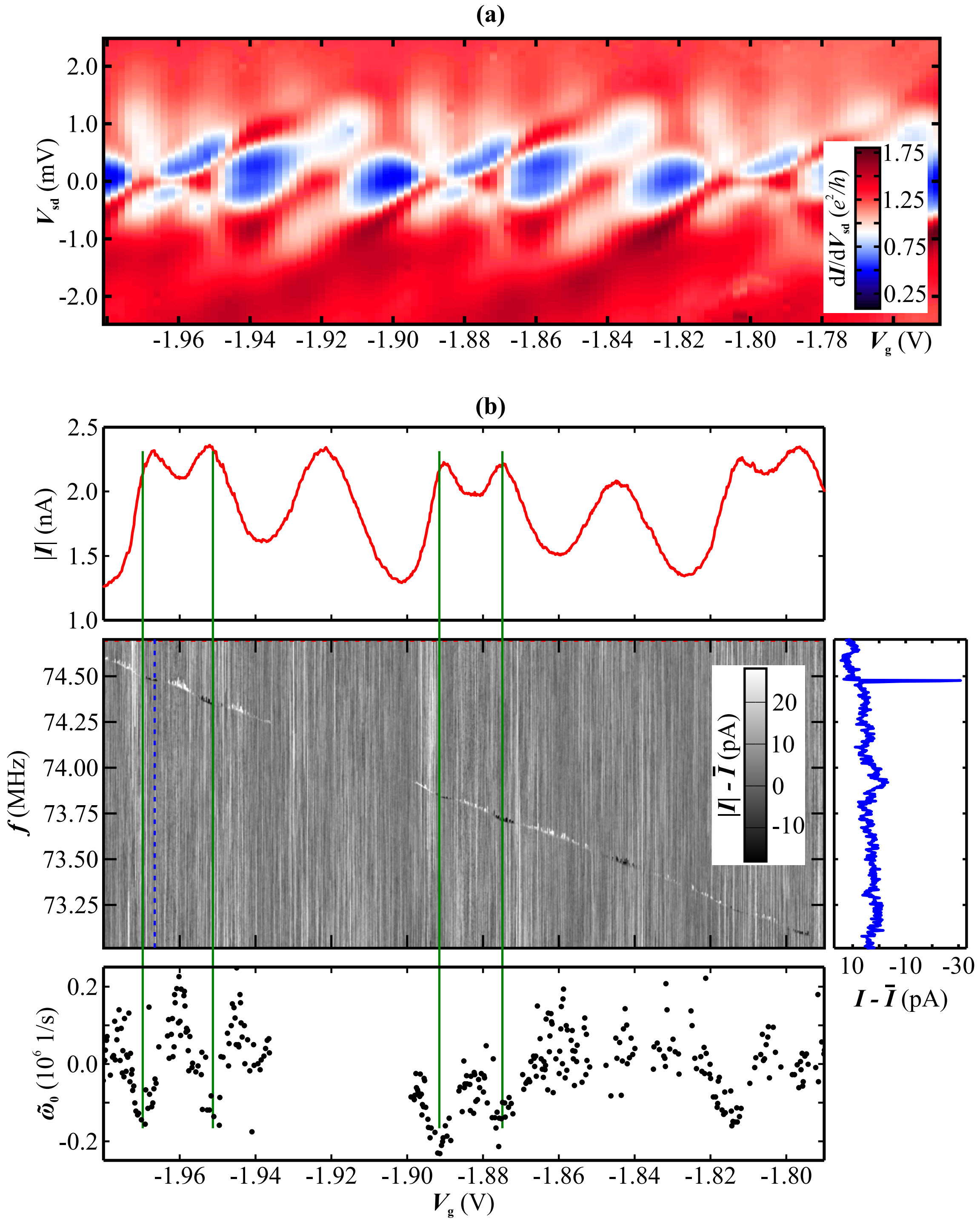

Figure 5.7: **(a)** Stability diagram $G\left(V_{\mathrm{sd}}, V_{\mathrm{g}}\right)$. **(b)** Resonance frequency dependence in the Fabry-Pérot regime. Experimental parameters for the dc readout setup are $V_{\mathrm{sd}} = -0.1\,\mathrm{mV}$, $P_{\mathrm{rf}} = -13.7\,\mathrm{dBm}$, and f-step size $\Delta f = 2.5\,\mathrm{kHz}$ at base temperature. The current shift $I - \bar{I}$ for each frequency trace is plotted as a 2d-colormap. Top panel: the simultaneously measured current without any resonant signal at $f = 74.75\,\mathrm{MHz}$. Right panel: plot of the current $I - \bar{I}$ as a function of f at $V_{\mathrm{g}} = -1.9668\,\mathrm{V}$. Bottom panel: reduced resonance frequency $\tilde{\omega}_0$ as a function of V_{g}. The green vertical lines indicate the (overlapped) charge transitions.

5.6 Low electron numbers regime

In contrast to section 5.5, the nanotube forms in electron conduction close to the band gap a quantum dot with strong Coulomb blockade. The transport characterization measurements in chapter 4 at the electron side confirms this statement. A successful measurement resolving the f_0 dip at $N_{\mathrm{el}} = 1$ was not performed for the present CNT device. A measurement resolving the resonant driving of the CNT as a function of V_{g} is plotted in Figure 5.8, for $V_{\mathrm{sd}} = -2\,\mathrm{mV}$ however. The best settings in this region lead to an evaluation as plotted in Figure 5.9.

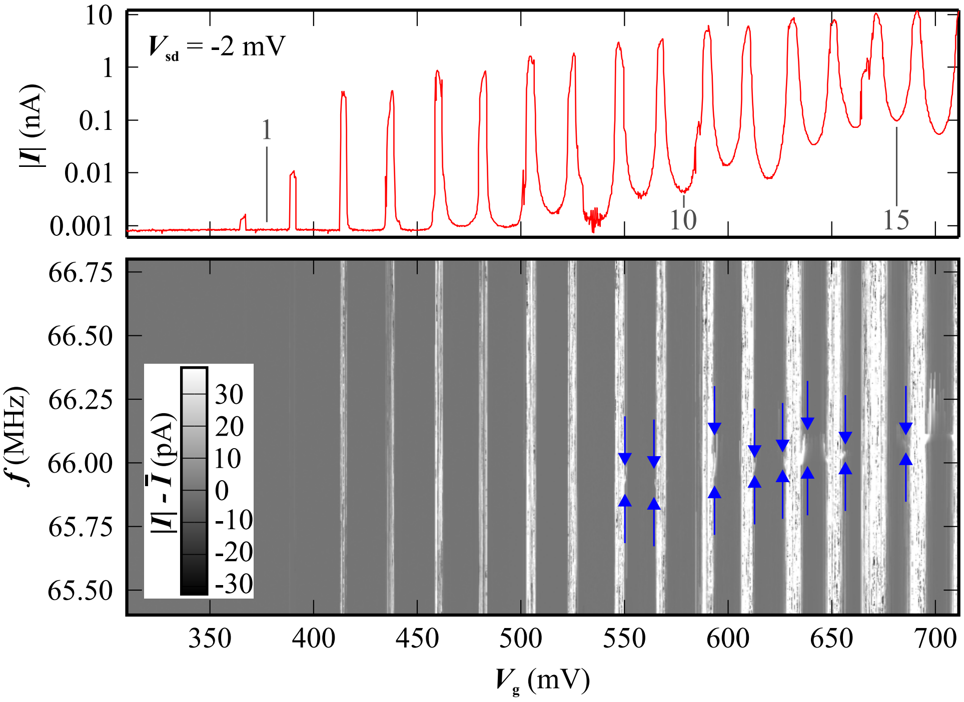

Figure 5.8: Grayscale map of the current shift $|I| - \bar{I}$ as a function of f and V_{g}. Some $I - \bar{I}$ peaks at resonant driving of the CNT are indicated in between two vertical blue arrows. Experimental parameters for the dc readout setup are $V_{\mathrm{sd}} = -2\,\mathrm{mV}$, $P_{\mathrm{rf}} = -13.7\,\mathrm{dBm}$, and f-step size $\Delta f = 1.4\,\mathrm{kHz}$ at base temperature.

The mechanical model fit for $\omega_0(V_{\mathrm{g}})$ is also plotted, indicating a double-dip because of the $\partial\langle N\rangle/\partial V_{\mathrm{g}}$ behavior at higher bias: here, $\langle N\rangle\left(V_{\mathrm{g}}\right)$ exhibits a saddle point or even a plateau around the charge transition, depending on Γ. According to [Meerwaldt et al., 2012], the mechanical oscillation only brings about a small change in average charge, and the resonance frequency returns towards its original value.

The transport quantities $\alpha_{\mathrm{g}}, \alpha_{\mathrm{s}}, C_{\mathrm{g}}, C_{\mathrm{s}}, C_{\Sigma}$ of each level are extracted from Figure 4.5 in section 4.3. A diameter of $d = 1.4\,\mathrm{nm}$ is assumed.

Additional parameters needed for further calculation are stated in Table 5.5; the model parameters for the red colored fits can be found in Table 5.6. The extrema of the Coulomb oscillations on the gate axis – $V_{g,1}, V_{g,2}$ – are set as constants for fitting the resonance frequency evolution. Here, since the parabolic contribution from the continuous charging is almost absent, the formula 5.21 can be fitted to the bare ω_0 data. Furthermore, C_Σ and m need not be adapted to the data, and only Γ and $\mathrm{d}C_g/\mathrm{d}z$ are used as model parameters. It turns out that tunneling barrier widths as well as lifetime broadening Γ are in the same order of magnitude as stated in the evaluation in [Meerwaldt et al., 2012]. These transport parameters in the GHz range indicate therefore strong Coulomb blockade.

Device parameters			
α_g, α_s	see Fig. 4.5(a)	V_{sd}	$-0.5\,\mathrm{mV}$
C_g, C_s, C_Σ	see Fig. 4.5(b)	L	$1200\,\mathrm{nm}$
m	$4.0136\,\mathrm{kg}$	h_0	$550\,\mathrm{nm}$

Table 5.5: Device parameters used for fits in Figure 5.9.

Model parameters for transport characteristics					
$N_0\,(1)$	11	12	13	14	15
$V_{g,1}/V_{g,2}\,(\mathrm{mV})$	589.2	608.6	630.5	650.4	672.0
$a_L/a_R\,(\mathrm{GHz})$	52/52		74/78	18/18	
$b_L/b_R\,(\mathrm{GHz})$		36/36		16/20	81/81
$\Gamma\,(\mathrm{GHz})$	431		527	414	
Model parameters for mechanic behavior					
$\omega_0/(2\pi)\,(10^6\,1/\mathrm{s})$	65.9178		65.9766	65.9992	
$\kappa\,(10^5\,\mathrm{Vs}^{-1})$	2.30898		1.56332	2.42284	
$\Omega_0\,(10^8\,1/\mathrm{s})$	4.12843		4.13396	4.12625	
$\frac{\mathrm{d}C_g}{\mathrm{d}z}\,(-10^{-12}\,\mathrm{F/m})$	2.60932		2.33148	2.08606	
$\Gamma\,(\mathrm{GHz})$	442		555	621	

Table 5.6: Model Parameters for fits in Figure 5.9.

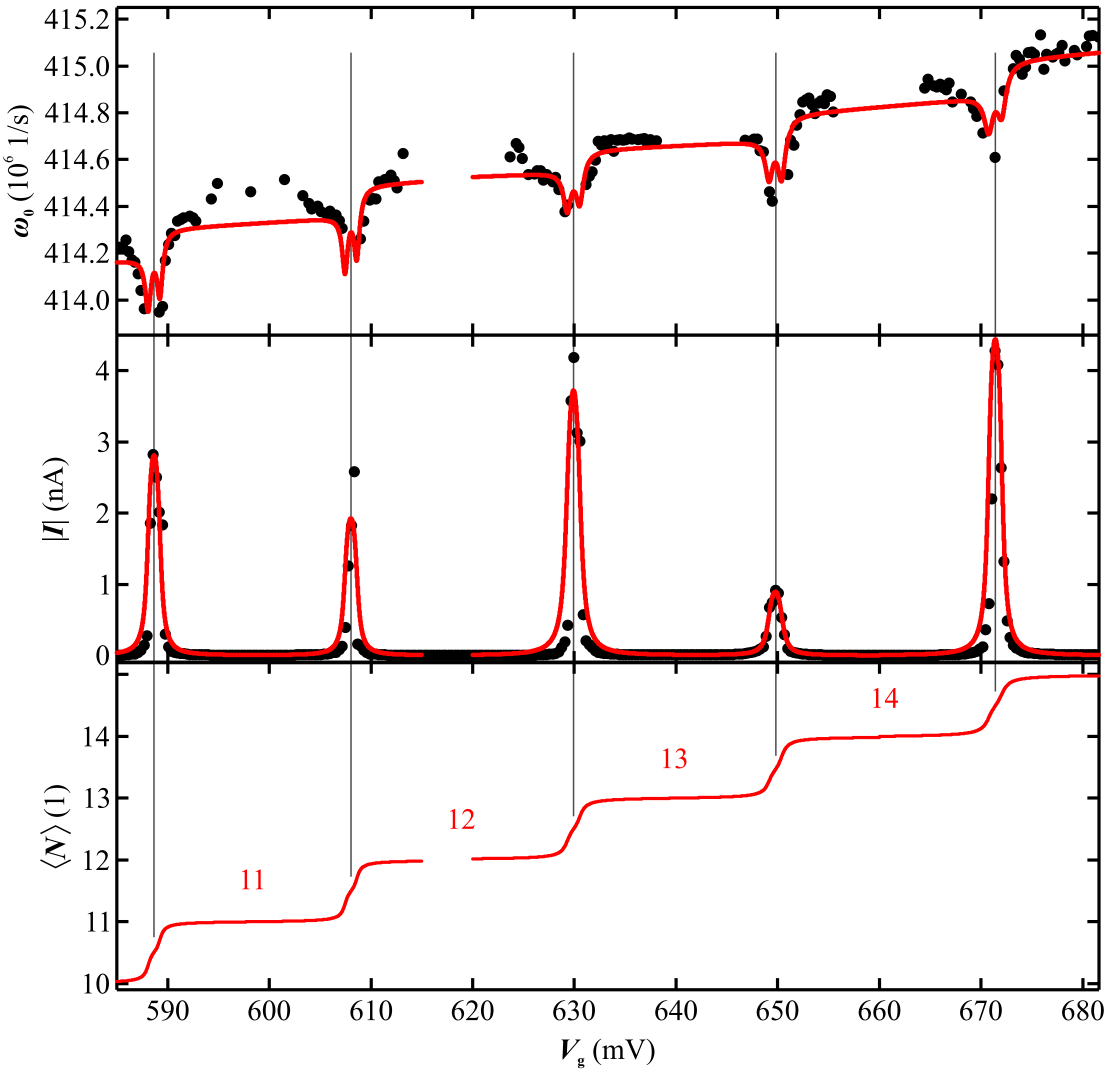

Figure 5.9: Extracted resonance frequency $\omega_0\left(V_g\right)$, and $I\left(V_g\right)$ taken from a measurement comparable to that shown in Figure 5.8. The resulting mean occupation $\langle N \rangle$ as a function of V_g is plotted in the panel above. All three diagrams use the same V_g axis. Experimental parameters for the dc readout setup are $V_{sd} = -0.5\,\text{mV}$, $P_{rf} = -14.84\,\text{dBm}$, and f-step size $\Delta f = 0.2\,\text{kHz}$ at base temperature. See table 5.6 for the fit parameters.

5.7 Strong coupling regime

The following measurements examine the resonance frequency dependence in the strong coupling regime as already examined by means of transport spectroscopy in section 4.5. The corresponding measurement is plotted in Figure 5.10. It shows an interesting feature: the reduced mechanical resonance frequency $\tilde{\omega}_0$ exhibits clear minima, revealing also a single electron transition for $N_{\mathrm{el}} = 270$. In contrast, a conductance minimum revealing the $4N+2 = 270$ valley are not resolved in the $I\left(V_{\mathrm{g}}\right)$-characteristic, as it is the case starting from $N_{\mathrm{el}} = 254$ for this regime, see also Figure 4.9(b). The detection current I_{LIA} exhibits a higher noise level in the transition range in between both states, as can be seen for the rf traces around $5.76 \leq V_{\mathrm{g}} \leq 5.765$.

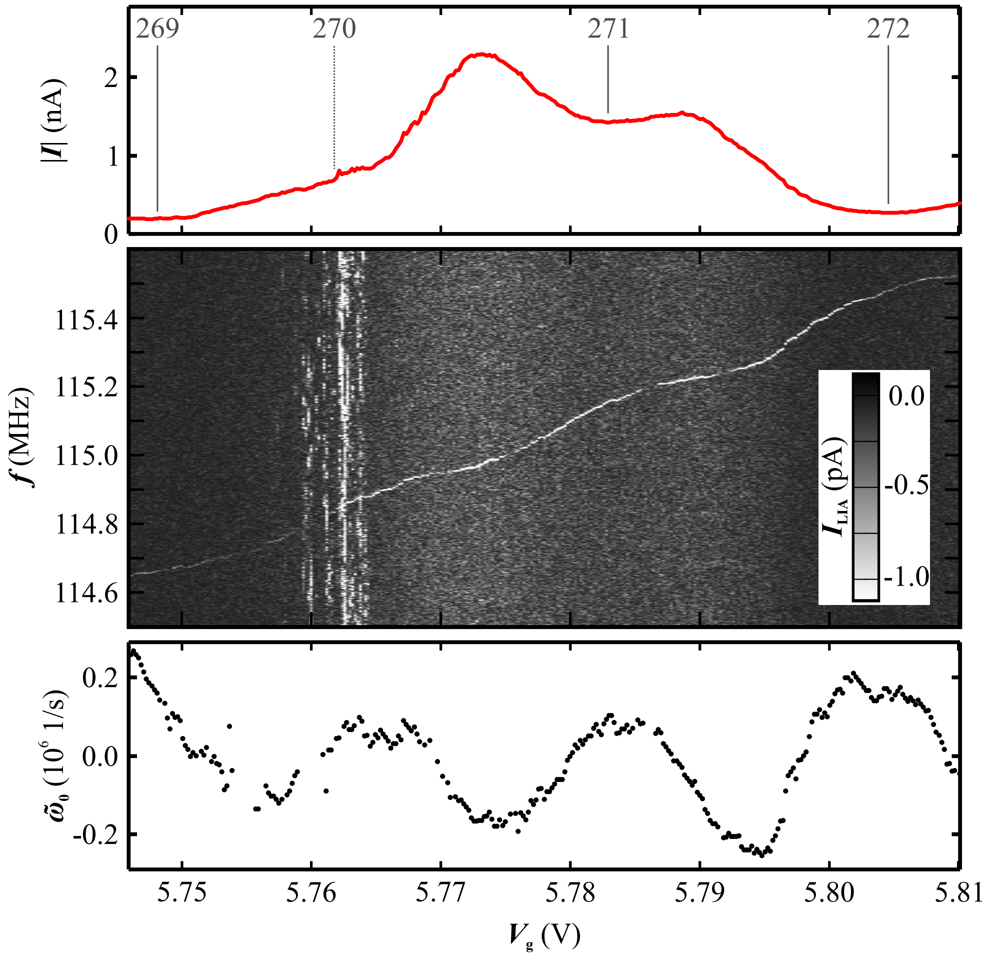

Figure 5.10: Grayscale map of the current modulation I_{LIA} as a function of f and V_{g}. Extracted and reduced resonance frequency $\tilde{\omega}_0$ (panel below), and $I\left(V_{\mathrm{g}}\right)$ characteristic (panel above). Experimental parameters for the LIA-readout setup are $V_{\mathrm{sd}} = -0.1\,\mathrm{mV}$, $P_{\mathrm{rf}} = -18.5\,\mathrm{dBm}$, f-step size $\Delta f = 1.5\,\mathrm{kHz}$, and V_{g} step size $\Delta V_{\mathrm{g}} = 0.2\,\mathrm{mV}$ at base temperature.

Furthermore, the depth of the $\tilde{\omega}_0$ dips is with $\approx 0.4 \cdot 10^6\,\mathrm{s}^{-1}$ in the same range as for low electron numbers. This observation indicates that the mechanical charge detection technique is not affected by transport phenomena like co-tunneling and Kondo effect. The depth is characteristic for the device itself, and seems to depend on the length L, respectively mass m of the resonator or CNT.

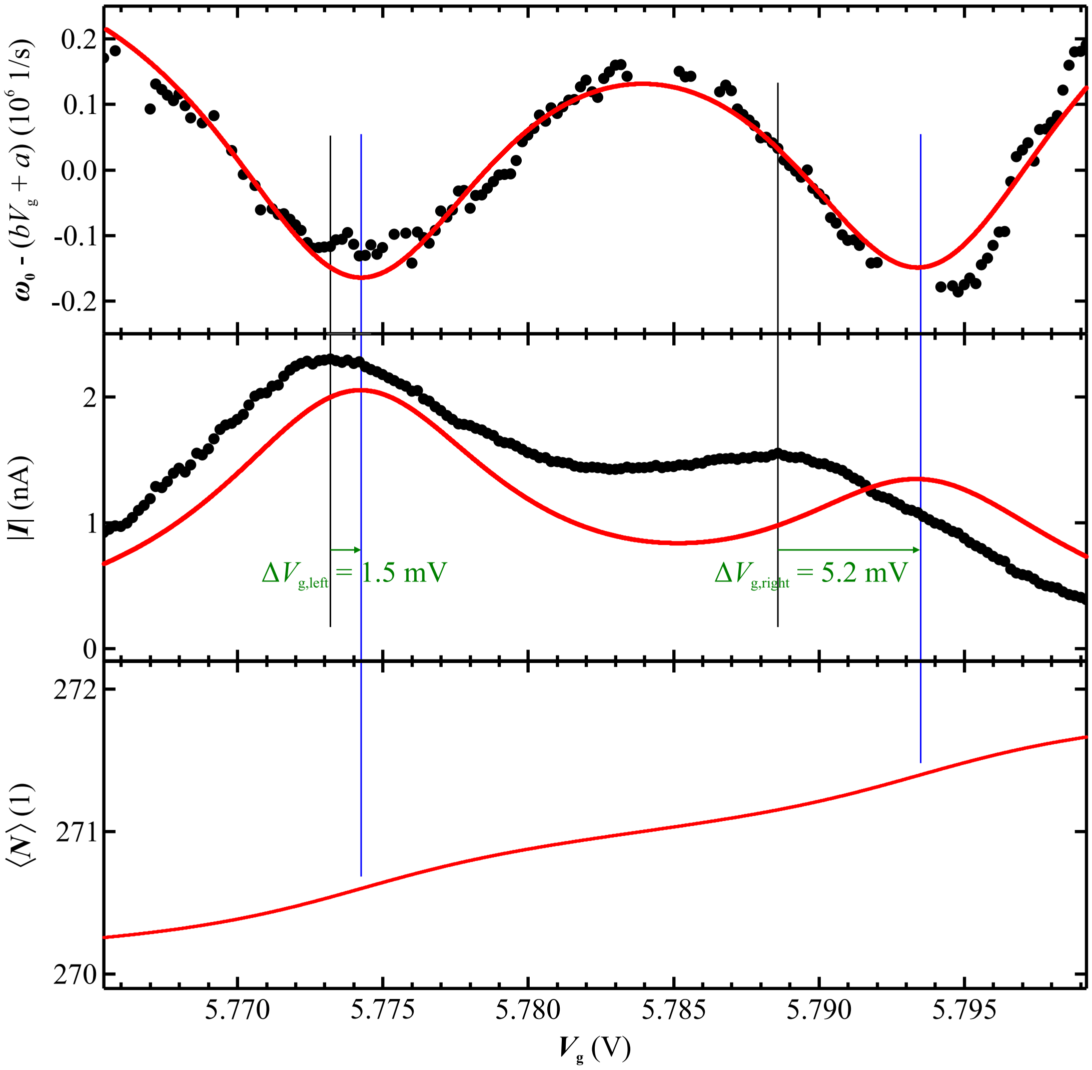

Figure 5.11: Extracted reduced resonance frequency $\tilde{\omega}_0 = \omega_0 - \left(a + b \cdot V_g\right)$, and $I\left(V_g\right)$ trace taken from the measurement as plotted in Figure 5.10. The resulting mean occupation $\langle N \rangle$ as a function of V_g is plotted in the panel above. All three diagrams use the same V_g axis.

The dimension of the Coulomb blockade valleys on the gate axis is reflected by the width of the dips. For comparison, see the dips for the old device in Figure 5.6 which are of ca. 60 mV width in contrast to the present one with about 16 mV. Consequently, the extracted gate shifts in between I and $\tilde{\omega}_0$ extrema which are attributed to the Kondo effect are smaller than for the old device. On the one hand, the shift for the peak left to the Kondo degenerated valley is smaller than for the right one, which is also observed for the old device. On the other hand, it points to the opposite side. The experimentally extracted absolute amounts are given in Figure 5.11, the parameters for the corresponding fits in Table 5.7, following the same evaluation procedure as described in section 5.4.

According to Table 2.3, the dot is in the intermediate transport regime – case (IV) –, but not open. This results in higher values for a_{L}, a_{R}, b_{L}, b_{R}, and lifetime broadening of the dot level Γ in contrast to the model parameters used for the strong Coulomb blockade regime, see Table 5.6. The fit for the mechanical resonance frequency behavior is obtained using these model parameters. Besides C_Σ, also m is reduced in comparison with the measurement in the strong Coulomb blockade regime. It seems that the mechanical tension reduces the resonator length as well as charging the electronic length of the dot. The resonator mass m here can be changed because of a changing of the mode shape.

Device parameters			
α_{g}	0.07926	V_{sd}	$-0.1\,\mathrm{mV}$
α_{s}	0.55410	N_0	270
C_{g}	$9.6832\,\mathrm{aF}$	ω_0	$2\pi\cdot 115.16\cdot 10^6\,1/\mathrm{s}$
C_{s}	$68.6328\,\mathrm{aF}$	L	$1200\,\mathrm{nm}$
C_Σ	$122.685\,\mathrm{aF}$	h_0	$550\,\mathrm{nm}$
Model parameters from $I\left(V_{\mathrm{g}}\right)$ measurement			
a_{L}	$362.7\,\mathrm{GHz}$	Γ	$1.305\,\mathrm{THz}$
a_{R}	$362.7\,\mathrm{GHz}$	$V_{\mathrm{g},1}$	$5.7737\,\mathrm{V}$
b_{L}	$218.9\,\mathrm{GHz}$	$V_{\mathrm{g},2}$	$5.78875\,\mathrm{V}$
b_{R}	$218.9\,\mathrm{GHz}$		
Model parameters from mechanical resonance detection			
κ	$4.5462\cdot 10^3\,(\mathrm{Vs})^{-1}$	m	$3.086\cdot 10^{-21}\,\mathrm{kg}$
Ω_0	$-2.8192\cdot 10^6\,1/\mathrm{s}$	$\frac{\mathrm{d}C_{\mathrm{g}}}{\mathrm{d}z}$	$-2.357\,\mathrm{pF/m}$
C_Σ	$70.2685\,\mathrm{aF}$	$V_{\mathrm{g},1}^{\mathrm{mech.}}$	$5.77477\,\mathrm{V}$
Γ	$1.436\,\mathrm{THz}$	$V_{\mathrm{g},2}^{\mathrm{mech.}}$	$5.79422\,\mathrm{V}$

Table 5.7: Model and device parameters and for the calculations around valley $\langle N\rangle = 271$.

$\langle N\rangle = 271$	Gate shifts	
	exp.	fits
Left: $V_{\mathrm{g},1}^{\mathrm{mech.}} - V_{\mathrm{g},1}$	$1.5\,\mathrm{mV}$	$1.07\,\mathrm{mV}$
Right: $V_{\mathrm{g},2}^{\mathrm{mech.}} - V_{\mathrm{g},2}$	$5.2\,\mathrm{mV}$	$5.47\,\mathrm{mV}$

Table 5.8: Extracted and calculated gate shifts around $\langle N\rangle = 271$.

5.8 Temperature dependence of the Kondo peak

The mechanical charge detection experiment is carried out for several temperatures in order to examine the evolution of the resonance frequency due to the Kondo effect. In section 4.5, the critical temperature of the appearance of the Kondo effect for the $N = 271$ valley is calculated to be $T_\mathrm{K} = 1.1\,\mathrm{K}$. The measurement exhibits still two shifts at 1.7 K, see Figure 5.12(b). The temperature dependent evaluation as presented in section 4.6 gives a range in between 1 to 5 K. At 5 K, Coulomb oscillation are still present as can be seen in the $|I|\left(V_\mathrm{g}\right)$ trace but thermally broadened. This leads to oscillations from 0.96 to 1.2 nA. An analysis of the resonance frequency evolution is still possible even though the characteristic minima is not as clear as for low temperature.
Additional data sets are plotted and evaluated in Figure 5.13. The obvious drift of the gate axis makes assignment of N_el difficult. Since the temperature difference between Figure 5.12(b) and 5.13(a) is only 300 mK the shape of the current oscillations exhibiting a triple of peaks for $N = 270$, 271, 272, is used to define the numbers as indicated.
All extracted gate shifts are plotted as a function of temperature in Figure 5.14. The width of the error bars on the V_g axis is set equal to the step size for each measurement. A logarithmic fit, corresponding to [Wingreen and Meir, 1994], is adapted to the experimental data. It is plotted as red lines in both diagrams, for left and right shifts.

Having in mind that the detection mechanism by mechanical resonance is not affected by higher-order effects as co-tunneling or Kondo effect, a localization of single-electron transitions with respect to V_g is possible by the minima of the $\tilde{\omega}_0\left(V_\mathrm{g}\right)$ dependence. In contrast, the transport through the dot is affected by the Kondo effect leading to shifted extrema in the current, see [Goldhaber-Gordon et al., 1998a; Kretinin et al., 2012] as well as the transport measurements as presented in section 4.6. By increasing temperature, i. e. exceeding the Kondo temperature and reaching the temperature-broadened transport regime - see case (II) in Table 2.2 - the gate shift between $\tilde{\omega}_0$ minima and $I\left(V_\mathrm{g}\right)$ maxima of the Coulomb oscillation of each N_el valley disappears. This observation confirms the exclusive dependence of $\tilde{\omega}_0\left(V_\mathrm{g}\right)$ on the change of the average charge, $\partial\langle N\rangle/\partial V_\mathrm{g}$, due to single-electron tunneling. The presented evaluation on these observations is in analogy to recent publications, see [Desjardins et al., 2017].

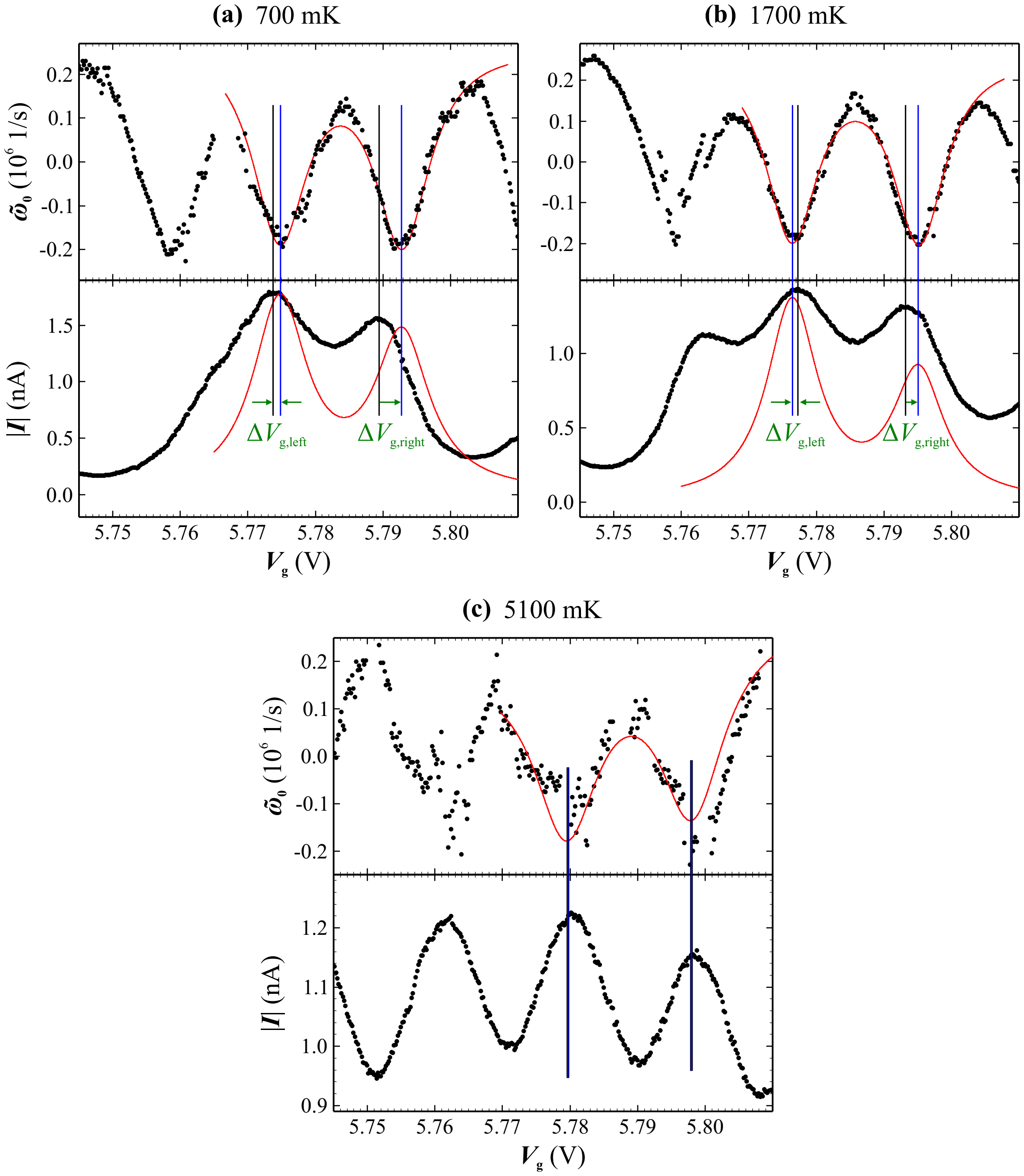

Figure 5.12: Evolution of the relative gate shifts around $\langle N \rangle = 271$ as a function of temperature. The experimental parameters are chosen equal to the measurement presented in Figure 5.10 for better comparison: **(a)** at 700 mK, **(b)** at 1700 mK, and **(c)** at 5100 mK. The corresponding fits are included as red lines. The experimentally extracted shifts between current maxima and reduced resonance frequency minima are confined within bars, black for the current $|I|$ maximum and blue for $\tilde{\omega}_0$ minimum.

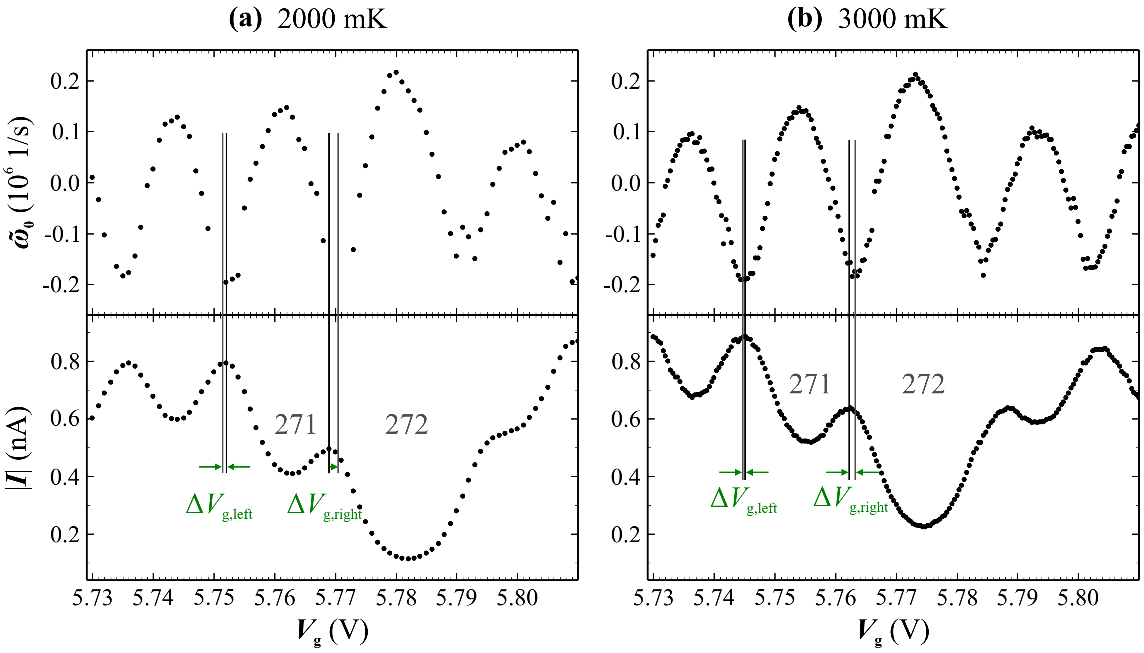

Figure 5.13: Comparison of current and mechanical resonance evolution, regarding gate shifts in between $|I|$ maximum and $\tilde{\omega}_0$ minimum. Due to an overall gate drift, the extrema are found at lower V_g values. Both measurements were performed about one month later compared to those evaluated in Figure 5.12. **(a)** 2000 mK, with step sizes of 4 kHz, respectively 1 mV. **(b)** 3000 mK with step sizes of 1.5 kHz, respectively 0.4 mV.

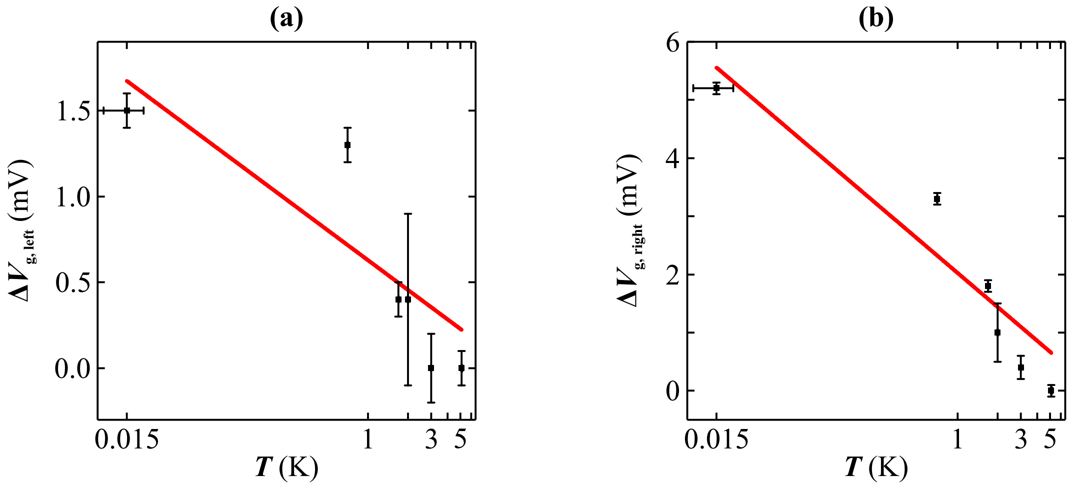

Figure 5.14: Evolution of the extracted shifts from Figures 5.12 and 5.13 between $|I|$ maximum and $\tilde{\omega}_0$ minimum with temperature. The data points are fitted to the relation $\Delta V_g \propto \log\left(10^{\mathfrak{a}} \cdot T^{\mathfrak{b}}\right)$. **(a)** $\Delta V_{g,left}$ using $\mathfrak{a} = 0.00234\,\mathrm{V}$ and $\mathfrak{b} = -0.00057\,\mathrm{V}/\log(\mathrm{mK})$ as parameters. **(b)** $\Delta V_{g,right}$ using $\mathfrak{a} = 0.00783\,\mathrm{V}$ and $\mathfrak{b} = -0.00194\,\mathrm{V}/\log(\mathrm{mK})$ as parameters.

Chapter 6

Optimization of molybdenum rhenium alloys

Large parts of this chapter have already been published as [Götz et al., 2016] and are reprinted with permission by © IOP Publishing Limited. Alloys of rhenium and molybdenum have been shown to exhibit superconducting transition temperatures up to 15 K [Testardi et al., 1971; Gavaler et al., 1972; Postnikov et al., 1977]. Rhenium and molybdenum rhenium alloy thin films remain stable under carbon nanotube CVD growth conditions and subsequently still exhibit superconducting behavior [Schneider, 2014]. In addition, after in-situ growth they provide transparent electronic contacts to carbon nanotubes [Schneider et al., 2012; Stiller et al., 2013; Schmid et al., 2015a].

In this chapter, molybdenum rhenium alloy films are characterized with respect to their composition and their transport properties at low temperature. In the first section, alloy thin films deposited via simultaneous sputtering from two sources, i. e., co-sputtering are examined and evaluated. Specific emphasis is placed on the effect of the carbon nanotube growth conditions on the film. Starting point is the experience of previous work in our group [Schupp, 2014]. The applied co-sputtering technique to obtain $\mathrm{Mo_{1\text{-}x}Re_x}$ alloy thin films is depicted and described in section A.6.

Based on these findings, two premixed MoRe targets have been acquired. Fabricated films have been undergone the same characterization procedure as for the co-sputtered samples. The results are written down in the second section of this chapter.

In order to obtain the alloy composition, X-ray photoelectron spectroscopy (XPS) is performed on the co-sputtered as well as single-sputtered films [Talvacchio et al., 1986; Seleznev et al., 2008]. Within a predefined area of four to ten square millimeters the samples are irradiated by a monochromatic X-ray source, and the resulting emitted photoelectrons are collected and spectroscopically analyzed with respect to energy and intensity. The chemical sensitivity is given by the element-specific distribution of binding energies E_B

of the electronic core levels, [Kronseder, 2015].

Hall bar structures are patterned on the films using RIE, see section A.8. After bonding to standard chip carriers, low temperature experiments are performed using a ^{4}He-can, and a ^{3}He-cryostat, for testing superconducting transport properties such as critical temperature T_c, critical current density j_c, and the corresponding temperature dependence. The utilized measurement setups are similar to those depicted in Figure 3.9 and described in subsection 3.5.3.

6.1 Co-sputtered MoRe films

6.1.1 Resulting alloys

Characteristic XPS data of a co-sputtered film are plotted in Figure 6.1(a). The signal peaks corresponding to atomic and molecular core levels have been identified following [Moulder et al., 1992]. The black curve in Figure 6.1(a) reveals the chemical composition of the topmost surface layers. In addition to characteristic peaks originating from molybdenum and rhenium core levels, also significant oxygen and carbon peaks are observed. This is likely due to the fact that all samples have been exposed to air during transfer from the sputtering device into the UHV chamber of the XPS setup.

Adsorbates and the film itself can be etched by in-situ Ar-sputtering in the XPS chamber for obtaining spectra from lower layers. An etching step lasts several minutes at a chamber pressure of less than $3 \cdot 10^{-8}$ mbar (the base pressure is $5 \cdot 10^{-10}$ mbar). Etching steps are repeated until the oxygen 1s-peak only negligibly contributes to the whole spectrum (at most about 10 %). The red line in Figure 6.1(a) displays the resulting spectrum. Note that also the carbon peak is now strongly suppressed. Subsequent tests using a profilometer show that approximately 5 nm of the films were removed. All spectra obtained after such a corresponding etching step are henceforth denoted as "bulk" spectra.

Figure 6.1(b) and 6.1(c) display details of the spectrum close to the Mo 3d- and Re 4f-peaks, referenced to the C 1s-peak [Seleznev et al., 2008]. The additional structure in the Mo 3d surface spectrum originates from MoO_3 and MoO_2 forming at the alloy surface [Scanlon et al., 2010; Talvacchio et al., 1986]. It decreases during etching until disappearing in the bulk where only the two Mo $3d_{5/2}$- and Mo $3d_{3/2}$-peaks are part of the spectrum. In contrast, at the Re 4f-peak neither changes in the line shape nor peak shifts are observed in the surface compared to the bulk spectrum, indicating the absence of rhenium oxides at the surface and in the bulk layers. All films examined in this thesis exhibit the same behavior for the rhenium peaks [Talvacchio et al., 1986; Seleznev et al., 2008].

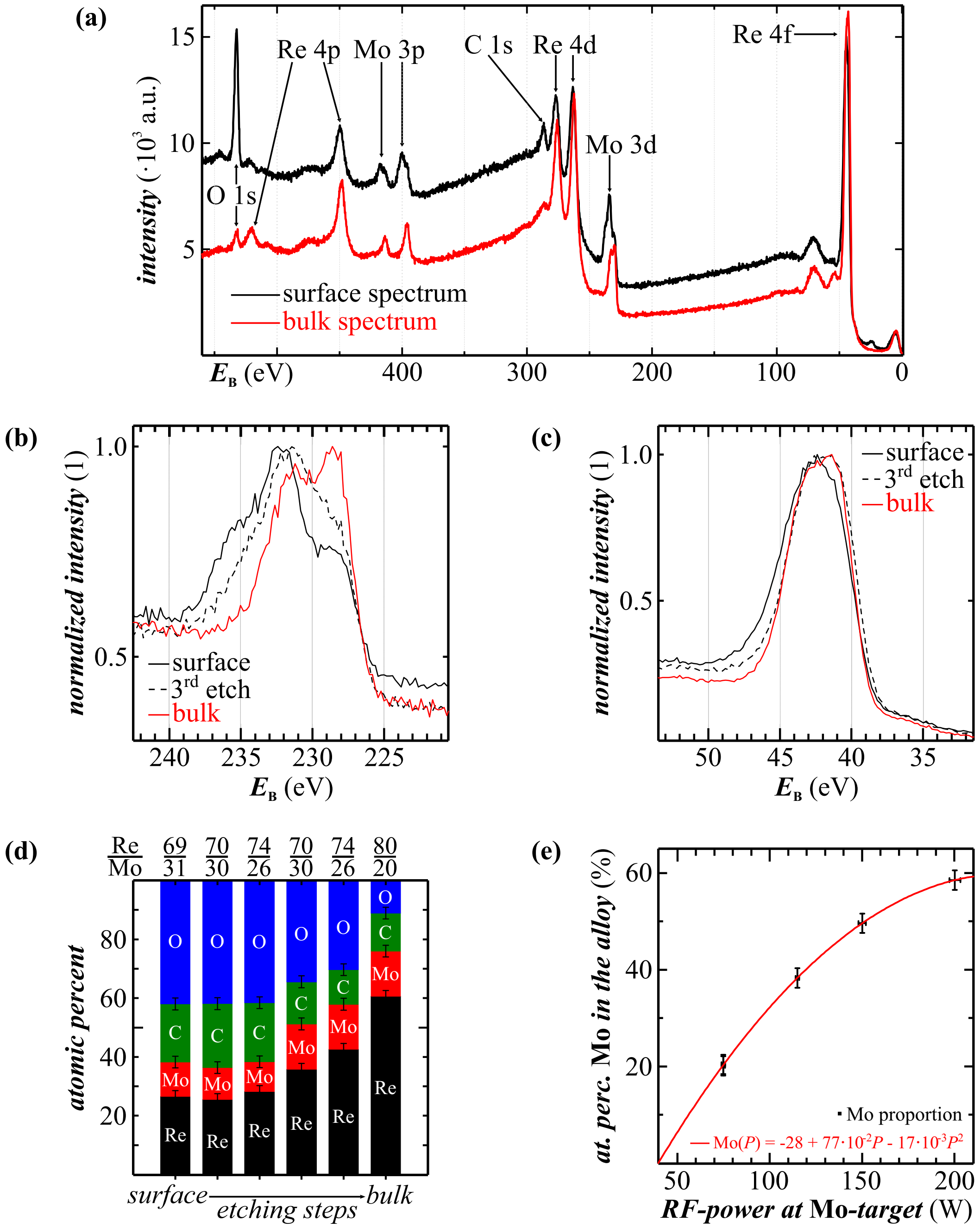

Figure 6.1: **(a)** XPS spectrum of a deposited, unstructured film on a p^{++}-Si/SiO$_2$ substrate. A power setting of $P_{\mathrm{Mo}} = 75\,\mathrm{W}$ at the molybdenum source was used. The black line represents the chemical composition of the as-grown sample surface, the red line was recorded after removing approximately 5 nm of the film by in-situ argon-ion beam sputtering within the XPS chamber. **(b)**, **(c)** Normalized detail spectra close to the Mo 3d-peaks **(b)** and the Re 4f-peaks **(c)** (see text). The energetic step size is set to 0.2 eV. **(d)** Depth profile of the atomic composition, calculated from XPS spectra as in (a), from surface to $\sim 5\,\mathrm{nm}$ depth (subsequently named bulk). The resulting MoRe-alloy composition after each step is stated above. **(e)** Relative molybdenum atomic percentage in the bulk film for different power settings P_{Mo} at the molybdenum target (see text). From [Götz et al., 2016], © IOP Publishing Limited 2016, reprinted with permission.

All rhenium peaks of the film are shifted by 1.3 eV to higher E_B-values, compared to the literature values of pure rhenium. Similar values have been identified in [Seleznev et al., 2008] as chemical shift due to the Mo-Re compound formation.
Using the method of area sensitivity factors and evaluating the Mo 3d-, Re 4f-, C 1s-, and O 1s-peaks, the atomic concentrations of the sample have been estimated [Moulder et al., 1992]. Figure 6.1(d) displays the atomic concentrations as a function of depth. While the exposure to air leads to significant carbon and oxygen percentages at the surfaces, these both decrease strongly; for the "bulk" spectrum about 10 % of carbon remains.
Subsequently the molybdenum-rhenium alloy ratio is obtained by normalizing to the sum of both sputtered metals. The resulting alloy ratios of all co-sputtered films vary as a function of depth, see Figure 6.1(d). This is in agreement with observations in [Seleznev et al., 2008] and explained there by diffusion of molybdenum atoms from the bulk to the surface in order to form stable molybdenum oxides, and corresponding enrichment of rhenium atoms in the film interior.
As can be clearly seen in Figure 6.1(e), where the resulting alloy ratio in the bulk film is plotted as a function of rf power P_Mo applied to the molybdenum sputter source, the resulting molybdenum contribution in the alloy can be controlled over a wide range. The solid line in Figure 6.1(e) is a quadratic fit to the data points.

6.1.2 Influence of CNT growth environment

Chips including MoRe thin films are exposed to the growth process typically used to locally grow few clean single-wall carbon nanotubes [Kong et al., 1998b]. The procedure is already described in subsection 3.2.2, and documented step by step in section A.11 of the appendix.
The XPS spectrum of a molybdenum rhenium alloy sputtered with $P_\mathrm{Mo} = 75\,\mathrm{W}$ after exposure to the CVD environment is shown in Figure 6.2(a), and a normalized detail plot of the Mo 3d peak in Figure 6.2(b). A strong carbon peak is visible even in the bulk. Furthermore in both surface and bulk molybdenum spectra oxide peaks are not observed, as visible in Figure 6.1(b).
Having in mind that molybdenum oxides exhibit drastically lower melting points of 795 °C for $\mathrm{MoO_3}$ and 1100 °C for $\mathrm{MoO_2}$ [Wiberg et al., 1995] than pure molybdenum with 2610 °C [Stoecker and Hartnack, 2007], the data indicates that reduction of the oxide to atomic molybdenum takes place during CVD. An additionally possible process is the formation of molybdenum carbides. The expected XPS peak of $\mathrm{Mo_2C}$ ($E_\mathrm{B} = 227.75\,\mathrm{eV}$) is very close to that of Mo $3d_{5/2}$ ($E_\mathrm{B} = 228\,\mathrm{eV}$), which makes detection challenging with our experimental resolution.

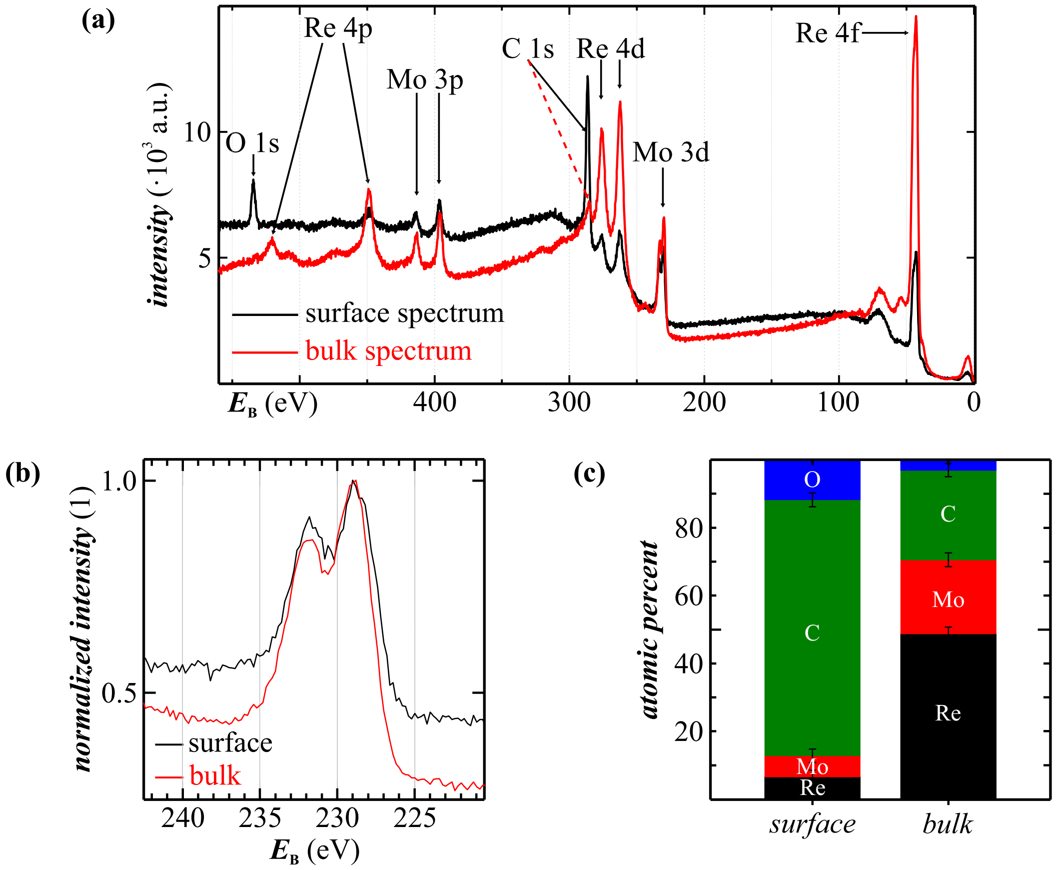

Figure 6.2: **(a)** XPS spectrum of a molybdenum rhenium film sputtered at $P_{\mathrm{Mo}} = 75\,\mathrm{W}$, after being exposed to 30 min carbon nanotube CVD growth environment at 850 °C. The energy step size is 0.2 eV. **(b)** Detail zoom of the Mo 3d peak. **(c)** Composition of the film at the surface and at ∼ 5 nm depth (atomic percentage); note the large carbon contribution. From [Götz et al., 2016], © IOP Publishing Limited 2016, reprinted with permission.

Interestingly, molybdenum carbides display superconductivity with critical temperatures $6\,\mathrm{K} \lesssim T_c \lesssim 9\,\mathrm{K}$. However, typically the growth of molybdenum carbide out of pure molybdenum, for example in a nitrogen-xylene atmosphere, takes place at temperatures higher than 850 °C, see [Morton et al., 1971].

The area sensitivity factor analyzing method results in a bulk composition of 26 % carbon, 22 % molybdenum, and 49 % rhenium plus negligible oxygen residues. Since the etching time for the bulk spectra has been kept constant, it is obvious that the high carbon contribution does not have its origin in atmospheric adsorbates but in diffusion of carbon into the alloy during CVD. The relative bulk atomic ratio of the sputtered metals is $\mathrm{Mo}_{31}\mathrm{Re}_{69}$, indicating structural changes during CVD. In particular, the high temperature may lead to vertical segregation processes similar to those described in the previous section, but over a larger depth range.

Spectroscopy on a second sample using twice the gas flow of methane results in a composition of 12 % molybdenum, 23 % rhenium, and even 58 % carbon in the bulk. From this we conclude that the penetration of carbon into the alloy also increases. However, the resulting sputtered metal ratio of $\mathrm{Mo}_{34}\mathrm{Re}_{66}$ still remains close to the previous sample.

6.1.3 dc characterization

To characterize the electronic properties of the co-sputtered films at room temperature as well as at cryogenic temperatures, the fabricated thin films on top of SiO_2 or $\mathrm{Al}_2\mathrm{O}_3$ substrates are patterned into Hall bars by means of optical lithography and $\mathrm{SF}_6/\mathrm{Ar}$ reactive ion etching (see Figure 6.3(a)). Afterwards, selected structures are placed into the CVD furnace and exposed to the nanotube growth environment for several minutes. All measurements have been performed on films either examined by XPS or deposited simultaneously to these in the same deposition step. Devices using two different alloy compositions have been examined, namely $\mathrm{Mo}_{20}\mathrm{Re}_{80}$ and $\mathrm{Mo}_{58}\mathrm{Re}_{42}$ obtained with $P_{\mathrm{Mo}} = 75\,\mathrm{W}$ and $P_{\mathrm{Mo}} = 200\,\mathrm{W}$, respectively.

At room temperature, compared to $\mathrm{Mo}_{58}\mathrm{Re}_{42}$ both resistivity and sheet resistance of the $\mathrm{Mo}_{20}\mathrm{Re}_{80}$ samples are higher by a factor 3–5: before CVD we obtain $\rho \simeq 3.0 \cdot 10^{-7}\,\Omega\mathrm{m}$ for $\mathrm{Mo}_{58}\mathrm{Re}_{42}$ and $\rho \simeq 9.0 \cdot 10^{-7}\,\Omega\mathrm{m}$ for $\mathrm{Mo}_{20}\mathrm{Re}_{80}$. Resistances slightly increase during exposition to the CVD environment, to $\rho \simeq 4.0 \cdot 10^{-7}\,\Omega\mathrm{m}$ for $\mathrm{Mo}_{58}\mathrm{Re}_{42}$ and $13 \cdot 10^{-7}\,\Omega\mathrm{m} \lesssim \rho \lesssim 15 \cdot 10^{-7}\,\Omega\mathrm{m}$ for $\mathrm{Mo}_{20}\mathrm{Re}_{80}$.

Results of low-temperature measurements performed on $\mathrm{Mo}_{20}\mathrm{Re}_{80}$ devices are plotted in Figure 6.3(b) and Figure 6.3(c). Independent from CVD-exposure, the residual-rest-resistance values *RRR* for all $\mathrm{Mo}_{20}\mathrm{Re}_{80}$ devices are in the range $0.8 \lesssim RRR \lesssim 1.0$. Figure 6.3(b) displays the critical current of a $\mathrm{Mo}_{20}\mathrm{Re}_{80}$ film (Hall bar geometry B, with $T_c = 9.2\,\mathrm{K}$) after 10 min CVD exposure. It carries a supercurrent up to $I_c \gtrsim 80\,\mathrm{mA}$, corresponding to a critical current density of $j_c \gtrsim 2.7 \cdot 10^5\,\mathrm{A/mm}^2$, over a wide temperature range up to circa 5 K before the transition to a normal conductor takes place above 8 K. This very high value for j_c is well in accordance with the results of [Aziz et al., 2014], where after high-temperature annealing critical current densities of up to $1.8 \cdot 10^5\,\mathrm{A/mm}^2$ through suspended $\mathrm{Mo}_{50}\mathrm{Re}_{50}$-nanostructures were reported.

A second $\mathrm{Mo}_{20}\mathrm{Re}_{80}$ Hall bar device (type A, $T_c = 8.3\,\mathrm{K}$), not exposed to CVD, exhibits a critical current $I_c \approx 114\,\mathrm{mA}$ at $T = 4.2\,\mathrm{K}$, corresponding to a lower current density $j_c = 2.8 \cdot 10^4\,\mathrm{A/mm}^2$. Also much longer exposure to the CVD environment again lowers the reachable critical current density.

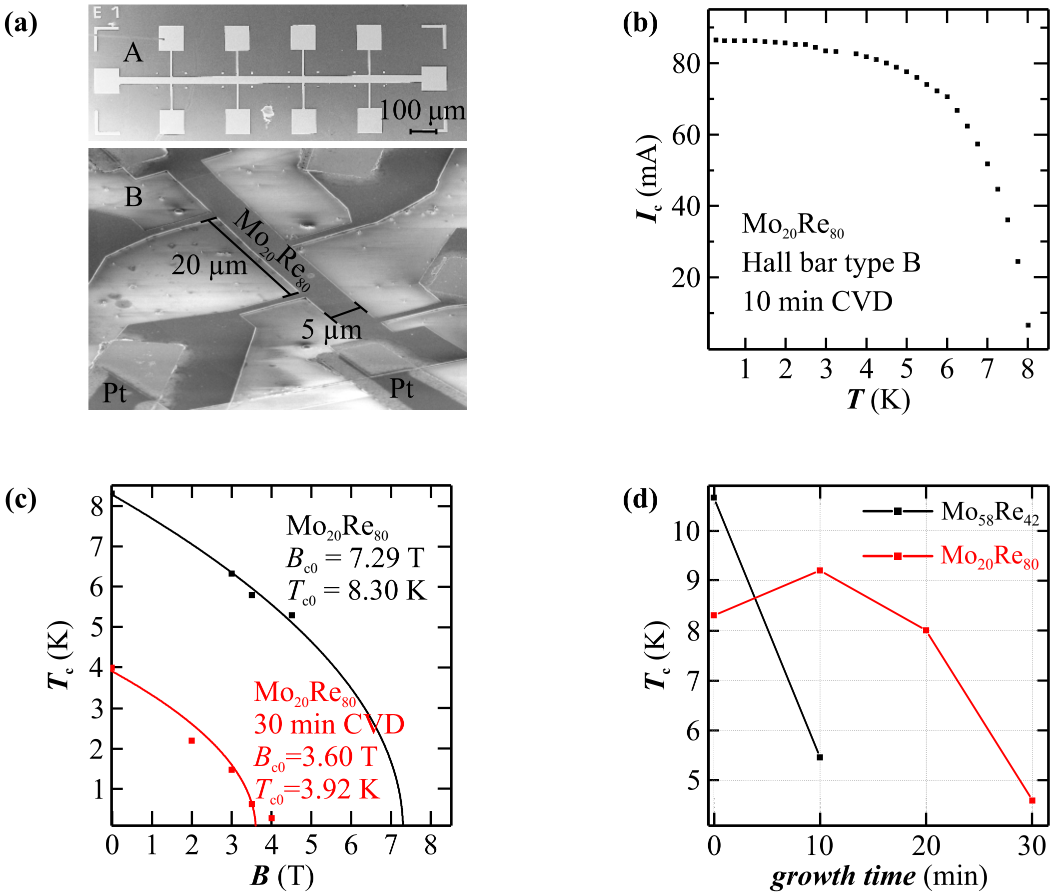

Figure 6.3: dc characterization of co-sputtered MoRe. **(a)** Exemplary SEM micrographs of test Hall bar structures, denoted as type A and B. Dimensions are for type A width $W_A = 28\,\mu m$ and film thickness $d_A \approx 150\,nm$, for type B $W_B = 5\,\mu m$ and $d_B \approx 60\,nm$. **(b)** Measured critical current I_c through a Hall bar device (type B), $Mo_{20}Re_{80}$, as a function of temperature. **(c)** Critical temperature T_c of $Mo_{20}Re_{80}$ films as a function of applied magnetic field B, with and without CVD growth exposure. **(d)** Measured critical temperature T_c as a function of CH_4/H_2 flow time ("growth time") during the CVD process. Straight lines are guides to the eye. From [Götz et al., 2016], © IOP Publishing Limited 2016, reprinted with permission.

Figure 6.3(c) displays data on the magnetic field dependence of the critical temperature. Fitting the empirical relation $B_c(T) = B_{c0} \cdot \left(1 - (T/T_{c0})^2\right)$ [Tinkham and McKay, 1996] results in high characteristic values $B_{c0} = 7.3\,T$ and $T_{c0} = 8.3\,K$ expected for molybdenum rhenium alloys, where T_{c0} denotes the zero field critical temperature and B_{c0} the extrapolated critical field at zero temperature.

Again, as observed for critical currents, prolonged (30 min) CVD exposure results in a strong decrease of both values to here $B_{c0} = 3.6\,T$ and $T_{c0} = 3.9\,K$ [Singh et al., 2014; Aziz et al., 2014]. This effect is also visible in Figure 6.3(d), displaying the critical temperature for two different alloy compositions as function of growth time. Even for only 10 minutes growth time, T_c of the $Mo_{58}Re_{42}$ film decreases to the half, well in accordance with the results of [Singh et al., 2014]. Interestingly, in contrast the $Mo_{20}Re_{80}$ alloy keeps its critical temperature range of $8\,K \leq T_c \leq 9\,K$ for growth times up to 20 minutes, only reaching $< 5\,K$ after 30 minutes of exposure to the CH_4/H_2 flow.

6.2 MoRe films of premixed targets

XPS is carried out in one step on four different $4\,mm \cdot 4\,mm$ p^{++}-Si/SiO_2 chips fully covered by MoRe films of 50 nm thickness. The films are fabricated by dc sputtering of premixed $Mo_{70}Re_{30}$, respectively $Mo_{30}Re_{70}$ targets in the Orion setup, see subsection A.6 for fabrication details. Two chips containing either the molybdenum- or the rhenium-rich films were subsequently exposed to CNT growth environment for 15 min during the standard CVD process, see subsection A.11.

6.2.1 XPS properties of the pristine films

The absolute atomic concentrations resulting from each spectrum is once again estimated using the method of area sensitivity factors with consideration of the Mo 3d-, Re 4f-, C 1s-, and O 1s-peaks [Moulder et al., 1992]. In the next step, the relative atomic ratios of both molybdenum and rhenium are calculated dividing the each single element concentration by the sum of both elements which is the complete alloy.

Figures 6.4(a) and (b) display atomic ratios of both examined pristine alloys. In Figure 6.4(a) the relative contributions are plotted as a function of depth: the values obtained from the surface spectrum are denoted as "*surface*", and the subsequent ones estimated from spectra which were recorded after a certain etching step are indexed from 1 to 8. For a better comparison, all films have been etched under the same settings to the in-situ dc argon sputtering source, this is 1.4 kV acceleration voltage at an emission current of 25 mA, and 5.5 mm · 5.5 mm raster size.

It turns out for both alloys that molybdenum enriches at the surface whereas it is depleted step by step in the bulk. In contrast, rhenium gradually enriches in deeper layers of the alloys. The vertical segregation is hence also observed as for the co-sputtered films and the samples examined in [Seleznev et al., 2008]. The results from the spectra recorded after etching step 4 can be compared to the bulk values for co-sputtered films as stated in Figure 6.1(d) and (e). Therefore, the relative atomic bulk ratios as stated in Figure 6.4(b) are taken from this etching step.

(a)

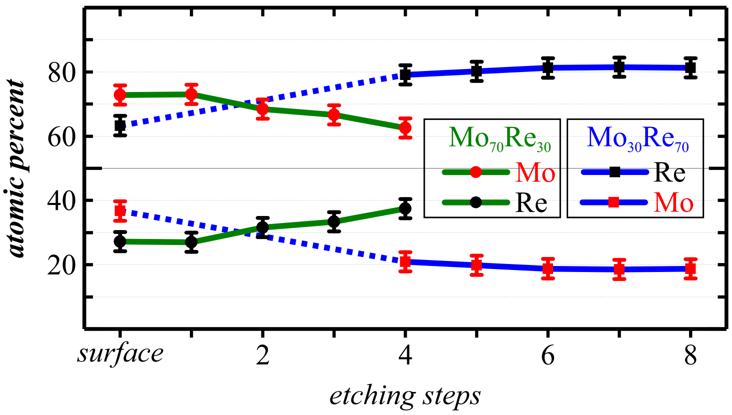

(b)

Mo : Re (at. %)	**compositions from XPS**	
nominally	surface	bulk
30 : 70	**37 : 63**	**20 : 80**
70 : 30	**73 : 27**	**63 : 37**

Figure 6.4: Relative atomic ratios of both alloys from XPS spectroscopy, including depth profiles. **(a)** Atomic percentages of Mo and Re in the alloy starting from the surface and continued into deeper layers. Note that the etching steps are not equidistant in time: after surface examination, the next three spectra for $Mo_{70}Re_{30}$ were taken after 1 min of etching each. The spectra at the fourth step were taken after 5 min etching time in total, the subsequent spectra for $Mo_{30}Re_{70}$ after 7, 10, 15, respectively 35 min of etching time in total. **(b)** Overview of nominal and measured alloy compositions. The composition after etching step 4 is denoted as "bulk".

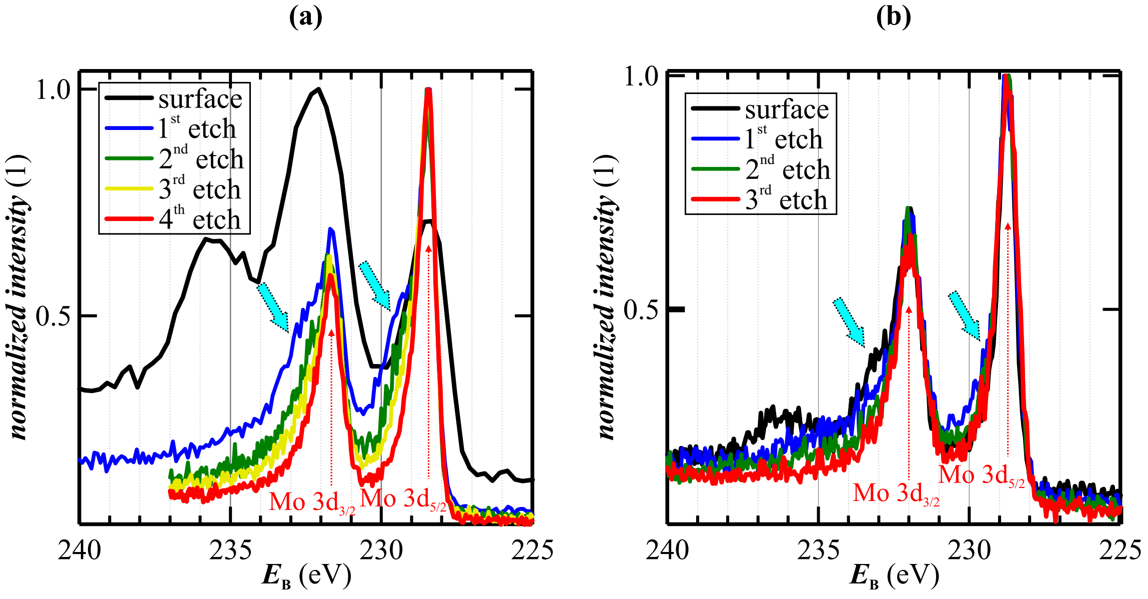

Figure 6.5: Normalized detail XPS spectra of $Mo_{70}Re_{30}$ films around Mo 3d. The etching step sequence is equal for both diagrams. **(a)** Pristine alloy as in Figure 6.4. **(b)** After 15 min CVD growth time. The spectra are recorded using an energetic step size of 0.05 eV, with exception of the surface spectrum in **(a)** (black line), using 0.2 eV, which is a zoom of a large-range spectrum as plotted in Figures 6.1(a) and 6.2(a). The pristine Mo $3d_{3/2}$ and Mo $3d_{5/2}$ peaks are indicated.

Furthermore, the trend of the atomic ratio is evaluated for the rhenium-rich alloy of the $Mo_{30}Re_{70}$ premixed target. As can be seen, the atomic alloy ratio stays stable at Mo-20 %Re-80 % even after the last etching step with a total etching time of 35 min. In contrast, the molybdenum-rich film compositions at the surface is slightly closer to the nominal value of the $Mo_{70}Re_{30}$ target. Within the error range of the present XPS analysis of 3 %, both bulk compositions distinctly deviate from the nominal values of the premixed targets by 7 %, respectively 10 %. It can be concluded that the alloy sputter targets de facto exhibit an atomic ratio of $Mo_{63}Re_{37}$ and $Mo_{20}Re_{80}$ instead of $Mo_{70}Re_{30}$ and $Mo_{30}Re_{70}$.

In order to obtain knowledge about surface oxidation, a detailed glance is thrown at the Mo 3d-peak of the molybdenum-rich alloy as can be seen in Figure 6.5(a): the normalized spectra exhibit the characteristic three-peak shape at the surface. This pattern is according to [Baltrusaitis et al., 2015; Scanlon et al., 2010] a result of three molybdenum oxide species, namely MoO_2, MoO_3, and Mo_2O_5. After the first etching step, the peak at $E_B \simeq 236\,\text{eV}$ is completely gone indicating that at least one species only arises at the surface. Comparing the subsequent spectra in the bulk, the peaks become sharper. The maxima at $E_B = (231.70 \pm 0.05)$ eV and $E_B = (228.45 \pm 0.05)$ eV are attributed to the Mo $3d_{3/2}$ and Mo $3d_{5/2}$ orbitals. These results are in well agreement with literature [Moulder et al., 1992; Seleznev et al., 2008], indicating that the alloy compound formation has less influence on the XPS spectrum for the premixed targets. Since the peaks do not shift within the error range with respect to the E_B axis, additional oxide species almost do not contribute to the spectra even after the first etching step. Since the shape of both peaks does not distinctly change anymore between step 2 and 4, all molybdenum oxides are removed not later than after step 4.

For completeness, the Re 4f-peak splits into Re $4f_{5/2}$ and Re $4f_{7/2}$ orbital peaks but without any additional recorded structure which may be attributed to rhenium oxide species, see also Figure 6.1(d).

6.2.2 CVD influence on the film properties

The oxide evolution of a molybdenum-rich alloy film exposed to the CNT growth environment can be tracked in Figure 6.5(b): a residuum of the third peak at 236 eV is detected at the surface spectrum, and the two peaks do not change in shape and location of maxima anymore. These are located at $E_B = (232.00 \pm 0.05)$ eV and $E_B = (228.80 \pm 0.05)$ eV and attributed to pristine Mo $3d_{3/2}$ and Mo $3d_{5/2}$ orbitals. The observed surface oxide reduction as for co-sputtered films, see Figure 6.2(b), hence takes also place for premixed target films but less pronounced.

(a)

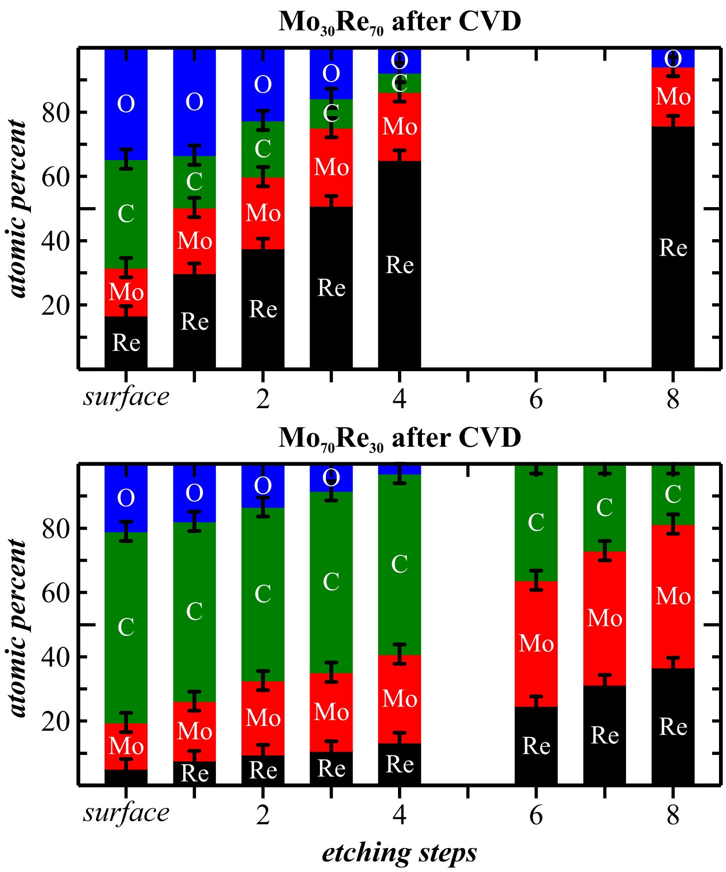

(b)

Mo : Re (at. %)	**XPS compositions after CVD**	
nominally	surface	bulk
30 : 70	**47 : 53**	**20 : 80**
70 : 30	**73 : 27**	**55 : 45**

Figure 6.6: Influence of CNT growth environment to $Mo_{70}Re_{30}$ and $Mo_{30}Re_{70}$ films. The films were exposed to the same simulated standard CVD process of 15 min growth time. **(a)** Depth profile of the atomic composition beginning from the surface, via 5 min total etching time at step 4, and ending after circa 40 min total etching time at step 8. **(b)** Overview of nominal and measured alloy compositions after CVD of $Mo_{70}Re_{30}$ and $Mo_{30}Re_{70}$. The composition after etching step 8 is used as "bulk" value.

The melting points of MoO_3, and Mo_2O_5, [Wiberg et al., 1995], range distinctly below CNT growth temperature of 850 °C. This is the reason why surface oxide reduction preferably removes these species and therefore, by comparison with pristine alloys, the third peak can be attributed to them. In addition, the "shoulders" which can be tracked at the remaining two peaks are attributed to MoO_2 species on both diagrams in Figure 6.5 (see cyan colored arrows). In addition, this pattern is completely gone after the second etching step in the film undergone CVD process.

Figure 6.6 displays the influence of CNT growth environment on the sputtered alloys of both premixed targets. Figure 6.6(a) plots the depth profile of the absolute film composition and Figure 6.6(b) the resulting relative atomic concentrations in the alloy. Clearly the rhenium-rich film is much less sensitive to carbon diffusion: here carbon does not contribute to the spectrum at all after etching step 4, whereas for nominal-$Mo_{70}Re_{30}$, circa 20 % of the film consists of carbon still after the last etching step. Structural changes originating from CVD process also affect the molybdenum-rich film stronger than the rhenium-rich one in the bulk. Even though the last etching step was used for molybdenum-rich film bulk values in Figure 6.6(b), the atomic composition changes by 8 % with respect to the pristine determination of $Mo_{63}Re_{37}$. Taking the same etching step 4 for comparison, this structural composition shift reduces to 4 % but resulting in more molybdenum in the alloy as for the pristine alloy. In contrast, the rhenium-rich alloy of $Mo_{20}Re_{80}$ pristine composition stays stable, respectively exhibits a composition of Mo-25 %Re-75 % after etching step 4.

Finally, structural changes due to chemical reduction reactions at the surface, vertical segregation of molybdenum as well as heating affect both alloys, but in the bulk the same composition as for the pristine film can be only found for $Mo_{20}Re_{80}$. The molybdenum-rich film supports the enrichment of molybdenum atoms to the upmost layers of the film filling the place of the removed oxides. This also changes the atomic alloy composition below the surface; note that the surface composition for molybdenum-rich films is constant. Then, during the CNT growth sequence, carbon can diffuse deeply into the bulk because there is more place for it than in the rhenium-rich film.

6.2.3 dc characterization

The dc measurements for devices from the premixed targets have been evaluated precisely in [Hüttner, 2017]. In short, MoRe of both targets is sputtered onto the same substrates as for the XPS experiments. The on-chip material is patterned by optical lithography, leading to 50 nm thick Hall bars of type A, as can be seen in Figure 6.3(a). For completeness, some transport properties are stated here. The room temperature resistivity for $Mo_{20}Re_{80}$ increases slightly from $5.62 \cdot 10^{-7}\,\Omega\text{m}$ to $6.92 \cdot 10^{-7}\,\Omega\text{m}$ due to CVD growth environment. The room temperature resistivity for $Mo_{63}Re_{37}$ samples is in the same range. Residual rest resistances *RRR* range in between 1 and 1.5. The superconducting critical temperature of all samples ranges in between 7.3 to 8.3 K. The CVD process with 15 min growth time has almost no influence on T_c, which is distinctly different to the co-sputtered molybdenum-rich alloy. The critical current density at 4 K is above $2.0 \cdot 10^4\,\text{A/mm}^2$, comparable to the co-sputtered devices.

Chapter 7

Low temperature transport in suspended carbon nanotubes on molybdenum rhenium contacts

Millikelvin temperature measurements of CNTs suspended on MoRe contacts are evaluated within this chapter. Experience with these superconductors obtained during the measurements of chapter 6 led to the decision to use the rhenium-rich alloys as electrode material: on the one hand, co-sputtered $Mo_{20}Re_{80}$ exhibits a higher resilience during the overgrowth process, and on the other hand $Mo_{20}Re_{80}$ films originating from the premixed target are less sensitive to carbon diffusion during CVD. Furthermore, rhenium-rich alloys of both sputtering techniques remain structurally stable after the growth process. During fabrication, see chapter 3, only the "inner structures", i. e. the contacts and leads close to the nanotube, consist of molybdenum rhenium alloys. It turns out that the first liftoff-recipe, where metallization is done using one EBL step, is sufficient for structures of premixed targets whereas the second recipe with the help of two EBL steps is needed for co-sputtered ones in order to realize flat electrode surfaces, see Figure 3.2(b).
Low temperature measurements are carried out in the dilution cryostat described in section 3.4. In contrast to the measurements of chapter 4, the dc cable filtering was improved by the RC filter stage, as shown in Figure 3.7(b). Copper powder filters filtering noise in the high GHz range are not used compared to previous works [Keijzers, 2012; Schneider, 2014] measuring supercurrents through CNTs at low temperatures.

7.1 Co-sputtered MoRe-CNT device

Fabrication details of this device are stated in section B.2 in appendix B. Metallization processes follow the principles described in chapter 3, and the mask depicted in panel 2 of Figure 3.2(a) is used for the electrode structure. It consists of 57 nm co-sputtered MoRe, and the electrode stripes of 1.5 µm width are separated by a trench of 500 nm width. The on-chip CNT growth was carried out at standard conditions at a duration of 20 min, see section A.11. At the probe station, the device "32 up" exhibited a room-temperature gate characteristic as plotted in the diagram in Figure 3.4(b). A SEM micrograph of the device, recorded after measurements, can be found in Figure 3.3(a), panel 2.
After bonding and insertion into the cryostat insert, one contact, namely #4, exhibited a shortcut to ground, see bond plan in Figure B.2. Consequently, another setup for voltage-biased measurements was used, see Figure 7.1, for which pin #4 serves as grounded source.

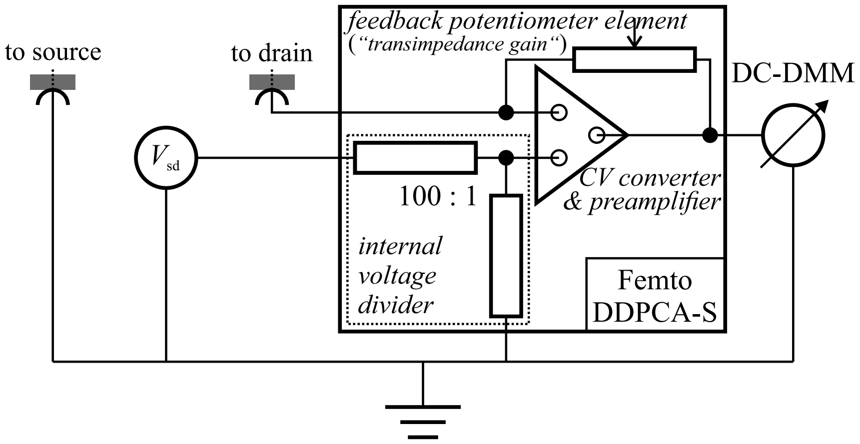

Figure 7.1: Femto transimpedance amplifier for voltage-bias measurements with grounded source. This is alternative to the commonly used voltage-bias measurement as depicted in Figure 3.8.

7.1.1 Characterization at base temperature

Figure 7.2(a) depicts $G(V_g)$ characteristics spanning two example ranges around a low conductance region. This supposed band gap is situated approximately at $2\,\text{V} \leq V_g \leq 2.5\,\text{V}$, see diagram below. For $V_g < 2\,\text{V}$, Coulomb oscillations are observed exhibiting peak values at about $3.5\,e^2/h$. This indicates the presence of a highly transparent system. However, an unambiguous Fabry-Pérot transport regime is absent; this statement can be confirmed by the large difference between conductance peaks and neighboring conductance minima. Some of these range even close to $0\,e^2/h$.

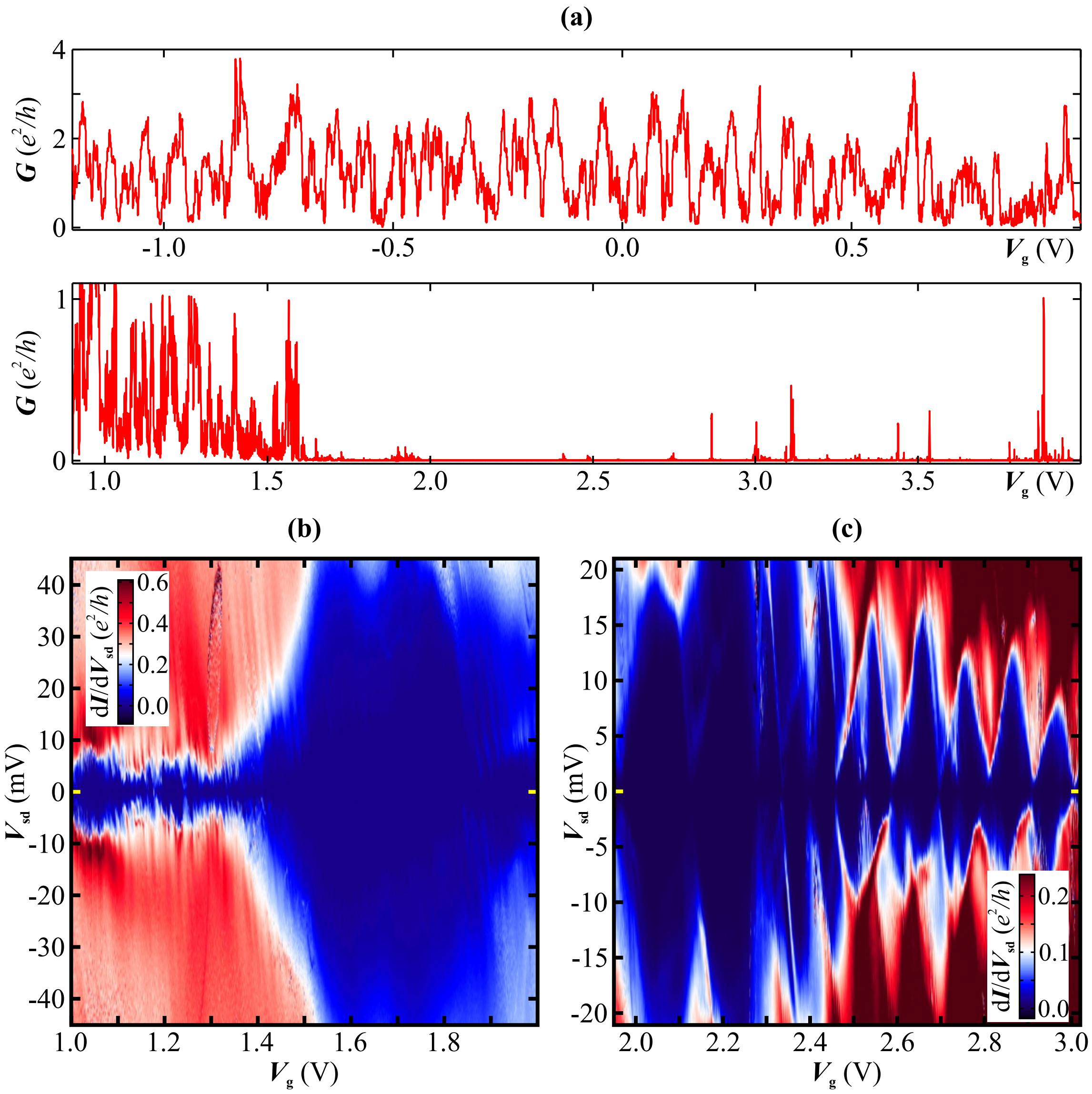

Figure 7.2: Voltage-biased measurements co-sputtered MoRe-CNT device at base temperature using the voltage-bias setup with the transimpedance amplifier, see Figure 7.1. **(a)** $G\left(V_\mathrm{g}\right)$ characteristic at constant $V_\mathrm{sd} = 50\,\mu\mathrm{V}$. **(b)** Stability diagram left-hand side of the low-conductance region. **(c)** Stability diagram right-hand side of the low conductance region. **(b)** and **(c)** display two different measurements.

Furthermore, a regular pattern of conductance oscillations which is typically observed for quantum dots in the Coulomb blockade regime cannot be made out, for comparison see transport spectroscopy measurements presented in chapter 4. Right-hand side of the supposed band gap, Coulomb blockade as well as Coulomb oscillations ranging at a lower conductance scale of $< 1\,e^2/h$ are detected.

Both stability diagrams plotted in Figures 7.2(b) and (c) support the presence of an irregu-

lar quantum dot system. In Figure 7.2(b), the V_{sd}-range was chosen to be larger in order to resolve the band gap. Indeed, a band gap-like pattern is situated beginning from $V_{\mathrm{g}} \approx 1.5\,\mathrm{V}$ to $2\,\mathrm{V}$: large diamonds of a size of $\Delta V_{\mathrm{sd}} \approx 80\,\mathrm{mV}$ is resolved, but overlapped by a second one of the same size. The region there is additionally distorted by a structure which can be made out in the range of circa $\pm 10\,\mathrm{mV}$. Left-hand side of the band gaps, these diamonds exhibit a rather regular shape, see Figure 7.2(b) for $V_{\mathrm{g}} \lesssim 1.3\,\mathrm{V}$. Right-hand side of the band gaps, diamonds are probed beginning with the size of $V_{\mathrm{sd}} \approx \pm 20\,\mathrm{mV}$ on the bias axis, and $\Delta V_{\mathrm{g}} \approx 100\,\mathrm{mV}$ on the gate axis. The diamonds of both CNT quantum dots intersect each other, and from their similar shape one can conclude that they originate from two quantum dots of similar size. SEM of the device was performed after the measurements presented in this section: only one link suspended in between both electrode stripes was recorded, as can be seen in the inset of the SEM micrograph in Figure 3.3(a), panel 2. Consequently, the device consists of one suspended bundle of at least two CNTs.
Furthermore, feedback effects resulting in local modifications of the current respectively conductance through the dots are detected, for example at about $V_{\mathrm{g}} \approx 1.3\,\mathrm{V}$ on the positive bias axis. These signatures indicate a mechanically active system which acts as a quantum dot, see also chapter 4 and [Usmani, 2006; Schmid et al., 2012; Schmid et al., 2015b].

7.1.2 Current-bias measurement

A highly conducting region is already detected in the $G\left(V_{\mathrm{g}}\right)$ characteristics for $V_{\mathrm{g}} \lesssim -0.8\,\mathrm{V}$, see Figure 7.2(a). A current-biased stability diagram of this region is plotted in Figure 7.3(b). The four-terminal measurement setup is used which described in subsection 3.5.3 and depicted in Figure 3.9. In this most promising V_{g} range, the CNT is examined regarding induced superconductivity according to previous work, see [Pallecchi, 2009; Keijzers, 2012; Schneider, 2014]. Here, no voltage-drop was probed despite of an applied biased current I_{sd} in the size of few nanoampères.
The fast sweeping axis is the dc current I_{sd} defined by a dc voltage supply and a series resistor of $10\,\mathrm{M\Omega}$. An additional ac current is impressed by the lock-in amplifier with a series resistor of $1\,\mathrm{G\Omega}$: its frequency is $f_{\mathrm{LIA}} = 137.36\,\mathrm{Hz}$, and since the rms-voltage is $V_{\mathrm{ac}} = 0.1\,\mathrm{V}$, the resulting impressed (rms-)ac current is $I_{\mathrm{ac}} = 100\,\mathrm{pA}$. With the supplies and corresponding series resistors connected to pin #20, and pin #4 set to ground at the breakout box, the net current is hence defined in between these two terminals. The voltage drop at the CNTs is obtained by probing the other two terminals, namely #19 and #3. Both contacts are connected to the differential voltage amplifier, which supplies a voltage signal to the lock-in amplifier. The differential resistance dR is then obtained dividing the voltage drop by I_{ac}.

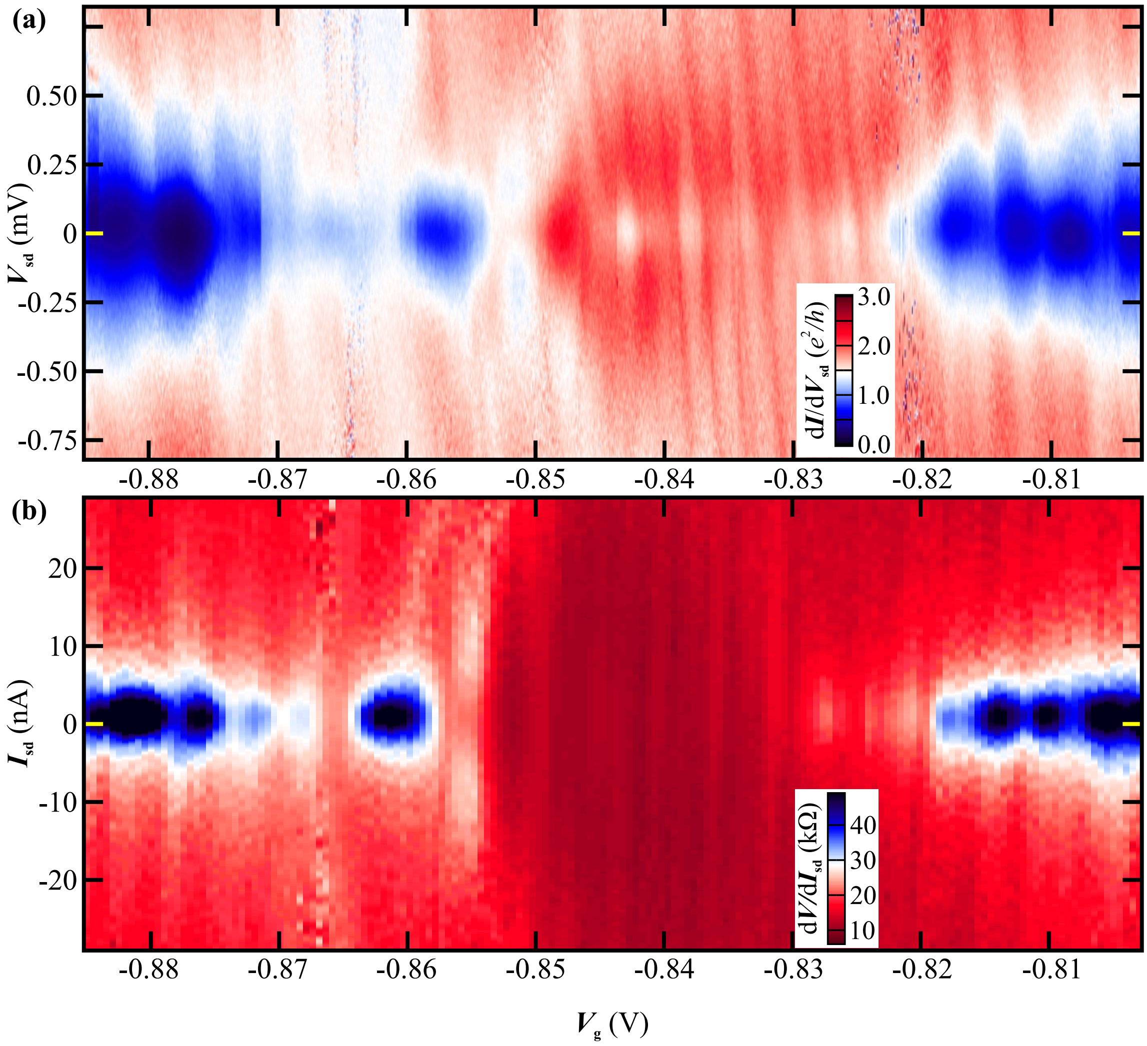

Figure 7.3: Comparison of voltage-bias and four-terminal current-bias measurement in the same V_g range at base temperature. **(a)** Stability diagram mapping the differential conductance $G = dI/dV_{sd}$ using the setup of Figure 7.1. **(b)** Current-bias stability diagram mapping the differential resistance dV/dI_{sd} as a result of voltage drop and impressed ac current; for the setup details see Figure 3.9 and subsection 3.5.3. The color scale range is chosen in a way that the conductance in **(a)** resembles the differential resistance in **(b)**.

The trend of the differential resistance as a function of V_g is as expected from the previously performed two-terminal voltage-bias measurement, see Figure 7.3(a). Hence, the setup and the device design are appropriate for four-terminal measurements at the CNT(s). Nevertheless, no regions with supercurrents, i. e. $dV/dI_{sd} = 0$ for non-zero I_{sd} are detected. For small I_{sd}, the smallest differential resistance of $\approx 10\,\mathrm{k\Omega}$ is detected around $V_g \approx -0.845\,\mathrm{V}$.

7.2 Premixed MoRe-CNT device

Another attempt to induce superconductivity from molybdenum rhenium contacts to an overgrown carbon nanotube is carried out using $Mo_{20}Re_{80}$ originating from the premixed rhenium-rich target.
Fabrication details can be found in appendix B.3. Metallization processes follow the principles described in chapter 3, and the mask depicted in panel 3 of Figure 3.2(a) is used for the electrode structure. It consists of 50 nm of premixed $Mo_{20}Re_{80}$ plus in-situ platinum capping of ≈ 3.5 nm. The electrode stripes of 2.5 µm width are separated by a trench of 850 nm width. The on-chip CNT growth was carried out at standard conditions at a duration of 15 min, see appendix A.11. At the probe station, the device "45 right" exhibited a room-temperature gate characteristic as plotted in the diagram in Figure 3.4(c). The SEM micrograph of Figure 3.3(a), panel 3, depicts a similar device geometry but with the same catalyst deposition area.

7.2.1 Characterization at base temperature

Voltage-biased measurements at base temperature of $\lesssim 15$ mK in the dilution cryostat are performed to examine the premixed MoRe-CNT device. The underlying measurement setup is depicted in Figure 3.8 and described in subsection 3.5.2.
Figure 7.4 depicts the gate voltage dependence of the current I. First observation is the localization of the small band gap in the V_g range: from -75 mV to $+50$ mV. Relatively high values for V_{sd} are necessary to resolve Coulomb oscillations. In other words, the present quantum dot system is confined in between very thick tunneling barriers: by consideration of the peak currents, the overall two-terminal resistance of the device ranges at $\gtrsim 1\,\mathrm{M\Omega}$. There is an obvious large change of the properties at the $Mo_{20}Re_{80}$-CNT interfaces since the device resistance range at room-temperature was of $\gtrsim 29\,\mathrm{k\Omega}$, see also the diagram in Figure 3.4(c). This temperature-depending effect results in large tunneling resistances, but leaves the regular quantum dot behavior untouched. Indexing of the first hole and electron transitions in Figure 7.4 is confirmed by the stability diagrams in Figure 7.5.
The stability diagram of Figure 7.5(a) showing the hole transport regime reveals regular Coulomb blockade valleys: their dimension at the V_{sd} axis distinctly decreases from the first hole valley until $N_h = 7$. With increasing hole number, respectively decreasing V_g, the dimensions do not change significantly anymore. The regular Coulomb blockade diamonds are overlapped by inelastic co-tunneling features, starting from $N_h = 4$ for negative V_{sd}.

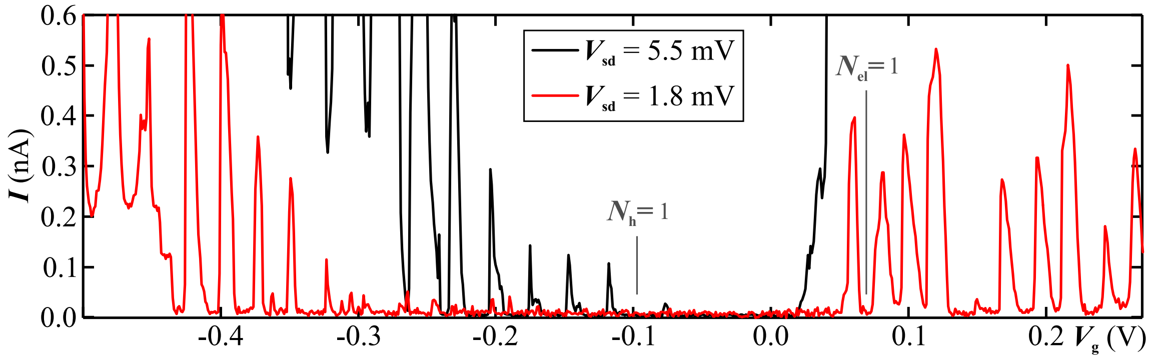

Figure 7.4: Transport regimes of the premixed MoRe-CNT device. Gate dependence of the current I for constant bias V_{sd}. The first hole transition, and the band gap can be identified. The $N_{\mathrm{el}} = 1$ charging state is confirmed by the stability diagram of Figure 7.5(b).

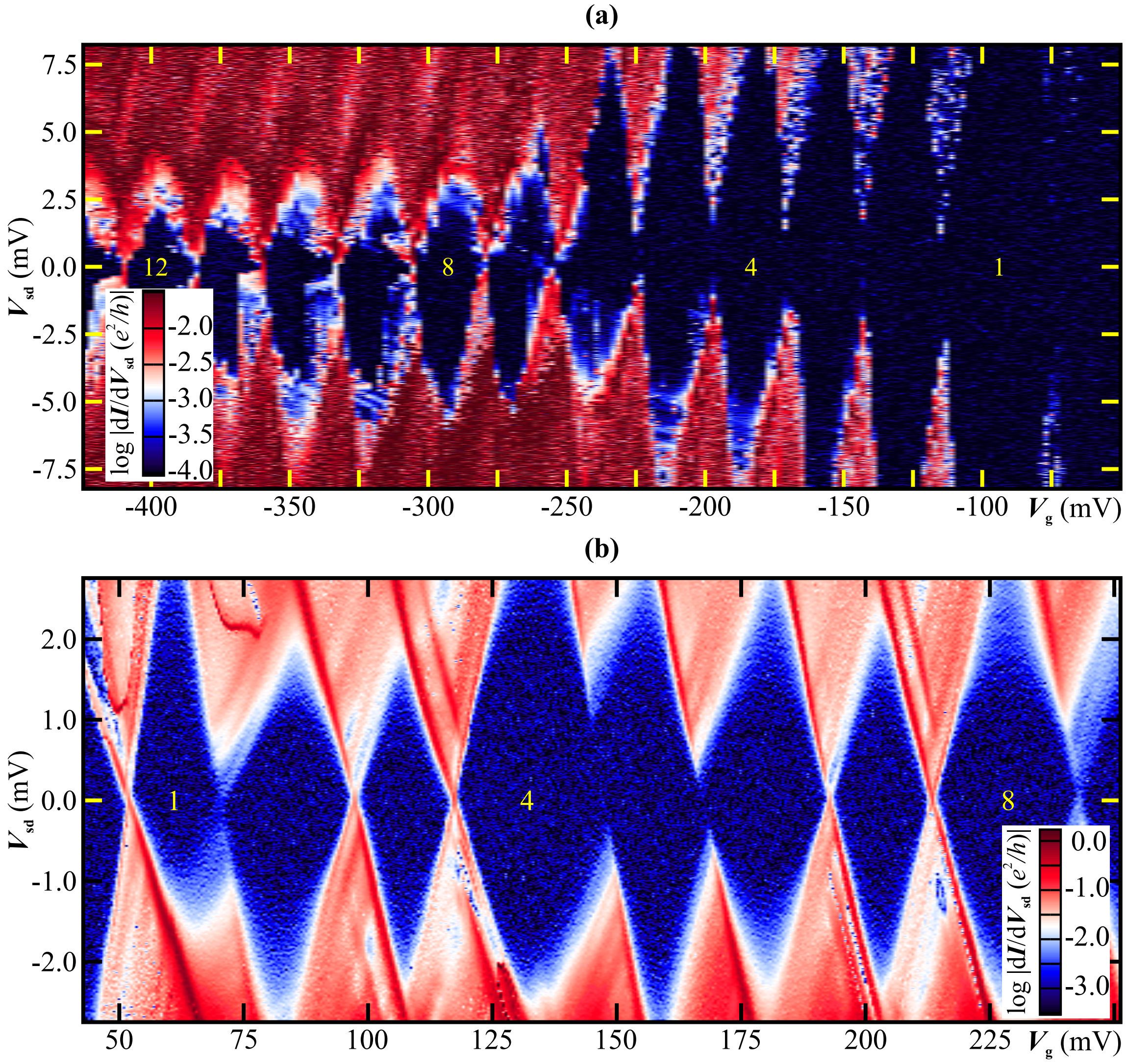

Figure 7.5: Stability diagrams of the premixed MoRe-CNT device using a dc voltage-bias setup according to Figure 3.8. **(a)** Hole transport regime for $12 \leq N_{\mathrm{h}} \leq 1$. **(b)** Electron transport regime from $1 \leq N_{\mathrm{el}} \leq 8$.

In contrast, the stability diagram at the electron transport regime shows regular Coulomb diamonds, and only sequential tunneling features are detected, see Figure 7.5(b).
Coulomb oscillations are not resolved at zero bias from the fourth to the fifth, and to the next valley which is attributed to the lower preamplifier sensitivity setting compared to the $I\left(V_\mathrm{g}\right)$-measurement of Figure 7.4. Higher-order transport effects like co-tunneling, Kondo effect, or even like Fabry-Pérot transport are suppressed due to the high tunneling resistances R_t.

7.2.2 Quantum dot spectroscopy

In spite of the highly resistive system, quantum dot spectroscopy is performed regarding capacitive coupling and charging energies of the CNT quantum dot. The results are shown in Figure 7.6, taking the measurements shown in Figure 7.5 into consideration. In addition, the band gap is traced comparable to the stability diagram shown in Figure 4.2 resulting in

$$E_\mathrm{G}^\mathrm{CNT} = (47.7 \pm 5.7)\,\mathrm{meV} \quad , \tag{7.1}$$

for the present CNT suspended on $\mathrm{Mo_{20}Re_{80}}$-Pt contacts. The data plotted in Figure 7.6 are mean values for both V_sd sides, and the error bars are a systematic consequence of the plot dimensions as well as V_sd, and V_g step sizes during the different measurements.
As can be seen, the capacitive coupling to the gate, C_g does not distinctly change except close to the band gap being denoted as "0" in the N_h diagrams. No additional changes in the charging energies E_C due to different spin or orbit shell filling can be made out. At the hole transport side, E_C increases with decreasing hole number to the band gap, whereas it immediately reduces to circa 2.5 meV for $N_\mathrm{el} = 1$. This is comparable to the values for $N_\mathrm{h} \geqslant 8$ at the hole transport side.

(a) ***Conversion factors*** $\boldsymbol{\alpha}_{\mathrm{g}}$, $\boldsymbol{\alpha}_{\mathrm{s}}$ (1)

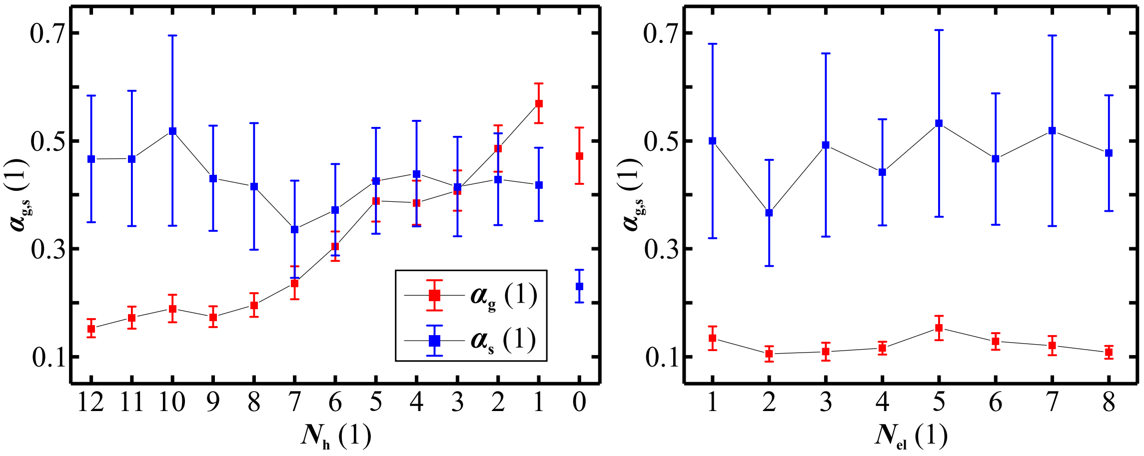

(b) ***Capacitive couplings*** C_g, C_s, C_Σ (10^{-18} F)

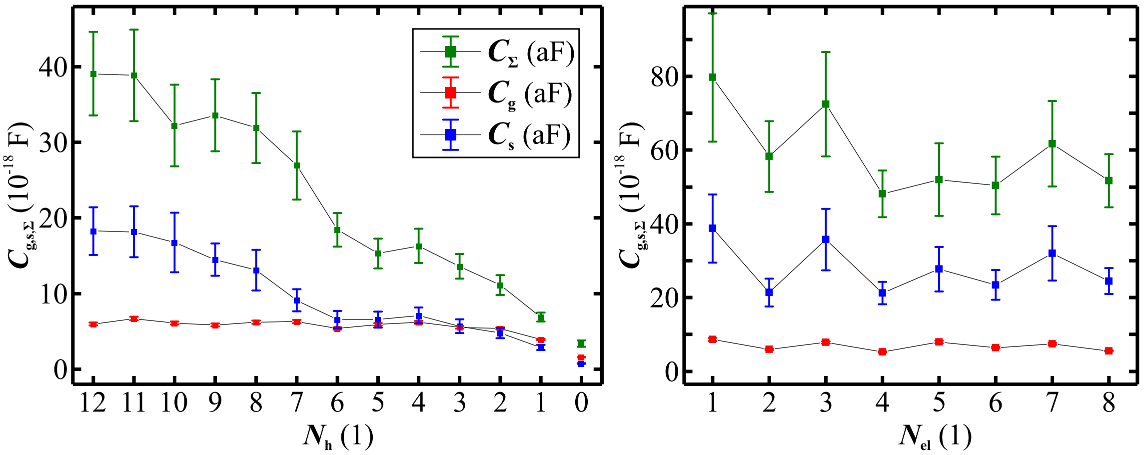

(c) ***Addition energy*** E_{add} (meV)

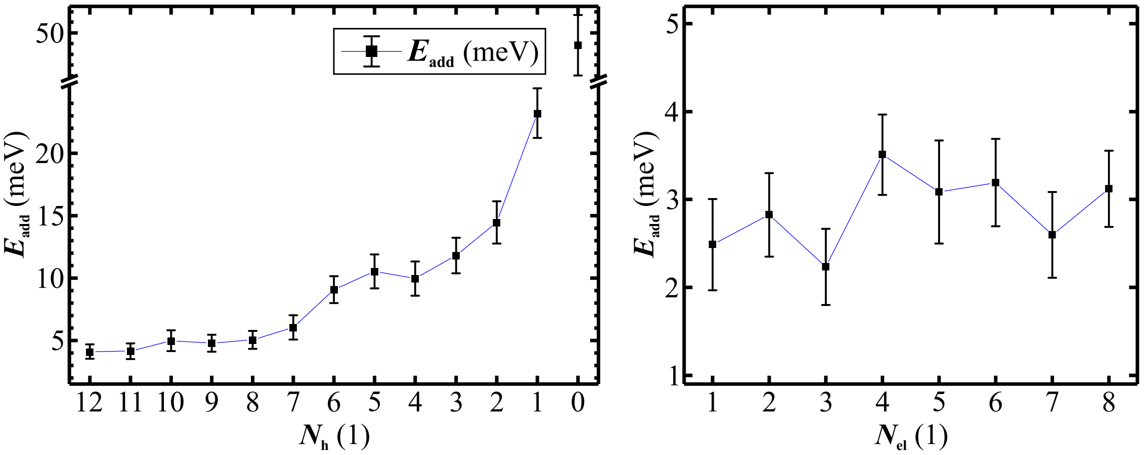

Figure 7.6: Spectroscopy of the stability diagrams of Figure 7.5 for both hole and electron transport regime. Band gap properties are included on the left-hand side hole diagrams, and labeled as "0". **(a)** Conversion factors α_{g} and α_{s}. **(b)** Capacitive coupling constants C_{g}, C_{s}, and C_Σ. **(c)** Addition energies E_{add}.

Chapter 8

Development of nanotube transfer techniques

This chapter deals with the progress establishing a further fabrication method alternative to the overgrowth technique. This technique, namely the transfer of a carbon nanotube from a growth substrate to a separate device chip, has already been applied and optimized in other research groups, see [Wu et al., 2010; Pei et al., 2012; Waissman et al., 2013; Viennot et al., 2014; Gramich et al., 2015]. The first CNT transfer similar to a stamping technique was published in [Huang et al., 2005]. Since then, it was proven several times that clean and suspended carbon nanotube devices can be fabricated that way. The progress in our group as well as observations and upcoming problems are discussed in the following.

8.1 Starting point and motivation

The main limitation of the overgrowth method is the small choice of materials possible as electrodes. Not only a high melting point of a metal or an alloy is required, it also has to be chemically inert in the face of growth conditions. Thin films, e. g. 50 nm thickness of metals or alloys are affected even though the bulk material exhibits a melting point much higher than the applied growth temperatures.

Elements which serve as reliable thin film electrodes are platinum and rhenium [Hüttel et al., 2009; Steele et al., 2009b; Schmid et al., 2012; Keijzers, 2012; Schmid et al., 2015a; Dirnaichner et al., 2016]. Besides molybdenum rhenium alloys [Schneider et al., 2012; Schneider et al., 2014], electrodes with several layers of metals like vanadium, niobium, and tungsten are in usage. However, these multilayer films are always capped by platinum or rhenium, [Cao et al., 2005; Steele et al., 2009a; Eichler et al., 2011; Ganzhorn and Wernsdorfer, 2012; Laird et al., 2012; Häkkinen et al., 2015].

Furthermore, the CVD growth process was adapted in terms of preserving the chip materials. In addition to the electrodes, this concerns the insulating SiO_2 layer and the underlying p^{++}-Si substrate. The growth temperature as well as the time had to be gradually reduced and also the flow of the process gases was lowered in order to lessen the bulk contamination by carbon [Götz et al., 2016].
Separating the nanotube growth and the device fabrication circumvents these disadvantages. On the one hand, any CNT growth chip can be chosen that withstands the CVD conditions, and the growth process itself can be carried out in the best way it works. On the other hand, no limitations of material choice for the device chip are expected.
This requires a method to transfer a carbon nanotube from the growth chip to the device chip. Two approaches for this process are developed in Regensburg. The first is to transfer the CNT directly onto the electrodes: a CNT is suspended over large and deep grooves and is transferred by approaching the device chip with the electrodes on top into these grooves. Here, both chips do not touch each other. This attempt is similar to the transfer technique described in [Waissman et al., 2013]. The second one is the direct transfer of the catalyst material and grown carbon nanotubes [Viennot et al., 2014]. Elevated areas carrying the catalyst on it are pressed onto the device chip. When the device chip is withdrawn from the growth chip, catalyst material remains on the device chip, with carbon nanotubes attached along. Because of the high stiffness of the nanotubes, it is expected that they are not damaged during this process. All stamping procedures are carried out at the mask aligner setup. It turned out, that the groove approach often results in a transfer of nanotube bundles which only were long enough to reach the other ridge. In contrast to [Waissman et al., 2013], it was not possible to probe the nanotube segments electrically before transfer. Consequently, only the second approach is used in the following.

8.2 Building up a new fabrication process

The first step is the selection of suitable materials for both stamp and device chips. A stamp chip must withstand the CVD growth conditions. Furthermore, it has to be mechanically stable since it is pressed hard against a target during the stamping procedure itself. For a precise alignment between both chips, it is necessary that the stamp chip is transparent. In addition to that, a flat surface is indispensable for stamping as well as for a proper lithography. The material of choice fulfilling these requirements is two-sided polished quartz, which is crystalline SiO_2.

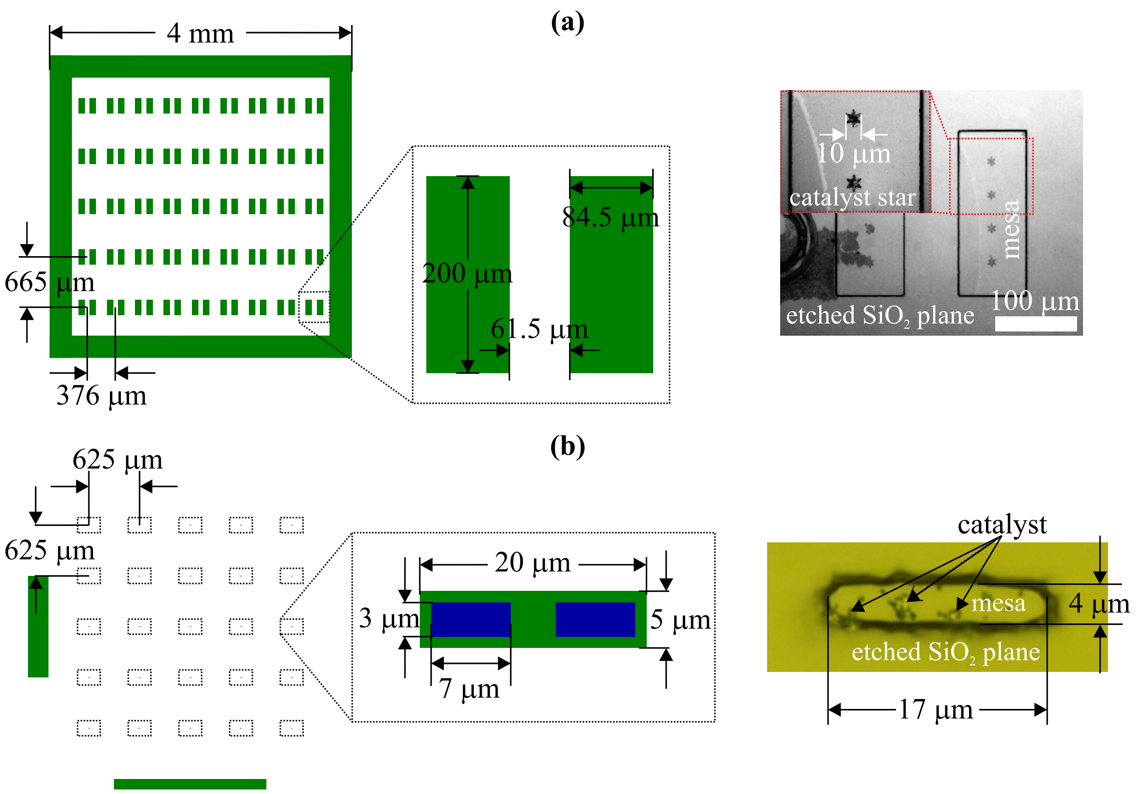

Figure 8.1: Evolution of the stamp chip design. **(a)** The optical mask with characteristic dimensions is shown. In the beginning, large mesas are used as stamps. Small catalyst structures are patterned onto the $\approx 2.5\,\mu\text{m}$ high mesas by EBL. **(b)** Design of the smaller sized stamps which were used to transfer CNTs to device chips. The height of these stamps after RIE is $\approx 1.3\,\mu\text{m}$. The spacing of the stamp mesas is chosen to be exactly the same as that for the reserved places on the device chip. Consequently, only the stamp mesas hit simultaneously the desired places on the device chips. In an additional optical lithography step, two smaller (blue) rectangles which are aligned to each stamp mesa define the places where the catalyst is deposited later. The microscope pictures reveal successful catalyst deposition onto the stamps of both types.

After stamping, the carbon enriched catalyst material should be removed in order to recycle the stamp chip. This was by and by realized by placing the stamp chips into a hot solution of NaOH for about two hours with subsequent cleaning in an O_2 plasma.
The stamp substrate is patterned in a way that only small elevated areas called "mesas" really touch the target chip at desired places. The remainder of the chip is deepened and also transparent. To reach this result, optical lithography is performed using the resist AZ 9260 of minimum $5\,\mu\text{m}$ single-layer thickness to define the mesas. In the subsequent reactive ion etching process, the blank areas are etched using a CHF_3/O_2 plasma. The mesa height is restricted by the etching rate for the resist, which is found to be $(2.56 \pm 0.01)\,\mu\text{m/h}$. This way, mesas of $2.5\,\mu\text{m}$ height were realized, see [Steger, 2015].

In the next step, the catalyst deposition areas on top of the mesas are defined. This is first done by means of electron beam lithography. A double layer of PMMA (see Table A.3) is spincoated on the stamp chip, and afterwards a thin aluminum layer of circa 10 nm is deposited in order to avoid charging effects during EBL. This layer must be removed by a 0.2 molar solution of KOH directly after SEM exposure and before development is performed. Alternatively to this laborious EBL-step, catalyst deposition is carried out using optical lithography. Since the usual methanol-based catalyst suspension solves optical resists like AZ 9260, an isopropanol-based catalyst suspension is prepared (see Table A.7). In comparison to the standard CVD process (see appendix A.11), the flow rates of CH_4 and H_2 are increased to 810 sccm and 200 sccm during a growth time of 20 min and growth temperature of 1040 °C. These changes are expected to cause longer but less clean tubes to grow out of the catalyst material [Kong et al., 1998b].

The structures on the electrode chip must provide a place where the stamps can be pressed at. In a safe distance including a tolerance of few µm, the electrodes are patterned and separated by a trench exhibiting a length $2\,\mu\mathrm{m} \geq L \geq 500\,\mathrm{nm}$. The inner structures, i. e., the electrodes and leads, are connected to bond pads with dimensions of $100/150\,\mu\mathrm{m} \cdot 100\,\mu\mathrm{m}$. In first tests, the chosen electrode material was a multilayer consisting of 5 nm of titanium, 50 . . . 80 nm of niobium and 5 nm rhenium or platinum. Titanium acts as an adhesion layer between SiO_2 and the superconductor niobium, and rhenium or platinum as capping material to prevent oxidation of the niobium at the surface. Both elements also typically exhibit a good electrical contact to carbon nanotubes. In later structures, bond pads and outer leads were made of titanium and platinum, whereas electrodes and inner leads consisted of a co-sputtered $Mo_{58}Re_{42}$ alloy with a thickness of 50 nm.
The niobium containing electrode chips which are defined in one optical lithography step plus subsequent lift-off. In contrast, the second $Mo_{58}Re_{42}$ electrodes are etched out from a square using SF_6/Ar plasma during RIE. This step is carried out with in-situ deepening the trench using the bare electrode structures as an etching mask, see also subsection 3.1.2 and Figure 3.2(b).

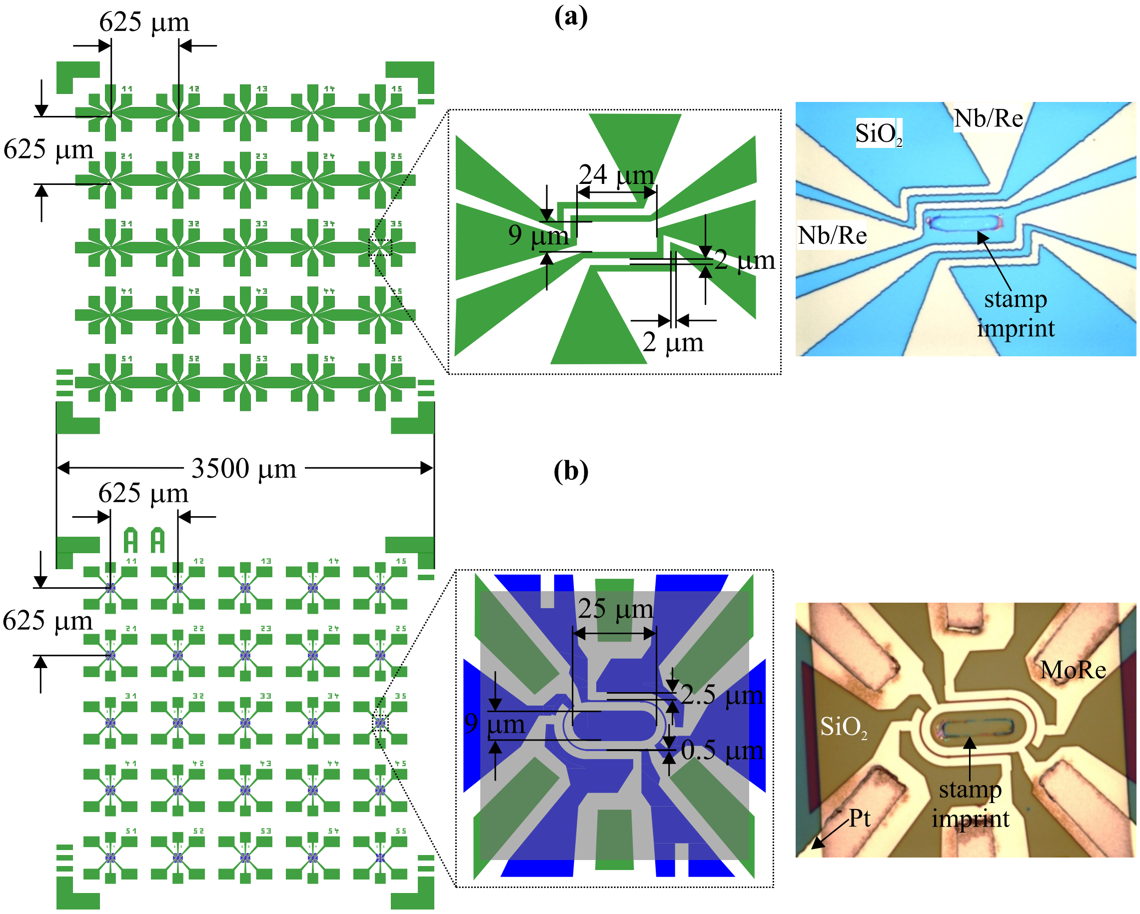

Figure 8.2: Evolution of the device chip design. **(a)** The optical mask for a device chip to be fabricated in one optical lithography step plus lift-off. Eight contact pads are used for one device, and a pair is linked to one electrode. The horizontal contact pads in between of two neighboring devices can be used for both. The 2 µm width of the trench in between two electrodes is at the lower limit realizable by optical lithography. **(b)** Here, the optical mask is used for contact pads and larger leads only. The inner structures are patterned by EBL in two steps: at first, a square is structured which is of the desired metal or alloy. In the subsequent EBL step, an etching mask is written to pattern the electrodes and smaller leads out of the square. In doing so, one inner electrode and two different electrodes above and below are linked to two bond pads. The microscope pictures show devices of both types after stamping, exhibiting the typically observed imprint of the stamp mesa into the SiO_2 surface.

As stated before, the stamp procedure was carried out using a mask aligner with its x, y, z, Φ alignment stage. When doing so, the stamp chip is glued upside down on a glass plate which is inserted into the mask holder. After alignment, stamp chip and electrode chip are pressed against each other using the z-manipulator. The details are specified in [Steger, 2015; Berndt, 2016].

The stamped device chips are exposed to a subsequent annealing step for five minutes in a 475 °C hot argon atmosphere (plus heating up and cooling down). This procedure demonstrably leads to a better contact between the transferred carbon nanotubes and the electrodes.

8.3 Characterization of the transferred nanotubes

The objective of the first stamping experiments was to demonstrate that carbon nanotubes could be transferred using this approach. A blank one-side polished sapphire chip was chosen as a target. using scanning electron microscopy (SEM), transferred catalyst material as well as CNTs are observed on the Al_2O_3 substrates. Carbon nanotubes are detected in between the catalyst material, but also leaving the defined catalyst areas on the stamp chip, see Figure 8.3. Such nanotubes are of particular interest concerning future applications and are examined by atomic force microscopy (AFM). Here, typical diameters of single-walled carbon nanotubes are measured and also bundles of SWCNTs are identified [Steger, 2015].
As a last confirmation, the sapphire chips are placed into the plasma-preen device and after an ashing process re-examined by SEM. It was observed that the nanotubes as well as carbon residues on the catalyst material are burned away already by a short exposure to oxygen plasma.

As next step, the stamping procedure was carried out using prefabricated chips with contact electrodes on it (see Figure 8.2) and appropriate smaller sized stamps, see Figure 8.1(b), carrying the catalyst and potentially carbon nanotubes. The devices are tested directly after argon annealing at room temperature using the probe station measurement setup (as depicted in Figure 2.5(a)). The most interesting ones are plotted in Figure 8.4.
A current between electrode pairs was measured for 1/4 of all possible devices. 17 % of all devices exhibited a rather small back gate dependence of the current whereas clear small or large gap carbon nanotube behavior as function of gate voltage is observed for only 8 % [Berndt, 2016]. Two small gap nanotube gatetraces are shown in Figure 8.4.

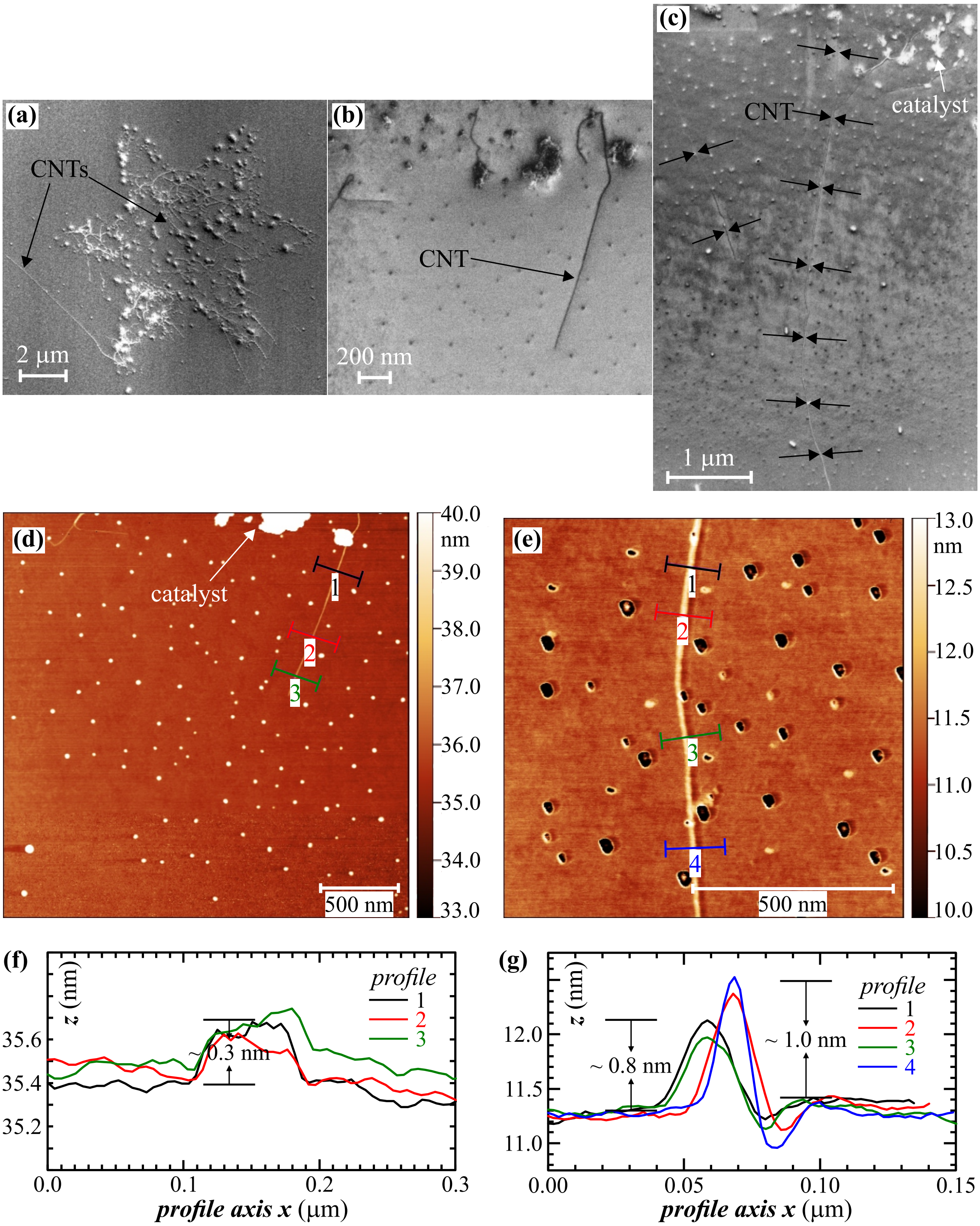

Figure 8.3: Transfer of CNTs onto sapphire substrates by stamping. Scanning electron micrographs of the target substrate **(a)**, **(b)**, and **(c)** reveal transferred catalyst material: it still exhibits the same pattern as on the stamps, but also material originating from unstructured areas is transferred. **(d)** and **(e)**: possible carbon nanotubes are examined more exactly by atomic force microscopy using Tapping Mode. **(f)** and **(g)**: this method, typical heights for single wall carbon nanotubes lying on flat substrates are measured.

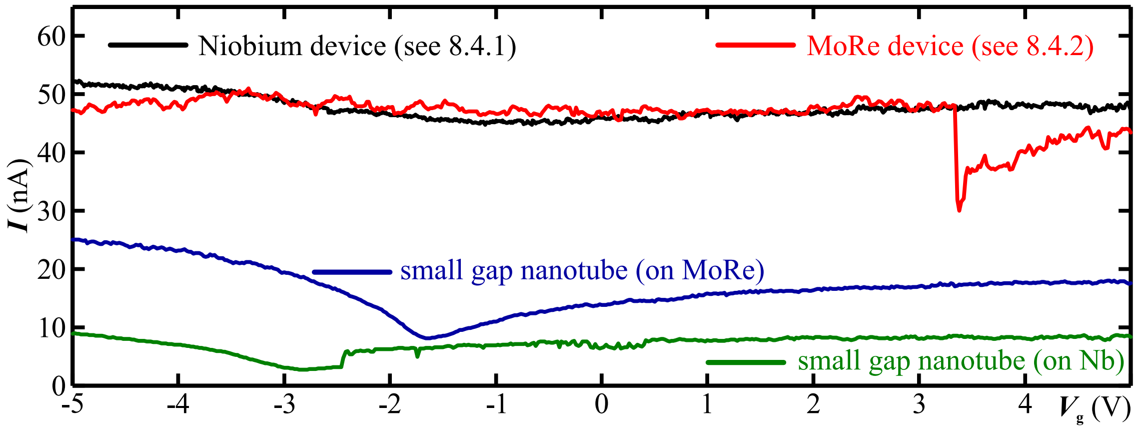

Figure 8.4: Room temperature measurements of the current I as function of gate voltage V_g for nanotube devices fabricated by stamp transfer. The bias voltage V_{sd} is set to 2 or 3 mV. Two rarely detected small gap nanotube devices on $Mo_{58}Re_{42}$ are shown.

8.4 Low temperature measurements

Low temperature measurements in the dilution cryostat were performed on two different devices fabricated by stamping. Stamp chips with a design following Figure 8.1(b) were used. Isopropanol-based catalyst suspension (see Table A.7 in section A.9) was drop-cast onto the lithographed stamping mesas and the growth process was applied as described above. After stamping and room temperature dc characterization, the device chips are fixed in the standard chipcarriers using two-component silver epoxy. The bond pads are connected to the chipcarrier pins by aluminum bonding.

The low temperature measurements are carried out following the commonly used voltage-bias measurement setup, as depicted in Figure 3.8 and described in subsection 3.5.2.

8.4.1 Niobium device

The design of this device chip can be seen in Figure 8.2(a). The electrodes are built up layer by layer from the SiO_2 substrate to the top by titanium, niobium and rhenium with a total thickness of 90 nm. Here, the titanium sticking and rhenium capping layer are each 5 nm thick. The trench width defined by the optical mask is of 2 µm (see Figure 8.2(a)) and the trench depth given by the total electrode thickness plus subsequent RIE is 200 nm in total.

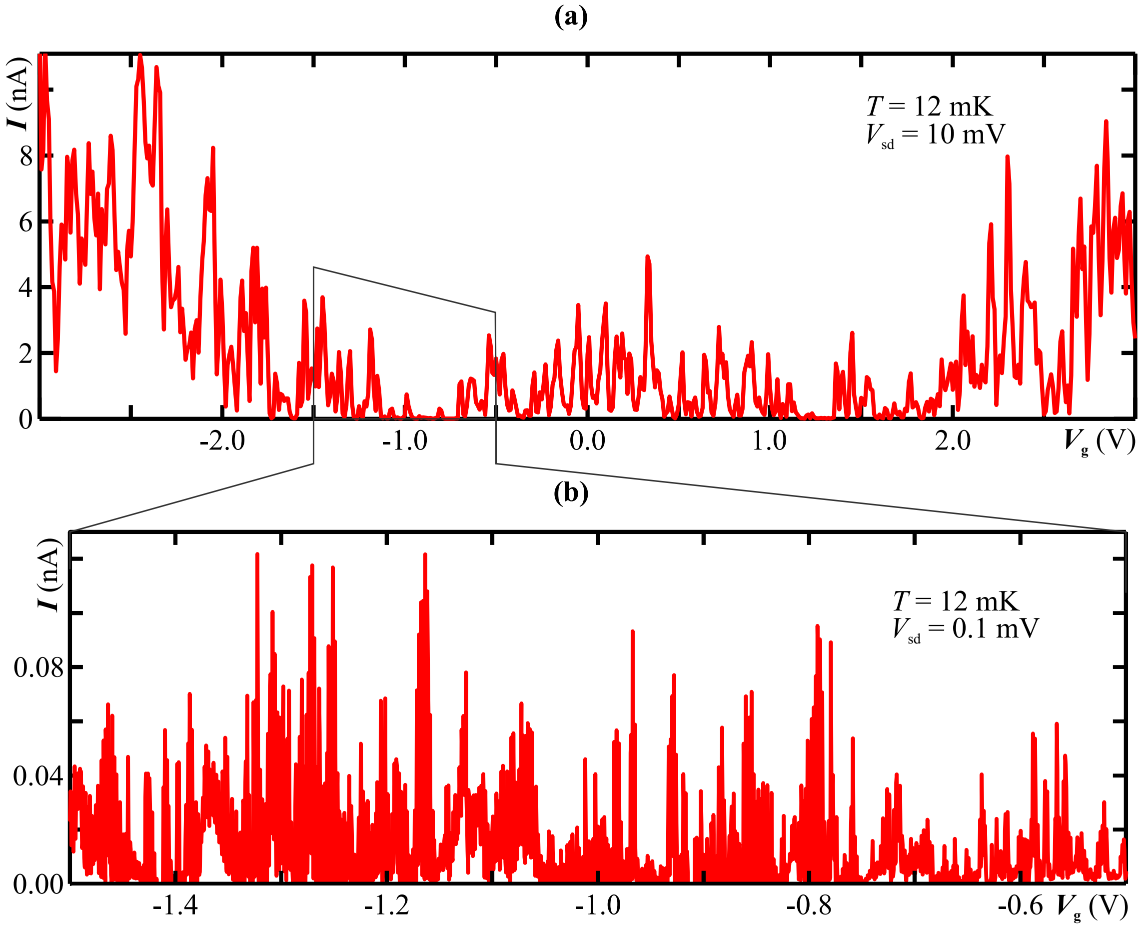

Figure 8.5: Measured current I as function of gate voltage V_g at base temperature, for constant bias voltages. **(a)** Overview plot where a rather high bias, $V_\mathrm{sd} = 10\,\mathrm{mV}$, is applied. **(b)** Detailed plot showing Coulomb oscillations in a region around $V_\mathrm{g} = -1\,\mathrm{V}$ at low bias $V_\mathrm{sd} = 0.1\,\mathrm{mV}$.

Figure 8.5 shows two current-gate voltage diagrams of the niobium device at base temperature of the cryostat. Coulomb oscillations are observed but do not appear regularly with respect to the back gate voltage. One exemplary region where a band gap is suspected in Figure 8.5(a) is examined in detail in Figure 8.5(b): this measurement reveals additional structures which cannot be attributed to only one quantum dot in the system. It seems that at least two quantum dots contribute to the transport measurement. This is confirmed by the stability diagram for the gate voltage region in between $V_\mathrm{g} = -1.19 \ldots -1.16\,\mathrm{V}$, as shown in Figure 8.6: a continuous structure of Coulomb diamonds appears exhibiting a charging energy of $E_\mathrm{C} \approx 2\,\mathrm{meV}$ and a width on the gate axis of about $5\,\mathrm{mV}$. The conductance pattern of this quantum dot is overlapped by a second one with a rather smaller size for both directions, i. e. $E_\mathrm{C} \leq 1\,\mathrm{meV}$ and $\Delta V_\mathrm{g} \approx 1\,\mathrm{mV}$.

Since the diamonds are closing at zero bias voltage, it is concluded that the carbon nanotube quantum dots are clean (there are no impurities acting on the transport measurements), and that in addition no BCS gap in the leads is observed. Regarding the length scales of $L = 2\,\mu\mathrm{m}$ and $h = 200\,\mathrm{nm}$, the nanotubes are not necessarily completely suspended over the trench. The pattern of intersecting diamonds is due to a bundle of several tubes suspended in between the electrodes; for comparison, see also the stability diagrams in Figures 7.2(b) and (c).

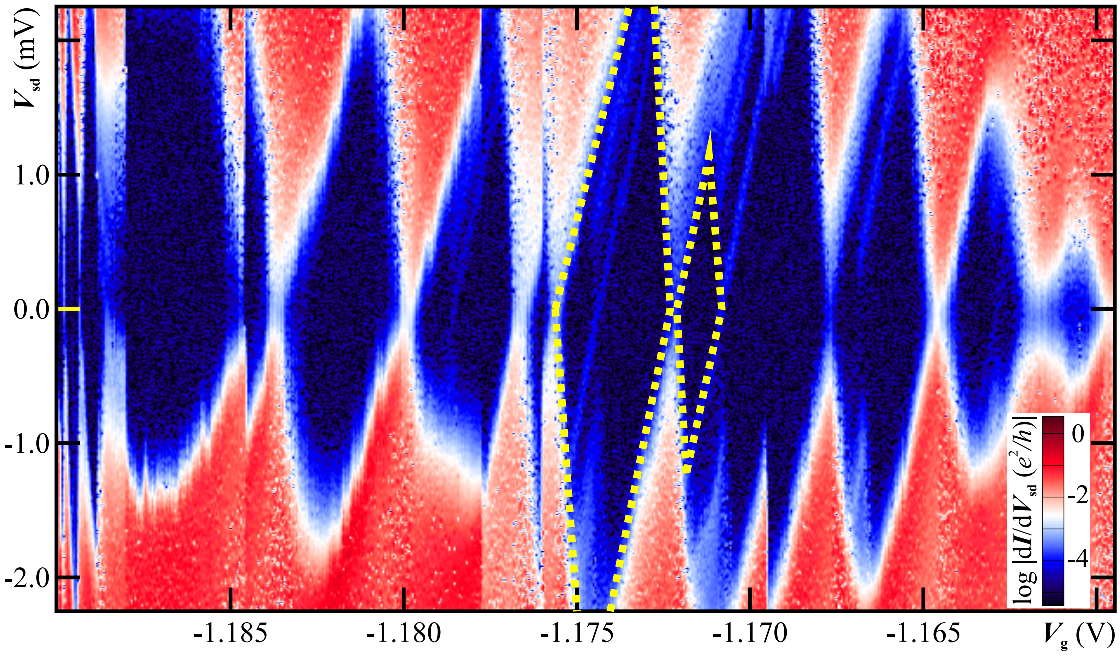

Figure 8.6: Stability diagram of the niobium device at base temperature $10\,\mathrm{mK} \leq T_{\mathrm{base}} \leq 15\,\mathrm{mK}$. The conductance as function of (V_g, V_{sd}) is mapped in a logarithm scale in order to uncover additional structures in the blockade regions. Two different diamond sizes originating from different quantum dots are exemplary indicated as yellow dashed lines.

8.4.2 MoRe device

The layout of this device chip is shown in Figure 8.2(b). The electrodes consist of a co-sputtered $Mo_{58}Re_{42}$ layer of 50 nm plus a rhenium capping layer of 3 nm thickness. The trench width is of 500 nm and the trench depth is of 160 nm in total.

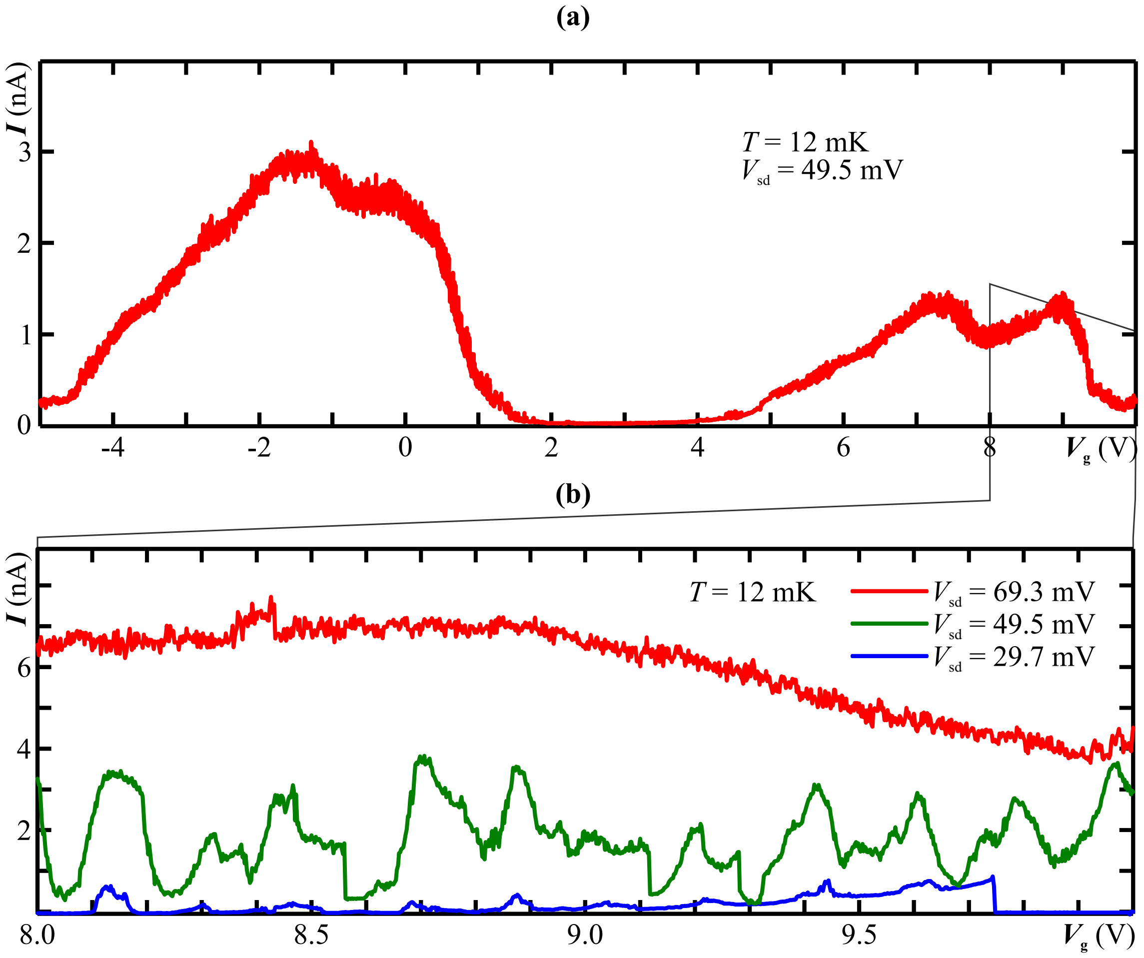

Figure 8.7: Measured current I as function of gate voltage V_g at base temperature for constant bias voltages. **(a)** Overview plot. **(b)** Detailed plot showing distorted Coulomb oscillations in a region around $V_g = 8\,\mathrm{V}$ for bias voltages $V_{sd} \geqslant 28\,\mathrm{mV}$.

The current-gate voltage measurements at cryogenic temperatures, as plotted in Figure 8.7, show a highly resistive device. A transport gap in between $1.5\,\mathrm{V} \leq V_g \leq 4\,\mathrm{V}$ is observed. A rather high bias voltage of 50 mV is applied to measure current oscillations in the few nanoampère range. These oscillations are examined more closely in the V_g-range from 8 to 10 V, as plotted in Figure 8.7(b). It turns out, that bias voltages higher than ±28 mV are needed to resolve current oscillations.

A transport spectroscopy diagram in this region is recorded in Figure 8.8. It is visible, that conducting regions for positive and negative bias are separated by a continuous gap on the scale of $\approx 40\,\mathrm{mV}$. Beyond that bias-gap region, a Coulomb diamond like behavior on both sides can be made out.

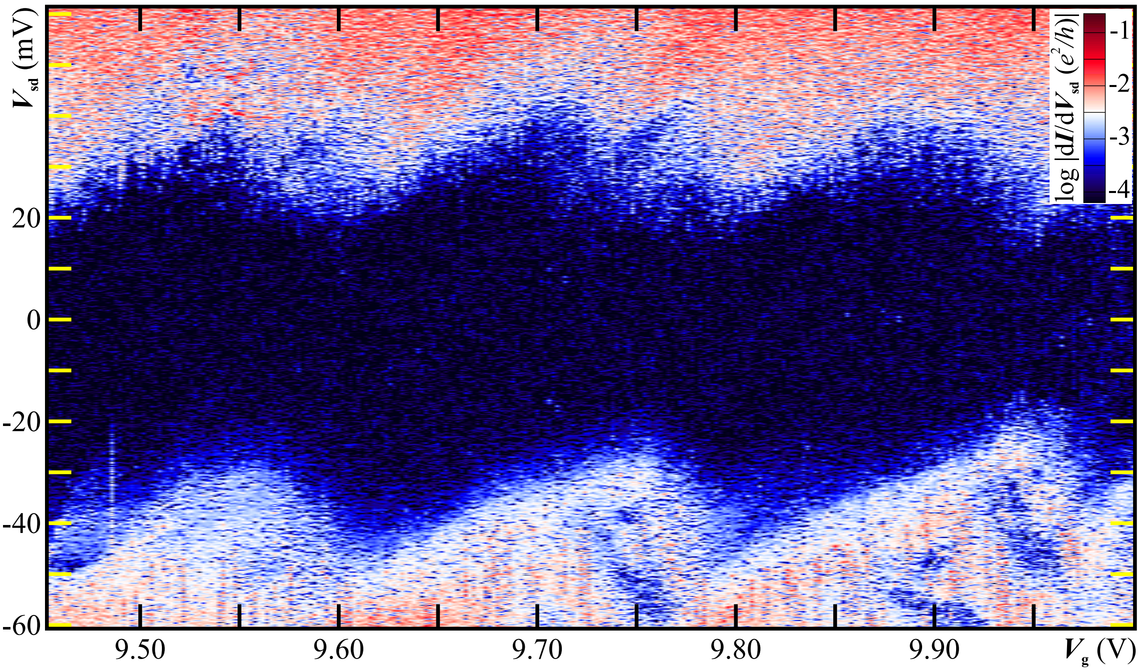

Figure 8.8: Stability diagram $dI/dV_{sd}\left(V_g, V_{sd}\right)$ of the device at base temperature $10\,\text{mK} \leq T \leq 15\,\text{mK}$. The conductance is mapped in a logarithmic scale.

The transport-gap cannot be attributed to a BCS gap which is expected to be of less than $\pm 1\,\text{mV}$. It can, however, be caused by an impurity on the nanotube itself or additional interface defects between CNT and the alloy surface, leading to an additional voltage drop and double quantum dot behavior, see [Hüttel et al., 2007].

In addition to these observations, a gate leakage appears for gate voltages $V_g \geqslant 17\,\text{V}$. This leakage at rather high V_g is a consequence of an electrical contact between CNT and the p^{++}-Si-layer, which may be located at a position where the insulating SiO$_2$-layer was damaged during the stamping procedure.

Chapter 9

Conclusion and outlook

Within this thesis, a diverse set of experiments on carbon nanotube quantum dots is presented and evaluated. Different fabrication methods, and improvement of single steps of established known procedures are used to obtain suspended CNT devices [Kong et al., 1998b; Cao et al., 2005; Schmid, 2010]. In particular, an ultraclean carbon nanotube quantum dot is examined regarding low-temperature transport. Furthermore, its outstanding nano-electromechanical properties are used to infer the charge distribution in the Kondo regime. Theoretical calculations from previous work [Steele et al., 2009b; Meerwaldt et al., 2012] are extended to model the CNT quantum dot as nano-electromechanical system. Applying these results to a second device (see [Schmid, 2015]) delivers a characteristic shift which is attributed to the Kondo effect. This is in very good agreement with other experimental observations, see [Sprinzak et al., 2002; Desjardins et al., 2017].
The next part of this thesis deals with optimization of molybdenum rhenium alloys for CNT contact materials. In short, this alloy is the third material besides platinum and pristine rhenium at all to withstand carbon nanotube growth conditions. At the end of this work, the stamping approach for carbon nanotube devices delivers first low-temperature transport results of our group.

In chapter 3, further development of the so-called "overgrowth fabrication" is described. Several process steps were improved and modified during this thesis. A first improvement is to countersink the bond pads, leading to thicker layers and simultaneously stable links to the inner structures. Second, by introducing an additional lithography step, namely an etching mask, flat surfaces as well as clean edges are realized to improve electrical properties of the electrodes as interface to carbon nanotubes. This recipe is particularly necessary when co-sputtered molybdenum-rhenium alloys are used as inner structures. Here, two particle beams from both sputtered targets hit the substrate, which excludes a precise alignment of the sample holder with respect to one beam direction. Furthermore, a direct relation between trench depth and height of the deposited catalyst material for successful carbon nanotube overgrowth is observed. This dependence is illustrated in Figure 3.3. At last, the insert setup was modified by introducing RC filters in the dc cabling.

Chapter 4 presents transport spectroscopy of an ultraclean carbon nanotube quantum dot at cryostat temperatures of $\lesssim 15\,\mathrm{mK}$. All transport regimes and phenomena as stated in chapter 2 are found: exclusive Fabry-Pérot is observed in the hole transport regime for $V_\mathrm{g} \ll 0\,\mathrm{V}$, next to an intermediate mixed-valence region which appears from circa $-3.5\,\mathrm{V}$ to the first hole Coulomb oscillations at $\approx 0.2\,\mathrm{V}$. The conductance is enhanced, but single-charging effects are still apparent as can be seen in Figure 5.7(a), and in agreement with observations in [Makarovski et al., 2007]. A detailed theoretical analysis of the Fabry-Pérot transport pattern lead to an estimate for the chiral angle in previous work, see [Dirnaichner et al., 2016]. Hole and electron transport regime are clearly separated by a band gap. The electron transport regime exhibits strong Coulomb blockade for the first electron numbers, which displays mechanical instabilities [Usmani, 2006; Schmid et al., 2012; Schmid et al., 2015b] and co-tunneling transport features [De Franceschi et al., 2001]. At electron numbers of $N_\mathrm{el} \approx 80$, the Kondo effect as a zero-bias anomaly is detected in the stability diagrams [Kondo, 1964; Goldhaber-Gordon et al., 1998a; Kretinin et al., 2012; Cleuziou et al., 2013; Schmid et al., 2015a]. For gate voltages of $\gtrsim 4.5\,\mathrm{V}$, respectively electron numbers $N_\mathrm{el} \gtrsim 200$, the transport pattern shows two different conductance ranges: for the $4N$ and $4N+1$ charging states, the conductance ranges at about $0.1\,e^2/h$ whereas it is close to $1\,e^2/h$ for $4N+2$ and $4N+3$. Stability diagrams at higher temperature reveal thermal-broadened regular Coulomb blockade excluding a possible second quantum dot system.

An open end of a rf line in the cryostat is used to emit electromagnetic waves which drive the suspended nanotube into mechanical resonance. After being characterized regarding its transport properties, see chapter 4, measurements on nanomechanical phenomena are shown in the subsequent chapter 5. The vibrational mode is used to trace the average electronic occupation of the quantum dot; it is inferred from a characteristic dip in the resonance frequency as a function of the gate voltage [Steele et al., 2009b; Meerwaldt et al., 2012].

The behavior of the resonance frequency is examined precisely in the strong coupling regime at $N_\mathrm{el} = 270$. It is shown that considering first order tunneling alone provides a good model for the average charge $\langle N\rangle\left(V_\mathrm{g}\right)$ and the mechanical resonance frequency $f_0\left(V_\mathrm{g}\right)$. A distinct shift between the Kondo current maxima and the maxima of the charge compressibility $\partial\langle N\rangle/\partial V_g$ decays logarithmically with increasing temperature. Both results are in excellent agreement with both previous observations using different experimental techniques, [Sprinzak et al., 2002; Desjardins et al., 2017] and theoretical modeling [Wingreen and Meir, 1994; Gerland et al., 2000].

The following chapters 6 and 7 deal with optimization of superconducting molybdenum rhenium alloys to withstand the overgrowth process at first, then with low-temperature transport measurements of carbon nanotube devices suspended in between electrodes of $Mo_{20}Re_{80}$.
X-ray photoelectron spectroscopy characterization demonstrates that co-sputtering process from two independent targets can generate MoRe thin films of controlled alloy composition. Traces of molybdenum oxides are observed at the film surface after ambient air exposure. When exposing the thin films to the carbon nanotube CVD growth environment, a significant amount of carbon is incorporated into the film. No clear indications for the formation of molybdenum carbide can be found; the surface oxide is absent after CVD, pointing towards its reduction in the 850 °C H_2 atmosphere.
Similar XPS analysis is performed on thin molybdenum rhenium films originating from premixed targets with nominal compositions of $Mo_{30}Re_{70}$ and $Mo_{70}Re_{30}$. The measured bulk alloy compositions deviate from these values: the rhenium-rich alloy displays a composition of $Mo_{20}Re_{80}$, the same as the preferred co-sputtered alloy. The oxide species at the Mo 3d peaks are spectroscopically examined, and identified regarding their evolution into the bulk as well as due to reduction reactions during CVD [Scanlon et al., 2010; Baltrusaitis et al., 2015; Götz et al., 2016]. Carbon incorporation due to CNT growth is also observed for the thin films fabricated from premixed targets; it is in the bulk distinctly enhanced for the molybdenum-rich one.
In electrical characterization, a higher resilience to the CVD process for co-sputtered $Mo_{20}Re_{80}$ films is observed; the critical temperature only drops below $T_c = 8\,\mathrm{K}$ for growth times $> 20\,\mathrm{min}$. For shorter growth times, data indicates that the CVD process may have effects similar to the annealing discussed in [Aziz et al., 2014], i. e., enhancing the critical temperature and critical current density. In contrast, regarding electrical characterization both premixed molybdenum- and rhenium-rich films remain almost stable when exposed to the CVD procedure of 15 min duration [Hüttner, 2017].

Carbon nanotubes are grown onto prefabricated electrodes of $Mo_{20}Re_{80}$ using both sputtering techniques. Low-temperature transport measurements of these devices are shown in chapter 7. The transport spectroscopy for the co-sputtered device reveals a multiple quantum dots system which comes from a bundle of two carbon nanotubes at least. A four-terminal current-bias measurement is carried out but did not resolve supercurrents through the nanotubes as measured in previous work containing suspended carbon nanotube on MoRe alloys measurements [Schneider, 2014]. The stability diagrams of the premixed MoRe device exhibit a regular single quantum dot on both electron and hole transport regimes. Unfortunately, the platinum capping caused an huge interface resistance resulting in thick tunneling barriers.

In order to circumvent the restriction of suitable contact materials for the overgrowth technique, another fabrication approach was performed. The main objective of chapter 8 was to prove that carbon nanotubes can be stamped onto arbitrary target chips. It is shown that single-walled carbon nanotubes are transferred along with the stamped catalyst material and fall over prefabricated electrodes with a trench in between. In spite of a bad yield, room temperature characterization revealed characteristic clean carbon nanotube conductance curves as function of the global back gate voltage V_g. However, large contact resistances between stamped tubes and untreated electrodes were observed, even though the surface consists of rare metals like platinum. They are likely caused by insulating adsorbates of N_2 or O_2 molecules on the metal surface. The electrical contact was clearly improved by introducing an additional annealing step.

Low temperature measurements showed quantum dot behavior of carbon nanotubes, but was affected by additional features, like multiple dots and gate leakages.

In order to avoid such leakages, it is necessary to separate the tubes electrically from the stamp imprints. This can be realized by placing adjacent electrodes in between measuring geometry and stamp imprints. A carbon nanotube is then locally cut by applying large currents through the segments lying in between these additional electrodes, as already been demonstrated in [Waissman et al., 2013].

The transfer of carbon nanotubes being suspended in between two stamping mesas is an advancement of the attempt described here. First attempts in this direction resulted in a failure, see [Himmler, 2017]. The most important aspect for realization is the ratio of the mesa heights and the distance between both. As discussed in [Homma et al., 2009], a ratio of less than 0.5 leads to a decreasing yield of suspended nanotubes. Having in mind, that the whole measuring geometry plus possible cutting electrodes must have room in between both mesas, required distances of circa 15 µm need a height of 7.5 µm at least. Such mesas cannot be fabricated by the same RIE procedure anymore. Also wet chemical etching using HF for example is excluded due to undercut effects. Using quartz forks as stamps is a promising outlook, as shown in [Gramich et al., 2015]. A measurement setup will be used which enables the in-situ electrical characterization of a possible device immediately after stamping has been carried out. This offers the chance to reuse the device for further stamping tries if no CNT was transferred to this measuring circuit.

A necessity has taken a back seat during the development of the local stamping fabrication procedure, namely the confinement of the catalyst deposition. As already known from the overgrowth technique, a small area reserved for the growth catalyst leads to less numbers of outgrown tubes during CVD. As consequence, the number of tubes suspended over adjacent electrodes is hopefully reduced to one and even the probability to produce bundles of several tubes is decreased. The same result is expected for the growth on stamp chips. Especially for stamps, a lithography avoids deposition of too much catalyst material. This high amount is stamped or transferred to the device chips and results in undesired gate leakages since catalyst material as well as the attached carbon is electrically conducting and causes links to other devices or to the bare p^{++}-Si at the edges of the chips. The so-called catalyst lithography should be therefore always considered and performed in future stamping fabrication procedures, may it be on chips for the non-contact attempt or on mesas, pillars or forks using the contact-stamping method.

Appendix A

Fabrication methods, techniques and parameters

This chapter summarizes all fabrication techniques and procedures that have been used during this thesis. Furthermore, it should give an overview of the used setups and parameters.

A.1 Wafer material preparation

Starting point for the fabrication procedure is the 4" p^{++}-Si/SiO$_2$ wafer which is produced by the company "SiMat". It has a total thickness of 500...550 µm, in which the highly boron-doped silicon layer is capped by thermally grown silicon-oxide of 500 nm thickness.

A.1.1 Scribing

For the subsequent fabrication process smaller pieces of the wafer are in usage. In order to cut 4.5 mm · 4.5 mm, later 8.5 mm · 8.5 mm chips from the bare wafer, a diamond scriber is used. During the thesis, the old scriber "SÜSS HR 100" was replaced by the new "RV-129e" which enabled a proper breaking of the material at all.
At first, the wafer is broken into two halves, then a strip is broken with the width of the desired edge length. Afterwards, quadratic pieces are separated from that strip.
The predetermined breaking line is defined and deepened by moving the scriber twice or three times over the wafer with the oxide on top. The scriber applies a force to the wafer adjusted by a weight that is aligned to a scale bar. For that use, it is set to 5.5 cm on the scale bar which is equivalent to a force range among 134 to 160 cN. The breaking itself is carried out by placing the breaking line exactly over a fixed and round cannula plus pushing the material down at both sides with the help of two tweezers.

A.1.2 Precleaning

This precleaning procedure is carried out to remove all grains and dust from the wafer surface originating from the scribing as well as the residues from the fabrication or long time storage.

1. Immerge the quadratic chips into an acetone-filled beaker and put it into the ultrasonic bath.
2. Expose the chip to the US for at least 5 min.
3. Blow dry with N_2.
4. Storage in isopropanol.
5. Blow dry.
6. Insert the chips into the plasma cleaning device "Plasma-Preen I".
7. Expose the chips to oxygen plasma for 5 min at 50 % power at a pressure of 1.5 mbar.
8. Remove the chips from the plasma-preen after the process.

A.2 Cleaning

This is the usual performed cleaning step using two beakers with acetone, one with isopropanol and a N_2 blow dry gun.

1. Immerge the chip into an acetone beaker and leave it for 1 to 2 min.
2. Rinse with acetone spray bottle.
3. Immerge the chip into the second acetone beaker and leave it for about 1 min.
4. Blow dry and store the chip in the beaker filled with isopropanol until the subsequent process can start.
5. Blow dry.

A.3 Optical lithography

Optical lithography was used during this thesis to pattern the bond pads and leads plus rough alignment structures. In this procedure two spin-coaters have been used, namely the "CPS 10" by Semitec and later the "SPIN150i" by SPS-Europe. The spin parameters for the new one were adjusted such that the spin procedures are equivalent for the same resists. Two different resists of the Shipley series - S1805 and S1813 - were chosen for this process. The exposure is carried out in a mask aligner of type MJB3 by Karl Suss MicroTec containing a mercury UV lamp. Since the necessary exposure time is highly depending on the actual UV emission intensity as well as on the thickness of the mask, a dose test must be performed by varying only the exposure time before the real process is carried out. The subsequent development uses the "All Resist 300-47", short AR 300-47 developer.

1. After the last blow dry from the standard cleaning procedure (see section A.2), place the chip above the hole in the center of the spin coater chuck.
2. Set the spin parameters 4500 min^{-1} for 30 s at maximum acceleration.
3. Put some drops onto the chip until it is fully covered with resist.
4. Start the spin coater immediately.
5. Prebake the chip with the resist on it at 90 °C, the durations are 2 min for S1805 and 4 min for S1813.
6. Mount the chip into the mask aligner, align the chip to the desired mask using the set screws for x- and y-direction as well as for rotation. Put chip and mask together by using the lever and the small set screw for the z-direction.
7. Expose chip and mask to UV irradiation. For the same mask, the times are 85 s for S1805, and 2 min 15 s for S1813.
8. Develop the chip using AR 300-47. At the beginning of the thesis, the fluid was in motion using a stir bar which was later omitted. Also the time was reduced from 100 s to 40 s.
9. Stop the development by immerging into a cascade bath filled with clean water for at least 30 s.
10. Blow dry with N_2.

The bare places of SiO_2 define the metallic structures evaporated during the subsequent procedures.

A.4 Electron Beam Lithography

This sections contains the parameters for the resins, the SEM setups and the development step in the end.

A.4.1 PMMA spinning and usage

The solvent changed during the PHD time from chlorobenzene to anisole. Therefore the concentration of PMMA, i. e. Poly(methyl methacrylate) was adjusted. For example, PMMA-950k4% (chlorobenzene) was replaced by PMMA-950k5% (anisole) and PMMA-200k7% (chlorobenzene) was replaced by PMMA-200k9% (anisole). For spinning parameters see Tabulars A.1 and A.2.

sequence	acceleration min^{-1}/s	speed (min^{-1})	duration (s)
1st	10000	3200	5
2nd	750	6000	30

Table A.1: PMMA standard spin parameters for the new spin-coater SPIN150i.

sequence	acceleration (1) scale	speed (min^{-1})	duration (s)
1st	0	3000	5
2nd	9	8000	30

Table A.2: PMMA standard spin parameters for the old spin-coater CPS 10. The acceleration to the set speed can be adjusted to ten grades whereas "0" is the fast, "9" the slow setting. An exact measurement showed that the set speed during the second sequence was indeed only 6000 rpm.

The standard spin-on process for all PMMA fluids was performed in the following:

1. Clean the spin coater chuck from previous spin-on procedures so that the chip is sufficiently sucked onto the surface of the chuck and lying completely plane on it.

2. Suck few droplets of PMMA out of the bottle into a pipette. Store the pipette vertically in a way that its cannula does not touch anything else.
3. After the last blow dry from the standard cleaning procedure (see section A.2), place the chip above the centered hole of the spin coater chuck.
4. Set the standard spin programs depending on the used spin coater, see Tab. A.1 and Tab. A.2.
5. Start the spin coater. During the first spin-on sequence drop the PMMA onto the chip. The amount of PMMA drops is also depending on the size of the chip, f. ex. one drop is enough for a $4.5\,\mathrm{mm} \cdot 4.5\,\mathrm{mm}$ chip.
6. After the spin-on process has finished remove the chip from the chuck and put it onto the heating plate to harden the PMMA. Bakeout time is of 8 min at a set temperature 150 °C.
7. Further layers of PMMA should be spun on after the bakeout, and beginning from step 3.

Table A.3 shows the used anisole-based PMMA systems during this thesis.

PMMA layer,s	thickness (nm)	subsequent process
PMMA-200k9%	300-400	metal lift-off
PMMA-950k5%	300	RIE
PMMA-950k5%/PMMA-950k5%	600	RIE
PMMA-200k9%/PMMA-950k2%	$\geqslant 400$	catalyst deposition and lift-off
PMMA-200k9%/PMMA-950k5%	$\geqslant 500$	catalyst deposition and lift-off

Table A.3: Optimized PMMA systems for subsequent processes.

A.4.2 SEM

In the beginning the "Zeiss-Auriga" system has been used for EBL but was gradually replaced by the Supra-SEM system (which is also denoted as "Strunk-SEM") in which an interferometric stage leads to a more precise alignment. The procedure here is depicted using the "Strunk-SEM":

1. Build in the chips with the PMMA resin on it.

2. After pump down, switch on EHT. For all EBL processes, the 30 µm aperture at 25 kV acceleration voltage was used.

3. Adjustment of the beam (stigmatism and aperture align) is carried out at the Faraday Cup at a working distance of ca. 8.3 mm. This value is kept constant for the whole EBL process.

4. Measure the beam current by placing the gun directly over the hole on the Faraday Cup. For these settings the beam current usually ranges around 330 pA.

5. Move to the chip and focus the detector by using the z-manipulator.

6. Adjust the microscope and the lithography program coarsely. Use the large alignment markers and bars at the edges of the chip and mark the positions in the program. This has to be done for at least 5 places on a $8\,\mathrm{mm} \cdot 8\,\mathrm{mm}$ and until the stage angle correction is at about $\pm 2°$ and focus plane tilt $\leq 0.5°$.

7. Start lithography. The fine adjustment at the inner structures via image matching was reduced to every tenth structure by using the interferometric stage in the Strunk-SEM.

8. After lithography has finished, build the chip out of the setup.

A.4.3 Development

The development of the irradiated PMMA areas was carried out in the following:

1. Immerge the chip into a premixed solution of MIBK : isopropanol with a volume ratio of 1 : 3. The development time was also reduced from 2 min to 1 min 30 s.

2. To stop the development, immerge the chip directly into a beaker with pure isopropanol for 30 s at least.

3. Blow dry.

4. Check the developed structures using a microscope.

The last step is required every time. If the lithography was not successful, all subsequent processes on that chip will be a waste of time and material. In that case, put the chip into hot acetone to remove all PMMA and repeat the EBL until success.

A.5 Metal Evaporation setup I: Univex 450A

The Univex system offers two possibilities for film deposition, these are e-beam and thermal evaporation. The sources in the main chamber are filled with the desired materials each time before a session starts. Furthermore a special sample holder enables to place the chips closer to the evaporating sources which doubles the deposition rate. It is therefore called rate doubler in the following. The usual base pressure after a pumping time of ca. 1.5 h is of ca. $5 \cdot 10^{-6}$ mbar.

During this thesis the setup was used for the in-situ deposition of titanium and platinum in which titanium has been thermally evaporated and platinum by using the e-beam source. The procedure is depicted as follows:

1. Preparation. Glue the chips onto the rate doubler. Refill the evaporation targets if necessary. The platinum source for the e-beam target is used and the little vessel for the thermal evaporation of titanium. Insert all three items to the specified places in the chamber. Remove the cover from the sputter target.

2. Sink down the hoist and pump the chamber down to its base pressure range (ca. $5 \cdot 10^{-6}$ mbar).

3. Quartz sensor settings. These parameters should be set just before evaporation starts. Since the rate doubler as sample holder is used, the rate value on the sensor screen has to be doubled. The parameters for the sensor are:

material	density (g/cm^3)	z-ratio (1)	tooling factor (1)
titanium	4.50	0.628	140
platinum	21.09	0.245	120

4. Ar-sputtering. The surface of the chip is cleaned and roughened by using the sputtering target. The acceleration voltage is set to 2 kV. Argon is injected into the main chamber and the flow is controlled by a needle valve: at a chamber pressure of ca. $3 \cdot 10^{-3}$ mbar the emission current is of 20 mA. Place the rate doubler above the sputtering target and clean the surface of the chips for 2 min.

5. Thermal evaporation of titanium. White heat is observed at 140 A set to the controller, at 165...190 A, the sensor measures a rate of 0.2 to 0.3 Å/s. Place the rate doubler above the source as soon as titanium is evaporated into the chamber.

6. Pumping sequence. With the help of the ion getter effect during the titanium evaporation the main chamber is pumped down to a pressure of $4 \cdot 10^{-7}$ mbar within several hours, usually over night.

7. E-beam evaporation of platinum. Acceleration voltage is set to 6 kV and the emission current is controlled by a potentiometer. It should never exceed 300 mA. For platinum evaporation potentiometer values of 3.3 to 4.0 are used to reach an evaporation rate of 0.2 to 0.9 Å/s at the quartz sensor. The chamber pressure for these settings is of 0.8 to $1.1 \cdot 10^{-5}$ mbar during evaporation.

8. Removal. Switch off power supply for the evaporation systems and for the turbo pump. After 20 min for turbo pump run down, start carefully venting the chamber with N_2. Open the hoist and put the sample holder with the metallized chips out of the chamber.

A.6 Metal Evaporation setup II: Orion

The Orion setup consists of the ATC-Orion 5 sputtering system in combination with an electron-beam evaporator. The evaporator is installed below the sputtering system and linked to the main chamber using the central source. All five sources can carry a 2” sputter target. The sputtering and the e-beam evaporation system are cooled by a cooling water cycle. The base pressure of the system is in the 10^{-8} to low 10^{-7} mbar range.

All chips are glued onto a sample holder and transferred into the load lock of the system. After the load lock is pumped down to pressures of about $5 \cdot 10^{-6}$ mbar, the sample holder is transferred into the main chamber and placed upon a stage which allows the holder to be moved in the z-direction as well as to be rotated and tilted. The height and tilt can be adjusted on scale bars in inches, whereas rotation is set by a lever.

The setup was used for co-sputtering MoRe alloys, evaporation of titanium and platinum and sputtering premixed MoRe targets.

A.6.1 Co-sputtering MoRe

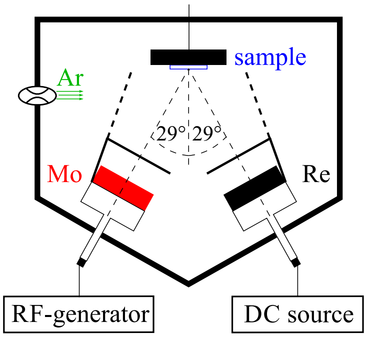

Figure A.1: Sketch of the Orion dual-source sputtering setup. The sample holder is placed approximately 13.5 cm above and in the middle of both targets which are mounted at a distance of circa 15 cm to each other. The molybdenum target is driven by a radiofrequency source with impedance matching, the rhenium target using a dc source. The mass flow controller setting the argon flow into the chamber is also indicated. From [Götz et al., 2016], © IOP Publishing Limited 2016, reprinted with permission.

1. Place the sample holder in the chamber as follows:

parameter	position	remark
height	3.6	at the transfer height
rotation	-90°	lever points to wall
tilt	34	plane to the floor

2. Inject argon gas into the main chamber. Set a rate of 40 sccm to the Bronkhorst flow controller.

3. Close the shutter in front of the turbo pump of the main chamber until the pressure is in between $1 \cdot 10^{-1}$ to $3 \cdot 10^{-1}$ mbar.

4. Check whether the RF power supply with impedance matcher is connected to the source containing the molybdenum target.

5. Ignite the plasma above the molybdenum target. Directly after the ignition, set the load and tune capacitances for the impedance matcher to keep the reflected power ≤ 4 W. These values are strongly depending on the set power and chamber pressure, f. ex. at this point for $P_{\text{Mo}} = 75$ W you need $(C_{\text{load}}, C_{\text{tune}}) = (310, 500)$.

6. If the plasma remains stable (look into the main chamber) reduce the main chamber pressure to $7 \cdot 10^{-3}$ mbar by opening the shutter in front of the turbo pump.
7. Reset $(C_{\text{load}}, C_{\text{tune}})$-tuple quickly, for example to about $(296, 595)$ for $P_{\text{Mo}} = 75\,\text{W}$.
8. Ignite the plasma above the rhenium target using the dc power supply.
9. If both targets are still sputtered, open the shutters above using the switches. Otherwise you must repeat the steps beginning from step 5.
10. Cover the inspection glass immediately.
11. Keep the main chamber pressure at $7 \cdot 10^{-3}$ mbar over the whole deposition time.
12. The deposition rate to the chips is determined by stopping the time and profiling the films after the process for several times. The results are

P_{Re} (W)	P_{Mo} (W)	rate (Å/s)
43	75	0.8
43	200	2.1

13. To finish the deposition, push the switches to close both shutters above the targets.
14. Switch off the power at both devices.
15. Set the argon flow controller to zero and reopen the shutter in front of the turbo pump.
16. Reset the stage containing the sample holder to the transfer position.
17. Put the sample holder back to the load lock to take it out of the setup.

A.6.2 E-beam evaporation

1. Place the sample holder in the chamber as follows:

parameter	position	remark
height	4.1	at the height of the quartz sensor
rotation	0	lever parallel to load lock
tilt	34	plane to the floor

2. Align the e-beam gun to the desired evaporation source.
3. Switch on the quartz sensor control device. Choose the program for the desired material. The quartz sensor parameters for certain materials are:

material	density $(\mathrm{g}/\mathrm{cm}^3)$	z-ratio (1)	tooling factor (1)
titanium	4.50	0.63	130
platinum	21.09	0.25	101
gold	19.3	0.38	122

4. Switch on the power supply for the e-gun.
5. The controller for the potentiometer is set to milliampères ("MA"), push the on-button.
6. Slightly increase the emission current by turning the knob.
7. The deposition rate at the sample holder and the resulting film thickness can be checked at the quartz sensor. Depending on the base pressure at the beginning, the main chamber pressure slightly increases to about $2 \cdot 10^{-7}$ mbar.
8. Decrease the emission current slowly so that the exact film thickness at the chip is reached.
9. Turn the knob to its lowest value and push the off-button. Switch off the power supply for the e-gun.
10. Reset the stage containing the sample holder to the transfer position.
11. Put the sample holder back to the load lock to take it out of the setup.

A.6.3 Sputtering premixed MoRe

1. Place the sample holder in the chamber as follows:

parameter	position	remark
height	4.1	at the height of the quartz sensor
rotation	0	lever parallel to load lock
tilt	47	plane to the $\mathrm{Mo}_{30}\mathrm{Re}_{70}$ target
tilt	21	plane to the $\mathrm{Mo}_{70}\mathrm{Re}_{30}$ target

2. Switch on the quartz sensor control device. Choose the program for the desired material. The quartz sensor parameters for certain materials are:

material	density (g/cm^3)	z-ratio (1)	tooling factor (1)
$Mo_{30}Re_{70}$	17.89	0.18	92
$Mo_{70}Re_{30}$	13.45	2.25	219

3. Inject argon gas into the main chamber. Set a rate of 40 sccm to the Bronkhorst flow controller.
4. Close the shutter in front of the turbo pump of the main chamber until the pressure is in between $5 \cdot 10^{-2}$ to $1 \cdot 10^{-1}$ mbar .
5. Ignite the plasma above the desired target using the dc power supply. The set power for $Mo_{30}Re_{70}$ is 43 W, and for $Mo_{70}Re_{30}$ 75 W.
6. Reduce chamber pressure quickly to $7 \cdot 10^{-3}$ mbar.
7. If the plasma remains stable, open the shutter by using the switch and cover the inspection glass immediately. Otherwise you have to repeat beginning from step 4.
8. The rate and the resulting film thickness can be controlled at the quartz sensor device. For the power settings mentioned above, a rate of ca. 0.7 Å/s is obtained for both targets.
9. As soon as the desired film thickness is achieved, close the shutter above the target.
10. Switch off the power at the dc supply.
11. Set the argon flow controller to zero and reopen the shutter in front of the turbo pump.
12. Reset the stage containing the sample holder to the transfer position.
13. Put the sample holder back to the load lock to take it out of the setup.

A.7 Lift-off

The lift-off process takes place in a hot acetone environment using a heating plate, a tighten beaker and several syringes. The usage of ultrasonic pulses is usually avoided.

The chips usually glued upon a sample holder from a previous evaporation process. This glue at the backside of the chip has to be removed by carefully rubbing against a clean room nonwoven.

1. Immerge the chip into an acetone beaker. Close the beaker with an adequate plastic lid.
2. Store the beaker on a heating plate with a set temperature of 60 °C for at least 1 h.
3. Lift-off by using a syringe filled with acetone. The chip must be in the liquid over the whole time. This step is repeated twice with two syringes having cannulas of varying thickness.
4. Check the success in a microscope whereas the chip is stored in a petri dish filled with acetone.
5. If necessary: repeat step 3 including exposure to short ultrasonic pulses.
6. Cleaning according to procedure A.2.

A.8 Reactive ion etching (RIE)

All plasma-etching procedures were carried out using the Oxford Plasmalab 80 Plus System (internally also denoted as "RIE Strunk"). When the hoist is up, chips can be placed in the center of the substrate electrode. After closing and pump down the base pressure ranges in between 2 to $3 \cdot 10^{-6}$ Torr. This pressure unit is used in the control software "RIE 2000" by default and therefore all recipes concerning RIE are expressed as Torr or mTorr. Some conversions are

$$\begin{aligned} 10\,\text{mTorr} &\approx 1.333 \cdot 10^{-2}\,\text{mbar}\,, \\ 1\,\text{mTorr} &\approx 1.333 \cdot 10^{-3}\,\text{mbar}\,, \\ 10^{-6}\,\text{Torr} = 10^{-3}\,\text{mTorr} &\approx 1.333 \cdot 10^{-6}\,\text{mbar}\,. \end{aligned}$$

The gases flowing into the chamber are controlled by electronic flow meters and inserted by a shower head gas inlet optimized for RIE. The plasma is ignited using a 13.56 MHz rf-source that drives a parallel plate reactor. The substrate electrode acts as one plate which linked to the rf-source, and the shower head gas inlet as the other plate connected to ground. The system provides the following process gases: sulfur hexafluoride SF_6, fluoroform CHF_3 (other names are "carbon trifluoride", "methyl trifluoride" and officially "trifluoromethane"), oxygen O_2, argon Ar, hydrogen H_2, and methane CH_4. The tabulars A.4 and A.5 should give an overview of the single etching steps. The subsequent etching recipes were used during the fabrication procedures. The recipes and also the specific steps were optimized during the PHD time. The most important change was to replace pure CHF_3 by a mixture of CHF_3/O_2 as process gases for SiO_2 etching. This was done in order to avoid deposition of organic carbon-containing layers (internally also denoted as "teflon") on the surface of the chip.

A.8.1 Overview steps

step	flow (sccm)	pressure (mTorr)	remark
Pump	-	-	2 min chamber pumping
Ar-Purge	50	100	10 s purging with argon

Table A.4: Pump and Purge step, short PAP. This recipe is repeated twice at least and added after etching every time before the venting sequence starts.

gas,es	flow (sccm)	pressure (mTorr)	power (W)	etching rate (nm/min)	for materials
O_2	100	100	200	chamber cleaning	
O_2/SF_6	80/20	100	250	chamber cleaning	
SF_6/Ar	20/10	15	100	41 33 > 150	MoRe alloys or Pt SiO_2 PMMA
CHF_3/O_2	50/5	55	150	27 - 28 > 200	SiO_2 PMMA
Ar	40	40	150	8	all materials
O_2	50	100	200	≈ 100	PMMA or S1805

Table A.5: Single RIE steps with set parameters and etching rates for several materials. The gas compositions and the flow into the chamber, the process pressure as well as the power to the RF source were set constant for all subsequent etching recipes.

A.8.2 Process I - Deepen bond pads

1. Chamber cleaning with O_2/SF_6 plus PAP according to Tab. A.4.
2. Etching into SiO_2 using CHF_3/O_2.
3. Etching everything using Ar.
4. PAP.

A.8.3 Process II - Etching mask

1. Chamber cleaning with O_2/SF_6.
2. Chamber Conditioning with SF_6/Ar plus PAP according to Tab. A.4.
3. Etching of MoRe and SiO_2 using SF_6/Ar.
4. PAP three times.
5. Etching into SiO_2 using CHF_3/O_2.
6. Etching everything using Ar.
7. PAP.

A.8.4 Process III - Trench etching

1. Chamber cleaning with O_2/SF_6 plus PAP according to Tab. A.4.
2. Etching into SiO_2 using CHF_3/O_2.
3. Etching everything using Ar.
4. PAP.

A.9 Carbon nanotube growth catalyst

The growth catalyst consists of three main solid parts which are solved in methanol or isopropanol. This fluid is therefore denoted as "catalyst suspension" in the following. The three solid parts are:

1. Aluminumoxide Al_2O_3 nanopowder. The primary particle size is of 14 nm and the specific surface area of the material is of $85 \dots 115\,\mathrm{m^2/g}$. It provides a large surface area for the catalyst. It is produced by Degussa GmbH.
2. Molybdenyl acetylacetonate, short $MoO_2(acac)_2$.
   Exact linear formula is $\left[CH_3COCH = C(O^-)CH_3\right]_2 MoO_2$. This powder is the first catalytic active substance for CNT growth exhibiting a yellow ocher color. It is produced by Sigma-Aldrich Chemie GmbH.
3. Iron(III) nitrate nonahydrate $Fe(NO_3)_3 \cdot 9H_2O$. The second catalytic active material is delivered as violet crystalline grains which are stomped to a smaller size. It is fabricated by Fluka Chemie AG, later Sigma-Aldrich Chemie GmbH.

There are three different catalyst suspensions which have been used for the CNT growth for this thesis.

A.9.1 Catalyst Suspension I

This suspension was prepared at the end of 2013.

Substance	Methanol (solvent)	Al_2O_3	$MoO_2(acac)_2$	$Fe(NO_3)_3{\cdot}9H_2O$
Amount	30 ml	30 mg	10 mg	40 mg

Table A.6: Catalyst suspension I.

A.9.2 Catalyst Suspension II

This suspension was prepared on November 6th, 2015.

Substance	Isopropanol (solvent)	Al_2O_3	$MoO_2(acac)_2$	$Fe(NO_3)_3{\cdot}9H_2O$
Amount	30 ml	30 mg	11 mg	40 mg

Table A.7: Isopropanol-based catalyst suspension commonly used for stamp chips.

A.9.3 Catalyst Suspension III

This suspension was prepared on April 28th, 2016.

Substance	Methanol (solvent)	Al_2O_3	$MoO_2(acac)_2$	$Fe(NO_3)_3 \cdot 9H_2O$
Amount	30 ml	30 mg	8.1 mg	41 mg

Table A.8: Catalyst suspension III.

After the solid parts have been mixed and put into the solvent, the bottle containing the suspension is exposed to the ultrasonic bath for at least 1 h.

A.10 Catalyst Deposition and Lift-off

1. Leave the bottle with the catalyst suspension for at least 45 min in the ultrasonic bath.
2. Clean the pipettes inside and outside using spray bottles: first with isopropanol with subsequent blow dry, then with methanol (only if a methanol based catalyst suspension is used) plus blow dry. Storage of the pipettes in a way such that the cannula does not touch anything, f.ex. upon a beaker with the cannula lying in its opening.
3. Heat up lift-off-acetone in a beaker including a magnetic bar upon a heating plate in combination with a magnetic stirrer. Set temperature is 60 °C, the beaker is covered using an aluminum foil until it is needed. Prepare a beaker with isopropanol close to the lift-off-acetone beaker.
4. Immerge the precleaned pipette into the suspension bottle and suck some droplets through the cannula. During this step the bottle is still placed in the running ultrasonic bath but its screw plug is removed.
5. Put some few droplets onto the chip until the suspension forms a bowing. Wait some seconds.
6. Short and hard blow dry with N_2. The chip must be fixed with the tweezers during that step.
7. Bake the chip on a heating plate for 6 min with a set temperature of 150 °C.
8. Lift-off preparation: hold the chip with the tweezers upside down. This can be achieved securely with the following instruction: take the chip with one tweezers

and rotate to the left side by 90°, then grab with another tweezers from the opposite direction.

9. Lift-off: uncover the beaker including hot acetone and immerge the chip into the fluid directly upon the rotating stir bar. Hold the chip at this place for 4 min. After that time put the chip directly into the beaker with isopropanol for 30 s to stop the lift-off process. Afterwards, carefully upturn the chip and blow dry with N_2.

10. Catch a glimpse under the microscope. The catalyst particles at the predefined places on a SiO_2 substrate are visible using the 100-times magnification lens.

A.11 Setup for chemical vapor deposition and growth process

All CNT growth processes were performed using the tube furnace TF55030C-1 fabricated by Lindberg/Blue. The furnace is placed in a flow box and carries a quartz tube which can be linked to several gas lines; these are argon (purity grade 6.0), hydrogen (purity grade 5.0), methane (purity grade 2.5) and ethene (purity grade 2.5). The flow can be adjusted by manual meters for all lines and for the H_2- as well as for the CH_4-line by electronic mass flow controllers from Bronkhorst. The standard recipe was established in Regensburg over the last years and contains the following steps:

1. Place the chip containing the catalyst onto a glass plate suitable for a quartz tube with KF25 flanges at both ends. The tube itself must be clean, i.e. it has been exposed to processes only using methane and hydrogen as growth gases.

2. Move the glass plate with the chip on it carefully in the tube until the chip is placed directly above the temperature sensor.

3. Connect the tube with the gas inlet and exhaust line by using the insulating clips and metallic O-rings.

4. Flush the lines as well as the tube by opening the gas inlet for Ar, H_2 and CH_4 with the highest possible flow rate for at least 2 min.

5. Set the flow rates for CH_4 to 10 sccm and for H_2 to 20 sccm at the electronic mass flow controllers. The Ar flow is set at the manual flow meter to level 14 what is equal to 1500 sccm.

6. After the gas flow has stabilized close the CH_4 line at the plug after the mass flow controller.
7. Close the furnace and heat the tube up to a set temperature of 850 °C. During that ramp up the tube is flushed by an Ar/H_2 gas mixture with a flow ratio of $1500/20$.
8. As soon as the actual temperature remains stable at 850 °C, close the Ar line and reopen the plug at the CH_4 line. The carbon nanotube growth immediately starts. During the growth step, the tube is therefore flushed with a CH_4/H_2 gas mixture with a flow ratio of $10/20$. It lasts usually between $10 \ldots 20$ min.
9. Stop the growth process by closing the plug at the CH_4 line. Reopen the Ar line and open the lid of the furnace.
10. The chip is cooled down in a Ar/H_2 atmosphere with a flow ratio of $1500/20$ until the sensor shows an actual temperature of 100 °C.
11. Close all gas lines to the quartz tube and separate the tube from the line at the flanges.
12. Move the glass plate carefully out of the tube. Then, put the sample in an ESD-safe box using metallic tweezers.

A.12 Preparation and bonding

After the growth step has been carried out, the chip with all possible devices is tested at the probe station. The most promising devices (see chapter 3 for selection rules) on the chips will be further processed. Two-component silver epoxy is used to fix the chips into the chipcarrier because it is still conductive at low temperatures and provides a connection between the plane and the p^{++}-Si-device-chip-layer acting both as global back gate to the nanotubes.

A.12.1 Installing into the chipcarrier

1. Precleaning of the chipcarriers following section A.2.
2. Preparation of the two component silver epoxy. Mixing up components A and B in a little plastic bowl using toothpicks.
3. Scratching the backside of the chip with a small blade.

4. Placing a small amount of the silver epoxy into the chipcarrier. A tip of the toothpick is enough.

5. Put the chip into the carrier. Carefully push against the epoxy by touching at the edges with metallic tweezers.

6. Check under the microscope. If epoxy has been swollen from the ground to the top of the chip, the devices may be shortcut to the back gate.

7. Let the epoxy dry for at least one day.

A.12.2 Bonding

The chip is bonded at the aluminum bonder "West Bond - Model 5400 B". A prepared bond plan serves as orientation.

1. Testing. The bonder is on, check all connections to ground using a multimeter. The voltage drop (ac and dc) between clamp and chuck must not be higher than 10 mV.

2. Place the chipcarrier onto the chuck.

3. Place the bonds. Parameters are:
    - Bond 1, on the chipcarrier: 180 W bond power, 100 ms bond time.
    - Backbend is on, set to 60 steps.
    - Bond height is set to 60 to 80 steps for short bonds, 105 to 120 steps for long bonds.
    - Bond 2, on the bond pad: 140 W bond power, 95 ms bond time.
    - Clamps are closed over the whole time.

4. After bonding has been finished, put the chipcarrier back into the ESD-safe box. The samples are ready for installation into the cryostat.

Appendix B

Device fabrication recipes

This chapter contains detailed fabrication recipes of the three devices which are presented in this thesis.

B.1 Platinum sample

B.1.1 Metallization I for bond pads and outer leads

1. Optical Lithography: S1805 resist, 90 s exposure, 60 s development time.
2. RIE: Deepen structures using Argon plasma (see Tab. A.5) by 50 nm.
3. Evaporation: In the Orion chamber, see section A.6. Thicknesses are 15 nm Ti, followed by 85 nm Pt. Step height 50 nm expected.
4. Lift-off.

B.1.2 Metallization II

1. EBL: Using PMMA-200k7%. EBL is performed at the Auriga-SEM. Mask parameters: electrode width of 1.5 µm and trench length of 1.2 µm. Development as standard.
2. Evaporation in the Orion chamber, see section A.6. Thicknesses are 10 nm Ti, followed by 40 nm Pt.
3. Lift-off.

B.1.3 Reactive ion etching

For trench etching, using recipe as stated in subsection A.8.

- 3 min 42 s in CHF_3/O_2-plasma.
- 30 s in Ar-plasma.

In total, 104 nm of SiO_2 were removed. The trench depth in total is of 150 nm.

B.1.4 Catalyst deposition and lift-off

1. EBL: double layer of PMMA-200k7%/PMMA-950k2%, performed at the Auriga-SEM. Development standard. The predefined deposition area is a triangle of 5 µm edge length placed into the center of the inner structures. The edge-to-edge distance (the distance of the triangle edge to the inner edge of the inner electrode) is of 4.6 µm.
2. Deposition and Lift-off: standard procedure as written in section A.10. Catalyst was taken from suspension according to Table A.6.

B.1.5 Chemical vapor deposition

On 14/02/2014, CVD was performed using standard growth procedure, i. e. 10/20 sccm CH_4/H_2 flow for 20 min.

B.1.6 Bond plan chip BB

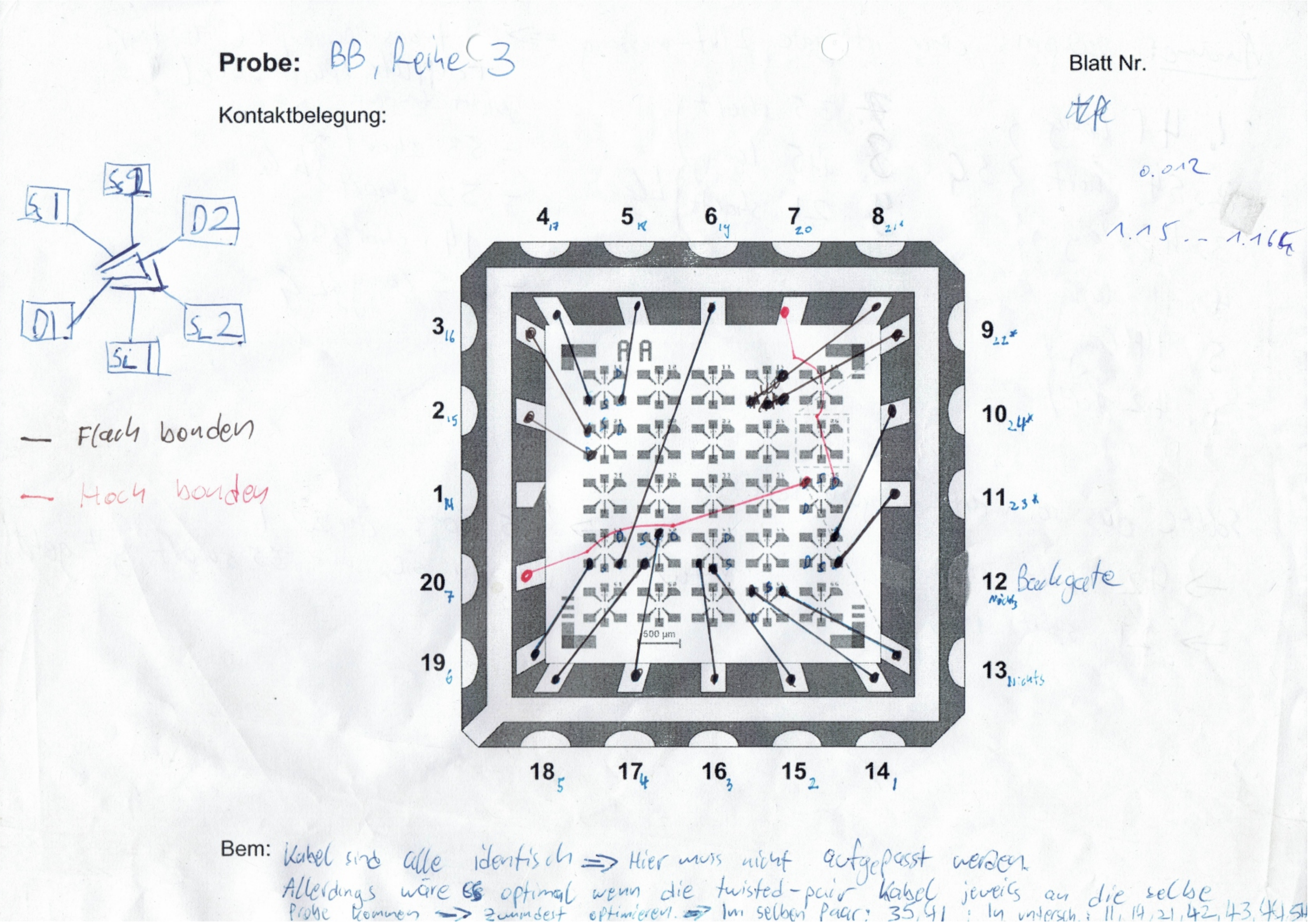

Bem: Kabel sind alle identisch ⇒ Hier muss nicht aufgepasst werden.
Allerdings wäre es optimal wenn die twisted-pair Kabel jeweils an die selbe
Probe kommen ⟶ zumindest optimieren. ⇒ Im selben Paar: 35, 41 ; In untersch.: 11, 14, 21, 42, 43, 44, 5

Figure B.1: Bondplan of Chip BB-TiPt. The notes are Felix' annotations.

B.2 Co-sputtered MoRe sample

B.2.1 Metallization I

1. Optical Lithography: S 1813 resist, 125 s exposure, 60 s development time.
2. RIE: Deepen structures using process as stated in subsection A.8. CHF_3/O_2 step for 150 s and Ar step for 60 s, depth is of 76 nm.
3. Evaporation in the Univex, see section A.5: Evaporation of 6 nm titanium; presputtering for 45 s; evaporation of 95 nm platinum. Step height of 26 nm expected.
4. Lift-off after 12 hours in hot acetone, following recipe in section A.7.

B.2.2 Metallization II

1. EBL. Mask for squares with 70 µm edge length. Resin PMMA-200k9% is used. EBL performed at the Supra-SEM using 120 µm aperture at 25 kV acceleration voltage, and 4156 pA beam current. Development as standard.
2. Evaporation in the Orion chamber, see section A.6: Co-sputtering of $Mo_{20}Re_{80}$ according to subsection A.6. Power settings are $P_{\mathrm{Mo}} = 75\,\mathrm{W}$, and $P_{\mathrm{Re}} = 43\,\mathrm{W}$, settings for impedance matching at deposition $(C_{\mathrm{load}}, C_{\mathrm{tune}}) = (296, 595)$. Sputtering time is of 750 s, resulting in a thickness on chip of 57 nm.
3. Lift-off after 12 hours in hot acetone following recipe in section A.7.

B.2.3 Etching mask

1. EBL using PMMA-950k5% at the Supra-SEM: aperture size 30 µm, acceleration voltage 25 kV, and beam current of 315 pA. Development standard. Mask parameters: electrode width of 1.5 µm and trench length of 500 nm.
2. RIE: Etching mask recipe used, see subsection A.8:
    - 2 min in SF_6 plasma
    - 5 min 30 s in CHF_3/O_2-plasma.
    - 30 s in Ar-plasma.
3. Cleaning. The chips are put into acetone beaker directly after removing from RIE. Exposure to short ultrasonic pulses by holding upside-down with tweezers. Storage in hot acetone for about 1 hour.

B.2.4 Catalyst deposition and lift-off

1. EBL: double layer of PMMA-200k9%/PMMA-950k2%, performed at the Supra-SEM. Development standard. The predefined deposition area is a rectangle with dimensions of 10 µm · 2 µm placed into the center of the inner structures at position 32. The edge-to-edge distance is of 4.4 µm.
2. Deposition and Lift-off: standard procedure as written in section A.10. Catalyst was taken from suspension according to Table A.6.

B.2.5 Chemical vapor deposition

On 26/02/2015, CVD was performed using standard growth procedure, i.e. 10/20 sccm CH_4/H_2 for 20 min.

B.2.6 Bond plan Chip AA

		
Sample	**Lead**	**PIN**
15	b	8
15	e	11
15	a	7
15	d	9
33 Low	a	5
33 Low	f	17
33 Low	d	13
33 Low	e	15
32 Up	a	20
32 Up	f	19
32 Up	b	3
32 Up	c	4

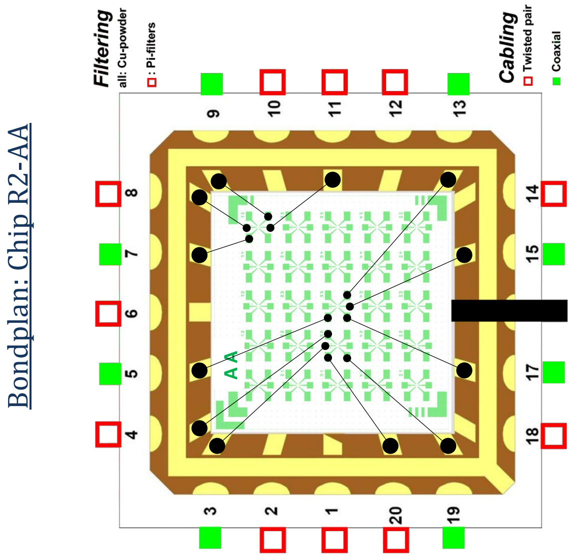

Figure B.2: Bondplan of Chip AA of co-sputtered MoRe.

B.3 Premixed MoRe sample

B.3.1 Metallization I

1. Optical Lithography: S 1813 resist, 135 s exposure, 45 s development time.
2. RIE: Deepen structures using process as stated in subsection A.8. CHF_3/O_2 step for 160 s and Ar step for 60 s, depth is of 80 nm.
3. Evaporation in the Univex, see section A.5: Presputtering for 2 min; evaporation of 10.8 nm titanium; presputtering for 2 min 30 s; evaporation of 96 nm platinum. Step height of 20 nm expected.
4. Lift-off after five hours in hot acetone, following recipe in section A.7.

B.3.2 Metallization II

1. EBL using PMMA-200k9% at the Supra-SEM. Mask parameters: electrode width of 2.5 µm and trench length of 850 nm. Development as standard.
2. Evaporation in the Orion chamber, see section A.6: Sputtering of $Mo_{30}Re_{70}$ target according to subsection A.6, thickness on chip is of 50.2 nm. In-situ e-beam evaporation of platinum according to subsection A.6, thickness is of 10.0 nm in total.
3. Lift-off following recipe in section A.7.

B.3.3 Reactive ion etching

Trench etching recipe used, see subsection A.8:

- 3 min 42 s in CHF_3/O_2-plasma.
- 45 s in Ar-plasma.

107 nm of SiO_2 were removed, and also 7 nm from the platinum capping layer of the inner structures by the Ar-plasma step. The trench depth in total is of 160 nm. Since the last Ar-step also etches the metallized surface, circa 6 nm of the platinum capping layer are removed; the expected after-RIE thickness of the capping is therefore of 3 . . . 4 nm.

B.3.4 Catalyst deposition and lift-off

1. EBL: double layer of PMMA-200k9%/PMMA-950k5%, performed at the Supra-SEM. Development standard. The predefined deposition area is a reduced ellipse with semi axis lengths of 16 µm, respectively 2 µm placed into the center of the inner structures at position 45. The edge-to-edge distance is of 3.5 µm.

2. Deposition and Lift-off: standard procedure as written in section A.10. Catalyst was taken from suspension according to Table A.8.

B.3.5 Chemical vapor deposition

On 11/11/2016, CVD was performed using standard growth procedure, i.e. 10/20 sccm CH_4/H_2 for 15 min.

B.3.6 Bond plan AC

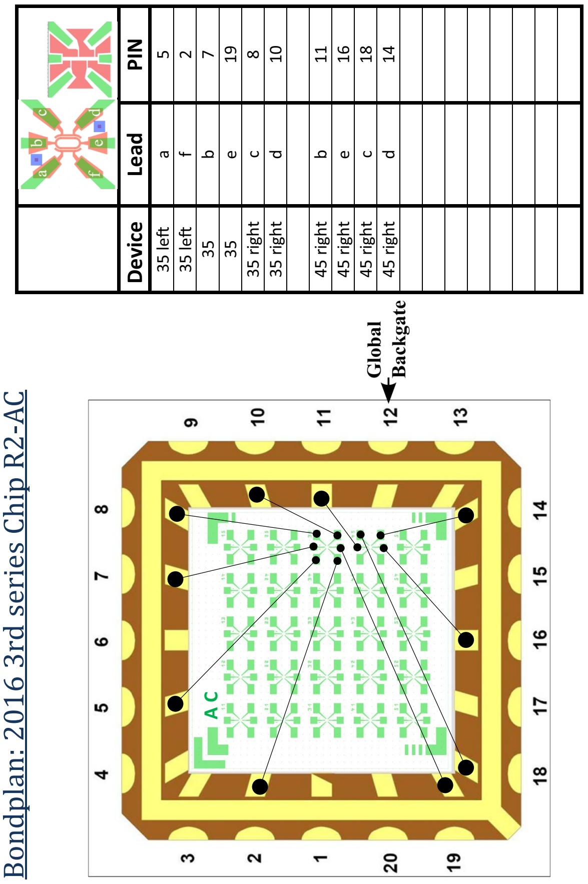

Device	Lead	PIN
35 left	a	5
35 left	f	2
35	b	7
35	e	19
35 right	c	8
35 right	d	10
45 right	b	11
45 right	e	16
45 right	c	18
45 right	d	14

Figure B.3: Bondplan Chip AC.

Bibliography

[Anderson, 1961] P. W. Anderson. *Localized Magnetic States in Metals*. `Physical Review` **124** (1), pp. 41–53, (Oct. 1961). DOI: `10.1103/PhysRev.124.41` (cit. on p. 30).

[Averin et al., 1991] D. V. Averin, A. N. Korotkov, and K. K. Likharev. *Theory of single-electron charging of quantum wells and dots*. `Physical Review B` **44** (12), pp. 6199–6211, (Sept. 1991). DOI: `10.1103/PhysRevB.44.6199` (cit. on p. 27).

[Aziz et al., 2014] M. Aziz, D. C. Hudson, and S. Russo. *Molybdenum-rhenium superconducting suspended nanostructures*. `Applied Physics Letters` **104**, p. 233102, (2014). DOI: `10.1063/1.4883115` (cit. on pp. 108, 109, 139).

[Balshaw, 2001] N. H. Balshaw. *Practical Cryogenics - An Introduction to Laboratory Cryogenics*. Oxford Instruments Superconductivity Limited, 2001. ISBN: 0952759403 (cit. on p. 47).

[Baltrusaitis et al., 2015] J. Baltrusaitis, B. Mendoza-Sanchez, V. Fernandez, R. Veenstra, N. Dukstiene, A. Roberts, and N. Fairley. *Generalized molybdenum oxide surface chemical state XPS determination via informed amorphous sample model*. `Applied Surface Science` **326**, pp. 151–161, (2015). ISSN: 0169-4332. DOI: `10.1016/j.apsusc.2014.11.077` (cit. on pp. 112, 139).

[Beenakker, 1991] C. W. J. Beenakker. *Theory of Coulomb-blockade oscillations in the conductance of a quantum dot*. `Physical Review B` **44** (4), pp. 1646–1656, (July 1991). DOI: `10.1103/PhysRevB.44.1646` (cit. on p. 23).

[Benyamini et al., 2014] A. Benyamini, A. Hamo, S. Viola Kusminskiy, F. von Oppen, and S. Ilani. *Real-space tailoring of the electron-phonon coupling in ultraclean nanotube mechanical resonators*. `Nature Physics` **10** (2), pp. 151–156, (Jan. 2014). ISSN: 1745-2473. DOI: `10.1038/nphys2842` (cit. on pp. 8, 81).

[Berndt, 2016] D. Berndt. *Stamp transfer of carbon nanotubes for nano-electromechanics*. Master thesis. Universität Regensburg, (June 2016) (cit. on pp. 129, 130).

[Bethune et al., 1993] D. S. Bethune, C. H. Klang, M. S. de Vries, G. Gorman, R. Savoy, J. Vazquez, and R. Beyers. *Cobalt-catalysed growth of carbon nanotubes with single-atomic-layer walls*. `Nature` **363** (6430), pp. 605–607, (June 1993). DOI: `10.1038/363605a0` (cit. on pp. 7, 11).

[Blase et al., 1994] X. Blase, L. X. Benedict, E. L. Shirley, and S. G. Louie. *Hybridization effects and metallicity in small radius carbon nanotubes*. `Physical Review Letters` **72** (12), pp. 1878–1881, (Mar. 1994). DOI: `10.1103/PhysRevLett.72.1878` (cit. on p. 18).

[Blien et al., 2016] S. Blien, K. J. G. Götz, P. L. Stiller, T. Mayer, T. Huber, O. Vavra, and A. K. Hüttel. *Towards carbon nanotube growth into superconducting microwave resonator geometries*. `physica status solidi (b)` **253** (12), pp. 2385–2390, (2016). ISSN: 1521-3951. DOI: `10.1002/pssb.201600217` (cit. on p. 37).

[Borda et al., 2003] L. Borda, G. Zaránd, W. Hofstetter, B. I. Halperin, and Jan von Delft. *SU(4) Fermi Liquid State and Spin Filtering in a Double Quantum Dot System*. `Physical Review Letters` **90** (2), p. 026602, (Jan. 2003). DOI: `10.1103/PhysRevLett.90.026602` (cit. on p. 68).

[Cao et al., 2005] J. Cao, Q. Wang, and H. Dai. *Electron transport in very clean, as-grown suspended carbon nanotubes*. `Nature Materials` **4**, pp. 745–749, (Sept. 2005). DOI: `10.1038/nmat1478` (cit. on pp. 8, 16, 25, 37, 42, 56, 125, 137).

[Castro Neto et al., 2009] A. H. Castro Neto, F. Guinea, N. M. R. Peres, K. S. Novoselov, and A. K. Geim. *The electronic properties of graphene*. `Reviews of Modern Physics` **81** (1), pp. 109–162, (Jan. 2009). DOI: `10.1103/RevModPhys.81.109` (cit. on pp. 7, 19).

[Charlier et al., 2007] J.-C. Charlier, X. Blase, and S. Roche. *Electronic and transport properties of nanotubes*. `Reviews of Modern Physics` **79** (2), pp. 677–732, (May 2007). DOI: `10.1103/RevModPhys.79.677` (cit. on p. 11).

[Choi et al., 2005] M.-S. Choi, R. López, and R. Aguado. *SU(4) Kondo Effect in Carbon Nanotubes*. `Physical Review Letters` **95** (6), p. 067204, (Aug. 2005). DOI: `10.1103/PhysRevLett.95.067204` (cit. on p. 69).

[Cleland, 2003] A. N. Cleland. *Foundations of nanomechanics: from solid-state theory to device applications*. Springer Science & Business Media, 2003. ISBN: 978-3-662-05287-7 (cit. on p. 74).

[Cleuziou et al., 2013] J. P. Cleuziou, N. V. N'Guyen, S. Florens, and W. Wernsdorfer. *Interplay of the Kondo Effect and Strong Spin-Orbit Coupling in Multihole Ultraclean Carbon Nanotubes*. `Physical Review Letters` **111** (13), p. 136803, (Sept. 2013). DOI: `10.1103/PhysRevLett.111.136803` (cit. on pp. 34, 64, 138).

[Cronenwett et al., 1998] S. M. Cronenwett, T. H. Oosterkamp, and L. P. Kouwenhoven. *A tunable Kondo effect in quantum dots*. `Science` **281** (5376), pp. 540–544, (July 1998). DOI: `10.1126/science.281.5376.540` (cit. on p. 30).

[Datta, 1997] S. Datta. *Electronic Transport in Mesoscopic Systems*. Cambridge Studies in Semiconductor Physics and Microelectronic Engineering. Cambridge University Press, 1997, p. 377. ISBN: 0521599431 (cit. on p. 22).

[De Franceschi et al., 2001] S. De Franceschi, S. Sasaki, J. M. Elzerman, W. G. van der Wiel, S. Tarucha, and L. P. Kouwenhoven. *Electron Cotunneling in a Semiconductor Quantum Dot*. `Physical Review Letters` **86** (5), pp. 878–881, (Jan. 2001). DOI: `10.1103/PhysRevLett.86.878` (cit. on pp. 31, 138).

[Deshpande and Bockrath, 2008] V. V. Deshpande and M. Bockrath. *The one-dimensional Wigner crystal in carbon nanotubes*. `Nature Physics` **4**, pp. 314–318, (Mar. 2008). DOI: `10.1038/nphys895` (cit. on p. 64).

[Deshpande et al., 2009] V. V. Deshpande, B. Chandra, R. Caldwell, D. S. Novikov, J. Hone, and M. Bockrath. *Mott insulating state in ultraclean carbon nanotubes*. `Science` **323** (5910), pp. 106–110, (2009). DOI: `10.1126/science.1165799` (cit. on p. 58).

[Desjardins et al., 2017] M. M. Desjardins, J. J. Viennot, M. C. Dartiailh, L. E. Bruhat, M. R. Delbecq, M. Lee, M.-S. Choi, A. Cottet, and T. Kontos. *Observation of the frozen charge of a Kondo resonance*. `Nature` **545** (7652), p. 4, (2017). DOI: `10.1038/nature21704` (cit. on pp. 100, 137, 139).

[Dirnaichner, 2017] A. R. Dirnaichner. *Charge and spin transport in carbon nanotubes: From Coulomb blockade to Fabry-Perot interference*. Dissertation. Universität Regensburg, (Jan. 2017). URL: `https://epub.uni-regensburg.de/33800/` (cit. on pp. 35, 56, 58).

[Dirnaichner et al., 2016] A. Dirnaichner, M. del Valle, K. J. G. Götz, F. J. Schupp, N. Paradiso, M. Grifoni, Ch. Strunk, and A. K. Hüttel. *Secondary Electron Interference from Trigonal Warping in Clean Carbon Nanotubes*. `Physical Review`

`Letters` **117** (16), p. 166804, (Oct. 2016). DOI: `10.1103/PhysRevLett.117.166804` (cit. on pp. 58, 92, 125, 138).

[Eichler et al., 2011] A. Eichler, J. Chaste, J. Moser, and A. Bachtold. *Parametric Amplification and Self-Oscillation in a Nanotube Mechanical Resonator*. `Nano Letters` **11** (7). PMID: 21615135, pp. 2699–2703, (2011). DOI: `10.1021/nl200950d` (cit. on p. 125).

[Eichler et al., 2013] A. Eichler, J. Moser, M. I. Dykman, and A. Bachtold. *Symmetry breaking in a mechanical resonator from a carbon nanotube*. `Nature Communications` **4** (2843) (2013). DOI: `10.1038/ncomms3843` (cit. on pp. 42, 76).

[Enss and Hunklinger, 2000] Ch. Enss and S. Hunklinger. *Tieftemperaturphysik*. Springer-Verlag Berlin Heidelberg, 2000. DOI: `10.1007/978-3-642-57265-4` (cit. on p. 47).

[Fulton and Dolan, 1987] T. A. Fulton and G. J. Dolan. *Observation of single-electron charging effects in small tunnel junctions*. `Physical Review Letters` **59** (1), pp. 109–112, (July 1987). DOI: `10.1103/PhysRevLett.59.109` (cit. on pp. 7, 23).

[Gaass et al., 2011] M. Gaass, A. K. Hüttel, K. Kang, I. Weymann, J. von Delft, and Ch. Strunk. *Universality of the Kondo Effect in Quantum Dots with Ferromagnetic Leads*. `Physical Review Letters` **107** (17), p. 176808, (Oct. 2011). DOI: `10.1103/PhysRevLett.107.176808` (cit. on pp. 35, 42).

[Ganzhorn and Wernsdorfer, 2012] M. Ganzhorn and W. Wernsdorfer. *Dynamics and Dissipation Induced by Single-Electron Tunneling in Carbon Nanotube Nanoelectromechanical Systems*. `Physical Review Letters` **108** (17), p. 175502, (Apr. 2012). DOI: `10.1103/PhysRevLett.108.175502` (cit. on p. 125).

[Gavaler et al., 1972] J. R. Gavaler, M. A. Janocko, and C. K. Jones. *A-15 structure Mo-Re superconductor*. `Applied Physics Letters` **21** (4), pp. 179–180, (1972). DOI: `10.1063/1.1654334` (cit. on p. 103).

[Gerland et al., 2000] U. Gerland, J. von Delft, T. A. Costi, and Y. Oreg. *Transmission Phase Shift of a Quantum Dot with Kondo Correlations*. `Physical Review Letters` **84** (16), pp. 3710–3713, (Apr. 2000). DOI: `10.1103/PhysRevLett.84.3710` (cit. on p. 139).

[Glazman and Shekhter, 1989] L. I. Glazman and R. I. Shekhter. *Coulomb oscillations of the conductance in a laterally confined heterostructure*. `Journal of Physics: Condensed Matter` **1** (33), pp. 5811–5815, (1989). DOI: `10.1088/0953-8984/1/33/027` (cit. on pp. 7, 27).

[Goldhaber-Gordon et al., 1998a] D. Goldhaber-Gordon, J. Göres, M. A. Kastner, H. Shtrikman, D. Mahalu, and U. Meirav. *From the Kondo Regime to the Mixed-Valence Regime in a Single-Electron Transistor*. `Physical Review Letters` **81** (23), pp. 5225–5228, (Dec. 1998). DOI: `10.1103/PhysRevLett.81.5225` (cit. on pp. 33, 70, 100, 138).

[Goldhaber-Gordon et al., 1998b] D. Goldhaber-Gordon, H. Shtrikman, D. Mahalu, D. Abusch-Magder, U. Meirav, and M. A. Kastner. *Kondo effect in a single-electron transistor*. `Nature` **391** (156–159), p. 4, (Jan. 1998). DOI: `10.1038/34373` (cit. on p. 30).

[Gorter, 1951] C. J. Gorter. *A possible explanation of the increase of the electrical resistance of thin metal films at low temperatures and small field strengths*. `Physica` **17** (8), pp. 777–780, (1951). ISSN: 0031-8914. DOI: `10.1016/0031-8914(51)90098-5` (cit. on pp. 7, 23).

[Götz et al., 2016] K. J. G. Götz, S. Blien, P. L. Stiller, O. Vavra, T. Mayer, T. Huber, T. N. G. Meier, M. Kronseder, A. K. Hüttel, and Ch. Strunk. *Co-sputtered MoRe thin films for carbon nanotube growth-compatible superconducting coplanar resonators*. `Nanotechnology` **27** (13), p. 135202, (2016). DOI: `10.1088/0957-4484/27/13/135202` (cit. on pp. 9, 37, 103, 105, 107, 109, 126, 139, 151).

[Grabert and Devoret, 1993] H. Grabert and M. H. Devoret. *Single Charge Tunneling: Coulomb Blockade Phenomena in Nanostructures*. `Physics Today` **46** (4), pp. 62–63, (Apr. 1993). DOI: `10.1063/1.2808874` (cit. on p. 23).

[Gramich et al., 2015] J. Gramich, A. Baumgartner, M. Muoth, C. Hierold, and C. Schönenberger. *Fork stamping of pristine carbon nanotubes onto ferromagnetic contacts for spin-valve devices*. `physica status solidi (b)` **252** (11), pp. 2496–2502, (2015). DOI: `10.1002/pssb.201552213` (cit. on pp. 125, 140).

[Grove-Rasmussen et al., 2007] K. Grove-Rasmussen, H. I. Jørgensen, and P. E. Lindelof. *Fabry–Perot interference, Kondo effect and Coulomb blockade in carbon nanotubes*. `Physica E: Low-dimensional Systems and Nanostructures` **40** (1), pp. 92–98, (2007). ISSN: 1386-9477. DOI: `10.1016/j.physe.2007.05.015` (cit. on pp. 35, 92).

[Häkkinen et al., 2015] P. Häkkinen, A. Isacsson, A. Savin, J. Sulkko, and P. Hakonen. *Charge Sensitivity Enhancement via Mechanical Oscillation in Suspended Carbon Nanotube Devices*. `Nano Letters` **15** (3), pp. 1667–1672, (Feb. 2015). DOI: `10.1021/nl504282s` (cit. on pp. 42, 125).

[Hedman et al., 2015] D. Hedman, H. R. Barzegar, A. Rosén, T. Wågberg, and J. A. Larsson. *On the Stability and Abundance of Single Walled Carbon Nanotubes*. `Scientific Letters` **5** (16850) (2015). DOI: `10.1038/srep16850` (cit. on p. 58).

[Heisenberg, 1927] W. Heisenberg. *über den anschaulichen Inhalt der quantentheoretischen Kinematik und Mechanik*. `Zeitschrift für Physik` **43** (3), pp. 172–198, (Mar. 1927). DOI: `10.1007/BF01397280` (cit. on p. 24).

[Heyd et al., 1997] R. Heyd, A. Charlier, and E. McRae. *Uniaxial-stress effects on the electronic properties of carbon nanotubes*. `Physical Review B` **55** (11), pp. 6820–6824, (Mar. 1997). DOI: `10.1103/PhysRevB.55.6820` (cit. on p. 18).

[Himmler, 2017] W. Himmler. *Stamping of Carbon Nanotubes over trenches using small stamps*. Bachelor thesis. Universität Regensburg, (July 2017) (cit. on p. 140).

[Homma et al., 2009] Y. Homma, S. Chiashi, and Y. Kobayashi. *Suspended single-wall carbon nanotubes: synthesis and optical properties*. `Reports on Progress in Physics` **72** (6), p. 066502, (2009). DOI: `10.1088/0034-4885/72/6/066502` (cit. on p. 140).

[Huang et al., 2008] M. Huang, Y. Wu, B. Chandra, H. Yan, Y. Shan, T. F. Heinz, and J. Hone. *Direct Measurement of Strain-Induced Changes in the Band Structure of Carbon Nanotubes*. `Physical Review Letters` **100** (13), p. 136803, (Apr. 2008). DOI: `10.1103/PhysRevLett.100.136803` (cit. on p. 18).

[Huang et al., 2005] X. M. H. Huang, R. Caldwell, L. Huang, S. C. Jun, M. Huang, M. Y. Sfeir, S. P. O'Brien, and J. Hone. *Controlled Placement of Individual Carbon Nanotubes*. `Nano Letters` **5** (7), pp. 1515–1518, (2005). DOI: `10.1021/nl050886a` (cit. on p. 125).

[Hunklinger, 2007] S. Hunklinger. *Festkörperphysik*. Oldenbourg Wissenschaftsverlag GmbH, 2007. ISBN: 9783486575620 (cit. on p. 22).

[Hüttel, 2005] A. K. Hüttel. *Gekoppelte Quantenpunkte im Bereich niedrigster Elektronenzahlen*. Dissertation. LMU München, (June 2005) (cit. on p. 24).

[Hüttel et al., 2008] A. K. Hüttel, M. Poot, B. Witkamp, and H. S. J. van der Zant. *Nanoelectromechanics of suspended carbon nanotubes*. `New Journal of Physics` **10** (9), p. 095003, (2008). DOI: `10.1088/1367-2630/10/9/095003` (cit. on p. 73).

[Hüttel et al., 2009] A. K. Hüttel, G. A. Steele, B. Witkamp, M. Poot, L. P. Kouwenhoven, and H. S. J. van der Zant. *Carbon Nanotubes as Ultrahigh Quality Factor Mechanical Resonators*. `Nano Letters` **9** (7), pp. 2547–2552, (2009). DOI: `10.1021/nl900612h` (cit. on pp. 8, 76, 77, 125).

[Hüttel et al., 2007] A. K. Hüttel, B. Witkamp, and H. S. J. van der Zant. *Suspended carbon nanotube double quantum dots*. `physica status solidi (b)` **244** (11), pp. 4184–4187, (2007). ISSN: 1521-3951. DOI: `10.1002/pssb.200776182` (cit. on p. 136).

[Hüttner, 2017] N. Hüttner. *Superconducting high-frequency circuits*. Bachelor thesis. Universität Regensburg, (June 2017) (cit. on pp. 114, 139).

[Iijima, 1991] S. Iijima. *Helical microtubules of graphitic carbon*. `Nature` **354** (6348), pp. 56–58, (Nov. 1991). DOI: `10.1038/354056a0` (cit. on pp. 7, 11).

[Iijima and Ichihashi, 1993] S. Iijima and T. Ichihashi. *Single-shell carbon nanotubes of 1-nm diameter*. `Nature` **363** (6430), pp. 603–605, (June 1993). DOI: `10.1038/363603a0` (cit. on pp. 7, 11).

[Imry, 2002] Y. Imry. *Introduction to Mesoscopic Physics*. Mesoscopic physics and nanotechnology. Oxford University Press, 2002. ISBN: 9780198507383 (cit. on p. 22).

[Izumida et al., 2009] W. Izumida, K. Sato, and R. Saito. *SpinOrbit Interaction in Single Wall Carbon Nanotubes: Symmetry Adapted Tight-Binding Calculation and Effective Model Analysis*. `Journal of the Physical Society of Japan` **78** (7), p. 074707, (2009). DOI: `10.1143/JPSJ.78.074707` (cit. on p. 18).

[Jarillo-Herrero et al., 2005a] P. Jarillo-Herrero, J. Kong, H. S. J. van der Zant, C. Dekker, L. P. Kouwenhoven, and S. De Franceschi. *Electronic Transport Spectroscopy of Carbon Nanotubes in a Magnetic Field*. `Physical Review Letters` **94** (15), p. 156802, (Apr. 2005). DOI: `10.1103/PhysRevLett.94.156802` (cit. on p. 35).

[Jarillo-Herrero et al., 2005b] P. Jarillo-Herrero, J. Kong, H. S. J. van der Zant, C. Dekker, L. P. Kouwenhoven, and S. De Franceschi. *Orbital Kondo effect in carbon nanotubes*. `Nature` **434** (7032), pp. 484–488, (Jan. 2005). DOI: `10.1038/nature03422` (cit. on p. 34).

[Johnson et al., 1992] A. T. Johnson, L. P. Kouwenhoven, W. de Jong, N. C. van der Vaart, C. J. P. M. Harmans, and C. T. Foxon. *Zero-dimensional states and single electron charging in quantum dots*. `Physical Review Letters` **69** (10), pp. 1592–1595, (Sept. 1992). DOI: `10.1103/PhysRevLett.69.1592` (cit. on p. 30).

[Kane and Mele, 1997] C. L. Kane and E. J. Mele. *Size, Shape, and Low Energy Electronic Structure of Carbon Nanotubes*. `Physical Review Letters` **78** (10), pp. 1932–1935, (Mar. 1997). DOI: `10.1103/PhysRevLett.78.1932` (cit. on pp. 18, 19).

[Katsnelson, 2007] M. I. Katsnelson. *Graphene: carbon in two dimensions*. `Materials Today` **10** (12), pp. 20–27, (2007). ISSN: 1369-7021. DOI: `10.1016/S1369-7021(06)71788-6` (cit. on p. 15).

[Keijzers, 2012] H. Keijzers. *Josephson effects in carbon nanotube mechanical resonators and graphene*. Dissertation. TU Delft, (Oct. 2012). ISBN: 978-90-8593-130-0 (cit. on pp. 9, 40, 42, 56, 115, 118, 125).

[Kim et al., 2003] W. Kim, A. Javey, O. Vermesh, Q. Wang, Y. Li, and H. Dai. *Hysteresis Caused by Water Molecules in Carbon Nanotube Field-Effect Transistors*. `Nano Letters` **3** (2), pp. 193–198, (2003). DOI: `10.1021/nl0259232` (cit. on pp. 21, 45).

[Kirchhoff, 1845] G. R. Kirchhoff. *Ueber den Durchgang eines elektrischen Stromes durch eine Ebene, insbesondere durch eine kreisförmige*. **Band LXIV**. Annalen der Physik und Chemie. Verlag Johann Ambrosius Barth aus Leipzig, 1845, pp. 497–514. DOI: `10.1002/andp.18451400402` (cit. on p. 21).

[Kondo, 1964] J. Kondo. *Resistance Minimum in Dilute Magnetic Alloys*. `Progress of Theoretical Physics` **32** (1), p. 37, (1964). DOI: `10.1143/PTP.32.37` (cit. on pp. 8, 30, 138).

[Kong et al., 1998a] J. Kong, A. M. Cassell, and H. Dai. *Chemical vapor deposition of methane for single-walled carbon nanotubes*. `Chemical Physics Letters` **292**, pp. 567–574, (Aug. 1998). DOI: `10.1016/S0009-2614(98)00745-3` (cit. on pp. 11, 42, 44).

[Kong et al., 1998b] J. Kong, H. T. Soh, A. M. Cassell, C. F. Quate, and H. Dai. *Synthesis of individual single-walled carbon nanotubes on patterned silicon wafers*. `Nature` **395** (6705), p. 878, (1998). DOI: `10.1038/27632` (cit. on pp. 7, 11, 37, 42, 106, 128, 137).

[Korotkov et al., 1990] A. N. Korotkov, D. V. Averin, and K. K. Likharev. *Theory of single-electron charging of quantum wells and dots*. `Physica B: Condensed Matter` **165–166** (2), pp. 927–928, (Aug. 1990). DOI: `10.1016/S0921-4526(09)80049-5` (cit. on p. 27).

[Kouwenhoven et al., 1997] L. P. Kouwenhoven, C. M. Marcus, P. L. McEuen, S. Tarucha, R. M. Westervelt, and N. S. Wingreen. *Electron transport in quantum dots*. `Proceedings of the Advanced Study Institute on Mesoscopic Electron Transport`, p. 110, (1997). URL: `http://kouwenhovenlab.tudelft.nl/wp-content/uploads/2011/10/60-electron-transport.pdf` (cit. on p. 24).

[Kretinin et al., 2012] A. V. Kretinin, H. Shtrikman, and D. Mahalu. *Universal line shape of the Kondo zero-bias anomaly in a quantum dot*. `Physical Review B` **85** (20), p. 201301, (May 2012). DOI: `10.1103/PhysRevB.85.201301` (cit. on pp. 33, 64, 66, 69, 70, 100, 138).

[Kronseder, 2015] M. Kronseder. Notice. 2015 (cit. on p. 104).

[Kuemmeth et al., 2008] F. Kuemmeth, S. Ilani, D. C. Ralph, and P. L. McEuen. *Coupling of spin and orbital motion of electrons in carbon nanotubes*. `Nature` **452** (7186), pp. 448–452, (Mar. 2008). DOI: `10.1038/nature06822` (cit. on p. 35).

[Kugler, 2013] S. Kugler. *Kohlenstoff-Nanoröhrchen mit supraleitenden Kontakten als nanomechanische Resonatoren*. Master thesis. Universität Regensburg, (Feb. 2013) (cit. on p. 37).

[Kulik and Shekhter, 1975] I. O. Kulik and R. I. Shekhter. *Kinetic phenomena and charge discretness effects in granulated media*. `Sovjet Physics-JETP` **41** (2), pp. 308–316, (Feb. 1975). URL: `http://adsabs.harvard.edu/abs/1975JETP...41..308K` (cit. on pp. 7, 23).

[Laird et al., 2015] E. A. Laird, F. Kuemmeth, G. A. Steele, K. Grove-Rasmussen, J. Nygård, K. Flensberg, and L. P. Kouwenhoven. *Quantum transport in carbon nanotubes*. `Reviews of Modern Physics` **87** (3), pp. 703–764, (July 2015). DOI: `10.1103/RevModPhys.87.703` (cit. on pp. 11, 17, 19, 33).

[Laird et al., 2012] E. A. Laird, F. Pei, W. Tang, G. A. Steele, and L. P. Kouwenhoven. *A High Quality Factor Carbon Nanotube Mechanical Resonator at 39 GHz*. `Nano Letters` **12** (1). PMID: 22111547, pp. 193–197, (2012). DOI: `10.1021/nl203279v` (cit. on p. 125).

[Lassagne et al., 2009] B. Lassagne, Y. Tarakanov, J. Kinaret, D. Garcia-Sanchez, and A. Bachtold. *Coupling Mechanics to Charge Transport in Carbon Nanotube Mechanical Resonators*. `Science` **325** (5944), pp. 1107–1110, (2009). ISSN: 0036-8075. DOI: `10.1126/science.1174290` (cit. on pp. 8, 81).

[Laurent et al., 2010] Ch. Laurent, E. Flahaut, and A. Peigney. *The weight and density of carbon nanotubes versus the number of walls and diameter*. `Carbon` **48** (10), pp. 2994–2996, (2010). ISSN: 0008-6223. DOI: `10.1016/j.carbon.2010.04.010` (cit. on p. 88).

[Le Hur and Simon, 2003] K. Le Hur and P. Simon. *Smearing of charge fluctuations in a grain by spin-flip assisted tunneling*. `Physical Review B` **67** (20), p. 201308, (May 2003). DOI: `10.1103/PhysRevB.67.201308` (cit. on p. 68).

[Lefévre et al., 2005] R. Lefévre, M. F. Goffman, V. Derycke, C. Miko, L. Forró, J. P. Bourgoin, and P. Hesto. *Scaling Law in Carbon Nanotube Electromechanical Devices*. `Physical Review Letters` **95** (18), p. 185504, (Oct. 2005). DOI: `10.1103/PhysRevLett.95.185504` (cit. on p. 76).

[Lerner and Daunt, 1966] E. Lerner and J. G. Daunt. *Thermal and Electrical Conductivities of Mo-Re Alloys in the Superconducting and Normal States*. `Physical Review` **142** (1), pp. 251–258, (1966). DOI: `10.1103/PhysRev.142.251` (cit. on p. 8).

[Liang et al., 2001] W. Liang, M. Bockrath, D. Bozovic, J. H. Hafner, M. Tinkham, and H. Park. *Fabry - Perot interference in a nanotube electron waveguide*. `Nature` **411** (6838), pp. 665–669, (June 2001). DOI: `10.1038/35079517` (cit. on pp. 8, 35).

[Liang et al., 2002] W. Liang, M. Bockrath, and H. Park. *Shell Filling and Exchange Coupling in Metallic Single-Walled Carbon Nanotubes*. `Physical Review Letters` **88** (12), p. 126801, (Mar. 2002). DOI: `10.1103/PhysRevLett.88.126801` (cit. on pp. 25, 35).

[Makarovski et al., 2006] A. Makarovski, L. An, J. Liu, and G. Finkelstein. *Persistent orbital degeneracy in carbon nanotubes*. `Physical Review B` **74** (15), p. 155431, (Oct. 2006). DOI: `10.1103/PhysRevB.74.155431` (cit. on p. 64).

[Makarovski et al., 2007] A. Makarovski, J. Liu, and G. Finkelstein. *Evolution of Transport Regimes in Carbon Nanotube Quantum Dots*. `Physical Review Letters` **99** (6), p. 066801, (Aug. 2007). DOI: `10.1103/PhysRevLett.99.066801` (cit. on pp. 68, 70, 138).

[Meerwaldt, 2013] H. B. Meerwaldt. *Carbon nanotubes as electromechanical resonators*. Dissertation. TU Delft, (Apr. 2013). ISBN: 978-90-8593-151-5 (cit. on p. 92).

[Meerwaldt et al., 2012] H. B. Meerwaldt, G. Labadze, B. H. Schneider, A. Taspinar, Ya. M. Blanter, H. S. J. van der Zant, and G. A. Steele. *Probing the charge of a quantum dot with a nanomechanical resonator*. `Physical Review B` **86** (11), p. 115454, (Sept. 2012). DOI: `10.1103/PhysRevB.86.115454` (cit. on pp. 73, 80, 81, 83, 84, 94, 95, 137, 138).

[Meir et al., 1991] Y. Meir, N. S. Wingreen, and P. A. Lee. *Transport through a strongly interacting electron system: Theory of periodic conductance oscillations*. `Physical Review Letters` **66** (23), pp. 3048–3051, (June 1991). DOI: `10.1103/PhysRevLett.66.3048` (cit. on p. 27).

[Millikan, 1911] R. A. Millikan. *The isolation of an ion, a precision measurement of its charge, and the correction of Stoke's law*. `The Physical Review` **32** (4), pp. 349–397, (Apr. 1911). DOI: `10.1103/PhysRevSeriesI.32.349` (cit. on p. 7).

[Morton et al., 1971] N. Morton, B. W. James, G. H. Wostenholm, D. G. Pomfret, M. R. Davies, and J. L. Dykins. *Superconductivity of molybdenum and tungsten carbides*. `Journal of the Less Common Metals` **25**, pp. 97–106, (Sept. 1971). DOI: `10.1016/0022-5088(71)90070-1` (cit. on p. 107).

[Moser et al., 2014] J. Moser, A. Eichler, J. Güttinger, M. I. Dykman, and A. Bachtold. *Nanotube mechanical resonators with quality factors of up to 5 million*. `Nature Nanotechnology` **9** (12), pp. 1007–1011, (2014). DOI: `10.1038/nnano.2014.234` (cit. on p. 8).

[Moulder et al., 1992] J. F. Moulder, W. F. Stickle, P. E. Sobol, and K. D. Bomben. *Handbook of X-ray Photoelectron Spectroscopy*. 2nd ed. Perkin-Elmer Corporation, Physical Electronics Division, 1992. ISBN: 0-9627026-2-5 (cit. on pp. 104, 106, 110, 112).

[Nygård et al., 1999] J. Nygård, D. H. Cobden, M. Bockrath, P. L. McEuen, and P. E. Lindelof. *Electrical transport measurements on single-walled carbon nanotubes*. `Applied Physics A` **69**, pp. 297–304, (Aug. 1999). DOI: `10.1007/s003399900120` (cit. on p. 8).

[Pallecchi, 2009] E. Pallecchi. *Multiwall carbon nanotube Josephson junctions with niobium contacts*. Dissertation. Universität Regensburg, (Aug. 2009). URL: `https://epub.uni-regensburg.de/12323/` (cit. on p. 118).

[Pallecchi et al., 2008] E. Pallecchi, M. Gaass, and Ch. Strunk. *Carbon nanotube Josephson junctions with Nb contacts*. `Applied Physics Letters` **93**, p. 072501, (2008). DOI: `10.1063/1.2971034` (cit. on p. 9).

[Park et al., 2017] R. S. Park, G. Hills, J. Sohn, S. Mitra, M. M. Shulaker, and H. S. P. Wong. *Hysteresis-Free Carbon Nanotube Field-Effect Transistors*. `ACS Nano`, p. 7, (May 2017). DOI: `10.1021/acsnano.7b01164` (cit. on p. 45).

[Pascal-Levi et al., 2014] Y. Pascal-Levi, E. Shifman, M. Pal-Chowdhury, I. Kalifa, I. Sivan, T. Rabkin, and Y. E. Yaish. *Origin of Hysteresis in Carbon Nanotube Field-Effect Transistors*. `MRS Proceedings` **1659**, pp. 119–128, (2014). DOI: `10.1557/opl.2014.353` (cit. on p. 45).

[Pei et al., 2012] F. Pei, E. A. Laird, G. A. Steele, and L. P. Kouwenhoven. *Valley-spin blockade and spin resonance in carbon nanotubes*. `Nature Nanotechnology` **7** (10), pp. 630–634, (2012). ISSN: 1748-3387. DOI: `10.1038/nnano.2012.160` (cit. on p. 125).

[Poot, 2009] M. Poot. *Mechanical systems at the nanoscale*. Dissertation. TU Delft, (Dec. 2009). ISBN: 978-90-8593-062-4 (cit. on p. 78).

[Poot and van der Zant, 2012] M. Poot and H. S. J. van der Zant. *Mechanical systems in the quantum regime*. `Physics Reports` **511** (5), pp. 273–335, (2012). ISSN: 0370-1573. DOI: `10.1016/j.physrep.2011.12.004` (cit. on pp. 75, 76).

[Postnikov et al., 1977] V. S. Postnikov, V. V. Postnikov, and V. S. Zheleznyi. *Superconductivity in Mo-Re System Alloy Films Produced by Electron Beam Evaporation in High Vacuum*. `physica status solidi (a)` **39**, pp. 21–23, (1977). DOI: `10.1002/pssa.2210390148` (cit. on pp. 8, 103).

[Purewal et al., 2007] M. Purewal, B. H. Hong, A. Ravi, B. Chandra, J. Hone, and P. Kim. *Scaling of Resistance and Electron Mean Free Path of Single-Walled Carbon Nanotubes*. `Physical Review Letters` **98**, p. 186808, (Apr. 2007). DOI: `10.1103/PhysRevLett.98.186808` (cit. on p. 22).

[Radushkevich and Lukyanovich, 1952] L. V. Radushkevich and V. M. Lukyanovich. *On the structure of carbon formed by thermal decomposition of carbon monoxide on iron contacts*. `Zurn Fisic Chim` **26**, pp. 88–95, (1952) (cit. on pp. 7, 11).

[Ralph et al., 1995] D. C. Ralph, C. T. Black, and M. Tinkham. *Spectroscopic Measurements of Discrete Electronic States in Single Metal Particles*. `Physical Review Letters` **74** (16), pp. 3241–3244, (Apr. 1995). DOI: `10.1103/PhysRevLett.74.3241` (cit. on p. 23).

[Reed et al., 1988] M. A. Reed, J. N. Randall, R. J. Aggarwal, R. J. Matyi, T. M. Moore, and A. E. Wetsel. *Observation of discrete electronic states in a zero-dimensional semiconductor nanostructure*. `Physical Review Letters` **60** (6), pp. 535–537, (Feb. 1988). DOI: 10.1103/PhysRevLett.60.535 (cit. on p. 7).

[Saito et al., 1998] R. Saito, G. Dresselhaus, and M. S. Dresselhaus. *Physical Properties of Carbon Nanotubes*. Imperial College Press, 1998. ISBN: 9781860942235 (cit. on pp. 7, 14, 15).

[Sapmaz, 2006] S. Sapmaz. *Carbon nanotube quantum dots*. Dissertation. TU Delft, (June 2006) (cit. on pp. 31, 73).

[Sapmaz et al., 2003] S. Sapmaz, Ya. M. Blanter, L. Gurevich, and H. S. J. van der Zant. *Carbon nanotubes as nanoelectromechanical systems*. `Physical Review B` **67** (23), p. 235414, (June 2003). DOI: 10.1103/PhysRevB.67.235414 (cit. on p. 76).

[Sapmaz et al., 2006] S. Sapmaz, C. Meyer, P. Beliczynski, P. Jarillo-Herrero, and L. P. Kouwenhoven. *Excited State Spectroscopy in Carbon Nanotube Double Quantum Dots*. `Nano Letters` **6** (7). PMID: 16834409, pp. 1350–1355, (2006). DOI: 10.1021/nl052498e (cit. on pp. 25, 42).

[Sazonova et al., 2004] V. Sazonova, Y. Yaish, H. Ustunel, D. Roundy, T. A. Arias, and P. L. McEuen. *A tunable carbon nanotube electromechanical oscillator*. `Nature` **431** (7006), pp. 284–287, (Sept. 2004). ISSN: 0028-0836. DOI: 10.1038/nature02905 (cit. on pp. 8, 73).

[Scanlon et al., 2010] D. O. Scanlon, G. W. Watson, D. J. Payne, G. R. Atkinson, R. G. Egdell, and D. S. L. Law. *Theoretical and Experimental Study of the Electronic Structures of* MoO_3 *and* MoO_2. `The Journal of Physical Chemistry C` **114** (10), pp. 4636–4645, (2010). DOI: 10.1021/jp9093172 (cit. on pp. 104, 112, 139).

[Schmid, 2010] D. R. Schmid. *Growth of ultraclean carbon nanotubes for low temperature transport measurements*. Diploma thesis. Universität Regensburg, (Oct. 2010) (cit. on pp. 8, 31, 37, 137).

[Schmid, 2015] D. R. Schmid. *Suspended cabon nanotubes as electronical and nanoelectromechanical hybrid systems in the quantum limit*. Dissertation. Universität Regensburg, (June 2015). URL: https://epub.uni-regensburg.de/30072/ (cit. on pp. 37, 56, 86, 92, 137).

[Schmid et al., 2015a] D. R. Schmid, S. Smirnov, M. Margánska, A. Dirnaichner, P. L. Stiller, M. Grifoni, A. K. Hüttel, and Ch. Strunk. *Broken SU(4) symmetry in a Kondo-correlated carbon nanotube*. `Physical Review B` **91** (15), p. 155435, (Apr. 2015). DOI: `10.1103/PhysRevB.91.155435` (cit. on pp. 34, 35, 64, 86, 103, 125, 138).

[Schmid et al., 2015b] D. R. Schmid, P. L. Stiller, Ch. Strunk, and A. K. Hüttel. *Liquid-induced damping of mechanical feedback effects in single electron tunneling through a suspended carbon nanotube*. `Applied Physics Letters` **107** (12), p. 123110, (2015). DOI: `10.1063/1.4931775` (cit. on pp. 60, 86, 118, 138).

[Schmid et al., 2012] D. R. Schmid, P. L. Stiller, Ch. Strunk, and A. K. Hüttel. *Magnetic Damping of a carbon nanotube nano-electromechanical resonator*. `New Journal of Physics` **14** (08324) (2012). DOI: `10.1088/1367-2630/14/8/083024` (cit. on pp. 8, 60, 86, 118, 125, 138).

[Schneider, 2014] B. H. Schneider. *Suspended carbon nanotubes coupled to superconducting circuits*. Dissertation. TU Delft, (July 2014). ISBN: 978-94-6186-327-0 (cit. on pp. 42, 103, 115, 118, 140).

[Schneider et al., 2012] B. H. Schneider, S. Etaki, H. S. J. van der Zant, and G. A. Steele. *Coupling carbon nanotube mechanics to a superconducting circuit*. `Scientific Letters` **2** (599) (2012). DOI: `10.1038/srep00599` (cit. on pp. 9, 103, 125).

[Schneider et al., 2014] B. H. Schneider, V. Singh, W. J. Venstra, H. B. Meerwaldt, and G. A. Steele. *Observation of decoherence in a carbon nanotube mechanical resonator*. `Nature Communications` **5** (5819) (2014). DOI: `10.1038/ncomms6819` (cit. on p. 125).

[Schupp, 2014] F. J. Schupp. *Novel contact materials for carbon-nanotube nano-electromechanical resonators*. Master thesis. Universität Regensburg, (June 2014) (cit. on pp. 37, 40, 55, 78, 103).

[Seleznev et al., 2008] V. A. Seleznev, M. A. Tarkhov, B. M. Voronov, I. I. Milostnaya, V. Y. Lyakhno, A. S. Garbuz, M. Y. Mikhailov, O. M. Zhigalina, and G. N. Gol'tsman. *Deposition and characterization of few-nanometers-thick superconducting Mo-Re films*. `Superconductor Science and Technology` **21**, p. 115006, (2008). DOI: `10.1088/0953-2048/21/11/115006` (cit. on pp. 8, 103, 104, 106, 110, 112).

[Singh et al., 2014] V. Singh, B. H. Schneider, S. J. Bosman, E. P. J. Merkx, and G. A. Steele. *Molybdenum-rhenium alloy based high-Q superconducting mircowave resonators*. `Applied Physics Letters` **105**, p. 222601, (2014). DOI: 10.1063/1.4903042 (cit. on pp. 109, 110).

[Sprinzak et al., 2002] D. Sprinzak, Y. Ji, M. Heiblum, D. Mahalu, and H. Shtrikman. *Charge Distribution in a Kondo-Correlated Quantum Dot*. `Physical Review Letters` **88** (17), p. 176805, (Apr. 2002). DOI: 10.1103/PhysRevLett.88.176805 (cit. on pp. 8, 24, 137, 139).

[Steele et al., 2009a] G. A. Steele, G. Götz, and L. P. Kouwenhoven. *Tunable few-electron double quantum dots and Klein tunnelling in ultraclean carbon nanotubes*. `Nature Nanotechnology` **4** (6), pp. 363–367, (Apr. 2009). ISSN: 1748-3387. DOI: 10.1038/nnano.2009.71 (cit. on pp. 42, 125).

[Steele et al., 2009b] G. A. Steele, A. K. Hüttel, B. Witkamp, M. Poot, Meerwaldt H. B., L. P. Kouwenhoven, and H. S. van der Zant. *Strong coupling between single-electron tunneling and nanomechanical motion*. `Science` **325** (5944), pp. 1103–1107, (Aug. 2009). DOI: 10.1126/science.1176076 (cit. on pp. 8, 37, 60, 73, 80, 81, 125, 137, 138).

[Steger, 2015] P. Steger. *Grundlagen zum Stempeln von Carbon Nanotubes*. Bachelor thesis. Universität Regensburg, (Aug. 2015) (cit. on pp. 40, 127, 129, 130).

[Stiller et al., 2013] P. L. Stiller, S. Kugler, D. R. Schmid, Ch. Strunk, and A. K. Hüttel. *Negative frequency tuning of a carbon nanotube nano-electromechanical resonator under tension*. `physica status solidi (b)` **250** (12), pp. 2518–2522, (2013). DOI: 10.1002/pssb.201300073 (cit. on pp. 37, 56, 103).

[Stoecker and Hartnack, 2007] H. Stöcker and C. Hartnack. *Taschenbuch der Physik*. 5th ed. Verlag Harri Deutsch, 2007. ISBN: 3-8171-1720-5 (cit. on p. 106).

[Strunk, 2010] Ch. Strunk. *Tieftemperaturphysik-Vorlesungsskript*. 2010 (cit. on p. 47).

[Talvacchio et al., 1986] J. Talvacchio, M. A. Janocko, and J. Greggi. *Properties of Evaporated Mo-Re Thin-Film Superconductors*. `Journal of Low Temperature Physics` **64**, pp. 395–408, (1986). DOI: 10.1007/BF00681709 (cit. on pp. 103, 104).

[Tans et al., 1997] S. J. Tans, M. H. Devoret, H. Dai, A. Thess, R. E. Smalley, L. J. Geerligs, and C. Dekker. *Individual single-wall carbon nanotubes as quantum wires*. `Nature` **386** (6624), pp. 474–477, (Apr. 1997). DOI: 10.1038/386474a0 (cit. on pp. 8, 23).

[Testardi et al., 1971] L. R. Testardi, J. J. Hauser, and M. H. Read. *Enhanced Superconducting T_c and structural transformation in Mo-Re Alloys*. `Solid State Communications` **9**, pp. 1829–1831, (1971). DOI: `10.1016/0038-1098(71)90100-1` (cit. on p. 103).

[Thijssen and van der Zant, 2008] J. M. Thijssen and H. S. J. van der Zant. *Charge transport and single-electron effects in nanoscale systems*. `physica status solidi (b)` **245** (8), pp. 1455–1470, (2008). ISSN: 1521-3951. DOI: `10.1002/pssb.200743470` (cit. on p. 52).

[Tinkham and McKay, 1996] M. Tinkham and G. McKay. *Introduction to Superconductivity*. 2nd ed. Dover Publications, Inc., 1996. ISBN: 0-486-43503-2 (cit. on p. 109).

[Usmani, 2006] O. A. Usmani. *Strong Feedback in Nanoelectromechanical Systems*. Dissertation. TU Delft, (Dec. 2006). ISBN: 978-90-8593-023-5 (cit. on pp. 60, 118, 138).

[Ventura and Risegari, 2008] G. Ventura and L. Risegari. *The Art of Cryogenics - Low-Temperature Experimental Techniques*. 1st ed. Elsevier, 2008. ISBN: 978-0-08-044479-6 (cit. on p. 47).

[Viennot et al., 2014] J. J. Viennot, J. Palomo, and T. Kontos. *Stamping single wall nanotubes for circuit quantum electrodynamics*. `Applied Physics Letters` **104**, p. 133108, (Mar. 2014). DOI: `10.1063/1.4868868` (cit. on pp. 125, 126).

[von Klitzing et al., 1980] K. von Klitzing, G. Dorda, and M. Pepper. *New Method for High-Accuracy Determination of the Fine-Structure Constant Based on Quantized Hall Resistance*. `Physical Review Letters` **45** (6), pp. 494–497, (Aug. 1980). DOI: `10.1103/PhysRevLett.45.494` (cit. on p. 22).

[Waissman et al., 2013] J. Waissman, M. Honig, S. Pecker, A. Benyamini, A. Hamo, and S. Ilani. *Realization of pristine and locally tunable one-dimensional electron systems in carbon nanotubes*. `Nature Nanotechnology` **8**, pp. 569–574, (Aug. 2013). DOI: `10.1038/nnano.2013.143` (cit. on pp. 125, 126, 140).

[White and Todorov, 2001] C. T. White and T. N. Todorov. *Quantum electronics: Nanotubes go ballistic*. `Nature` **411** (6838), pp. 649–651, (June 2001). DOI: `10.1038/35079720` (cit. on p. 35).

[Wiberg et al., 1995] N. Wiberg, E. Wiberg, and A. F. Hollemann. *Lehrbuch der anorganischen Chemie*. 101st ed. Gruyter, 1995. ISBN: 3-11-012641-9 (cit. on pp. 106, 113).

[Wilson, 1975] K. G. Wilson. *The renormalization group: Critical phenomena and the Kondo problem*. `Review of Modern Physics` **47** (4), pp. 773–840, (Oct. 1975). DOI: `10.1103/RevModPhys.47.773` (cit. on p. 30).

[Wingreen and Meir, 1994] N. S. Wingreen and Y. Meir. *Anderson model out of equilibrium: Noncrossing-approximation approach to transport through a quantum dot*. `Physical Review B` **49** (16), pp. 11040–11052, (Apr. 1994). DOI: `10.1103/PhysRevB.49.11040` (cit. on pp. 100, 139).

[Witkamp et al., 2006] B. Witkamp, M. Poot, and H. S. J. van der Zant. *Bending-Mode Vibration of a Suspended Nanotube Resonator*. `Nano Letters` **6** (12). PMID: 17163728, pp. 2904–2908, (2006). DOI: `10.1021/nl062206p` (cit. on pp. 73, 76).

[Wu et al., 2010] C. C. Wu, C. H. Liu, and Z. Zhong. *One-Step Direct Transfer of Pristine Single-Walled Carbon Nanotubes for Functional Nanoelectronics*. `Nano Letters` **10** (3), pp. 1032–1036, (2010). DOI: `10.1021/nl904260k` (cit. on p. 125).

[Yang and Han, 2000] L. Yang and J. Han. *Electronic Structure of Deformed Carbon Nanotubes*. `Physical Review Letters` **85** (1), pp. 154–157, (July 2000). DOI: `10.1103/PhysRevLett.85.154` (cit. on p. 18).

[Zhou et al., 2005] X. Zhou, J.-Y. Park, S. Huang, J. Liu, and P. L. McEuen. *Band Structure, Phonon Scattering, and the Performance Limit of Single-Walled Carbon Nanotube Transistors*. `Physical Review Letters` **95** (14), p. 146805, (Sept. 2005). DOI: `10.1103/PhysRevLett.95.146805` (cit. on p. 16).

Acknowledgments

At this point, I would like to thank everyone for support of all manner during the last years.

First of all, thanks to PD Dr. Andreas Hüttel for the possibility to work on this interesting topic. This includes the help at all time of day concerning the supervision of the PHD thesis, publications, as well as technical and physical questions. This excellent mentoring is basis for the success of this thesis. Thank you very much!

Prof. Dr. Dieter Weiss let me work in his clean room and Prof. Dr. Christoph Strunk at his fabrication devices and cryostat setups. Thanks for this chance.

Besides the supervisors for the setups, the functionality of the equipment and organization of the chair is guaranteed by the efficiency of the technicians and secretaries, namely Uli Gürster, Thomas Haller, Daniel Pahl, Michael Weigl, Claudia Moser, and Elke Haushalter. Thank you all for all the help and assistance.

The awareness of the importance of team work was obtained during the last years. In our team, everyone brings in his own expertise but also needs the help and knowledge of the others. Thanks to Dr. Daniel Schmid for the familiarization of the carbon nanotube physics, Stefan Blien especially for the help with the dilution cryostat setup, Dr. Alois Dirnaichner and his programming skills, the former master students Felix Schupp and Dominik Berndt for the fabrication assistance, Thomas Huber, Alex Feigl and Pascal Brunner. The progress of the group is also continued by the current master and bachelor students Alexander Albang, Patrick Steger, Wolfgang Himmler, Niklas Hüttner, and Simon Reinhardt.

Thanks to other chair members for important advices over the years, Dr. Nicola Paradiso, Dr. Jonathan Eroms, Markus Ehlert, Michael Schafberger, Martin Oltscher, Robin Huber, Paul Linsmaier and Thomas Kuczmik.

Together with the supervisors of the XPS setup of the chair Prof. Dr. Back, Dr. Matthias Kronseder and Thomas Meier, it was possible to get a precise insight into our molybdenum rhenium alloys.

Special thanks go to the technicians responsible for the helium liquefaction setup, Thomas Solleder and Christian Heimerl.
Similarly thanks to the technicians of the mechanic workshop around Gerhard Armer and the electronic workshop around Dieter Riedl.

Last but not least, the most important acknowledgments go to my family.

Curriculum Vitae

Karl Johann Georg Götz, born on 25/12/1987 in Regensburg.

Education and research experience

11/2013 - 01/2018	**University of Regensburg: Faculty for Physics – Ph.D. student**
Thesis	*Carbon Nanotube quantum dots: Transport, mechanical charge*
this document	*detection, and fabrication development*
10/2010 - 02/2013	**University of Regensburg: Faculty for Physics – Master studies**
Thesis	*Magnetwiderstand in InAs-Quantentrögen und Nanostrukturen*
02/2013	Degree: Master of Science, Physics
10/2007 - 09/2010	**University of Regensburg: Faculty for Physics – Bachelor studies**
Thesis	*Untersuchung aluminiumoxidbeschichteter Graphen-Proben*
	mit dem Rasterkraftmikroskop Dimension Icon
02/2011	Degree: Bachelor of Science, Physics
09/1998 - 07/2007	**Gymnasium Parsberg**
07/2007	A-levels
09/1994 - 08/1998	**Grundschule Parsberg**

Publications

- K. J. G. Götz, D. R. Schmid, F. J. Schupp, P. L. Stiller, Ch. Strunk, and A. K. Hüttel: *Nanomechanical characterization of the Kondo charge dynamics in a carbon nanotube*; arXiv:1802.00522 (2018).
- A. Dirnaichner, M. del Valle, K. J. G. Götz, F. J. Schupp, N. Paradiso, M. Grifoni, Ch. Strunk, and A. K. Hüttel: *Secondary electron interference from trigonal warping in clean carbon nanotubes*; Physical Review Letters **117**, 166804, (2016).
- S. Blien, K. J. G. Götz, P. L. Stiller, T. Mayer, T. Huber, O. Vavra, and A. K. Hüttel: *Towards carbon nanotube growth into superconducting microwave resonator*; Physica Status Solidi (b) **253**, 12, 2385, (2016).
- K. J. G. Götz, S. Blien, P. L. Stiller, O. Vavra, T. Mayer, T. Huber, T. N. G. Meier, M. Kronseder, Ch. Strunk, and A. K. Hüttel: *Co-sputtered MoRe thin films for carbon nanotube growth-compatible superconducting coplanar resonators*; Nanotechnology **27**, 13, 135202, (2016).
- K. J. G. Götz, F. J. Schupp, D. R. Schmid, A. Pfeffer, Ch. Strunk, and A. K. Hüttel: *Modulated driving of a Carbon Nanotube Resonator*; Internal proceedings of the Research Trainee Group 1570, (2014).

Conferences

- Frühjahrstagung der Deutschen Physikalischen Gesellschaft; Regensburg, 06 - 11/03/2016; Poster, title: Co-sputtered MoRe as carbon nanotube growth-compatible superconductor.
- Winter school of the Johannes-Kepler-Universität Linz; Mauterndorf, 21 - 26/02/2016; Poster, title: Vibrational detection of the charging of a quantum dot in the Kondo regime.
- Internal Workshop of the Research Trainee Group 1570; Schönsee, 24 - 25/09/2014; Talk, title: Modulated driving of a Carbon Nanotube Resonator.

Nachträgliche Änderungen

- Seite 2: der Kolloquiumstermin wurde hinzugefügt mit dem Satz "*Das Kolloquium fand am 30.01.2018 statt*".
- Seite 16: die Formel im Satz "*..., known as quantization lines and running at an angle* $\pi/3+\theta$ *from the* k_x*-axis*" wurde umgeändert zu $\pi/2+\theta$.
- Seite 27: die Gleichung 2.25, $\Phi_{\mathrm{dot}} = \frac{Q}{C_\Sigma} + \frac{C_\mathrm{s}}{C_\Sigma} \cdot V_\mathrm{sd} + \frac{C_\mathrm{s}}{C_\Sigma} \cdot V_\mathrm{g}$, wurde korrigiert zu $\Phi_{\mathrm{dot}} = \frac{Q}{C_\Sigma} + \frac{C_\mathrm{s}}{C_\Sigma} \cdot V_\mathrm{sd} + \frac{C_\mathrm{g}}{C_\Sigma} \cdot V_\mathrm{g}$.
- Seite 28: die Formel $\frac{\mathrm{d}V_\mathrm{sd}}{\mathrm{d}V_\mathrm{g}} = -\frac{C_\mathrm{g}}{C_\Sigma} < 0$ wurde korrigiert zu $\frac{\mathrm{d}V_\mathrm{sd}}{\mathrm{d}V_\mathrm{g}} = -\frac{C_\mathrm{g}}{C_\mathrm{s}} < 0$.
- Seite 28: die Gleichung 2.33, $\lambda_1 = \frac{\Delta V_\mathrm{sd,1}}{\Delta V_\mathrm{g} - \Delta V_\mathrm{g,1}} = \frac{\Delta V_\mathrm{sd,2}}{\Delta V_\mathrm{g,2}} \equiv -\frac{C_\mathrm{g}}{C_\Sigma}$, wurde korrigiert zu $\lambda_1 = \frac{\Delta V_\mathrm{sd,1}}{\Delta V_\mathrm{g} - \Delta V_\mathrm{g,1}} = \frac{\Delta V_\mathrm{sd,2}}{\Delta V_\mathrm{g,2}} \equiv -\frac{C_\mathrm{g}}{C_\mathrm{s}}$.
- Seite 30: der Satz "*The additional density of states now leads to an even larger coupling between dot and leads, opening the tunneling barriers up*" wurde abgeändert zu "*An additional density of states leads to an even larger coupling between dot and leads, opening the tunneling barriers up*".
- Seite 33: Änderung des Wortes "*exited*" zu "*excited*".
- Seite 35: Einfügen des Wortes "*to*" in den Satz "*By applying an external B-field perpendicular to the nanotube axis, the four energy levels are resolved due to Zeeman-splitting* $g\mu_\mathrm{B}B_\perp$".
- Seite 48, Abbildung 3.6, Funktionsskizze links: der 1K-Topf (das graue Rechteck) ist nun so gezeichnet, dass er nicht mehr in Kontakt mit der Stillleitung steht.
- Seite 55: Entfernung des Wortes "*dry*" aus dem Satz "*The low-temperature measurements were carried out in the dry dilution cryostat which is presented in section 3.4, and including the first dc filtering setup, see Figure 3.7(a)*".

- Seite 64: der Satz "*It costs less energy to add an electron to the next orbital state than putting an electron into a level already filled with one having the other spin state*" wurde gestrichen.

- Seite 83: der Satz "*The width of the tunneling barriers between leads and dots is stated as prefactors* a_L*, respectively* a_R *to the tunneling integrals*" wurde abgeändert zu "*The width of the tunneling barriers between leads and dot is stated as prefactors* a_L*, respectively* a_R *to the tunneling integrals*".

- Seite 88: Einfügen des Wortes "*dot*" in den Satz "C_Σ *has to be adjusted for the same reasons as* C_g *to the value obtained from equation 5.10: the length of the resonator, respectively the vibrating CNT is not equal to spatial dimension of the quantum dot in this charging state*".

- Seite 88: Entfernung des Wortes "*of*" aus dem Satz "*The results of are plotted in Figure 5.6, showing the experimental data as well as resulting fits*".

- Seite 105, Bildunterschrift der Abbildung 6.1: das Wort "*sputtering*" im Satz "*The black line represents the chemical composition of the as-grown sample surface, the red line was recorded after removing approximately 5 nm of the film by in-situ argon-ion sputtering beam sputtering within the XPS chamber*" wurde entfernt.

- Seite 133: der Halbsatz "*...: this measurement reveals additional structures which cannot be attributed to a single quantum dot in the system*" wurde abgeändert zu "*...: this measurement reveals additional structures which cannot be attributed to only one quantum dot in the system*".

- Seite 145: die Überschrift von Abschnitt A.3, "*Optical Lithography*", wurde abgeändert zu "*Optical lithography*".

- Seite 155: die Überschrift von Abschnitt A.8, "*Reactive Ion Etching*" wurde abgeändert zu "*Reactive ion etching (RIE)*".

- Seite 157: die Überschrift von Abschnitt A.9, "*Carbon Nanotube Growth Catalyst*" wurde abgeändert zu "*Carbon nanotube growth catalyst*".

- Seite 191, Lebenslauf: der Zeitabschnitt für die Promotionsphase wurde von "*11/2013 - present*" zu "*11/2013 - 01/2018*" abgeändert.

- Seite 192, Publikationsliste: der inzwischen eingereichte Artikel mit den Ergebnissen aus den Kapiteln 4 und 5 wurde mitaufgenommen.